Master's thesis

NTNU
Norwegian University of Science and Technology
Faculty of Natural Sciences
Department of Materials Science and Engineering

Vibeke Rogde

Low-temperature microwave synthesis of ternary-layered 2D BiOCl crystals in a confined-space

Master's thesis in Chemical Engineering and Biotechnology
Supervisor: Ingrid Hallsteinsen
June 2022

NTNU
Norwegian University of
Science and Technology

Vibeke Rogde

Low-temperature microwave synthesis of ternary-layered 2D BiOCl crystals in a confined-space

Master’s thesis in Chemical Engineering and Biotechnology
Supervisor: Ingrid Hallsteinsen
June 2022

Norwegian University of Science and Technology
Faculty of Natural Sciences
Department of Materials Science and Engineering

NTNU
Norwegian University of
Science and Technology

Abstract

The increase in both emissions and pollutants is a direct consequence of an increase in urbanization and industrialization. Degradation of these pollutants can be achieved by the use of photocatalysts. A photocatalyst attracting attention is the 2D ternary layered BiOCl material. This structure has a wide tunable band gap, controllable growth of (001) facets favorable for photocatalytic activity and a stable structure which can also be tuned to better fit photocatalytic applications. Current methods of synthesizing BiOCl are associated with certain limitations such as the utilization of organic solvents, longer reaction time, lower production rate which makes them incompatible with industry-scale production. A space-confined, microwave-assisted method is currently being researched as an alternative approach.

In this thesis, a conventional microwave oven was utilized in order to synthesize 2D BiOCl crystals on silica and mica substrates. This method is fast, clean, applicable to industry, has low cost and low energy consumption and is environmentally friendly. The aim is to synthesize uniform, large-area, atomically thin, stoichiometric, and crystalline BiOCl. A variety of parameters were changed to investigate their eventual influence on crystal size and morphology. This was done to contribute to a categorization of growth parameters for the method and to achieve a controllable method of synthesizing BiOCl with a microwave oven. Characterization of the as-synthesized crystals was done with optical microscope, scanning electron microscope, energy-dispersive X-ray spectroscopy, Raman spectroscopy, atomic force microscopy and X-ray diffraction.

The parameters studied were microwave time, distance from the magnetron, microwave power, growth on mica substrates while changing microwave power and amount of precursor $BiCl_3$. Different morphologies were detected, among the most prominent were squares, octagons, and flowers. The resulting BiOCl squares had a size range of 11 to 24 µm with a thickness of 40 to 153 nm. For octagons the size was around 3 to 13 µm and thickness range of 40 to 170 nm. The flowers petals exhibited a thickness of 280 to 480 nm. These also had an enhanced exposure of (001) facets compared to a standard random-oriented BiOCl sample, and this facet is favorable for photocatalytic activity. The largest squares were generated by using a large amount of precursor on silica substrates in a confined space placed in the center of the microwave oven, and heated for 1 min at a power of 900 W. From the results it is hypothesized that octagons formed first when the diffusion of atoms was low, then squares grew which upon further diffusion resulted in a self-assembly process generating flowers. Octagons and squares were predominating on silica, whereas flowers were mostly observed on mica.

Sammendrag

Økningen i både utslipp og miljøgifter har vært en direkte konsekvens av den økende graden av urbanisering og industrialisering i verden. Nedbryting av disse forurensingene kan oppnås ved å bruke fotokatalysatorer. En fotokatalysator som har vekket interesse på dette området er 2D BiOCl materiale med en ternær lagdeling. Denne strukturen har et stort justerbart båndgap, kontrollerbar vekst av (001) gitterplan gunstig for fotokatalytisk bruk og en stabil struktur som også kan justeres til å bedre passe fotokatalytiske anvendelser. De eksisterende metodene for å syntetisere BiOCl kommer med en rekke begrensinger, som for eksempel, bruk av organisk løsemidler, lang reaksjonstid og lavere produksjonsrate, noe som gjør de inkompatible for produksjon på et industrielt nivå. En mikrobølge-assistert og plass-begrenset metode er under utvikling som et alternativ til de tradisjonelle metodene.

I denne avhandlingen ble en konvensjonell mikrobølgeovn brukt for å syntetisere 2D BiOCl krystaller på silica og mica substrater. Denne metoden er rask, ren, billig, bruker lite energi og er miljøvennlig. Dermed kan den være mer aktuelt for industriell produksjon. Målet er å syntetisere uniformt tynne, støkiometrisk og krystallinsk BiOCl med stort overflateareal. En rekke parameter ble justert under syntetiseringen for å kartlegge effekten på de syntetiserte krystallenes størrelse og morfologi. Dette ble gjort med mål om å danne en kategorisering av parametere for vekst for denne metoden og for å oppnå en kontrollerbar metode for syntetisering av BiOCl ved hjelp av en mikrobølgeovn. Karakterisering av de syntetiserte krystallene ble gjort ved bruk av optisk mikroskop, skanning elektronmikroskop, energidispersiv røntgenspektroskopi, Ramanspektroskopi, atomkraftmikroskopi og røntgendiffraksjon.

Parameterne studert var tid i mikrobølgeovnen, avstand fra magnetron i ovnen, effekt på ovnen, vekst på mica substrat ved varierende effekt på ovnen og mengde forløper $BiCl_3$. Forskjellige morfologier ble oppdaget, hvor de mest fremtredende var firkanter, åttekanter og blomster. BiOCl firkantene hadde en størrelse i rekkevidden 11 til 24 µm med en tykkelse på 40 til 153 nm. For åttekantene var størrelsen i rekkevidden 3 til 13 µm med tykkelse på 40 til 170 nm. Blomster "bladene" hadde en tykkelse på 280 til 480 nm. Disse hadde også en økt eksponering av (001) gitterplan sammenlignet med en ordinær tilfeldig orientert BiOCl prøve, som er gunstig for fotokatalytiske anvendelser. De største firkantene oppstod ved å bruke stor mengde forløper plassert på silica substrat i midten av mikrobølgeovnen og varmet i 1 min med en effekt på 900 W. Resultatet viser at det kan antas at åttekanter formes først når diffusjon av atomer var lav, deretter formes firkanter som ved økende diffusjon resulterer i en sammenslåingsprosess og dannelsen av blomstrer. Åttekanter og firkanter var dominerende på silica og blomster dominerte på mica.

Preface

This thesis is performed in aspiration of further investigating the research done in TMT4500 Specialization Project during Fall semester of 2021 [1]. Parts of the theory and method sections are based on the work conducted in the Specialization Project.

The research carried out in the Specialization Project was conducted during Fall semester 2021 in lab 148, Hearst Memorial Mining Building at UC Berkeley under supervision of professor Zakaria Al Balushi and by remote supervision from professor Ingrid Hallsteinsen, NTNU. During Spring semester 2022, the research and subsequent characterizations were done in Nanolab, Chemistry Block 1, Natural Science Building at NTNU in Trondheim under supervision by professor Ingrid Hallsteinsen.

Acknowledgments

The Research Council of Norway is acknowledged for the support to the Norwegian Micro- and Nano-Fabrication Facility, NorFab. Appreciation is given to fellow Al Balushi research member Jiayun Liang who shared preliminary research results aiding the discussion. Thanks to Jennifer Toy for making an initial step-by-step method. I would also like to thank my supervisor Ingrid for valuable input and support.

Last but not least, I would like to thank my supportive parents.

Vibeke Rogde
Trondheim, June 2022

Table of Contents

Abstract i

Sammendrag iii

Preface v

List of Figures x

List of Tables xiii

1 Introduction 1

1.1 Proposed technical approach and contribution . . . 1

1.2 Outline . . . 2

2 Theory 3

2.1 2D materials . . . 3

2.1.1 Different structures . . . 4

2.2 BiOCl properties and applications . . . 6

2.2.1 Photocatalysis . . . 6

2.2.2 BiOX . . . 7

2.2.3 BiOCl structure . . . 8

2.2.4 Band gap engineering and photocatalytic properties of BiOCl . . . 9

2.2.5 Defects and their influence on properties . . . 11

2.3 Synthesis of BiOCl . . . 13

2.3.1 Wet-chemistry approach . . . 13

2.3.2 Dry-chemistry approach . . . 15

2.3.3 Space-confined synthesis . . . 15

2.3.4 Microwave oven synthesis . . . 16

2.3.5 Space-confined microwave oven synthesis . . . 18

2.3.6 Hydrolysis of $BiCl_3$ . . . 18

2.3.7 Silica and mica substrates . . . 19

2.4 Crystallization of BiOCl . . . 22

2.4.1 Growth mechanism . . . 22

2.4.2 Solid-state decomposition in a microwave oven . . . 23

2.4.3 Nanoframes . . . 24

2.4.4 Surface cracks . . . 26

2.4.5 Flower-like structure 27
2.5 Experimental methods 30
2.5.1 Scanning electron microscopy (SEM) 30
2.5.2 Energy dispersive spectroscopy (EDS) 30
2.5.3 Raman spectroscopy 31
2.5.4 X-ray diffraction (XRD) 33
2.5.5 Atomic force microscopy (AFM) 35

3 Experimental **36**
3.1 Substrate preparation 36
3.2 Glovebox 36
3.3 Synthesis method 37
3.4 Parameter change 37
3.4.1 Synthesis challenges 38
3.5 Optical microscope (OM) 39
3.6 Scanning electron microscopy (SEM) 39
3.7 Energy dispersive spectroscopy (EDS) 40
3.8 Atomic force microscopy (AFM) 40
3.9 Raman spectroscopy 40
3.10 X-Ray diffraction (XRD) 41

4 Results **42**
4.1 Synthesis results 42
4.1.1 Overview 42
4.1.2 Morphology 42
4.1.3 Synthesis parameter 49
4.1.4 Microwave time 50
4.1.5 Distance from magnetron 51
4.1.6 Microwave power 52
4.1.7 Mica with microwave power change 54
4.1.8 Amount of source 55
4.1.9 Substrate location 57
4.1.10 Size distribution of silica N 60
4.2 Energy dispersive X-ray spectroscopy (EDS) results 62
4.3 Atomic force microscopy (AFM) results 66
4.4 Raman spectroscopy results 69

4.5 X-ray diffraction (XRD) results . . . 75

5 Discussion **79**

5.1 Growth trend . . . 79

5.2 Observed structures . . . 81

5.2.1 Squares, Octagons and Flowers . . . 81

5.2.2 Nanoframe . . . 86

5.2.3 Surface cracks . . . 87

5.2.4 Stacked structures . . . 87

5.3 Synthesis conditions . . . 88

5.3.1 Microwave time . . . 88

5.3.2 Distance . . . 89

5.3.3 Microwave power . . . 90

5.3.4 Mica with power change . . . 91

5.3.5 Amount of source . . . 92

5.3.6 Precursor treatment . . . 93

5.3.7 Confined space . . . 93

5.3.8 Microwave oven . . . 93

5.4 Sources of error . . . 94

6 Conclusion **95**

6.1 Further work . . . 96

Bibliography **97**

Appendix **111**

A Additional OM images . . . 111

B SEM size analysis . . . 112

C Additional EDS results . . . 114

D Additional AFM images . . . 116

D.1 Observations done . . . 116

D.2 Large octagons . . . 117

D.3 Nanoframes . . . 118

D.4 Color and thickness analysis . . . 119

E XRD calculations . . . 122

F Synthesis with varying amount of source . . . 123

G Code . . . 125

List of Figures

1 The figure illustrates the categorization of nanomaterials based on dimensionality [24]. 5

2 A schematic simplification of the working principle of a photocatalyst. 6

3 The application of various BiOX structures [13]. 8

4 The figure displays the structure of BiOCl [38], illustrating a) front view, b) top view and c) decahedral geometry. 8

5 The figure illustrates the structure of mica. 20

6 The figure illustrates the structure of silica, SiO_2/Si [116]. 21

7 The figure illustrates proposed growth direction of octagons and squares in literature [123]. 23

8 Illustration of a nanoframe [132]. 24

9 Illustration of the different types of cracks forming on square BiOCl and rounder square BiOCl [142]. 26

10 Illustration of three simultaneously prepared parallels for each parameter change. 37

11 Illustration of a quartz combustion boat with stacked substrates inside the microwave oven. 37

12 Schematic outline of the parameter changes during the synthesis scheme performed in this thesis. 38

13 Squares, octagon and flowers on a silica substrate imaged with OM and SEM. 43

14 The three most common morphologies in this thesis [1]. 43

15 Octagon and circle observed in SEM and OM. 44

16 Squares imaged with OM and SEM. 44

17 Various BiOCl nanoframes detected in OM and SEM. 45

18 Layered BiOCl crystals. 45

19 Flowers imaged in OM and SEM. 46

20 Broken or cracked BiOCl crystals images with OM and SEM. 47

21 Screw dislocation noticed in SEM. 47

22 Various layered BiOCl shapes discovered in SEM and OM. 48

23 Irregular shapes of unreacted precursor discovered in SEM and OM. 48

24 Layered crystals exhibiting various morphology. 49

25 Illustration of how the substrate was divided for size distribution analysis. 49

26 Illustration of size difference of 1 min vs 3 min at 1.1 with a scale bar of 50 µm. 50

(a) 1 min 50

(b) 3 min 50

27 Size analysis of microwave time synthesis. 50

(a) Squares 50

(b) Octagons 50

28 Shape comparison between Si-9.5cm and Si-15.5cm in section 1. 51

(a) Irregular shapes with stacking Si-9.5cm. 51

(b) Well-defined squares Si-15.5cm. 51

29 Size analysis of distance synthesis. 52

(a) Squares 52

(b) Octagons 52

30 Shape comparison between Si-900W and Si-750W at 1.2. 53

(a) Si-900W 53

(b) Si-750W 53

31 Size analysis of microwave power. 53

(a) Squares 53

(b) Octagons 53

32 1.1 overview images showing shape comparison between Mica-750W and Mica-500W. 54

(a) Mica-750W 54

(b) Mica-500W 54

33 Shape comparison on Mica-500W, Mica-750W and Mica-900W at section 2. 54

(a) Mica-500W 54

(b) Mica-750W 54

(c) Mica-900W 54

34 Size analysis of mica and microwave power. 55

(a) Squares 55

(b) Flower petals 55

35 Comparison between Si-small and Si-large in section 1. 56

(a) Vacant space at Si-small. 56

(b) Crystals on Si-large. 56

36 Size analysis of amount of source synthesis. 56

(a) Squares 56

(b) Octagons 56

37 Schematic illustration of the growth trend across N silica. 57

38 Observed trend on silica N taken at UC Berkeley. 59

38 Observed trend on silica N taken at UC Berkeley. 60

39 Illustration of how morphology and size changed towards the center of silica N substrate. 60

40 Size analysis of silica N of source synthesis. 61

(a) Squares 61

(b) Octagons 61

41 EDS analysis of a flower-like structure and surrounding squares of BiOCl on silica N performed at UC Berkeley. 62

42 The EDS analysis of squares with flower-like BiOCl on silica L substrate done at UC Berkeley. 63

43 Illustration of EDS analysis of mica L at NTNU with Pd and Pt. 64

44 Illustration of EDS analysis of mica L at NTNU without Pd and Pt. 64

45 Illustration of signal from pre-determined elements of area in Figure 44a. 65

46 Illustration of AFM analysis of a nanoframe. 66

47 Illustration of a typical AFM analysis of an octagon. 66

48 Illustration of AFM thickness profiles for square. 67

49 Illustration of ZSensor image and thickness profile for an octagon. 67

50 Illustration of AFM analysis of a cracked crystal. 67

51 Raman analysis of BiOCl flower-like structure on silica. 69

52 Illustration of square crystal on silica N for Raman analysis done at UC Berkeley. . 69

53 The figure illustrates the Raman spectra of BiOCl on silica substrate N performed at UC Berkeley. 70

54 The figure illustrates the Raman spectra of clean silica substrate performed at UC Berkeley. 70

55 Illustration of square crystal on silica D for Raman analysis done at NTNU. 70

56 The Raman spectra of BiOCl on silica D done at NTNU with 6 accumulations and 10 seconds integration time. 71

57 Flower on mica F where Raman analysis was performed. 71

58 The Raman spectra of BiOCl flower mica F substrate with 5 accumulations and 40 seconds integration time done at NTNU. 72

59 Illustration of the Raman active Bi-Cl bond in BiOCl marked in red [38]. 73

60 XRD spectra of BiOCl on silica I with wavelength contamination and corresponding facets. 75

61 XRD spectra of mica J with wavelength contamination and corresponding facets. . 76

62 XRD spectra of mica F (black) and mica J (red). 77

63 XRD spectra of silica I (black) vs mica J (red). 78

64 A proposed morphology development. 79

65 Proposed mechanism of nanoframe development. 87

66 A proposed flower formation mechanism. 89

67 Irregularities and cracks observed on the mica substrate by using OM at UC Berkeley 111

68 Si-15.5cm displaying low crystal density substrate section 1. 112

69 Si-3min section 3 displaying medium crystal density. 112

70 Si-1min section 1 showing large crystal density. 113
71 Mica-900W section 1 showing crystal growth on mica. 113
72 Image showing an area of the silica substrate that was covered in white powder. . . 113
73 Illustration of EDS results on silica L, where the aim was to identify elements in the flower-structure. 115
74 Irregular shapes with a hole in the center. 116
75 Figure of a smooth surface crystal. 116
76 Picture of large octagon used in analysis. 117
77 Picture of large octagon used in analysis. 117
78 Picture of large octagon used in analysis. 118
79 Illustration of AFM images of a large nanoframe used in analysis. 118
80 Illustration of AFM images of nanoframe used in analysis. 118
81 Illustration of AFM images of a large nanoframe used in analysis. 119
82 Illustration of AFM images of a large nanoframe used in analysis. 119
83 Illustration of AFM image of yellow square. 119
84 Illustration of AFM image of blue and red square. 120
85 Illustrations of AFM analysis of a yellow and red square. 120
86 Illustration of AFM image of blue square. 120
87 Illustration of AFM analysis of blue square. 121
88 AFM analysis of a yellow square. 121
89 AFM analysis of a blue, red and yellow square. 121
90 Illustration of the amount of precursor used in each individual parallel for the synthesis changing amount of precursor. 123
91 Illustration of the quartz combustion boats used in parallel 1 and 3. 124

List of Tables

1 Synthesis schemes and parameter change throughout this thesis. 39
2 Density of squares and octagons/circles in each section for each parallel in the microwave time synthesis. 51
3 Density of squares and octagons/circles in each section for each parallel in the distance synthesis. 52
4 Density of squares and octagons/circles in each section for each parallel in the microwave power synthesis. 54
5 Density of squares and octagons/circles in each section for each parallel in the mica and microwave power synthesis. 55
6 Density of squares and octagons/circles in each section for each parallel in the amount of source synthesis. 56

7 Density of squares and octagons/circles in each section for each parallel in the silica N synthesis. 61

8 Results of AFM measurement analysis for octagons, nanoframes, squares and a cracked crystal. 68

9 AFM thickness measurements of crystals with varying colors. 68

10 Raman modes for BiOCl grown on silica and mica substrates. 72

11 Unmatched peaks from mica J with database diffraction angle and facets. 77

12 All the observed diffraction angles for silica and mica as well as corresponding facets and database diffraction angle, ... 78

13 Silica 2θ values, facets and calculated lattice spacing 122

14 Mica 2θ values, facets and calculated lattice spacing 122

1 Introduction

Along with the observed increase in industrialization and urbanization, there is a subsequent increase in pollutant emissions such as organic, polymer, and biological compounds. There will be a need to accommodate the problems arising from these releases, where a preferred solution would be within the field of green technology. One approach would be to chemically transform these pollutants into non-hazardous and non-toxic components, ideally with no additional emission [2, 3]. These chemical transformations could be facilitated by a photocatalyst, preferably one which displays renewable energy conversion due to the environmental advantage.

Photocatalysis is a chemical reaction that is enabled by a photocatalyst which acts as an active site for inducing the chemical reaction. In order to have more active sites which facilitates more chemical transformation, an advantageous property of a photocatalyst is a large surface area. Further advantageous aspects would be if the process could be driven by visible light, instead of ultraviolet (UV) light. This is because UV light is only 10% of the solar radiation, thus in order to utilize more of this energy the photocatalyst should be responsive within this energy range. By increasing the utilization of solar radiation energy, the process of degrading organic pollutants in wastewater would become more environmentally friendly.

A type of material which has been studied and synthesized for use in photocatalytic applications is 2D materials. This is due to the fact that these structures show superior properties compared to their 3D bulk counterparts. What distinguishes 2D materials from 3D materials is that one of the three dimensions is restricted to a nano-size range, and this dimension is often thickness [4]. The 2D materials could be stacked together in a variety of ways, to tune the properties and thickness as desired for the specific application. Furthermore, this restriction and structural confinement provide the 2D materials with a higher surface-to-volume ratio and a higher surface activity compared to 3D materials [5]. All these favourable aspects make them advantageous in the application as a photocatalyst.

A type of 2D material showing great promise as a photocatalyst is a ternary layered structure, which provides structural and compositional tunability. Compared to binary 2D layered materials, the extra element contributes to more variations within the structure in addition to different properties [6]. More specifically a ternary 2D layered material obtaining an interest in the emerging field of study of visible-light-driven photocatalysis is bismuth oxyhalides, BiOX. The BiOX with the largest band gap is BiOCl, which is responsive within the UV light range. BiOCl has favourable structural features such as an open structure, layered structure, and internal electric field. The band gap is also thickness and morphology dependent thus it displays a tunable band gap, p-type conductivity, and exhibits good reduction-oxidation capacity. Due to these features, the structure has good prospects as a photocatalyst. If a material has a tunable band gap the application range will improve as it could then be responsive to both UV light and visible light, depending on the aimed use. A tunable band gap entails that by altering certain aspects of the material in a process called band gap engineering, the resulting band gap will either be narrowed or broadened. Band gap engineering can be achieved by doping, introducing defects, adjusting the thickness, and multiple other strategies. In order to perform band gap engineering, there is a necessity for a controlled synthesis.

When synthesizing BiOCl photocatalysts the most common ways are by a wet-chemistry approach. These are known, reliable methods but offer some disadvantages. The limitations include the use of organic solvents, longer reaction time, higher energy consumption, and lower production rate thus less suitable for large industry-scale production.

1.1 Proposed technical approach and contribution

The work in this thesis aims to achieve uniform growth of large-area, stoichiometric and crystalline BiOCl with a controlled synthesis method by utilizing a conventional household microwave oven. The method relies on a microwave oven which differs from conventional heating by the use of an electromagnetic field affecting dipoles within the material. The utilization of a confined-space and a microwave oven will affect the synthesized crystals in diverse ways. Prospects of the microwave-assisted method will be simplicity, rapidness, less energy consumption, and no use of organic solvents thus a more environmentally friendly approach. Compared to a wet-chemistry approach this method has the potential of being scalable to industry-level production of photocatalysts.

This thesis aims to contribute with an evaluation of the microwave-assisted method as well as an analysis of how the crystal growth can be influenced by systematically changing synthesis parameters. The parameters investigated are microwave time, distance from the magnetron, microwave power, utilization of mica substrate while changing microwave power, and changing amount of precursor.

1.2 Outline

The thesis is organized as follows: Section 2 presents a literature study and theory on the topics of 2D materials, properties and synthesis of BiOCl, crystallization of BiOCl and some characterization methods. Section 3 describes the experimental setup used to conduct the experiments presented. In Section 4 the results from the experiments are presented and are then discussed in Section 5. The thesis ends with a conclusion and some suggestions for further work in Section 6.

2 Theory

This section details different aspects of two dimensional (2D) materials, properties and application of BiOCl, issues with the current methods both wet-chemistry and dry-chemistry approach, and the crystallization of BiOCl.

2.1 2D materials

2D materials are materials where one of its three dimensions is compressed to the atomic thickness and these sheets differ from their 3D material counterparts as they display different physical properties, a direct consequence of size and dimensionality being important defining factors of the properties of a material [7, 8, 9]. 2D materials are ideally 1 unit cell thick, but can include thickness up to 10 atoms [10, 9]. Thus, these materials can theoretically replicate infinitely in two dimensions, but the thickness remains in an atomic size range [4]. The definition of 2D materials also involves that the sheets can be isolated as free-standing 1 unit cell thick layers that can be isolated from bulk material and exist without the need for a substrate [10, 9]. Depending on the composition and structural configuration these materials can be classified as insulators, metallic, semimetallic, semiconductors, or superconductors, emphasizing the vast range of possible applications [5, 7]. Characteristics of 2D materials are that they have a higher surface-to-volume ratio and higher surface activity than 3D bulk material [5]. 2D layered materials have relatively recently sparked interest in research fields when single-layer graphene was successfully separated from graphite crystals in 2004 [7, 10]. The atomically thin graphene sheets were mechanically exfoliated and peeled off from the crystal, earning researchers Geim and Novoselov the 2010 Nobel Prize in physics for their work [7, 11].

The reason why 2D materials are interesting and worthy of research is the properties these thin sheets possess as a result of the spatial confinement in one dimension. Thus by tuning the thickness there is a possibility of altering these properties as desired [4]. Optical, electrical, chemical, and mechanical properties of 2D materials differ from 3D bulk counterparts [7, 9]. The optical and electronic properties are impacted by the fact that electron movement is confined in an atomically thick dimension and there is no interlayer bonding between the 2D materials. As there is no interaction between layers, the electrons will be restricted to move along the 2D material, and the movement of electrons is an important factor in deciding upon the band structure [9]. Thin layers of 2D materials behave as elastic films hence this geometric effect alters the mechanical properties [7]. Furthermore, the chemical property change originates from the high surface to volume ratio [9].

All the observed effects of the 2D materials happen near or at the surface of the material. This is because all of the atoms are either situated on the surface or a few Ångstroms into the material, thus compared to 3D materials the atoms are generally more exposed to the external environment [4]. For instance changes in melting and critical point behavior, quantum confinement, and out-of-plane bending are observed upon reducing the dimensionality from 3D to 2D, as well as changes in short and long-range interactions [4]. Short-range interaction involves the symmetry of chemical bonding and coordination number. The latter is reduced when reducing dimensionality, thus leading to the rehybridization of valence electrons in the material. This can lead to a new symmetry appearing or structural transformation such as surface reconstruction where coordination number and symmetry may be affected as the confinement induces changes in electronic structure [4]. There was a discovered shift in band gap from indirect to direct upon thinning bulk MoS_2 by microexfoliation to semiconducting monolayer [12]. Long-range interactions include electrostatic, magnetostatic, and elastic interactions and prevail longer than interatomic distance [4].

As these 2D materials are thin layers or sheets, they can be stacked together to form a 2D layered material [10]. Intrinsically the 2D layered structures consist of a layered structure with strong intralayer bonding in the (001) plane by either covalent or ionic bonding and interlaminated weak van der Waals nonbonding interaction [13]. Each layer is free of dangling bonds, thus integration with adjacent layers is only facilitated through these weak interactions [7]. The weak vdW enables easy separation of each layer from bulk material by for instance exfoliation, and these layers can then be re-stacked into flat structures according to preferred design, without the need to consider lattice matching [7, 10, 4]. This feature of the 2D material is facilitated by them being free of dangling bonds, allowing stacking and incorporation even in heterostructures with nanostructures of other dimensionalities [7].

The aim of stacking different materials is to extend their light-response because the resulting composites will have a larger range of photocatalytic responses than each individual layer [14]. The reassembled layers can be used in nanoelectronic devices and sensitivity biosensors and as supercapacitors, photoconductive cells or p-n junction all depending on different factors taken into account when stacking the structure [9, 7]. It is also possible to stack organic-inorganic layers together forming a material that has vast potential with its multifunctional properties [15]. The quality and type of 2D material, stacking order and the stacking technique play crucial roles in improving the devices' performance and discovery of eventual new phenomena [7]. From the use of different materials and stacking order, unconventional characteristics may appear as different stacking angles gives rise to a change in lattice structure and energy band type. Furthermore, internal defects, surface cleanliness, dimensions, and the number of layers that make up the structure are all parameters that influence the physical and chemical properties of the resulting 2D layered material [7].

There are different 2D layered materials and the most commonly known is graphene. Graphene are free standing monolayers of carbon atoms, thus a monoelemental 2D layered material. By stacking the graphite together, graphite will be created [16]. Then there are binary 2D materials such as transition metal carbonitrides (MXene) which exhibits a layered structure where two or multiple layers of the transition metal (M) are intervened by layers of carbon and or nitrogen (X) [17]. Furthermore, transition metal dichalcogenides (TMDCs) are also binary 2D layered materials. These are semiconductors of type MX_2 where M represent a transition metal atom and X is a chalcogen atom. These are layered in a structure where there is alternation between layers of is chalocogen atoms and metal atoms [18]. Then there is ternary 2D layered materials which is a type of 2D material that is comprised of one metal and two non-metals. The additional element compared to binary 2D layered material provides other properties such as intrinsic ferromagnetism and higher electron mobility [19].

Separating of single layers from a layered crystal can be done by techniques such as mechanical exfoliation, surface assisted *in situ* growth and exfoliation into colloidal solutions also called liquid exfoliation [9]. 2D layered materials are being synthesized by different methods, chemical vapor deposition (CVD), physical vapor deposition (PVD), magnetron sputtering, and plasma laser deposition (PLD) to produce large-area materials. It has been proven difficult to synthesize these structures via a solid source due to the buckled elemental material having an anisotropic rhombohedral or trigonal crystals system [20]. Additionally, the growth conditions in a CVD system are highly influential on both the size and quality of the resulting material. Conditions such as temperature, confined space, precursor amount, and distance between precursor and substrate, therefore for a CVD system trials have to be made as each temperature provides a different flow pattern which is also linked to the placement of the substrate and so on [21]. Large-area 2D materials can be fabricated by facilitating a reduction in the metal-ion precursors melting point by using salts, such that the growth edges will be passivated [4]. Additionally, for a PLD system, it is reported that large area growth and high uniformity can occur if conditions facilitate for free migration of reactive atoms. This is achieved by using a low-power laser providing low energy for the impinging atoms [22]. Controllable synthesis of these by wafer-scale growth is being researched and is promising, but crystalline orientation and growth mechanism must be investigated further to get full control [20]. Of these, CVD and mechanical exfoliation are most commonly used [7]. Micromechanical exfoliation involves physically rubbing the crystal surface against another surface, leaving behind flakes among which there exists a few single high-quality layers at a time [7, 9]. CVD on the other hand grows large size 2D materials, but of poor quality [7].

2.1.1 Different structures

There are different classifications of nanomaterials, and within the 2D material, there exist morphologies and structural varieties as can be seen in Figure 1. Nanoplates are classified within the

2D category, as one dimension is confined in the range of nanoscale and usually this dimension is thickness. While nanosheets are similar to the nanoplates, they possess extended lateral dimensions meaning that both length and width are increased while thickness remains in the nanoscale [23].

Throughout this thesis, the synthesized product is denoted as crystals when talking about unspecified morphology and when talking about how the structures are stacked together the as-synthesised BiOCl are denoted as nanoplates.

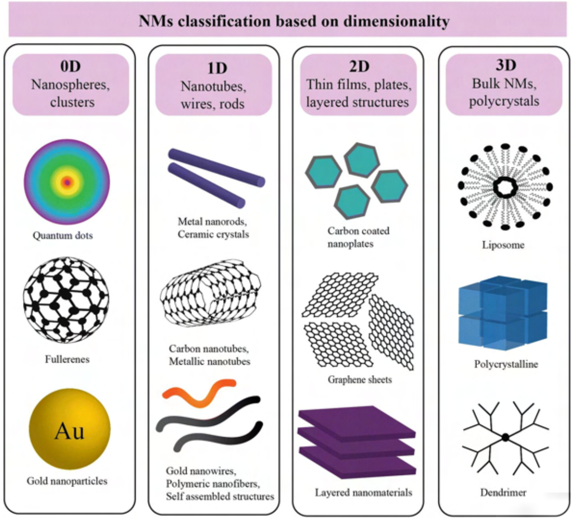

Figure 1: The figure illustrates the categorization of nanomaterials based on dimensionality [24].

2.2 BiOCl properties and applications

2.2.1 Photocatalysis

Photocatalysis is defined as a photonic energy-driven chemical reaction that is induced by and accompanied by a catalyst. The catalyst is not being consumed or reproduced in the reaction occurring, and only acts as an active site enabling the chemical transformation and increasing the reaction rate. Photocatalysts are usually semiconductors that have an electronic structure where the valence band (VB) is filled with electrons while the conduction band (CB) is empty [25]. The basic working principle of a photocatalyst is that photons of equal or greater energy than its band gap is absorbed which generates electron-hole pairs known as charge carriers. Then these are separated by different methods such as structural engineering to prevent unwanted recombination. Ultimately there is a transfer of the photogenerated charge carriers to the surface to partake in various reduction-oxidation (redox) reactions. This is illustrated in Figure 2.

Solar light is an inexhaustible energy source and using this will be a more environmentally friendly approach than synthetic ultraviolet (UV) light source [26]. Additionally, band gap engineering is done to overcome the obstacle of recombination of charge carriers, so they are not prevented from partaking in the redox reactions at the surface [27]. However, in successful photocatalytic processes UV light is still mostly used which limits its possible application and environmental benefits [25]. The challenge then remains to boost photocatalytic efficiency under visible light, by enhancing the kinetics to shorten the total reaction time [26].

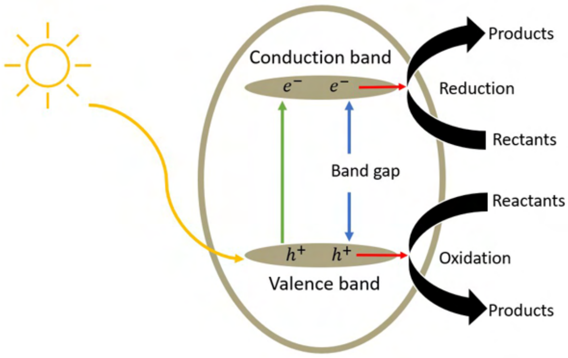

Figure 2: A schematic simplification of the working principle of a photocatalyst.

Gas absorption is analyzed in a BET (Brunauer, Emmett, and Teller) surface area analysis, where nitrogen gas is usually used. The gas is released into a container with the material and surface absorption happens under constant monitoring of pressure changes as absorption will alter the pressure. Layers of absorbed gas on the surface are then heated, released, and quantified. The amount of gas adsorbed is plotted versus relative pressure, and a BET isotherm is derived. With this information, a specific surface area of the sample is calculated. This process is used to determine the surface area for small particles of 1 to 100 nm since the surface area is of high importance for their properties [28]. A smaller BET surface area will be linked to limited exposure of active sites on the surface and this will restrict the adsorption capacity of the surface [29]. In performance evaluation of synthesized photocatalysts, various dyes are normally used such as Methyl orange (MO) and Rhodamine B (RhB). This is done as the degradation mechanism of these organic dyes have been previously studied and is straightforward [2].

The most investigated, commercially used photocatalyst is TiO_2 and there exists established knowledge of both properties and structure. It is a nontoxic compound with photostability, high oxidizing activity, and low-cost [30, 14, 3]. However, there is some limitation with this photocatalyst. Any facet-engineering of TiO_2 proved difficult as the highest percentage of exposed facets was only 80% in a study [31, 32]. Furthermore, the biggest limitation of this compound lies within the wide band gap of 3.0-3.2 eV which restricts the response to solar energy in the ultraviolet (UV) range [30, 14, 3]. Therefore, it is deemed necessary to design other photocatalysts with a visible light-responsive band gap or a wide band gap material that can be easily narrowed [14].

In general, bismuth-based 2D layered structures exhibit a stable structure, tunable band gap, and high carrier mobility advantageous for band gap engineering aimed to adjust certain properties such as photocatalytic performance [33]. Compared to TiO_2, BiOX also exhibits greater electron mobility. The structure has interesting light absorption capabilities as it can photo excite in different energy ranges, depending on the choice of halogen. This can be exploited in electronics and other fields of applications as photons from incoming radiation will be transformed into an electric signal by the photoelectric effect that was first described by Albert Einstein [34]. Due to the stacking of the layered structure, there is a high portion of exposed surfaces that can be utilized for the investigation of an eventual facet effect on the photocatalytic activity. Investigation of these ternary layered structures is therefore of interest for photocatalytic applications.

2.2.2 BiOX

There exists various studies on 2D layered bismuth oxyhalides, BiOX (X=I, Br or Cl) as they possesses an interesting ternary layered structure for photocatalytic applications [13, 30, 32, 35, 2, 3]. For instance, it is found that the photocatalytic activity of BiOCl single-crystalline nanosheets is facet dependent [32]. A study done by Zhao et al discovered that the (001) facet has higher activity in direct semiconductor photoexcitation driven pollutant degradation under UV light, than other facets. The same study discovered that for indirect degradation of dye photosensitization under visible light, the (010) surface showed the highest activity [36]. Investigation of these ternary layered structures is therefore of interest for photocatalytic applications.

The variable band gap of BiOX makes it interesting as changing the X will consequently change the band gap from the values of 1.8 eV (X=I), 2.7 eV (X=Br), and 3.3 eV (X=Cl), which can be exploited when exploring new light-harvesting materials [13]. By having atomically thin 2D layered materials with different band gaps alloyed together and carefully controlling composition ratios, the result could be various semiconducting materials with different, selective band gaps. Displaying a tuneable band gap is in general favorable as the structure can then be used in functional electronics or optoelectronic devices [37]. BiOX also possesses a thickness-dependent band gap, which can make it easy to influence optical and physicochemical properties only by altering the size [13]. The gradual decrease in band gap across the series of halogens is coherent with a reduction in electronegativity. Additionally changing the halogen in the structure will induce a change in the composition of the valence band (VB) [30]. Furthermore, in a study done by Zhang the band gap of BiOCl was 3.20 eV, BiOBr was 2.76 eV and BiOI was 1.77 eV. In this study it was discovered that the energy level of the VB was discovered to be influential on certain properties of BiOBr. In the study it was observed that BiOBr could absorb photons within the visible light region, which BiOCl is unable to do because of its large band gap, However, BiOBr exhibited a redox capacity poorer than that of BiOCl. This is due to the fact that BiOBr has a VB with a higher energy level than BiOCl, which negatively impacted the redox capacity of BiBr. From the same study, it was found that BiOI was the compound that was able to absorb most of the visible light as it has the smallest band gap. However, since the energy level of the VB is high in BiOI, this limits its ability to facilitate redox reactions [30].

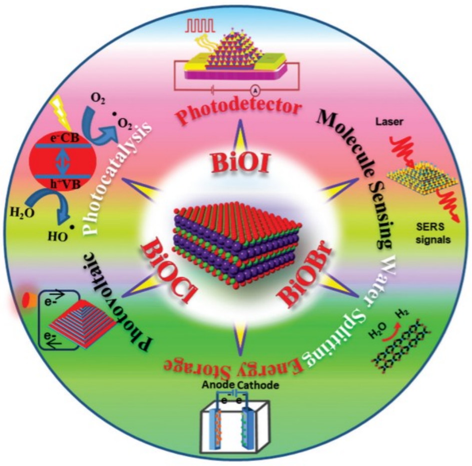

Figure 3: The application of various BiOX structures [13].

2.2.3 BiOCl structure

The atoms within the layers of BiOCl are held together by strong covalent interactions, while the interlayer interaction of the stacked structure consists of weak van der Waals forces through the chlorine atoms. Furthermore, the BiOCl layers consists of $[Bi_2O_2]^{2+}$ and sandwiched between double plates of these layers are halogen ions $[Cl]^-$ interlaced in the c- direction [6, 27, 38, 30, 32, 39, 40]. The BiOCl structure is illustrated in Figure 4. In the direction of the c-axis the structure is not closely packed, thus BiOCl has an open structure which can also be observed in Figure 4 [40]. Additionally, facilitated by the open structure, an internal electric field will form between the $[Bi_2O_2]^{2+}$ and the $[Cl]^-$ due to the charge difference. This can enable more transport of charge carriers and reduce the recombination rate of photogenerated charge carriers, ultimately leading to a higher photocatalytic efficiency [32, 40, 26]. As the BiOCl has an open structure it will promote polarization of orbitals, and in addition to the electric field, this results in higher separation rates of the charge carriers thus further enhancing the photocatalytic efficiency [30, 40, 13].

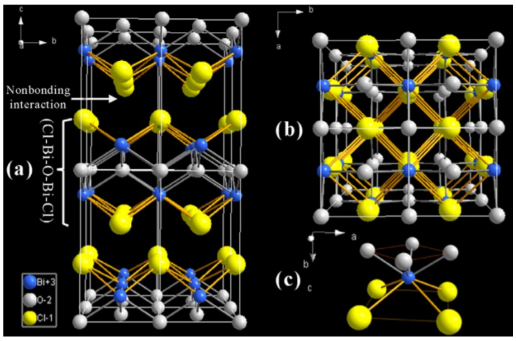

Figure 4: The figure displays the structure of BiOCl [38], illustrating a) front view, b) top view and c) decahedral geometry.

BiOCl is a multicomponent metal oxyhalide belonging to the group V-VI-VII compounds and has a high chemical stability even under UV light with nontoxicity and is resistant towards corrosion [6, 41]. It has a tetragonal matlockite structure (PbFCl type) with the space group P4/nmm (D_{4h}^7) [27, 42, 38]. This means that there are 6 atoms in the primitive cell with lattice parameters a=b=0.3891 nm and c=0.7369 nm, and with angles $\alpha = \beta = \gamma = 90$ °[27, 39, 32, 43, 44, 45, 46]. The structure of BiOCl will make it crystallize easily into a single-crystalline 2D nanosheets anisotropically through a hydrothermal or solvothermal method [27]. It is reported that one BiOCl nanosheet have a thickness of about 2.7 - 2.9 nm, consisting of four stacking units of [Cl - Bi - O

- Bi -Cl] [13, 47].

For BiOCl the successfully synthesized morphologies range from zero-dimensional (0D) nanoparticles and quantum dots, one-dimensional (1D) nanorods, nanowires, two-dimensional (2D) thin films, nanoplates, layered structures, nanosheets, nanobelts and lastly three-dimensional (3D) bulk materials and hierarchical architectures [48].

Furthermore, BiOCl has a p-type conductivity that in combination with n-type semiconductors, allows the formation of p-n heterojunction that enhances the charge carrier separation thus enhancing the photocatalytic performance of the combined material [33]. P-type conductivity is a term used for materials where the majority of the photogenerated charge carriers are holes, and electrons are the minority charge carriers. Thus there is a larger concentration of holes than electrons [49].

2.2.4 Band gap engineering and photocatalytic properties of BiOCl

To summarise, the wide band gap of BiOCl accompanied by other favorable features makes it a good candidate for photocatalysis. It has an internal electric field and open structure facilitating transport and separation of charge carriers, better redox capability because of a lower energy valence band (VB) compared to BrOI and BiOBr, and p-type conductivity facilitating the generation of p-n heterojunctions which are all favorable for photocatalysis. It is also discovered that the photocatalytic activity of BiOCl single-crystalline nanosheets is facet dependent [32]. A study found out that the (001) facet has higher activity in direct semiconductor photoexcitation driven pollutant degradation under UV light, than other facets. The same study discovered that for indirect degradation of dye photosensitization under visible light, the (010) surface showed the highest activity [36]. Investigation of these ternary layered structures is therefore of interest for photocatalytic applications. However, the limitation of BiOCl photocatalytic activity resides within the wide band gap which absorbs UV light, thus band gap engineering is needed [30, 13, 32, 40, 26, 33].

Band gap engineering involves controlling or changing the band gap energy of a material, to fit the energy of a specific electromagnetic radiation wavelength, and by this also induces changes to certain properties of the material. In the specific case of narrowing a wide band gap semiconductor by various ways, is to improve the poor solar energy conversion efficiency by overcoming the semiconductor's poor absorption within the visible light range, stated at 47% . This will result in the development of efficient visible-light photocatalysts for environmental applications using solar radiation.

BiOCl has an optical indirect band gap ranging from 3.0 to 3.5 eV where the value depends on the thickness, synthesis method, morphology, and other features. The indirect band gap will hinder the recombination of the excited electron with the hole, as the excited electron has to travel a k-space distance in order to reach the valence band (VB) before subsequently being emitted. Furthermore, because of its large band gap, the photocatalytic property of BiOCl under visible light is deemed negligible [50]. Despite this, the open layered structure of the BiOCl, internal electric field, and the indirect band gap are beneficial for the separation and transport of photogenerated charge carriers which is advantageous for a photocatalyst, making BiOCl a great candidate for photocatalysis. The photogenerated electrons and holes can then make their way unhindered to the surface, and partake in reactions with for instance an organic pollutant molecule [31, 51, 52].

Band gap engineering of BiOCl can be carried out by adjusting elemental ratios alongside the use of a precursor, facilitating the creation of various point defects, textural design, constructing heterojunctions, metal-metal oxide decoration, doping the structure with other elements, or by adjusting various growth conditions. Growth conditions that could be changed are different temperatures, adding solvents, changing reaction time, having a gaseous environment, or having the reaction occur in a solution [33, 14, 13, 48, 27]. Additionally, trapping of charge carriers by inducing OVs may improve photocatalytic response. However, in many systems, the reaction scheme is carried out with the surface OVs themselves and how reactive species interact with the substrate [27].

A study done by Li et al synthesized 3-7 nm thick, square nanosheets of BiOCl with a band gap of 3.25 eV by the use of a modified solvothermal method assisted by polyols [53]. Different polyols can be added to a synthesis scheme to control morphology and particle growth. Li and colleagues also studied the effect the concentration of Cl and the choice of Cl source had on thickness and morphology, and thus photocatalytic activity. They found that for both the Cl-sources, NaCl and CTAC, an excessive concentration resulted in wider and thicker BiOCl nanosheets. The perfect concentration of Cl source was found when the ratio of Bi:Cl was 1:1. With this ratio, ultrathin BiOCl with a thickness of 3-7 nm was generated, preferential for photocatalytic performance. These 3-7 nm thin square BiOCl nanosheets displayed an increased activity of photosensitization degradation of rhodamine B (RhB) under visible light, compared to thicker nanosheets of BiOCl. As the band gap of BiOCl in this study is stated to be 3.25 eV, the structure is not active under visible light. Therefore, the increased activity when reducing the thickness is ascribed to a higher surface area which is linked to more active sites for dye adsorption and thus degradation [53].

The higher surface area achieved upon reducing the thickness will be associated with an increase in surface energy, rendering the single, thin nanosheets thermodynamically unstable. This is the driving force for the nanosheets to stack together, creating a layered nanoplate structure that decreases the total surface energy during growth [54]. Additionally, one noticeable feature was distinctive between the two Cl sources. When using the same growth conditions, CTAC resulted in square-like nanosheets and NaCl gave round-shaped nanosheets where the latter had higher BET surface area, thus better photocatalytic performance. For the case of insufficient Cl-source concentration the results were irregular shaped BiOCl [53]. It was discovered that both carrier migration and light absorption will be enhanced when reducing the thickness of bismuth semiconductors below 10 nm. This is attributed to the large specific surface area that is a consequence of reducing the thickness to the nanometer scale and ascribed to the phonon confinement effects [55] [54]. When reducing size and dimensionality these effects will subsequently occur in the material, and it may lead to both an increase or decrease of band gap energy [56]. There is still limited knowledge of these effects that need to be studied further [56]. However, this gives an indication of how thickness and synthesis schemes can affect the resulting band gap.

The band gap can also be narrowed by doping which also induces changes to the photocatalytic property of the material [30, 14]. Doping can be done either by pre-treating the precursor or by post-treatment of the already prepared 2D layered material [14]. Band gap engineering by doping is also shown in a theoretical study by Zhang et al where Sb and I atoms were co-doped to reduce the band gap of BiOCl and enhance the optical absorption coefficient. From the theoretical study with DFT calculations, the effect of the co-doping is ascribed to the electronegativity between the Sb/I atoms and Bi/Cl atoms. The calculated band gap was 2.90 eV, deviating some from the experimental value of 3.20 eV [30]. A study doped BiOCl with fluorine ions, and both the crystal lattice and surface properties were altered and the structure had a band gap of 3.47 eV. This resulted in a 99.7% photocatalytic degradation of RhB by the doped BiOCl within 35 min under visible light irradiation [57]. Another study doped BiOCl with boron which resulted in higher exposure of (001) facets and showed great degradation of RhB under the illumination of a Xenon lamp. After 100 min of irradiation, pure BiOCl degraded 51.7% of the RhB while B-BiOCl exhibited a degradation rate of 81.5% [58, 31]. This enhanced photodegradation was explained by a higher exposure of (001) facets in B-BiOCl which promotes charge carrier separation, as well as increased specific surface area [58]. Another study synthesized square BiOCl with a thickness of 190 nm by a hydrothermal process which under Xenon arc lamp had a degradation rate of 35% after 6 min. Using the same process the BiOCl was doped with carbon and only by adding 1 mmol of glucose did the degradation rate increase to 80% under the same conditions. The two structures had the same band gap of 3.4 eV thus the difference in photocatalytic performance is based within the structure where carbon facilitates for separation and transfer of photoinduced charge carriers [59].

Band gap engineering can also be done by adjusting the halogen ratios of Bi/Cl, where a bigger ratio gives a smaller band gap, which ultimately alters the optical properties of these crystals [27]. When changing the atomic ratio of BiOCl the primary aim is to narrow the band gap, but it will also change the composition of the structure [54]. Through a dehalogenation process the photoabsorption range could be altered from UV region corresponding to the BiOCl structure, to visible light region with structures like Bi_3O_4Cl and $Bi_{12}O_{17}Cl_2$ [27]. The oxygen-rich structures of $Bi_{12}O_{17}Cl_2$ and $Bi_{24}O_{31}Cl_{10}$ has band gaps of 2.57 eV and 2.71 eV, respectively [60, 61]. Thus both structures can absorb visible light [54]. $Bi_{12}O_{17}Cl_2$ was synthesized through a hydrothermal route that was assisted by a water-soluble polymer. The addition of the polymer was deemed crucial for constructing the oxygen rich BiOCl structure [60]. The other structure, $Bi_{24}O_{31}Cl_{10}$, was created in a study by Jin et al, by adding $NH_3 \cdot H_2O$ to a hydrothermal synthesis of BiOCl. In the study both $Bi_{24}O_{31}Cl_{10}$ and BiOCl were synthesising according to this manner with and without adding $NH_3 \cdot H_2O$. It was discovered that $Bi_{24}O_{31}Cl_{10}$ had a narrower band gap of 2.71 eV compared to the 3.42 eV band gap of the synthesized BiOCl, showing the significance of $NH_3 \cdot H_2O$ in the synthesis [61]. Additionally, for chlorine-rich BiOCl, the band gap will be more narrow [54]. This is shown in nanosheets of $Bi_{12}O_{15}Cl_6$ where the corresponding band gap is 2.36 eV, also within the visible light region [62]. These nanosheets were fabricated by a facile solvothermal route before being thermally treated. The nanosheets showed an enhanced photocatalytic performance compared to synthesized BiOCl nanosheets upon removal of the non-dye pollutant bisphenol A under visible light. This may indicate that by doping a general structure with a halogen may lead to a decrease in band gap energy, which can be linked to the previous statement that there is a gradual decrease in band gap of BiOX across the series of halogens [30].

The reasoning behind the halogens' effect on the band gap energy could be found in the density functional theory (DFT) calculations. Based on DFT calculations it is found that the upper valence band (VB) contains Bi 6s and O 2p orbital states and there is also a small contribution from Cl 3p states [32, 40]. This is because the electronegativity of oxygen is stronger than that of chlorine, the O 2p states have a lower energy level than Cl 3p thus there is only a contribution from Cl to the VB. The upper VB is called the highest occupied molecular orbital (HOMO) [40]. The lower conduction band (CB) is called lowest unoccupied molecular orbital (LUMO) and contains mainly Bi 6p orbitals [13, 30, 54]. This entails that by changing the bismuth and oxygen halide ratio and content, the position of the CB and VB can change. Either making the band gap smaller or larger, depending on the aimed application of the resulting structure [13, 54]. The Bi 6s orbitals have a greater radial extension meaning these valence orbitals will give a better overlap than 4f and 5d valence orbitals, which is linked to higher mobility of photoinduced charge carriers. This is one of the reasons for the enhanced stability of bismuth-based photocatalysts [30]. For instance, as oxygen content increases the oxygen 2p states become more dominating in the VB, thus giving oxygen-rich BiOCl structures a band gap energy closer to that of Bi_2O_3, 2.38 eV [63]. Demonstrating that VB can be tuned by changing the O/Cl ratio [54].

2.2.5 Defects and their influence on properties

The most important and prominent lattice vacancies in the 2D BiOX structures are oxygen vacancies (OVs) and generating these OVs at the surface is the most common method of narrowing the wide BiOCl band gap [62, 13, 27]. The high fraction of exposed surface makes the 2D nanostructure ideal for insight on an atomic level into OVs influence on thermodynamics and kinetics of photocatalytic processes [27]. OVs narrow the band gap because they can function as electron donors as they have an energy level in between the band gap [64]. The phenomenon of lowering the band gap energy is also explained by the overlap of nonlocalized OV states with the valence band (VB), and by this reducing the band gap [65].

The most important and prominent lattice vacancies in the 2D BiOX structures are oxygen vacancies (OVs) and generating these OVs at the surface is the most common method of narrowing the wide BiOCl band gap [62, 13, 27]. The high fraction of exposed surface makes the 2D nanostructure ideal for insight on an atomic level into OVs influence on thermodynamics and kinetics of photocatalytic processes. Compared to traditional metal oxides OVs are effortlessly induced on BiOCl under O_2 deficient and ultraviolet (UV) or thermal conditions. This is due to the fact that at the surface the Bi-O bond energy is low and the bond length is large, thus it takes a small amount of energy to create an oxygen vacancy at the surface, especially in an environment that lacks oxygen [27, 66]. The thermal condition creates a higher diffusion of OVs in the xy plane, enabling the generation of more OVs [33]. At higher temperatures the OVs are generally more stable at the surface of a structure rather than in the bulk, this is verified both in theoretical and experimental studies. At low concentrations of OVs, the surface diffusion and hopping between adjacent oxygen sites dominate. On the contrary, there is a "traffic jam" when the concentration of OVs increases and they repel each other making it difficult for additional OVs to be generated.

This is counteracted by thermal condition as it increases the diffusion of OVs [67]. However, inducing surface OVs has a capacity limit related to how many OVs can be present at the surface, thus to further narrow the band gap other methods must be utilized [62]. OVs narrow the band gap because they can function as electron donors as they have an energy level in between the band gap [64]. The phenomenon of lowering the band gap energy is also explained by the overlap of nonlocalized OV states with the valence band (VB), and by this reducing the band gap [65].

Point defects like these OVs will in general function as traps for photogenerated charge carriers, and surface OVs are especially important in mediating photogenerated charge carrier separation and in photocatalytic processes for transferring charge between the different surfaces [64]. OVs are also active sites for adsorption of O_2 molecules and sites for activation to form superoxide anion radicals [64]. In the PTT study, BiOCl was synthesized by a hydrothermal method, and OVs were introduced on the surface by UV light irradiation. In the (001) plane of BiOCl, there is a high density of oxygen atoms such that OVs are easily generated by UV light energy [66].

In addition to OVs, other lattice defects might appear. For instance, under bismuth rich rather than oxygen-rich conditions defects like $\mathrm{Bi}_{\mathrm{Cl}}^{\bullet\bullet\bullet\bullet}$ and $\mathrm{Bi}_{\mathrm{i}}^{\bullet\bullet\bullet}$ are easily formed. Cl is easily replaced by an O atom or a Bi atom due to weak interaction between Bi-Cl [33]. The Bi-Cl interaction is quite weak compared to the strong forces between the electronegative Cl-O, with a bond length of 3.3 Å [30]. Generally, for all chemically synthesized materials it is impossible to avoid introducing hydrogen due to its small radius and size making it easy for the atoms to get in interstitial or vacancy positions [30]. However, defects in ultrathin BiOCl exists mostly as triple Bi-O-Bi vacancy associates $\mathrm{V}_{\mathrm{Bi}}^{'''}\mathrm{V}_{\mathrm{O}}^{\bullet\bullet}\mathrm{V}_{\mathrm{Bi}}^{'''}$, and not isolated defects like a bismuth vacancy $\mathrm{V}_{\mathrm{Bi}}^{'''}$. The change in dominating defects is caused by a reduction of thickness from nanoplates to atomic size-ranged nanosheets, whereupon reducing the thickness the predominant vacancies become more enhanced. The BiOCl nanoplates had a valence band (VB) energy maximum of 2.22 eV while the conduction band (CB) minimum was -1.03 eV vs. normal hydrogen electrode (NHE) consistent with literature [68, 39, 69]. Nanosheets and nanoplates exhibit some distinctive features and as mentioned in Section 2.1 they have different lateral sizes whereas nanosheets have an extended length and width compared to nanoplates. The nanosheets had an energy up-shift for VB compared to nanoplates, with a VB of 1.17 eV and a CB minimum of -1.83 eV. Both the width of VB and minimum energy of CB are noteworthy features when it comes to kinetic and thermodynamic requirements. As the width of the VB increases, so does the separation of charge carriers as a wider VB gives rise to higher mobility among the generated holes. Resulting in a better photo-oxidation of holes. The minimum energy of CB is important to its photocatalytic property. Firstly, an increase in minimum energy of CB can make the charge carriers more negative thus facilitating a reaction with molecular oxygen and creating superoxide ions, these superoxide radicals are important for photocatalytic degradation of for instance RhB [70, 39]. In addition to this, it will promote the transfer of photoexcited electrons to other reactants thus restricting the recombination of electron-hole pairs. The consequence is that the nanosheets display a higher photocatalytic activity than that of nanoplates, due to these features of the VB and CB [39]. In summary, the triple vacancy associates reported in the study made the surface of the BiOCl nanosheets negatively charged as well as decreased the band gap, and enhanced degradation of phenol compared to BiOCl nanoplates.

Screw dislocations are topological defects of the crystal lattice that can appear. They appear during facets growth under weak supersaturated conditions [71]. Kossel, Stranski, and Volmer's growth theory could not explain why growth could occur at a supersaturation far below the normal level needed to induce nucleation. It was suggested in a new theory that screw locations appear on crystal surfaces under these growth conditions, and these screw locations function as a starting point for further growth of the dislocation [72]. Screw dislocations look like a spiral staircase as the lattice planes shift by one layer from the starting point, at the end of the dislocation a step or surface ledge emerges and stretches to the edge of the facet and so on [71]. This enables growth covering the crystal by step formation emerging from the starting point.

2.3 Synthesis of BiOCl

Preparation technique is, as stated earlier, crucial as it affects structural features including size, morphology, and exposed facets [73, 74]. It will also have an impact on the environment, cost of production, necessary safety precautions and synthesis scale [74]. For synthesizing BiOCl 2D materials the most common ways are by wet-chemistry methods such as hydrothermal and solvothermal methods, and the most frequently used bismuth source is bismuth nitrate pentahydrate, $\mathrm{Bi(NO3)3 \cdot 5\,H2O}$, [73, 74]. Other traditional wet-chemistry methods include chemical etching and deposition-precipitation [75]. Methods such as solid-state milling at room temperature and microwave-assisted route can also be utilized. The latter uses a solution and microwave reactor [75, 73].

The difficulties with controlling stoichiometry comes from the use of precursors $\mathrm{BiCl3}$ and $\mathrm{Bi(NO3)3}$ which are easily hydrolyzed in air, thus will decompose to BiO when the control of heating is unsuitable [6]. When using bismuth nitrate pentahydrate, $\mathrm{Bi(NO3)3 \cdot 5\,H2O}$, to create bismuth-based photocatalysts the compound gives rise to some challenges concerning the reaction time. The precursor is inexpensive and available but has a low water solubility thus the reaction with anions, for instance, ceCO˙3ˆ2-, in an aqueous solution, will be a heterogeneous reaction. Hence the reaction will take a long time to reach completion. A way of assuring that the reaction can happen homogeneously and thus rapidly is by adding acids, urea, or organic solvents to prevent hydrolysis of the $\mathrm{Bi(NO3)3}$ compound. However, this can affect the products. For instance, could incorporation of acid into the solution inhibits the growth of $\mathrm{(Bi2O2)}^{2+}$ cations, which is advantageous for tunability of synthesis of certain morphologies and hierarchical structures of bismuth-based photocatalysts with a layered structure. This is because such structures are formed as a result of combination of $\mathrm{(Bi2O2)}^{2+}$ cations and X^{-} and $\mathrm{CO3}^{2-}$ anions, and ultimately X-Bi-O-Bi-X nuclei growth [73]. Additionally, can the choice of acid also affect the product and its microstructure. The surface of a crystal responds differently to different acids, and the adsorption capacity will vary whether an inorganic or organic acid is being used. As the crystal surface adsorption capacity varies for different acids, the growth sites will not be covered uniformly, thus leading to an affected nucleation and growth rate of the facets [76]. The reaction kinetics can also be tuned by conducting it in solvothermal or hydrothermal conditions, which simulate an atmosphere of high pressure and temperature thus increasing the reaction process [76, 48].

2.3.1 Wet-chemistry approach

The main difference between hydrothermal and solvothermal methods is the use of organic solvents in the reaction in a solvothermal approach. Normally various organic solvents are used in this process, and among these ethylene glycol is the most frequently used [66, 77]. An advantage to both methods is that particle size, morphology, surface defects, facets, and crystalline phase of the product can be tuned by altering reaction conditions such as solvent type, precursor, temperature, pH, and additives such as surfactants [73, 74, 77]. The vast ways of controlling the features and thus properties with these wet-chemistry methods indicate that there is a high level of control of the resulting material, which is a great advantage for utilization of these approaches [74].

For instance to control the microstructure, dulcitol, $\mathrm{C6H14O6}$, was used as a surfactant in a hydrothermal synthesis of BiOCl nanosheets. By having an excessive amount of dulcitol present it induced a decrease of exposed (001) facets, this was due to an excessive amount of surfactant making the mixture more viscous thus restricting the growth of said crystal facets. However, dulcitol also significantly decreased the thickness of the nanosheets, but the concentration was imperative. From the study, it was deduced that pH and dulcitol did have a significant impact on the thickness of the nanosheets and growth of facets, but if both parameters were increased too much the grain size became non-uniform and the nanosheet became thick [78]. A study using the hydrothermal method concluded with acidic conditions of pH equal to 4 resulted in thinner BiOCl nanosheets with a superior photocatalytic degradation of RhB under visible light. This was due to the small thickness, high oxygen vacancy concentration, and exposed (001) facets of BiOCl synthesized under acidic conditions [78].

Advantages of using wet methods such as hydro- and solvothermal processes are that the photocatalysts produced will have greater photocatalytic performance with regards to quality, characterized by the Brunauer-Emmett-Teller (BET) surface area. Generally, wet-chemistry methods produce materials of higher quality compared to dry-chemistry methods, thus these are preferred for usage in specialized applications [74, 79]. These specialized applications include use in electrical industry as semiconductor materials or as photoelectric converters [79, 6].

Furthermore, by using a solvothermal method harmful compounds from the organic solvents could potentially be released into the environment making, it a less environmentally friendly route than hydrothermal synthesis [79, 74].

Generelly, there is a consensus that wet production methods will be restricted by a longer reaction time and thus lower production rate, making them unsuitable for large-scale production for industry. The low production rate is ascribed both to the longer reaction time and to the batch character of the processes. For hydro- and solvothermal methods the batch character is especially significant as they often utilizes autoclaves [79, 74, 73]. Thus, in order to commercialize this method and produce in a large scale quantity, there is a need for large amounts of water to make this happen which is neither environmentally friendly nor easily applicable [74]. Furthermore, both methods will have a disadvantage related to leakage of particles into the water used [74]. Generally, all the traditional synthesis methods listed above; precipitation, hydro- and solvothermal, and chemical etching are limited by longer time consumption and operational difficulties caused by multiple-step synthesis [75].

The precipitation method is based on hydrolysis reaction either at room temperature or in water-bath conditions [73]. The technique is based on removing dissolved compounds from a solution by inducing a chemical reaction. The chemical reaction makes the compound insoluble, which can then be removed from the solution by filtering. The success of the method depends on a number of a parameter such as concentration of participating compounds, pH, surfactants, thermal energy, or presence of any constituents that could potentially inhibit the precipitation reaction [80]. An advantage to this method is that it is easy to control the morphology of the synthesized bismuth-based photocatalysts. This can be done by adding surfactants or shape-controlling agents which also controls the size of the products. Polyvinylpyrrolidone (PVP) have been utilized to decrease BiOI nanoplate thickness and thiourea was used to introduced oxygen vacancies which narrowed the BiOCl band gap to visible light [81, 82]. A disadvantage to this method is that high crystallinity products with active facets exposed on the surfaces are rarely synthesized. It is also difficult to obtain products with desired defects [73]. The precipitation method is also linked with having higher production costs as there are many conditions that need to be in place to successfully use this method and has an insufficient production rate, hence the method is not applicable for industry-scale production [79].

Another method mentioned initially for synthesizing BiOCl is a microwave-assisted route, which has attracted growing interest due to several advantageous attributes. It is a clean procedure, straightforward, low cost, low energy consumption, and environmentally friendly. Microwave-assisted heating can be used for hydrothermal, solvothermal, or direct heating of a solvent and the method gives control of the simultaneous growth of the crystals. In addition to this, compared to the methods mentioned above there is rapid heating, lower temperatures, highly selective heating, and a large reduction of reaction time, there is an equivalent reduction in energy use, cost and improved production efficiency [83, 77, 73]. It can also be easily scaled up to industry levels. Another advantage of the process of microwave heating is that it gives a uniform nucleation environment for the BiOCl facilitated by the uniform heating method. This results in narrow size distribution for the produced crystals and with higher purity than the other synthesis methods [73, 83]. In addition to this, it may increase the crystallinity of the material resulting in large surface areas with larger pore widths and volumes [83]. The use of microwaves can also induce phase transformations within the material, which could be useful to investigate further [73]. There is also reports of more oxygen vacancies (OVs) on the surface being induced when using a microwave-assisted solvothermal method compared to conventional solvothermal method or precipitation route. Thus the microwave heating is the factor that is inducing these OVs [83]. Depending on the aimed use, this can both be an advantage or disadvantage.

2.3.2 Dry-chemistry approach

In general, the synthesis of BiOCl has mainly focused on liquid phase schemes [6]. This gives rise to certain issues that stem from the synthesis method, and that will affect the field of application for the resulting BiOCl.

Based on mentioned disadvantages, proposing a synthesis without the need for organic solvents as well as simplifying the process could potentially be advantageous for the field of fabricating photocatalysts. One of the synthesis methods mentioned was solid-state milling at room temperature which is a grinding process. It is an eco-friendly and solvent-free method that utilizes mechanical energy in order to facilitate a chemical reaction between the powders that are milled together or induce changes to elemental composition and structure [84, 73, 85]. The advantage of this method is that the milling could cause defects in solids and thus creating cores of nanoparticles. It may also increase the surface energy by decreasing the particle size of the precursor, leading to structural transformation with for instance the exposed facets and chemical reactions. This could potentially lead to the formation of intermediates [73]. If changes in size and morphology are the desired outcome, there is a necessity to form an intermediate that will then undergo further treatment such as hydrolysis.

Another advantage is that it has good prospects of being scaled up to industry volumes at a low cost compared to wet-chemistry methods [85]. One of the reasons is that there is no utilization of expensive organic solvent like in the solvothermal route or need for a large amount of water like in hydrothermal synthesis [74]. The process happens at room temperature so there is no requirement for additional thermal energy. Additionally, milling may as mentioned produce cores of nanoparticles by defect formation in solids. This leads to an enhancement in the physicochemical properties of the resulting material. Overall the method is more eco-friendly than solvothermal method, and there are no complicated preparation steps and neither harmful nor harsh reaction conditions [85, 73].

However, there are certain disadvantages linked to this method. It has for instance proven difficult to regulate the microstructure and morphology of photocatalysts by the means of milling. Additionally, when the aim is to produce bismuth-based photocatalyst with a decreased particle size and enhanced photocatalytic activity, there is a need for high-energy mills to make this happen, which is less fortunate from the energy consumption perspective. The choice of the precursor is also a critical factor as both composition and microstructure are determined by this, which has to be taken into consideration when using this method [73]. This is demonstrated by a study where Bi_2O_3 and $BiBr_3$ were milled with different molar ratios, resulting in $Bi_xO_yBr_z$ with different atomic composition and microstructure [86].

Another critical factor in the method is time, which is an additional parameter that has to be considered as it controls the morphology of the resulting material [73, 87]. This is demonstrated in a study where BiOBr was synthesized using $Bi(NO_3)_3 \cdot 5\,H_2O$ and KBr and by changing the milling time from 15 min to 60 min, resulted in an altered morphology from welded plates to uniformly thin single nanoplates [87]. Furthermore, a disadvantage of this method is the high risk of leakage of nanoparticles into the air, which consequently makes the method less environmental friendly [88]. Compared to liquid synthesis methods this solid reaction method generally gives a broader size distribution, which is attributed to the restricted production control this method gives [74]. Liquid synthesis method, hydro- and solvothermal, has vast ways of control during the process which is not applicable to solid reaction methods.

2.3.3 Space-confined synthesis

With a solution-free, space-confined chemical vapor deposition (CVD) synthesis, large-area and atomically thin BiOI crystals were successfully prepared on freshly cleaved fluorophlogopite mica substrates placed in a furnace. The sides of the square-shaped crystals were >100 µm, displaying a large area and a thickness of 1 to 4 nm for monolayer, bilayer, trilayer and tetralayer. The confined space was obtained by stacking two mica substrates together, creating a narrow gap between the substrates where the precursor was placed. As the substrates were stacked randomly together, there was no reassurance of uniform gap distance. The obtained crystals were tested as a light photodetector functioning in the visible light range, resulting in good photo response and high sensitivity. The photo response under 473 nm light, which is within the visible light range, was discovered to be 26 $\mathrm{mA\,W^{-1}}$ and a sensitive detectivity of $8.2 \cdot 10^{11}$ Jones. Furthermore, the photoresponse time was 0.12s for the rise and 0.25s for decay. For expanding the squared synthesized BiOI, a transfer from mica substrates to another substrate must be achieved. In this study the crystals were transferred onto SiO_2/Si substrates [89].

For chemical vapor deposition (CVD) growth in a confined space, a fluidic model was designed. It was discovered that an entrapment, in this case of O_2 gas molecules, increased the growth rate of 2D material hence decreasing the synthesis time [90]. The trapping effect will also shield the confined space from the external atmosphere, making it more unaffected and less sensitive to external conditions that may not be fully controlled during the synthesis [89]. The confined space effects on graphene growth on copper were studied, where the initial growth rate was < 0.4 µm/sec, and when a copper foil was placed on top of an oxide substrate creating a narrow gap the growth rate was increased to 60 µm/sec. The oxide substrate used was SiO_2/Si where the thickness of the SiO_2 was approximately 5 nm. It is discovered that the oxide from the substrate coating continuously releases oxygen in the confined space that entraps these gas molecules and contributes to the increased growth rate by lowering the decomposition energy barrier for the precursor [90]. However, the SiO_2/Si substrate will release oxygen if the heating temperature exceeds 800°C [91]. Another study fabricated TiO_2 nanowires from a $TiCl_3$ solution and the water vapor generated in the confined space was trapped. This lead to a pressure high enough to favor crystallization in the confined space [92].

The gap that the confined space creates is normally in the CVD method used strategically to alter the concentration fields of the reactants within the gap. This is executed on the basis that a narrow gap induces a reduction of both the concentration and flow velocity of reactive compounds within the confined space. This will subsequently induce a decrease in nucleation density and growth rate of the deposited compound. A larger gap will consequently result in the opposite outcome [93, 94]. Furthermore, in a CVD system the confined space can be simulated by a space-confined reactor, instead of stacked substrates [94]. For this setup, the boundary layer thickness is of special significance. The boundary layer thickness δ, represents the length between the bulk gas flow and the substrate surface [93]. This boundary layer thickness will usually in CVD systems be larger than the length of the space-confined reactor, meaning that the confined space and thus growth space will be within the region of δ. Based on this, a stable gas flow will be prompted that will generate a controllable and stable growth environment for the material. A simulation was carried out for a confined-space reactor in a CVD system, which confirmed that the gas flow velocity decreased within the confined space while the δ increased. This indicates that the mass transport of reactive compounds to the substrate was significantly reduced within the confined space. In regards to growth kinetics, this means that it moves towards a more mass transport limited region as opposed to surface-reaction. Mass-transport (diffusion) limited is favored for synthesizing large-area, high-quality 2D single crystals. Diffusion-limited growth kinetics for the confined space can be obtained by having a uniformly distributed concentration of reactive species and by reducing the substrate surface roughness [94]. This can be done by reducing the concentration of reactive species, having a lower flow rate in a CVD system, and stabilizing the growth conditions as much as possible. Furthermore, the substrate surface is a critical factor in 2D material growth in a confined-space method, and reducing the roughness is favorable. Substrates should be atomically flat to ensure free migration of atoms and chemically inert so that no reaction involving the substrate occurs [93].

2.3.4 Microwave oven synthesis

Heating by a microwave oven is considered a newer method, but reported to be quick and efficient with a more rapid heat transfer compared to conventional methods [95, 96]. A microwave oven synthesis shares the same benefits as a microwave-assisted method but with easier synthesis steps and a decreased time consumption. A benefit of using the microwave to heat the precursor is that the process is rapid and simple, thus offering more choices for structure-control growth of

2D material [83, 6]. Additionally, a microwave oven offers volumetric and selective heating, the equipment is compact and space-effective and the heating could be switched on and off swiftly. The environment will not be polluted as there is no combustion compounds being produced [95].

The microwave oven utilizes polar molecules rotating in an electromagnetic (elmag) field to convert elmag energy to thermal energy within the structure [6]. This type of heating is a process within electroheat-techniques among induction, radio frequency, direct resistance, and infrared heating [95]. The elmag irradiation of a microwave oven operates within the frequency of 0.3 GHz to 300 GHz, which corresponds to a photon energy of 0.0016 eV. This energy is insufficient for breaking chemical bonds, thus microwave irradiation can not induce chemical reactions [97, 96]. Microwave heating is based on dielectric heating effects which are dependent on the capacity of the material to absorb microwave energy, and subsequently convert it into thermal energy.

Microwave radiation with distinctive frequencies hit the material during heating, then the permanent dipole molecules or ions in the material will align in the applied electric field. The electric field oscillates and creates an alternating electric field that changes direction, subsequently, this affects the aligned dipoles that will try to realign themselves with the changing electric field. This constant realignment causes molecular friction and dielectric loss, which is energy loss that is released as heat [97]. The loss mechanism is based on how capable the material polarisation is to keep up with the rapid alternating electric field [95]. The material's ability to realign the dipoles to the applied field frequency will impact the amount of heat that is generated through this process. In the case that the dipoles do not have sufficient time to realign themselves, there would be no heat generated within the material [96]. A domestic microwave oven normally has a frequency of 2.45 GHz which is within a frequency regime where the dipoles have time to align themselves with the electric field but not sufficient time to follow the alternating field precisely [98, 97]. However, the thermal and nonthermal effects of the microwave during synthesis procedures remain poorly understood [99].

Some studies have been performed with the aim to outline the effects of size, volume and position of the irradiated material on the microwave power and how the electric field propagates in the equipment [100, 101, 102]. The is a nonuniform heating problem within household microwave ovens where the temperature distribution is nonhomogenous and can vary by a dozen °C which can cause safety problems in food with regards to microbes [102, 100]. This non-uniformity problem expands to both temperature and moisture and will be enhanced when the volume of the irradiated material increases [101].

In a recent study done in 2016, it was discovered that both the location and shape of the irradiated material, denoted as load, affected the operating frequency of the various microwave ovens tested. In the research, an experimental heating pattern was compared with simulation models for rotary and stationary settings, and an input frequency of 800W was used although the actual input was discovered to vary with load specifications. It was discovered that for the rotary model the heating pattern of the load was less sensitive to the experienced shift in microwave frequency than in the stationary model. This is because the constant rotation facilitated an equal probability of the load edges receiving the same amount of incoming electric field. Oppositely, the stationary model resulted in distinctive and individual focus points of the electric field. In general, the operating frequency differed from the input frequency and constantly changes with time in terms of load geometry, size, and location [100].

This is supported by another study that concluded with the electric field is particularly dependent on the load position in the cavity. In this study, a dielectric, water, was used as the load and the position was changed from farther away, at the center, or close to the wave-input position. The average temperature rising rate was calculated for the "far away" position to be 0.086 °C/min. The center position has a rate of 0.31°C/min, while the close position had a rate of 0.018 °C/min. Clearly, the center had a greater temperature rising rate as the farther away position had a rate of 28% of the center and the close only had 6% of the center rate value [102].

2.3.5 Space-confined microwave oven synthesis

Square BiOCl crystals were synthesized by Kang et al. by placing the precursor $BiCl_3$ in a confined space between two stacked SiO_2/Si substrates. A distinctive difference was the utilization of a conventional household microwave oven as a heating element. The stacked substrates were placed in the center of the microwave oven and subsequently heated for 1-3 min at 700W after being hydrolyzed in air. The substrates were then washed in water to secure any unreacted precursor was removed. Resulting in BiOCl flakes with edge size 10 µm and thickness around 248 nm with good crystalline morphology as there were no observations of granular deposits on the surface. While illuminated with a 266 nm laser, which is in the UV light range, the responsivity was calculated to be 8 $\mathrm{A\,W^{-1}}$ and a photoresponse time of 18ps. For a growth time exceeding 5 minutes or an open space synthesis, the resulting crystals were inhomogeneous and thicker. Thus the study reported that the confined space and growth time were critical factors to obtain uniform crystals. In this study, there were also some observations of terrace structures on the BiOCl crystals [6].

This method by Kang and colleagues is the basis of the synthesis strategy performed in this thesis. Two substrates are stacked together and the precursor, $BiCl_3$ powder, is placed in the confined space between them. Both mica and silica SiO_2/Si are used to investigate earlier statements about growth on these substrates. The precursor hydrolyzes easily in air, so it must be kept in inert conditions before it is ready to be heated. The system is then left in ambient air for 1 minute, giving the solid precursor time to react with the moisture in the air resulting in the formation of the intermediate hydrate $BiCl_3 \cdot H_2O$. The intermediate hydrate between the two substrates is then heated in the microwave oven by molecular interactions with the elmag field. During this heating, the hydrate molecule will decompose into square BiOCl crystals on the substrate.

$$\mathrm{BiCl_3\,(s) + H_2O\,(g) \xrightarrow{\mathit{Air}} BiCl_3 \cdot H_2O \xrightarrow{\Delta} BiOCl\,(s) + 2\,HCl\,(g)} \tag{1}$$

2.3.6 Hydrolysis of $BiCl_3$

A study performed in 2010 analyzed the mechanism in which $BiCl_3$ was hydrolyzed into an intermediate hydrate $BiCl_3 \cdot H_2O$ [103]. This intermediate hydrate has a monoclinic crystal structure with a layered structure with a stacking direction [001]. Between the crystal structures of $BiCl_3 \cdot H_2O$ and $BiCl_3$ there is a topological relation when considering the cations structure, where they have monocline angle $\beta = 106.6°$and $\eta = 106.7°$, respectfully. Upon uptake of the water molecule the $BiCl_3$ increases in volume by $26.5 \cdot 10^6$ pm^3 per formula unit. The study performed X-ray powder diffraction to analyze the kinetics of the two consecutive heterogeneous reactions of formation of BiOCl from $BiCl_3$ via the intermediate hydrate $BiCl_3 \cdot H_2O$. First the hydrolyzation reaction of $BiCl_3$ to $BiCl_3 \cdot H_2O$, then the decomposition to BiOCl. The reactions were studied at room temperature by quantitative analysis of time-dependent powder diffraction pattern. When exposed to moisture in the air, the precursor $BiCl_3$ reacts immediately and forms the hydrate. According to the Johnson-Mehl-Avrami equation the induction period was determined to be around 8 minutes, after this, the reaction accelerates. The half-life time of the reaction is determined to be around 45 minutes. The second reaction, decomposition to BiOCl, is a slower reaction and is 99% completed at 622 min. Thermogravimetric (TG) analysis was also performed of the gas atmosphere at different and increasing temperatures. From this Wosylus et al discovered that below 50°C the topochemical reaction between $BiCl_3$ powder and H_2O gas results in an intermediate hydrate. Upon constant conditions, there is then a slow and irreversible decomposition occurring of the intermediate hydrate to the final products BiOCl and HCl. However, above 50C °there is a direct reaction from $BiCl_3$ to the product BiOCl, thus not generating an intermediate compound [103].

The electronegativity difference, ΔEN between atoms in a single bond can be used to give an indication of which bonding type that exist between them. There are certain values of ΔEN that accounts for which bonding type exists in a molecule, although it is debated and not recognized by scientist throughout. There are some deviation to the specific numbers but a ΔEN around 0.4-0.5 indicates a purely covalent bond. With a difference in electronegativity, ΔEN, of 0.4 to 1.8 a polar covalent bond will most likely exist. Lastly, a ΔEN above 1.8 will be calculated for ionic bonding, thus non-covalent [104]. For the decomposition from $BiCl_3 \cdot H_2O$ to BiOCl there are certain bonding and structural rearrangement that must occur. There will be breaking and formation of covalent bonds and breaking of hydrogen bonds within the water molecule. Two of the Bi-Cl bond must be broken in the intermediate hydrate and with using the Pauling's scale an ΔEN of 1.26 indicates that these are polar covalent bonds. It is also a stronger bond than the H-Cl bond as the electronegativity is increased.

Furthermore, hydrogen bonds within the water molecule must be broken in order to create BiOCl with the oxygen atom from the water molecule. These bonds, H-O, have a bond length of 97 pm and bond enthalpy of 463 $\mathrm{kJ\,mol^{-1}}$. Bond enthalpy for single bonds is defined as the enthalpy change that is needed in order to break one mole of bonds. For diatomic molecules this follow directly of a dissociation, while and average is calculated for polyatomic molecules. Lastly, one of other the major structural aspects is the formation of the H-Cl bond, which has a ΔEN of 0.96 according to Pauling's scale indicating a polar covalent bond. The bond length is 128 pm and bond enthalpy of 431 $\mathrm{kJ\,mol^{-1}}$ [105].

The concentration of precursor has been proven to be of significance for the resulting crystals. In the study performed by Zeng et al of BiOI grown in the confined space between two mica substrates, the effect of precursor concentration BiI_3 was investigated. The inner space is referencing the confined space, while the external space refers to the neighbouring substrates of the two stacked substrates. When the external concentration of precursor was low, the trapping effect of the confined space induced an increase in concentration of BiI_3 at the inner space. This enhanced concentration gave rise to a higher collision frequency of the precursor molecules in the inner space. The higher collision frequency lead to an increased amount of absorbed precursor molecules within the confined space. In the occurrence where the external precursor concentration was high, the concentration at the inner space was nevertheless relatively low, thus suitable conditions for 2D nucleation and growth of crystals. However, as a consequence of the high concentration there was a massive vapor phase nucleation occurring at the external space which facilitated growth of particles on this external surface. These are unwanted particles [89].

2.3.7 Silica and mica substrates

Two different substrates have been used in this thesis, in order to compare how growth of BiOCl was influenced by the different properties of each material. Both substrate are known, commonly used substrates which will give established structural knowledge, and basis of comparison with various synthesis done in other studies. These substrate were also utilized in previous research performed at UC Berkeley, therefore it is deemed beneficial to use these in order to work further on the preliminary research obtained in the Specialization Project [1].

Muscovite is an atomically flat, layered, easily cleaned, thin and brittle substrate and is the most common type of mica mineral group [106]. The chemical composition of muscovite is somewhat complex and depending on the quality classification of the substrates. In general muscovite contains different percentage of silica SiO_2, alumina Al_2O_3, potassium oxide K_2O, ferric oxide Fe_2O_3 and sodium oxide Na_2O. There may be traces of titanium oxide TiO_2, calcium oxide CaO, magnesia MgO, phosphorus P, sulphur S and graphite C [107]. The structure is shown in the Figure 5 where two layers are illustrated [108]. Furthermore, muscovite is an insulator which makes it not applicable as a substrate for some applications within the field of nanoelectronics [106].

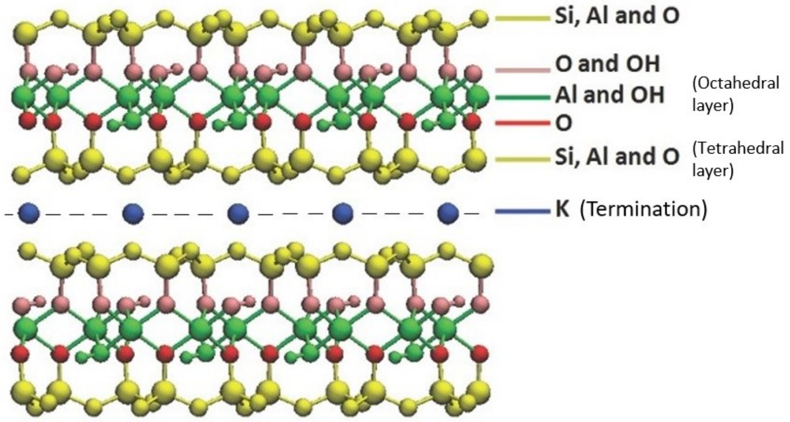

Figure 5: The figure illustrates the structure of mica.

Muscovite has a monoclinic crystal system with lattice parameters a=5.201Å, b=9.022Å, c=20.0430Å, β=95.78°while $\alpha = \gamma$=90°. The space group is C 2/c [109, 110]. The material consists of a layered structure where sheets of minerals are separated by intercalating ions, as seen in Figure 5, this ion is potassium, K^+. Each layer consist of a tetrahedral layer that is confined by alternating sheets of K^+ ions and octahedral layers [111, 112]. In the octahedral layers Al^{3+} occupy the M2 octahedral sites while the M1 sites are unoccupied. Each $Al3^+$ ion is coordinated by two OH molecules and four non-bridging O atoms. Furthermore, in tetrahedral layers a random occupancy of 75% silicon and 25% of aluminium at T1 and T2 tetrahedral sites is to be expected [112]. Throughout this thesis, muscovite will be denoted as mica.

As this layered structure is held together by weak van der Waals interaction between ions it makes it easy to cleave the mica into its consisting layers resulting in thin sheets that can be readily used as highly elastic substrates. Cleaving of the mica happens along its natural cleavage layers along the K ions in Figure 5, thus cracks typically develop along any direction that differs from the cutting direction [111]. Upon cleaving, the mica may become negatively charged hence there is a need for a positive ion to bind compounds to the surface. The net negative charge also give rise to contamination from positive charged particles from the environment [111].

A contamination study on muscovite analyzed the surface composition where it was concluded that carbon or a carbon compounds are the biggest contaminants when mica is exposed to air. However, CO_2, CO and CH_4 from air does not adsorb on the mica surface without the presence of an extra adsorption component, most likely H_2O. Additionally, if the cleaved mica sheets are left in ambient air hours after cleaving, it is of no importance if the cleaving process occurred in atmospheric air or in ultra high vacuum. The contamination will be similar [113].

Silica substrate, SiO_2/Si, is structured with silicon atoms passivated by a native oxide. These wafers are have either a thick or a thin oxide layer of SiO_2 with a high particulate count, making them desirable for their electronic properties [114]. The SiO_2 function as a high quality, electrically insulating protective layer on the surface of the silicon wafer. The SiO_2/Si wafer has a dominant role in the silicon device industry and is a well-known, widely used semiconductor material.

For instance in metal-oxide-semiconductor (MOS) where a crucial part is that Si (100) i thermally oxidized, resulting in growth of thin SiO_2 layers that has a high electrical quality. Thermally oxidation usually takes place at temperatures of 900 to 1300 in the presence of oxygen compounds. The high quality of both the layer and the interface is important for the MOS technology to function well [115].

Figure 6 shows the silica substrate structure with silicon atoms bonding to the silicon dioxide layer. This is a proposed model for the interface structure in the silica substrate. At the surface some silicon atoms stay unbonded, and the unpaired electrons will remain in the vicinity of these atoms. This forms dangling bonds on the silicon surface atoms [116].

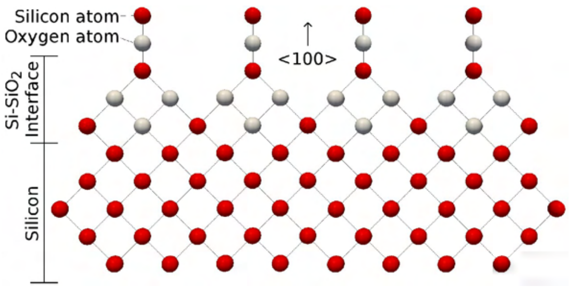

Figure 6: The figure illustrates the structure of silica, SiO_2/Si [116].

A study compared the growth of BiOI on mica to growth on, SiO_2/Si, silica substrates. From the study the crystals grown on mica were around 1 to 4 nm thick, while on silica the plates were bent and twisted. It is known that silica has dangling bonds on the surface while mica does not, which could be influential considering growth mechanism on the substrates [89]. It is proposed that these dangling bonds introduces a high energy barrier for the adatoms to migrate over thus the barrier obstruct the free migration and diffusion growth of these adatoms on the substrate surface [117]. The dangling bonds will pin the nuclei and obstruct growth in the lateral direction [22]. Additionally, with the dangling bonds the nucleation density will serve as reactive sites for further nucleation which is unfavorable for growth of 2D crystals. On the contrary, it is advantageous for growth of 3D materials and out-of-plane nanosheets which is more likely to happen on these unpassivated surfaces [89, 22]. As growth of 2D materials on silica substrates is challenging due to abundance of reactive sites, it is the exact opposite on mica substrates. On an inert mica surface it is difficult to start nucleation as a consequence of the absence of high-energy nucleation centers and absorption of reactants [118, 119]. At areas with low density of dangling bonds there will be free migration of atoms that will attach to nuclei and grow in-plane nanosheets [22].

Another study reported similar findings where BiOCl were grown on silica and mica and a comparison was given. According to this study BiOCl crystals that were grown on silica had a size of 10 µm with a thickness of 248 nm determined from an atomic force microscope (AFM) image. While on mica substrates the BiOCl crystals had a reported thickness of 8.7 nm and with a size smaller than silica synthesized BiOCl [6]. This was also explained on the basis that silica substrates has dangling bonds on the surface, whereas mica does not. It is stated in the study that on mica surface the free migration of adatoms during growth is easier than on the SiO_2/Si surface. Comparison between silica grown crystals and mica grown crystals found that the former will give improved optoelectronic performance. It is also stated that the range of applications of crystals synthesized on silica are broader as integrated circuits often are rooted in silicon substrates and any transfer to silicon based industry is simplified [120].

2.4 Crystallization of BiOCl

2.4.1 Growth mechanism

For crystals to grow there has to be a disturbance in the system by either thermal, chemical and/or mechanical approach. A change in temperature, pH, chemical potential, electrochemical potential, strain and pressure are all used to achieve this. Without these disruptions to the system it will remain in equilibrium with the mother phase and the Gibbs free energy, ΔG is at its minimum in the system and there will not be growth [72]. Nucleation, growth and assembly processes of a nanocrystal are critical knowledge when the aim is to synthesis them with precise morphology and uniform size [121].
Growth mechanism in wet-chemistry methods is more studied than for solid decomposition. Generally, in a solution the bismuth and chlorine sources are dissolved into corresponding ions, Bi^{3+} and Cl^{-}. The bismuth ion is then hydrolyzed into an intermediate $(Bi_2O_2)^{2+}$ which attracts the negatively charged chlorine ion, Cl^{-}. By Coulomb interaction these form a [Cl-Bi-O-Bi-Cl] nuclei with the bismuth and oxygen interconnected with covalent bonding and the nuclei stack together with weak van der Waals interaction forming layers, this structure is detailed in section 2.2.3 [121]. This initial nucleation stage occurs rapidly [122]. For an extension of the reaction time there are observations of the [Cl-Bi-O-Bi-Cl] layers stacking together progressively and eventually producing layered 2D structures. Plate-like structures are further assembled in the liquid by processes such as Kirkendall diffusion, Ostwald ripening, oriented attachment [121, 122].

There are certain parameters that may affect the growth mechanism. In a study it is discovered that pH and concentration of Bi^{3+} will be influential on the reaction process when synthesizing BiOCl by a hydrothermal method. If either the pH value or the concentration of Bi^{3+} were low, the nuclei would have a suppressed growth and small nanocrystals would form and assemble to granular structure. The concentration was regarded low when it was under 2 mol/L and a low pH was defined in this study as less than unity. On the contrary, if the values of either parameter were high the nuclei would grow into larger grains on the compromise of smaller nuclei, according to Gibbs-Thomson law. These grains grow by attachment of smaller, existing nuclei merging together to form flake-like structures. Furthermore, a link between pH, concentration of Bi^{3+} and percentage of exposed (001) facets was made. Small nanocrystals were deemed crucial in the formation of (001) oriented granular film, while growing larger grains was linked to a decrease in reactive (001) lattice planes. Hence the granular structure had a higher percentage of exposed (001) facets than flake-like structure and granular structure was made if the concentration of Bi^{3+} and pH level was low [123].

This can be connected to a classic growth theory perspective where it is established that the relative surface energies of the crystal facets determines the morphology of resulting nanocrystal. It is also known that the fastest growing facets are high energy ones, and for BiOCl the facet which exhibits the highest surface energy is (001) [36, 123].

Selective synthesizing BiOCl with high percentage of exposed (001) facets is of great interest when the aimed application and use of the BiOCl is for photocatalytic reactions. Under UV and visible light irradiation BiOCl with preferential orientation of (001) lattice plane exhibit superior photocatalytic degradation for direct photoexcitation of Rhodamine B (RhB) [123, 122].The (001) facet is also from a theoretical perspective assumed to exhibit highest photocatalytic activity due to low recombination rate of photogenerated charge carriers, high thermodynamic stability and good sunlight absorption [123]. The overall stability of different growth directions of low-index BiOCl facets were estimated from calculated cleavage energy. It was discovered that the lowest cleavage energy thus highest thermodynamic stability was linked to the (001)-Cl plane with the value of $0.026\ \mathrm{J\,m^{-2}}$ compared to the highest of $2.349\ \mathrm{J\,m^{-2}}$ belonging to both (001)-BiO and (001)-2Cl. The (001)-Cl is the facets where one layer of the halogen is terminated from the layered structure, and the negligible cleavage energy indicates an exceedingly high thermodynamic stability, which makes any formation of OVs on the surface of the (001) plane energetically unfavorable. Within the facets these surface OVs will act as active recombination centers of photo-induced charge carriers, because OVs induced defects level within the band gap of the material [124]. The high thermodynamic stability of the (001) facet makes it a preferred orientation for the Ostwald ripening growth along c-axis [123].

A structure where the facets w lowest surface energy is most exposed is the most favorable [125].

Researchers have reportedly observed synthesized crystals that grew in an octahedral shape with an angle between the facets found to be 135°[125, 123]. The observation of this geometry was reported to be a result of crystal growth direction. From the observations made in the research it was hypothesized that the tetrahedral structure of BiOCl preferred a octahedral shape formation if the crystal faces growing along the [110] direction were approximately equal to the faces growing along [100] direction, see Figure 7. Additionally, a cubic shape is formed the moment [010] growth direction is either stopped or significantly slower than the other directions, thus the (101) plane will vanish and form corners [123]. This is a similar description to the Ag growth on Fe_3O_4 with (001) facets on top and bottom, sides elongated in the [110] directions and the 135°angled sides in the octahedral shape growing in the [100] direction. In this fcc metal the (111) plane has the lowest surface energy, thus increasing planes parallel to the [110] direction will be favoring growth of (111) planes. Even though the (111) plane exhibits lowest surface energy, the (001) plane is the preferred orientation and displayed on top and bottom of the Ag crystal which increases the surface energy γ. So there is a constant competition of the surface energy aspect, which favors (111) facets, and the interface energy which prefers (001) epitaxial growth. Therefore, in this study it is stated that temperature is crucial to grow (001) dominant Ag, Au and Pt crystals [125].

By a hydrothermal method single crystalline BiOCl nanoplates were created and found to be comprised of (001) facet on top and bottom, while the four sides were (110) facets [126].

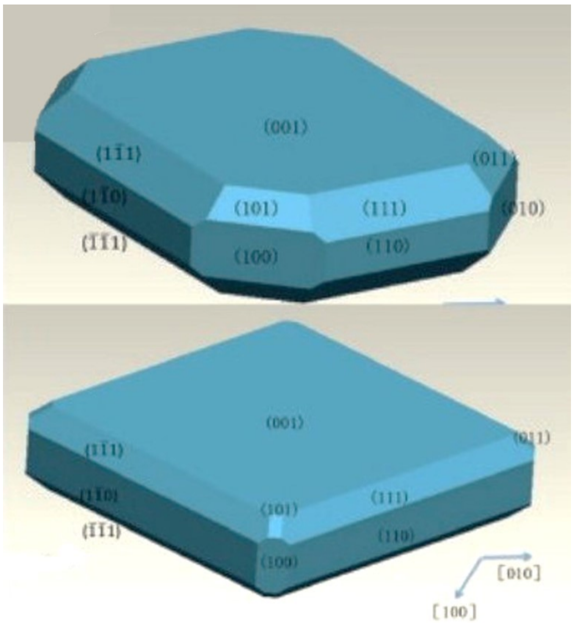

Figure 7: The figure illustrates proposed growth direction of octagons and squares in literature [123].

2.4.2 Solid-state decomposition in a microwave oven

There are various research studying the growth of crystals utilizing a microwave oven where fracture and re-formation of covalent bonds occurs, nonetheless the exact mechanism remains unknown. It is a solid-state decomposition of precursor by thermal energy utilizing electromagnetic field to heat up the precursor from within contrary to traditional heating processes. To observed macroscopic rated and get an idea of the mechanism step-by-step has proven to be hard for this type of decomposition. The more studied gas-liquid and liquid-phase reactions has a time frame controlled by molecularity and/or chemistry, while a solid-state decomposition has additional elements that need to be considered when figuring out the elementary steps of the transition. There is both a geometric aspect and a topochemical aspect [127].

This solid-state decomposition have in many cases produces gasses, like the study using a microwave oven to heat up CuO and $Bi(Fe(CN)_6) \cdot 5\,H_2O$ producing gases such as CO_2, NO_X and H_2O which was determined to be a crucial parameter in order to make ultra-fine powder [128]. A similar study was performed on $La[Co(CN)_6] \cdot 5\,H_2O$ where the traditional electric furnace was compared to the more experimental microwave oven approach. For the microwave oven the precursor was heated for 10 min at a power of 900W, while the furnace was set to 1000°for 120 min. An average crystal size was measured and by microwave oven the particle size was 16 nm compared to 500 nm by the furnace. The microwave oven method exhibited a significantly decreased crystal size. The decreased crystal size is believed to be caused by an increase in nucleation rate for the microwave oven irradiation. This is expected as the heating rate is higher for microwave oven than traditional heating methods. This is because microwaves have a larger penetration depth into the material thus it is heated from the inside, which trumps the heat conduction by traditional methods which is established at the surrounding medium and goes inwards [129].

Commonly with such reactions there will be a subsequently weight loss due to evaporation of gasses, and generally a weight loss until the end crystals are synthesized [128]. For both these reactions, $Bi(Fe(CN)_6) \cdot 5\,H_2O$ and $La[Co(CN)_6] \cdot 5\,H_2O$, the hydrated precursor experiences a weight loss of five water molecules upon microwave irradiation, then loss of the six cyanide groups.

It is also reported in some cases that after thermal decomposition the temperature has reached a maximum and will thus decrease, despite being irradiated by microwave radiation. This allegedly occurs if the product after decomposition is not a great microwave absorber. Generally, inorganic oxides are considered weak microwave absorbers [130].

2.4.3 Nanoframes

Nanoframes have been strategically synthesized for the use in catalytic reactions as the structure exhibit activity surpassing solid structures counterparts. Nanoframes are open structures comprised of interconnected ridges with no walls, and these ridges are commonly ultrathin (<5nm) and contains a high density of low-coordinated surface atoms. An illustration is provided in Figure 8. In addition to greater catalytic performance, open structures comprised of noble metal accommodates the limitation with cubic counterparts, like the noble metal scarcity [131].

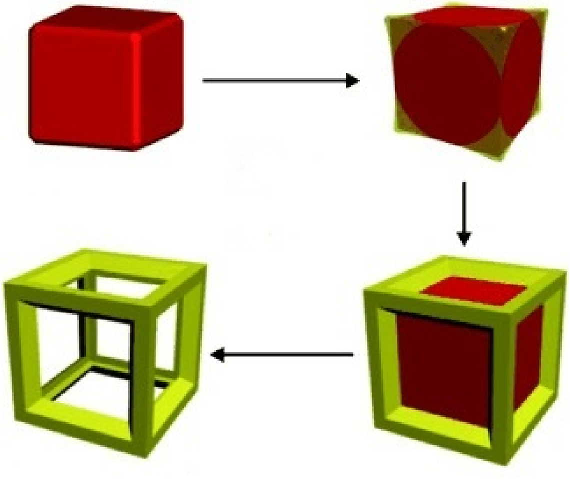

Figure 8: Illustration of a nanoframe [132].

Nanoframes of noble metals can be used in catalytic activities such as electrocatalysis, fuel fells and oxygen reduction reaction. They possesses advantageous properties for catalytic application such as large surface-to-volume ratio, highly reactive surface and enhancement in catalytic activity [131, 133]. Additionally, the structures can potentially be used in drug delivery but some stability issues must be solved beforehand [134]. The reason for nanoframes prominent catalytic performance is established within the structure. The ridges in the nanoframe are comprised of a high density of low-coordinated surface atoms [131]. These atoms will easily interact with reactants as they have rich dangling bonds. Additionally, these atoms function as catalytic sites thus contributes to the increased catalytic activity of nanoframes [135]. Other contributors to increased catalytic activity lies within the synthesizing of the nanoframes. Creating nanoframes usually occurs by oxidative etching and/or galvanic replacement, and these processes induce atomic steps, vacancies, dislocations, stacking faults, grain and twin boundaries and lattice strain. These defects functions as active sites for certain catalytic reactions thus increases the catalytic performance of the nanoframes [131].

The formation of nanoframes can to a great extent be divided into two categories; presynthesized template-assisted method or *in situ* formed template-assisted method. Additionally, as mentioned nanoframes are normally synthesised by oxidative etching and/or galvanic replacement. Oxidative etching is used as a segment in both categories, while creating nanoframes with a galvanic replacement reaction is the most powerful strategy within the presynthesized template method [133]. Generally, oxidative etching can be used to target specific faces creating face-selective carved nanoframes. This is done with the knowledge that the sites most prone to etching is the ones with the highest surface free energy. For a monometallic material these sites can be atoms situated at faces, vertices and edges and are caused by differences in coordination number. Additionally, various defects including dislocations, vacancies and twin and grain boundaries have an excessive amount of free energy making them more vulnerable to etching [136, 131]. In a bimetallic system, oxidative etching can be a targeted dealloying of atoms with a low reduction potential (metal A) positioned at the center and side faces of the nanocube, rendering a frame of atoms with high reduction potential (metal B). Achieving this alloyed structure can be done by carefully engineering elemental deposition for the faces, edges and vertices [131].

Etching can also be performed with various chemicals, HCl and ethanol being some of the most commonly used. In a wet-chemistry method Rh-Cu octahedral frames were synthesized using O_2 and HCl with preferential etching of 3d metals such as Cu and Ni [137]. Nanorods of Rh frame was in a similar manor synthesized by targeted etching of Au in Au-Rh core-shell nanorods using HCl. In the study it was discovered that the low-index facet (111) of Rh was not etched by the Cl^- [138]. Another study added HCl while growing Cu_2O nanocrystals fabricated nanoframes with framework of (110) faces and empty (100) faces. After growth the (100) faces filled up and the structures turned into nanocages. These were then selectively etched by HCl over the (110) faces creating a rhombic dodecahedral Cu_2O nanoframe with (100) framework. A noticeable result from this was that the rapidness of etching was greater for (110) faces than (100) ones. Without HCl added there was formation of solid nanocages proving the importance of the acid in nanoframe formation [139]. Cubic nanoframes of Cu_2O with etched (110) crystal faces were in another study synthesized by introducing HCl during growth. The HCl face-selectivity stems from the bonding found at the facets. From the study it is discovered that the Cu-O bond on the (100) face had the shortest length, thus the strongest bonding, under acidic conditions compared to the other low-index facets (111) and (110). Moreover, the relative facet stability were ranked (110)>(111)>(110) for Cu_2O [140]. A preferred face etching of the (110) face was also discovered for iron nanoframes created by adding sodium oleate, and without this compound star-shaped nanocubes were formed. The nanocubes created after adding sodium oleate were found to have a thickness difference between corners and centers upon extending reaction time. In this study there was no clear reasoning for the prominent etching of (110) faces [134].

The structure of nanoframes as described with ridges of low-coordinated surface atoms is a doubled edged sword. Low-coordinated surface atoms contributes to an enhancement in the catalytic performance, but its presence also provides instability to the structure making it metastable. This is especially true if these types of atoms are located on edge, vertices or high-index facet. The nanoframe structure are kinetically controlled product and from a thermodynamic perspective they are less favorable compared to cubic counterparts [131].

It is well known that nanoframes have a stability issue as it is observed changes to morphology upon increasing temperature or exposure to harsh conditions. An increased temperature will subsequently increase kinetic energy of the surface atoms. Upon adequate kinetic energy these atoms could escape the lattice location and transfer to sites with higher stability through a diffusion mechanism. Thus when used in catalytic reactions the nanoframes are expected to undergo changes both in regards to structure and composition, which may lead to deterioration of the nanoframe or complete failure of its performance in the reaction [131, 133]. This is seen in a study where Ru cuboctahedral nanoframes were kept intact in an inert environment up to 300°C, but when heated to 400°C the nanoframe ridges were fragmented due to thermal stress and dissolved as the atoms moved to a more favorable thermodynamic state [141]. To overcome the structural instability there are certain methods that can be done such as optimizing the composition or post-synthesis treatment of the structure [131].

2.4.4 Surface cracks

While etching is purposely utilized to form nanoframes, the process of etching have in other cases lead to an unwanted side effect on the prepared crystals. In a study observations of cracks forming on the surface of BiOCl crystals were made resulting from etching [142]. Depending on the type of crystals made, there were different types of cracks forming on the surface which can be seen in Figure 9. The study reported the wet-synthesis of square crystals with un-truncated corners in addition to rounder squares with truncated corners. The latter structure was synthesized when the system was not sealed, thus open environment with exposure to air. Without these conditions there was no observation made of rounder squares.

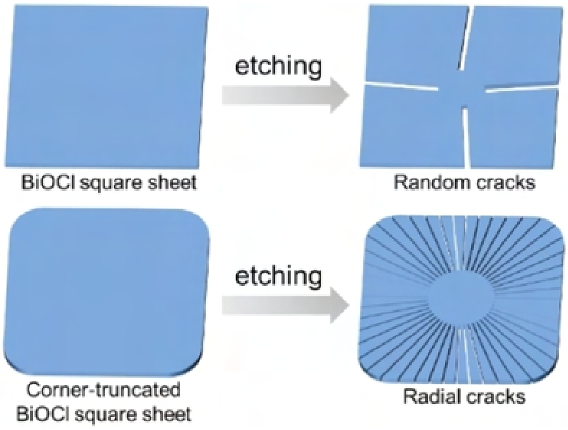

Figure 9: Illustration of the different types of cracks forming on square BiOCl and rounder square BiOCl [142].

Radial cracks was created on the rounder squares while on the squares the cracks were following the low-index facet direction, due to the facets low surface energy [142]. These facets usually have a higher surface energy compared to low-index facets and this is ascribed to the high density of kinks, steps, edges and that these facets are compromised of low-coordinated surface atoms. This type of surface atoms will exhibit rich dangling bonds thus increasing the surface energy [135]. The cracks created on the square were induced by etching, and with an extended etching period there was first no observational changes to the amount of cracks. Increasing the etching time further there was a gradual increase of the size of the cracks, they became wider. Additionally, the corners of the square became rounder exhibiting a truncated-corner structure. Expanding the etching time further the BiOCl nanosheets etched away completely. This etching process was accelerated with a decrease in pH by adding HCl, thus a proposed equation for formation of cracks was made, see Equation 2.

$$\mathrm{BiOCl} + 2\,\mathrm{H}^{+} \rightarrow \mathrm{Bi}^{3+} + \mathrm{H_2O} + \mathrm{Cl}^{-} \tag{2}$$

The origin and development of the two different types of cracks are inherently different, but both types are caused by etching leading to physical stress within the crystals. The formation of cracks on the square crystal spread in the direction of low-index facets due to lower surface energy, however the formation of radial cracks are not governed by this and it is therefore not an energetically favorable process. Additionally, formation of radial cracks should in theory be difficult as the BiOCl sheets were determined in the study to be single crystalline and highly anisotropic. These radial cracks are hypothesized to be originating from air bubbles which were only incorporated into the synthesis of rounder squares. These air bubbles could cause physical stress to the crystals, resulting in these radial cracks.

2.4.5 Flower-like structure

There are reports throughout the years of flower-like BiOCl structures being synthesised and having higher photocatalytic activity compared to the photocatalyst commonly used and commercially available TiO_2 and greater than pure hierarchial BiOCl under visible light irradiation [143, 144, 145]. Most of the synthesis schemes utilizes organic surfactants or templates to achieve these flower-like structures [145].

A template-based, room temperature synthesis resulted in BiOCl flowers with a narrow band gap of 2.87 eV. The nanopetals with a preferred growth along [110] direction were 17 to 23 nm thick and diameter of the flowers was on average around 1.5 µm. When using templates, a calcination step is essential in order to dislodging the template, additionally this step will result in a higher (110) orientational growth on the surface. Without the use of templates the team reported irregular shapes of the synthesised BiOCl structure, demonstrating the importance of templates in this method [146]. Without using templates, a surfacant-based synthesis fabricated BiOCl flower-like structures on Si substrate. The petals were 10 nm thick with a size of 200 nm and growth along [110] direction [38]. Other studies used a solvothermal synthesis and the organic solvent was deemed a crucial parameter for the formation of self-assembled flower-like structure from nanoplates [144, 145]. The disadvantage of using these methods is the use of toxic organic solvents in solvothermal synthesis, as mentioned previously in Section 2.3.1.

In 2013, Ye et al synthesised the same structure by a hydrolytic synthesis without the use of organic surfactant or templates. The study reports reaction time being a crucial factor in crystallization and assembly of these hierarcical flower-like nanostructures. The hydrolytic synthesis done by Ye et al showed that by increasing reaction time there was noticeable more flower formation, while a decline in number of nanosheets. This finding may suggest a dependency between these structures. Additionally, for this synthesis scheme they found a reaction time threshold, and when exceeding a reaction time of 60 min it induced overgrowth and a negative influence on the flower-like structure [143]. The same year of 2013 Li and colleagues did a microwave-assisted synthesis using mannitol and creating BiOX, where morphology and size was influenced by amount of halide, type of precursor and mannitol concentration. The bimuth source was bismuth nitrate pentahydrate, $Bi(NO_3)_3 \cdot 5\,H_2O$. By a low amount, 2mmol, of precursor NaCl it resulted in well-defined BiOCl nanosheets with a length of 30 nm, while increasing the amount to 4mmol lead to BiOCl nanoplates with length of 60 nm and thickness 10 nm. XRD of the two morphologies showed peak broadening for the nanosheets indicating smaller particle size. Interestingly, they found that the by choosing reaction precursors CTAC and CTAB they also served as soft templates facilitating the flower-like growth via interaction of precursor ions and petals, creating microstrain within the petals. This resulted in uniform flower-like structures of diameter 200-300 nm, with a band gap of 2.70 eV. It also resulted in a high removal capacity of Cr(VI) of 40.1 $\mathrm{mg\,g^{-1}}$, compared to that of 32.8 $\mathrm{mg\,g^{-1}}$ by nanosheets and 23.7 $\mathrm{mg\,g^{-1}}$ by nanoplates synthesized in the same study. They also analyzed the growth direction of nanopetals by XRD analysis. The group discovered that in distilled water the crystals preferred growth direction was along c-axis in the (001) direction, perpendicular to the platelets. However, when using mannitol it restricted the crystal anisotropic growth along (001) direction, which led to weak intensity signal of the (001) plane in the XRD spectra. The restrictive growth was confirmed upon increasing mannitol concentration and subsequently observing the intensity ratio between (001) and (110) decline, signifying a higher intensity of (110) plane signal [147].

In general the flower-like structure is reported to be self-assembled and compromised of several thin nanosheets , this was discovered by analyzing SEM images, and high magnification TEM confirmed that the nanopetals compromising the flower-like structure indeed consisted of nanoparticles [38, 143, 146, 144, 145, 147, 147]. By analyzing SEM pictures a possible self-assembly mechanism for the formation of flower-like hierarchial microstructure was proposed by Ye et al. BiOCl nanosheets are first formed by Ostwald ripening, then during growth the crystal structure of the compound will be a factor influencing the microstructural morphology, which in the case for BiOCl is a tetragonal crystal structure [148, 149, 150]. Ostwald ripening is a process in which smaller particles will deposit on larger ones due to the smaller particles being more soluble in the solution [151]. When there is no use of either templates or organic surfactants in the synthesis, the assembly of flower-like structure had its origin in the geometric constraints of its building blocks [152]. The nanosheets can easily generate curvature throughout its surface giving a flower-like structure when intercolliding with other curved nanosheets [143]. These curved nanosheets are denoted as nanopetals in coherence with the flower analogy. The layered growth of the nanopetals is ascribed to its unique electron structure and the lattice structure of Bi and Cl atoms [38].

The nanopetals are conglutinated in the center of the flower and spead out towards the edges to the flower, which is confirmed by analysis in TEM [146]. These nanopetals are mostly crystallizing along [110] direction in the tetragonal structure, perpendicular to the c-axis [38, 146, 153]. This is confirmed in XRD analysis and as the lattice spacing d_{hkl}, is measured to be 0.273 nm compatible with (110) planes, d_{110} [146]. The measured XRD ratio of (110)/(001) planes for BiOCl flower-like structure is higher than for BiOCl nanoplates, which supports that the nanopetals grow in the [110] direction but with an orientation of surfaces of (001) planes. The reason the nanopetals growth is dominated by [110] direction lies within the oxygen atom density of (110) facets versus (001) facets. As the (001) facets have a higher oxygen atom density, the growth in [001] direction should be dominating over the [110] direction. Paradoxically, will the high oxygen density on the (001) facets attract, in this case, glycerol that will suppress growth through interaction with this surface via its carbon atom, thus this will act as a capping agent and steric hindrance of growth. Additionally, if the growth along the [110] direction is higher than [001] direction the resulting crystal will be thinner and larger. The desired outcome is to synthesize nanopetals with high exposure of (001) facets, while making them thinner [153].

Compared to nanosheets of BiOCl that has a band gap of 3.0 to 3.5 eV, depending on the thickness and morphology, the flower-like structure has a narrower band gap. The band gap of this hierarchical structure is reported to be 2.70, 2.87 and 2.92 from different studies eV [147, 146, 154]. It is deduced, as mentioned, that the BiOCl samples with crystal growth along the (110) plane, like exhibited in the flower-like structure, have smaller band gap than those that have oriental growth along the (001) facet [146]. A study found that the necessary calcination step when utilizing templates would enhance the crystalline anisotropic growth of the BiOCl along the (110) direction, in similarity with the use of mannitol in a previous mentioned study. Subsequently, the band gap was measured before and after calcination to be 3.18 eV and 2.78 eV, respectively, thus indicating that a higher exposure of (110) planes is equivalent with a smaller band gap [146].

The flower-like structure of BiOCl exhibit greater photocalytic activity than nanosheets or nanoplates. In one study the flower-like structured displayed great degradation of RhB under visible light ($\lambda \geq 435$ nm). The degradation rate was calculated from experimental data to be 0.1186 /min for BiOCl after calcination [146]. In comparison, the overall rate of the first order photocatalytic decomposition kinetics of RhB for BiOCl nanosheets perfomed under UV light was reported in a study to be 0.057 /min [43]. Another study compared degradation rates of RhB for BiOCl flower-like structure with exposed (001) facets to that of BiOCl nanoplates under visible light. The flower-like structure exhibited a degradation rate of 0.272 /min and adsorption capability of 30.8% while the nanoplates 0.0324 /min with an adsorption of 0.9% under the same conditions. The flower-like structure also was 144 times better than TiO_2 for degradation of RhB. TiO_2 had a degradation rate constant of even though the two structures had similar BET surface area of 53.5 $m^2\,g^{-1}$ for BiOCl and 50 $m^2\,g^{-1}$ for TiO_2. Thus the flower-like structure with exposed (001) facets display fast degradation rate of and greater activity for degradation of photosensitized dye under visible light [153].

Furthermore, for flower-like structure it is credited to its unique hierarchial structure, large BET surface area and strong adsorptive ability. The large surface area contributes to more catalytic sites and will be more efficient when absorbing light as it is larger. For flower-like structure in a study, the BET specific surface area was $22.3\,\mathrm{m^2\,g^{-1}}$ and for BiOCl nanosheets 50 nm thick the BET surface area was $10.1\,\mathrm{m^2\,g^{-1}}$ [143]. It can also be credited to high exposure of (110) facets and high phase purity, narrow band gap and thin structure [146]. It was, however, determined that a large specific surface area was a less important factor compared to growth along (110) direction for photocatalytic performance. This was concluded based on test of samples that were not calcinated, but had a doubled surface area showed significantly worse degradation of RhB where after 60 min only 63% of the xanthene dye RhB was removed compared to the flower-like structure which displayed a complete degradation of all the RhB after 50 min [146].

The structure plays a role as the thin flower petals enhances the utilization of the incident photons in the photocatalytic process, by having multiple reflections within the center of the structure [143]. This is done by the nanopetals ability to promote the generated charge carriers to move faster from the center of the material and to the surface to participate in the redox reactions that is occurring on the surface [155].

2.5 Experimental methods

Following sections will give an overall description of some of the characterization methods used in this thesis, and what kind of information each method provides in addition to eventual limitations.

2.5.1 Scanning electron microscopy (SEM)

The signals available in SEM are secondary electrons (SE), backscattered electrons (BSE), electron beam induced current (EBIC), cathodoluminescence (CL), voltage-contrast imaging, Auger electrons, and X-rays. Some signals are more commonly used than others, but they give different information.

Secondary electrons (SE) can only escape the sample from shallow, near-surface layers in the material they provide the highest spatial resolution out of all the signals obtained in the SEM. Further down in the material layers, these electrons are trapped as they will continuously collide with other obstacles such as other atoms, electrons, etc. SE provides topographic information and some compositional contrast may be present.

Backscattered electrons (BSE) leave the sample surface with higher energy than SE. This is because BSE emerges from a larger penetration depth. BSE gives information about topography, mass thickness and crystallography as electrons channeling occurs [156, 157]. Additionally, BSE gives information about the composition of the specimen, where elements with a higher atomic number (Z) will give a brighter area in the image.

Characteristic X-rays come from the layers near the surface and are a result of incident electrons with high energy knocking out an electron close to the nuclei. To fill up the electron states again, there will be a continuous jump of electrons from higher energy states to lower ones to fill up the empty orbit. With every jump from one higher energy state to a lower one, the surplus of energy is emitted as X-rays. By measuring the energies (or wavelengths) of these X-rays and as each element has its pattern of characteristic X-rays, the chemical composition can then be deduced. Detectors of these X-rays are either Energy Dispersive X-ray Spectroscopy (EDS or EDX) or Wavelength Dispersive X-ray Spectroscopy (WDS or WDXS). Where EDS or EDX is most common [156].

2.5.2 Energy dispersive spectroscopy (EDS)

Engery Dispersive Spectroscopy (EDS) is a detector used in SEM that gives a qualitative analysis of the specimen [156].

Advantages of this technique are that is a fast elemental analysis technique, element detection for heavier elements than and including carbon and it has an ability to scan large areas or single spots. The disadvantage is among other that it generally has a low detection limit of 0.2-0.5% per element, thus it is a relatively insensitive analytical method. Furthermore, the output data is elemental based and not molecular. This could lead to falsely identifying an unknown material. For instance, if carbon is detected, it is very common to assume that this stems from an organic material present in the sample. However, this does not have to be the case. The signal could originate from inorganic carbon contamination on the surface such as products of carbonate corrosion, or accumulated carbon contamination from the electron microscope [158, 159].

Another setback with the EDS is the difficulties with a quantitative analysis of lighter elements, loosely defined as elements with atomic numbers less than 11 ($Z < 11$). Upon reduction of atomic number, and thus reduction of atomic weight, the ability to ionize the atoms worsens. Additionally, at the moment the atom is ionized it is more improbable that the atom produces X-rays, which results in a weaker detected signal for light elements compared to heavier ones [160, 159]. Furthermore, will heavier elements with increased atomic numbers give a higher detection limit in the EDS. In an EDS analysis, heavy elements can be simplified by elements using L or M lines, and the lighter ones use K lines. A lower detection limit for the lighter elements entails a need for a higher count of these elements. This can be achieved by increasing the counting time in the EDS and/or by increasing the beam current in the system [161]. The quantitative analysis of lighter elements will also be affected heavily by surface contamination or conductive coatings applied to prevent charging of the sample [159].

2.5.3 Raman spectroscopy

In Raman spectroscopy molecules are irradiated by an incident beam, this radiation is then scattered at certain frequencies, both the original frequency (Rayleigh scattering) and at frequency both higher and lower than this (Raman scattering) is found in the scattered radiation [162, 163]. The Rayleigh scattering is a strong and elastic scattering process which preserves and oscillates at the original frequency. While the Raman scattering is inelastic and weak, about 10^{-5} of incident beam and only 1 in $10^6 - 10^8$ of the scattered photons is Raman scattered [164, 165, 163]. The technique is a powerful way of analysing the structural and vibrational properties of a crystal [38].

The principle in Raman spectroscopy is using a monochromatic incident laser beam in the UV - visible light range to irradiate the sample, and then monitor the scattered radiation from the sample surface [162, 166]. The reasoning behind using a laser beam is that it has a high intensity, thus consequently ensuring an increased intensity of the scattered radiation. Furthermore, monochromatic radiation is used as this makes it easier to observe the scattered light even with small variations from the incident light. Monochromatic radiation has a near-constant frequency with a narrow frequency range, thus any divergence from this will be detectable [162].

Out of the Raman scattered radiation there are both anti-Stokes and Stokes radiation. Raman scattering where the incident photons are inelastic scattered with more energy (higher frequency) after the collision with the molecule, is called anti-Stokes radiation[162]. This happens as a result of a molecule making a downward shift from a high energy state to a lower one upon interaction with the incident photons, also called a blue-shift [164, 162]. The downwards transition between energy states results in an addition of energy to the incident photons [163]. Anti-Stokes lines are presented in the spectra on the right side of the incident photon frequency as they have a higher value [162, 164].

On the other hand, the radiation that emerges with lower energy (lower frequency) after the collision is called Stokes radiation. Stokes Raman scattering happens as the molecule makes an upward transition upon interaction with the incident photon, going from a lower molecular energy state to a higher one. This red-shift in frequency requires energy, which is taken from the incident photon [163, 164]. These signals are presented in the spectra lower than the initial frequency, thus on the left side [162].

Out of the two different Raman scattered radiation, the Stokes is favored as there are more atoms in the ground state rather than in an energetically excited state at room temperature, which is in accordance with Boltzmann distribution [164, 162, 166]. This is directly linked to the intensities of the Stokes and anti-Stokes lines, thus anti-Stokes may appear weak or not at all in the spectra [162, 166]. Therefore the spectra usually only display the Stokes vibrational lines which have a higher intensity mode than anti-Stokes [166, 163, 164, 165]. The difference in intensities in the Stokes and anti-Stokes bands can be used to determine the temperature [165]. Anti-Stokes is, however, utilized at occurrences when there is a need to avoid fluorescence interference, as this occurs only at the lower-energy side of the incoming frequency. Thus, by only displaying the anti-Stokes side the fluorescent interference is cut off [165].

Raman scattering by the molecule can lead to two types of transitions within the molecule's structure; rotational and vibrational. For rotational transition to happen in the molecule there is a certain selection rule that must be obeyed. This rule express that the molecule must be anisotropically polarizable to be rotationally Raman active, this is exhibited in non-spherical rotors. This involves linear and diatomic molecules as they possess anisotropic possibilities. Accordingly, spherical rotors such as the symmetric CH_4 molecule do not have rotational Raman scattering [162]. Raman spectroscopy is often said to be a vibrational spectroscopic technique, and studies with Raman spectroscopy have the vibrational Raman effect as its basis [164]. To be vibrational Raman active the polarizability of the molecule should change as the molecule itself vibrates [162],

[164]. In order to get a vibrational transition during the scattering process, the molecule has to be able to be stretched and squeezed by incident photons, hence polarizability plays a significant role in vibrational Raman [162].

The direction of the vibration motion is straightforward in diatomic molecules as it moves along the direction of the bond connecting the two nuclei. In polyatomic molecules, it is more complicated as the nuclei will function as harmonic oscillators, and several vibration modes and interactions will happen. Consequently, different types of vibrations occur depending on where the vibrations take place in the molecule [166]. There exist two types of vibration motions, denoted as stretching or bending. The former involves a change in interatomic bond distance and the latter covers changes in bond angle [167]. Bending vibrations are weaker in the Raman than stretching vibrations [166]. With regards to stretching vibrations, there are two types; symmetric and antisymmetric. Symmetric (in-phase) stretching vibrations oscillates in the direction of the molecular bonds, where two or more bonds move back and forth at the same pace, resulting in one frequency output. Antisymmetric (out-of-phase) stretching vibrations is the result of one bond being stretched while shrinking another, thus creating discrepant oscillation which gives off another frequency than the in-phase vibration [166]. A comparison is done of these two types of vibrations and it is discovered that symmetric usually generate the more intense Raman peaks than asymmetric [38].

As for the bending vibration there are four types, labeled as wagging, twisting, rocking and scissoring [167]. This signal gives off yet another frequency than previous mentioned vibration motions. The seemingly complicated vibration motions in a polyatomic molecule can all be deduced as superpositions of the primary vibration modes mentioned above. The Raman instrument can detect and deduce the superposition theory of complex motions [166].

The most intense, clear vibrational bands stem from vibrations with large changes in the polarizability of the molecule. This occurs in for instance $C{=}C$ and $C{\equiv}C$ bonds [163]. The triple bond gives the most intense signal, then the double bond, and lastly single bond which is the weakest Raman scatter. Generally for Raman spectroscopy a covalent bond have the strongest vibrations [166]. The vibrational transitions is present in the region of the spectra from 10^4 to 10^2 cm^{-1} [166].

Molecular vibrations are unique for every molecule and function as its fingerprint. Thereby analyzing the resulting vibrational spectra by sorting signals to corresponding bonds etc from a database, the irradiated molecule can ultimately be deduced [164]. Before starting the process to assign vibration peaks to bonds etc, it is important to be aware that two or multiple bonds can be observed as a group of atoms vibrating in the spectra, instead of individual bonds. This happens when the distance between the two bonds in the molecule is short and the energies are similar, allowing for interaction. This happens for instance with the CH_4 molecule, where it has both a symmetric and an antisymmetric stretch based on vibrations from the atoms as a group linked together by the bonds instead of two distinct CH stretches. On the contrary, if there is a large distance between the bonds and a large difference in energy the bonds can be observed individually. It can also be useful to have some knowledge about the sample beforehand, regarding the compounds that are most likely in the sample. To assign peaks spectroscopists usually use a combination of knowledge of the sample's expected frequencies and the likely intensities of the specific vibrations [165].

For inorganic solids, the Raman instrument is an equally powerful tool to interpret structures of the molecular units as free molecules. Explaining and interpreting structural features and molecular bonding, physical properties, and so on is still important in solid-state vibrational spectroscopy such as Raman. However, in most cases, a complete identification and assignment of all the observed Raman bands can not be achieved. This can only be done by using advanced force-constant calculations due to the real nature of the modes.

Frequency shift, thus changing the position of the observed peak to either higher or lower wavenumbers can be caused by different possible aspects of the solid-state. For instance will repulsive forces within the lattice of the solid cause a blueshift of the Raman bands, meaning that there will be an increase in frequency thus shifted towards a higher wavenumber. Intramolecular forces being weakened by intermolecular bonds will result in a redshift, to a maximum extent of 20-40 cm^{-1}. A redshift or blueshift can arise from an altering of polarity or intramolecular bonds [168].

2.5.4 X-ray diffraction (XRD)

X-ray diffraction is a powerful, non-destructive analytic tool that utilizes X-rays and succeeding diffraction of these by the atoms in the lattice to get information about and characterize the material [169].

The filament producing these electrons by thermionic emission consists of the element tungsten (W) [170]. Contamination from CuK_β is taken into account for XRD analysis as there could be insufficient filtering by the monochromator or Ni filter and is always considered an influencing factor in non-monochromatized equipment that is generating X-rays. Furthermore, the possible contamination from WL_{α_1} and WL_{α_2} stems from the filament consisting of tungsten (W). When the filament is heated over time the tungsten will start to evaporate and be deposited on the anode, commonly made up of copper (Cu). The more the anode ages the more tungsten is deposited on it, thus this potential characteristic contamination from tungsten (W) will increase. Therefore, these characteristic X-rays are taken into account as contaminating radiation in the XRD pattern [170].

The generated X-rays divides into K_α and K_β components. For any non-monochromatized equipment that generated X-rays the K_β component will always be present [170]. Of the K_α there is $\mathrm{K}_{\alpha 1}$ and $\mathrm{K}_{\alpha 2}$. The $\mathrm{K}_{\alpha 1}$ has a shorter wavelength, but twice the intensity. Because the wavelengths of these two types of K_α radiation does not differ too much, a weighted average of them are used.

The interaction between the X-rays and the atoms results in a constructive interference if and only if Braggs law, Equation 3, is satisfied [171, 169]. In the case that Braggs law is not satisfied, there is destructive interference. The reflection of the incident X-rays is only allowed if there is a constructive interference thus the intensity is non-zero. For destructive interference the reflection is disallowed and has minimal intensity [171].

Braggs law is given by

$$n \cdot \lambda = 2d_{hkl} \cdot \sin\theta, \tag{3}$$

where n is an integer number usually equal to unity, λ is the wavelength of the incident X-rays and d_{hkl} is the interplanar spacing between lattice planes. θ is a specific incident X-ray angle where diffraction occurs in the material, denoted as diffraction angle, [169].

The interlayer distance or spacing, Miller indices (hkl) and crystal system are linked with an equation and for a tetragonal crystal system where a=b the equation is presented in the equation

$$\frac{1}{d_{hkl}^2} = \frac{h^2 + k^2}{a^2} + \frac{l^2}{c^2}, \tag{4}$$

where a and c are lattice constants for the unit cell. Furthermore, d_{hkl} is the lattice spacing of the facet denoted by the miller indices h, k and l [172].

When the angle of incident X-rays is such that it satisfies Braggs law, constructive interference occurs and peak intensity is recorded [169]. The intensity pattern is detected, processed and then plotted as intensity of the diffraction maxima (lines or peaks) vs position (Bragg angle 2θ or interplanar distance d_{hkl}) [171]. The plot of intensity vs 2θ is called a diffractogram [173].

From the intensity and position of the diffraction peaks in the plot, the lattice spacing, d_{hkl}, can be deduced which gives a unique set of lattice spacing that corresponds to an atomic arrangement in a crystal and ultimately to the identity of atoms in a unit cell [173, 169, 171]. Thus, the plot correlates to a unique crystal structure, which can then be deduced by using Rietveld refinement and a database [171].

Ideally, an XRD pattern would display a narrow, delta function-like symmetry, and any deviance from this can be linked to an imperfect crystal lattice. Deviance can be categorized as peak shift, peak broadening, peak asymmetries, anisotropic peak broadening, or peak shape, where the latter refers to how the peak intensity declines from the top of the peak to the background [174, 175]. The peak can split into a doublet which means that there are not two distinct delta functioning peaks but two peaks that are conjoined. This change in peak shape can be traced back to a phase transformation or distortion of crystal symmetry to a lower symmetry. For instance, a transformation from cubic to tetragonal, or tetragonal to orthorhombic [176]. Peak asymmetries are caused by long-range internal stress within the sample as well as planar faults. The appearance of an asymmetric peak will be seen as a difference between the start of the peak to the center and the end of the peak to the center. The peak is asymmetric when these two lengths are not the same [174, 175]. Anisotropic broadening of the peaks is an effect caused by anisotropic crystallite shape or anisotropic strain and will be detailed later on in this section. The peak position is dependent on the wavelength of the incident X-rays and corresponds to a certain facet in the sample, and these lattice planes can be identified using a database. Any peak shift can be caused by internal stress or planar fault, with emphasis on stacking faults [177, 175]. The peak intensity correlated to the number of X-rays detected in a peak at a value of diffraction angle 2θ, signifying the count of X-rays coming from the corresponding facet. This value can vary with both instrumental and experimental parameters [171]. The significance of intensity and how it can be affected by different parameters will be explained later in this section. As for the broadening of XRD peaks, this can be influenced by instrumental parameters, eventual defects, and/or differences in crystallite smallness, micro stress and lattice strain [173]. Based on kinetic scattering theory, peak broadening will occur if the crystallite size is reduced below one micrometer or if a large enough amount of lattice defects exists in the analyzed sample. Specifically for dislocations, the density of these has to exceed $5 * 10^{12}\mathrm{m}^{-2}$ [174]. In addition, the Scherrer's equation can be utilized in order to connect peak broadening with crystal size. Scherrer's equation is given by

$$D = \frac{k \cdot \lambda}{\beta \cdot \cos\theta} \tag{5}$$

where k is the shape constant, β is the full width at half maximum (FWHM), D is the crystal size, λ is the wavelength of incident X-rays and θ is the Bragg angle where 2θ is the diffraction angle. The shape constant k, is commonly used as 0.9 without regarding morphology or reflection index. From this equation it can be seen that by increasing the crystal size D it will lead to a decrease in β, thus a decrease in FWHM will entail that the peaks becomes sharper. FWHM is a measurement of the width of the peak at half maximum, and the half width is used to indicate the peak width because at the top of the peak the width will be zero [178].

The peak position could also characterize the crystalline material in regards to the identification of the most exposed facets in the crystal. Obtained XRD patterns are compared to characteristic XRD patterns from a database in order to identify the material. These databases are based on XRD data performed with all the possible orientations of particles in the three spatial axes. This gives a standard intensity measurement for each orientation and thus each facet is linked to the incident angle of the XRD apparatus. If there exists a preferred orientation of particles within the material, there will be increased exposure of this facet and the peak corresponding to this orientation will have an increase in intensity compared to the standard. When there is a noticeable intensity difference between the database material and analyzed material this can then indicate that there is more or less exposure of the corresponding facet, and this can provide structural information of the analyzed material. The identification of facets through the XRD pattern can not be presumed as certain factors could affect the intensity of the peaks. This could be compositional factors such as the atom's ability to scatter X-rays, fractional coordinates, or occupancy of atomic sites, where vacancies and doping have proven to be of influence. A study compared the influence of oxygen vacancies to bismuth vacancies in BiOX and found that creating 10% of both vacancies led to a reduction in the intensity of the (001) peak by 35.80% and 19.25%, respectively [177]. The reduction in intensity upon creating atomic vacancies is logical as it reduces the occupied atomic sites, thus a smaller amount of atoms scatters the incoming X-rays. Other influential factors on the peak intensity in an XRD pattern are related to morphology, such as anisotropic strain or anisotropic crystallite size causing an anisotropic broadening of the peaks [175, 177]. For instance did a reduction in the thickness along the [001] direction of a-TiO_2 lead to a visibly broader and less intense (004) peak belonging to the [001] direction [179]. Additionally, growth along the [001] direction of BiOX nanowires led to more intense (001), (002), (003), and (004) peaks while the (110) peak became broader and less intense. However, if the most intense peaks are also among the broadest this indicates that the intensity in fact stems from preferred orientation and less from any possible anisotropic broadening. Or else the less intense peaks would be the broadest [177].

Generally, the diffractogram provides info about the long-range order in crystalline materials and short-range order in non-crystalline solids. From this the lattice constants and phases, average grain size, degree of crystallinity and crystal defects can be deduced [171, 169, 173]. Additionally, advanced XRD analysis gives information about the samples strain, preferred crystal orientation (texture), crystalline symmetry [171, 169].

2.5.5 Atomic force microscopy (AFM)

Atomic force microscopy (AFM) uses a sharp tip attached to a cantilever to scan a specified surface area, and the deflection of the cantilever is monitored by a laser beam, and this deflection is the basis of providing information about the sample. By using the height data that is generated with the AFM it is simple to measure the height, length, and width, and thus the volume of any species on the surface can be achieved [180]. This height data can be used to determine the thickness of a deposited layer on a substrate surface, by which AFM is stated to be the most reliable technique for this purpose [9].

3 Experimental

Following is the experimental section for the synthesis scheme used in this thesis based on a microwave oven. First the preparation and cleaning process of the silica substrates are explained. The glove box operating procedure is described, in addition to synthesis preparation steps done in this equipment. The operation and incorporation of the microwave oven into this synthesis scheme are then detailed. This section includes an overview of the characterization instrument used and how they were utilized in analyzing the substrates. Lastly, an overview of the parameter changes is given in a table.

Some of the results included in this thesis were obtained as part of the work done in the course TMT4500 at UC Berkeley and further characterized at NTNU [1]. These are the following substrates; silica I, silica L, silica F, silica D, silica N, mica F, mica J and mica L. A comparison is made to see if there are any differences between the two universities while performing the same method. The NTNU substrates are named as stated in Table 1.

3.1 Substrate preparation

The silica substrates used in the synthesis were Si (500 µm) coated with 1 µm of silicon oxide, SiO_2. Six silica substrates were cleaned by the following steps to ensure the minimal occurrence of dirt on the surface, as this could impact the crystal growth in various ways. The silica substrates were sonicated for 10 min in a beaker (150 mL) filled with 30 mL of acetone. After this, the substrates were transferred to a beaker (150 mL) filled with 30 mL isopropanol (IPA) and sonicated for 10 min. Lastly, the same procedure was done for a beaker (150 mL) filled with 30 mL distilled water. The substrates were subsequently dried with nitrogen gas. Three quartz combustion boats, a tweezer, and a spatula were cleaned with a tissue sprayed with IPA.

When using mica substrates in the synthesis no cleaning procedure was necessary. The mica was cleaved into six thin sheets with a razor blade in ambient air and these sheets were ready to be used as substrates.

3.2 Glovebox

The six substrates, a spatula, a tweezer, three quartz combustion boats, and two weighing containers were placed in the antechamber of the glovebox. A pumping and purging procedure with nitrogen gas was started for the antechamber, and this was repeated three times. One weighing container was placed on the scale inside the glovebox, and the other one on the outside of the scale. The three substrates were weighed separately in the weighing container situated on the scale, and then placed in the other weighing container. Then the spatula was used to place the powdered precursor, $BiCl_3$ (Sigma-Aldrich reagent grade, $\geq 98\%$) on the polished surface of the three substrates. The substrates were lifted vertically so that any precursor that was not attached to the polished surface would be removed. The procedure of removing additional precursor was stopped after the first trial synthesis, and the substrates were not lifted vertically but kept horizontal at all times to ensure that the precursor remained on the surface. Hereupon these substrates are denoted as source substrates. Then the source substrates were weighed with the polished surface facing upwards and with a precursor attached to it.

After this, the three source substrates were placed in each of the three individual quartz combustion boats using a tweezer, with the polished surface facing upwards, with space for air underneath them in the boats. Another substrate was then put on top of the source substrate, with the polished surface facing down towards the precursor. Resulting in a sandwich-like arrangement of two substrates, denoted as a parallel throughout the thesis, see Figure 10. Thus there are three parallels for each parameter change, resulting in six substrates.

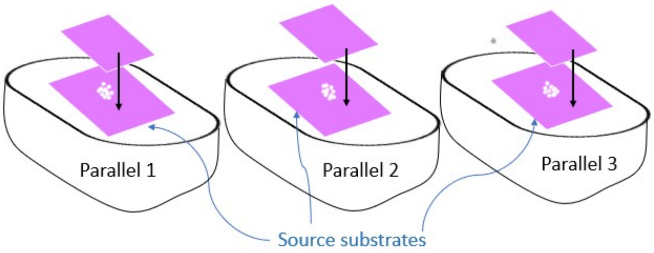

Figure 10: Illustration of three simultaneously prepared parallels for each parameter change.

3.3 Synthesis method

A deep, square baking dish in glass of 1.2 , was turned upside down, with the bottom facing up in a conventional microwave oven, MWP251 from Whirlpool. The spinning feature of the microwave oven was deactivated and the equipment was situated in a fume hood. Through the antechamber, one of the three systems was brought out of the glovebox and left in ambient air to be hydrolyzed for a maximum of one minute. After one minute in ambient air, the quartz combustion boat was placed on top of the glass dish with the short side facing directly towards the magnetron. The microwave oven was turned on for a predetermined heating time given in minutes at a given microwave power specified in watts. After the specified time the microwave oven door was opened to let out the HCl gas in the fume hood. By the use of heat protection gloves, the system was taken out of the microwave oven and the substrate edge facing the magnetron was marked with a permanent marker on the unpolished surface. The substrates were rinsed with distilled water, dried using nitrogen air, and placed in labelled boxes with lids. Then the next system was taken out of the glove box and went through the same procedure, only changing the parameter under scrutiny.

A similar synthesis scheme was done at UC Berkeley for 1 min, 1000W with the same conditions and execution as explained in this section. The source substrate was denoted as silica N and will be reoccurring throughout this thesis. The only exception to the synthesis method done for silica N was that a microwave oven from Black+Decker with power up to 1000W was used, the precursor was anhydrous powder $BiCl_3$ 99.998% (Sigma-Aldrich) and with silica substrates from Ossila with 90nm SiO_2 coating. Additionally, the synthesis was performed at another lab than Nanolab at NTNU like the synthesis described and characterized in this thesis.

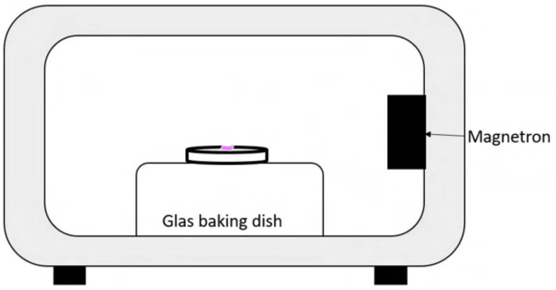

Figure 11: Illustration of a quartz combustion boat with stacked substrates inside the microwave oven.

3.4 Parameter change

For all the synthesis the precursor $BiCl_3$ was placed on the bottom substrate and is denoted as the source substrate. Each parameter was changed for three different values giving three parallels. A total of two substrates were used in every parallel resulting in six substrates for every parameter that was investigated. The system was placed in the same direction as the magnetron. First, a synthesis of changing the distance from the magnetron was performed. This was done as the distance variable was not considered or controlled in the synthesis done at UC Berkeley in fall 2021. The time was set to 1 min and power to 900 W and these values were consistently kept in other syntheses to give a basis for comparison. In the next synthesis, the microwave time was changed, and the middle distance was chosen. The amount of precursor used in these three parallels was increased compared to the first synthesis. However, for the first two synthesis schemes, only a small amount of precursor compared to synthesis at UC Berkeley was used due to difficulties with handling the precursor. This could influence the resulting size of as-synthesized crystals. In the next synthesis more precursor was added and the distance variable was again examined, with the same conditions as the first synthesis except for the procedure of handling the BiCl3. Then the influence of microwave power on crystal growth was studied, and the other parameters and synthesis conditions were kept consistent. Then the substrate type was changed for the next synthesis from silica to mica, and microwave power was changed to see the difference between the crystal growth on the two substrates with varying microwave power. Lastly, the amount of precursor was explored as this had been hypothesized to be of influence on the crystal growth when it comes to size and morphology. This was based on observations done in the OM and by the naked eye, for where there were observations of powder there were also crystals. In addition to the first synthesis with a significantly small amount of precursor, there were few occurrences of crystals. Also, from the first synthesis at UC Berkeley, the source substrate was completely covered in precursor resulting in a lot of brown spots later discovered to be flowers and no apparent trends. When the decreasing amount of precursor and centring on the surface larger, square crystals appeared. The last synthesis was done by changing the amount of precursor, but no quantitative weight could be produced, see the reasoning for this in Section 3.4.1.

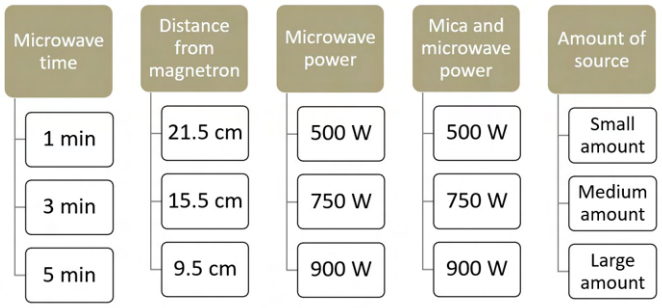

Figure 12: Schematic outline of the parameter changes during the synthesis scheme performed in this thesis.

3.4.1 Synthesis challenges

Due to the precursor not attaching easily to the substrate surface, various challenges arose. The issue with attaching the powdered precursor could stem from the BiCl3 at NTNU being more coarse compared to the one used at UC Berkeley. After placing the precursor and lifting the substrate vertically to lose any unattached BiCl3, only a few grains of powder stuck to the substrate. This made it difficult to weigh the precursor on the scale, as the scale could not detect such small variations, and thus because of the unreliability of the scale, the quantitative measurement of the amount of precursor was discarded.

Thus in the first trial synthesis, the amount of precursor was restricted to some grains of precursor. For the next synthesis where microwave time was changed, the precursor was placed and then patted down using the spatula, and more powdered was visually attached to the substrate surface. For the further synthesis schemes, it was decided to change the process of attaching the precursor to the substrate. The precursor was placed on the bottom substrate as usual, but instead of lifting the substrate vertically to shake off residual precursor, the substrate was kept horizontal. This ensured that there was a sufficient amount of precursor in the parallels. However, new challenges emerged with this synthesis change as it lead to a more prominent pile on the surface compared to the few grains earlier. There were no difficulties with placing the precursor in the center on the substrate surface as it kept sliding off or was spread on the surface with every small movement of the system. This problem was amplified when placing the top substrate on this pile of precursor, as it would make the top substrate unstable and move around more. The precursor was patted down, but there was still a noticeable bump. Compared to earlier parallels it was a considerable difference in the amount of source. When the precursor was not attached to the substrate, it was deemed impossible to weigh the substrate by the procedure explained earlier. Also during transportation from the glove box to the microwave oven, the precursor was further moved by the top substrate, thus centring of the precursor was impossible.

	Parallels			Other parameters			
Parameter change	Substrate names			Time[min]	Power[W]	Distance [cm]	Substrate type
Distance from magnetron[1]	Si-21.5cm*	Si-15.5cm*	Si-9.5cm*	1	900	21.5 - 15.5 - 9.5	Silica
Microwave time	Si-1min	Si-3min	Si-5min	1 - 3 - 5	900	15,5	Silica
Distance from magnetron	Si-21.5cm	Si-15.5cm	Si-9.5cm	1	900	21.5 - 15.5 - 9.5	Silica
Microwave power	Si-500W	Si-750W	Si-900W	1	500 - 750 - 900	15.5	Silica
Microwave power	Mica-500W	Mica-750W	Mica-900W	1	500 - 750 - 900	15.5	Mica
Amount of BiCl3[2]	Si-small	Si-medium	Si-large	1	900	15,5	Silica

Table 1: Synthesis schemes and parameter change throughout this thesis.

3.5 Optical microscope (OM)

At UC Berkeley the dried substrates were examined and imaged individually with the optical microscope (OM) apparatus, an Olympus BX60 using the software ISCapture® [181]. Whereas at Nanolab, a DIC microscope was used. The aim was to observe any trends in colour, the density of crystals, and morphology and get an idea of size changes that may have occurred throughout the surface of the substrates.

Characterization of only the source substrates was done based upon the fact that the other substrate functioned as a means to an end to facilitate the confined space. Additionally, it was discovered during the synthesis and subsequently OM characterization at UC Berkeley that there was no significant growth on the other substrates [1].

First, the crystals were observed with a magnification of 5x, then 10x, and so on until 100x. Different magnification was used to image the crystals depending on their size, and based on including other areas of interest such as grates on the surface or large brown spots.

3.6 Scanning electron microscopy (SEM)

The SEM equipment used at UC Berkeley was a Scios™ 2 DualBeam™, Focused Ion Beam Scanning Electron Microscope FIB-SEM, by Thermo Fisher Scientific. Three silica and two mica substrates were placed on individual SEM stubs by using carbon double-sided tape. The stubs were loaded on a standard sample holder inside the Scios™ 2 with adequate separation between each stub. At UC Berkeley a working distance of around 10-11 mm was used with a tilt of 0 °, mode set to secondary electrons (SE) and the ETD detector was utilized. The current for silica substrates was set to 50 pA and the voltage to 5 or 10 kV. The current for the mica substrates was 13 pA and the voltage to 5 kV.

At Nanolab, NTNU the FEI Apreo, Field Emmision Scanning Electron Microscope (SEM), was used to analyze the sample surface. The same sample procedure from UC Berkeley was used. The ETD detector in the chamber was utilized with a secondary electron (SE) signal, and a T2 detector

---

[1] This was performed as a test run for the synthesis scheme at NTNU in order to catch any challenges with equipment or to notice any differences compared to the lab work done at UC Berkeley.

[2] The descriptions ”small”, ”medium” and ”large” refer to the amount of precursor used. In Appendix F Figures 90a, 90b and 90c show the respective amounts.

was also used. For the mica substrates, a sputter coater for SEM sample preparation was used beforehand, and a coating of Pt/Pd (80/20) was sputtered on top of the mica surface.

The image processing and size distribution was performed using ImageJ and OriginPro® 2021b [182, 183]. In ImageJ, each crystal of the SEM image was measured and this was then transferred to OriginPro which generated the average size and standard deviation of the measurements.

3.7 Energy dispersive spectroscopy (EDS)

While the substrates were in the SEM equipment, the EDS detector was started by the EDS software AZtecLive® [184]. In the software the elements that were assumed to be present on the surface were predetermined. Then different analysis techniques were used in the software to produce various informative reports.

3.8 Atomic force microscopy (AFM)

The AFM Dimension Icon at NTNU Nanolab was used to analyze the surface with the ScanAsyst technique. ScanAsyst air probe was used, and after locating the area of interest the instrument started the thickness measurement at different scan sizes, making sure that the whole morphology was included in the resulting image. The AFM images were then analyzed in Gwyddion software [185].

For each ZSensor image, the crystal image was analyzed for thickness and length. The thickness measurements were performed by drawing multiple profile lines over the same crystal to get an average thickness from different directions across the crystal. These lines are denoted as "Profile 1", "Profile 2" and so on in the thickness measurement graphs. These measurements were then collected and categorized as octagons or squares, large or small based on length in Excel [186]. If a ZSensor image contained multiple crystals an average of both thickness and length was calculated for that image, then the thickness average was used in further calculations. In the case where the image only contained one crystal, the thickness measurement of this crystal was used directly for further calculations.

One unit cell corresponds to the lattice constant $C = 0.7369$ nm [43, 44, 46]. Thus one nanoplate that is compromised of four unit cell is calculated to be 2.9476 nm [13, 47]. Then the average thickness of the crystals in one AFM image was calculated. This average thickness was then divided by the thickness of four unit cells or one nanoplate, 2.9476 nm. Thus the calculated number corresponds to the number of nanoplates compromising the crystal, on average.

Each entry is from one AFM picture, some of the pictures contained multiple crystals thus an average was obtained for this picture and noted in the table, while other pictures only contained one crystal thus the dimension of this one crystal is noted in the table. The pictures analyzed are shown in Appendix D.

3.9 Raman spectroscopy

At UC Berkeley Raman analysis was performed with inVia™ Raman Confocal Microscope by Renishaw. The software WiRE™ was used in the analysis [187]. A laser beam of 638 nm was used to irradiate the silica samples. The laser power was set between 40-100 %. Exposure time, scan type and the number of accumulations were changed resulting in different spectres. At UC Berkeley only silica substrates were analyzed, as calibration of this substrate was already performed and thus the spectra were known. Spectrometer state was 1200 mm^{-1}.

The silica peak was known to be at 520cm^{-1}, thus this was first calibrated on the apparatus numerous times until it had a satisfactory calibration of 519.991 cm^{-1}. For the F silica substrate, a narrow spectrum was generated from an area where flower-like structures were detected. Then for the silica N substrate, multiple analyses were performed. First with 40% of laser power, 5 seconds of exposure time, and 10 accumulations with a static scan type. Static scan type covers a range of 200 to 500$\frac{1}{cm}$ on both side of the center [188]. Then the laser power was increased to 100%, and 5 accumulations and extended scan type were used, but the other parameters were kept constant giving a wide spectrum. This scan type gives a range between the upper and lower limit that is entered by the user and it is used when the static scan type can not cover the desired wavenumber range [188]. A clean silica substrate was also analyzed with the same parameters, in order to give a basis of comparison.

At NTNU silica and mica substrates were Raman analyzed using WITec software and Alpha 300R confocal Raman spectroscope [189]. A 532 nm excitation laser was used, and laser power of 100% equal to 66 MW. 6 accumulations were used and an integration time of 10 seconds for silica D, while 5 accumulations and 40 s integration time were used for mica F.

For the Raman analysis done at UC Berkeley, the resulting graphs are a result of different settings at different rounds of analysis giving wider or narrower spectra. While the Raman analysis at NTNU could not be tuned in a similar way, thus the graphs are plotted within different ranges to give both a narrow and a wide spectrum. The graphs were plotted and the peaks were found in Python™ according to the script displayed in Appendix G [190].

3.10 X-Ray diffraction (XRD)

The XRD analysis was performed at NTNU on DaVinci2, powder diffraction equipment. The substrate was set directly on a glass slit that was cut to fit the sample holder of the XRD instrument. A gracing incident analysis was started, after determining the height of the substrate and calibrating this offset value.

Both silica and mica were analyzed using gracing incident X-Ray Diffraction, with an incident angle of 1°for the silica and both 1°and 2°were used for the mica J and mica F, respectively. Divergence slit of 0.6 mm, primary soil 2.5°, secondary soil 0.2 °and the 0.02°step scan mode was performed for 2Θ in the range of 10°to 65°with a basis in the BiOCl XRD pattern found in the Powder Diffraction File™ (PDF®) database by the International Center for Diffraction Data [191].

The XRD spectra was analyzed using the software DIFFRAC.EVA and the TOPAS software [192, 193].

4 Results

The following section presents the most important results from the research done both at UC Berkeley and NTNU. OM and SEM were used to characterize the nanocrystals by size and shape, then further characterization and stoichiometry by EDS and Raman, and lastly crystallinity by XRD.

The OM observations are presented first, then SEM observations and size analysis of all the source substrates. After which are the EDS results from both universities, then AFM results of the observed structures in the OM and SEM. Lastly, the Raman and XRD results.

4.1 Synthesis results

The synthesis scheme was carried out as explained in Section 3.3 and Section 3.4. Each synthesis scheme investigated one individual parameter by changing it for three parallels, and an overview of the investigated parameters and changes in each parallel is given in Section 3.4, Table 1 and schematically illustrated in Figure 12. In each parallel two substrates were used to create the confined space, thus each synthesis scheme resulted in six substrates. Out of these only, the three source substrate were characterized further, and the reasoning for this is explained in Section 3.5.

In addition, to give the basis of a size distribution analysis, SEM was used to make observations of trends in morphology and to notice any eventual structures that could not or had not been observed with the OM. The results of the size distribution analysis and observations are given below.

4.1.1 Overview

The fundamental morphologies identified in SEM and kept throughout this thesis were flowers, octagons, and squares, which will be the analysis's primary focus. A typical image of squares and octagons are displayed below in Figure 13a. These octagons were seen in the OM as circles but later identified with SEM as octagons. Figure 13b shows a high-density area of crystals on the substrate surface while Figure 13c illustrates that flowers were seen as cloudy, brown spots in the OM. Furthermore, Figure 13d and 13e shows how the crystals grew near the substrate edge which was observed for every source substrate.

4.1.2 Morphology

Different morphology and structures were observed with both OM and SEM. The most common were squares, octagons, and flowers, and SEM images of these are displayed in Figure 14.

The circles noticed in the OM were for most cases discovered to be octagons, as in Figure 15a. However, in some cases, these were verified as circles in the SEM, as can be seen in Figure 15b. The observation of these structures can be seen in Figure 15c.

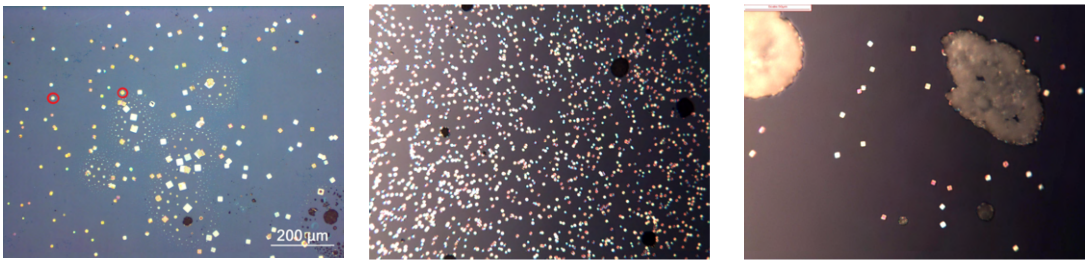

(a) Large octagon and small square equally same size taken at NTNU.

(b) High density of octagons, magnification x20 [1].

(c) Brown spot identified as flowers, magnification x50 [1].

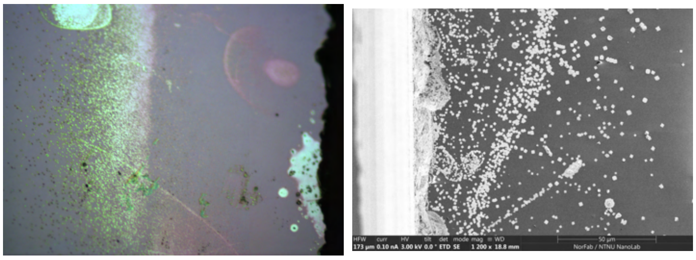

(d) Crystal growth along substrate edge, magnification x10.

(e) Crystal growth along substrate edge.

Figure 13: Squares, octagon and flowers on a silica substrate imaged with OM and SEM.

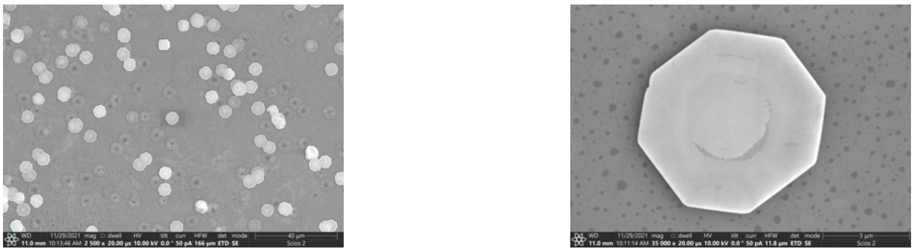

(a) High density area of octagons.

(b) Close up image of an octagon, size 8.4 µm.

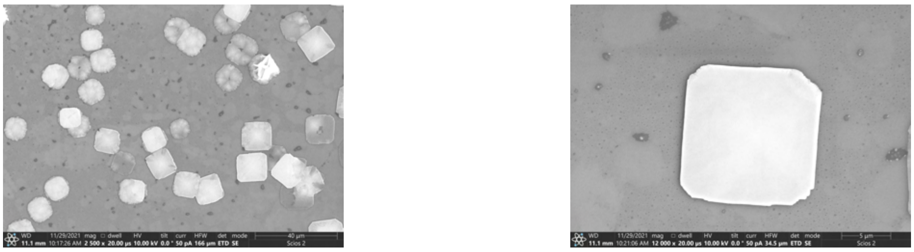

(c) High density area of squares with remnants of octagons.

(d) Close up image of square, size 13.7 µm.

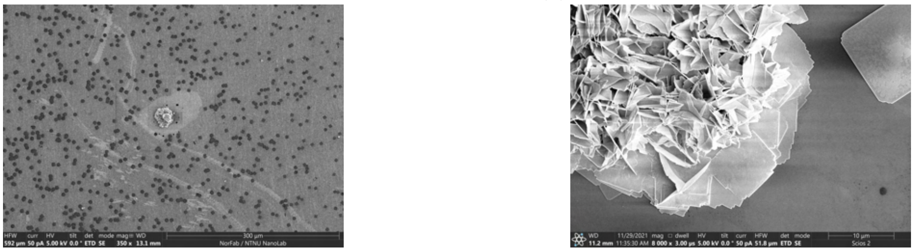

(e) Flower surrounded by square crystals on silica.

(f) Close up image of an flower, petal thickness of 0.143 µm.

Figure 14: The three most common morphologies in this thesis [1].

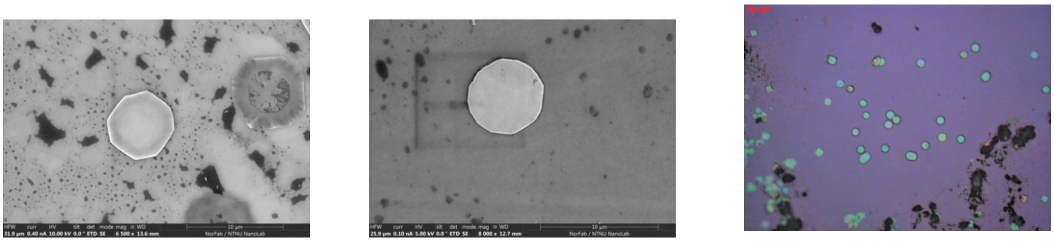

(a) Octagon

(b) Circle

(c) Octagons and squares on Si-small of average size 13.8 µm

Figure 15: Octagon and circle observed in SEM and OM.

Squares observed in the OM showed a range of vibrant colors, as seen in Figures 16a, 16b and 16c. The Figures 16d and 16e display small squares imaged with SEM, which clearly shows the well-defined geometry. In Figure 16e there is also a display of non-uniform stacking. These squares were seen less frequently on mica than on silica substrates.

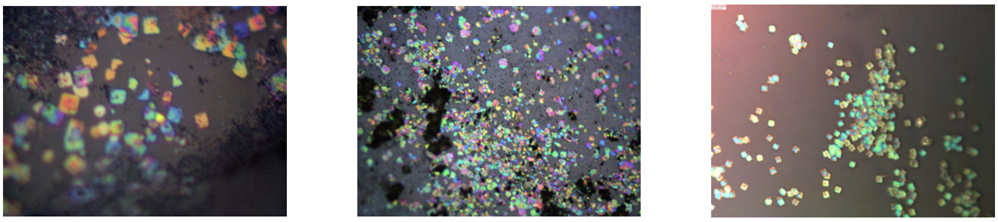

(a) Vibrant colored crystals on mica.

(b) Vibrant colored crystals on mica-900W.

(c) Image from project thesis on silica [1].

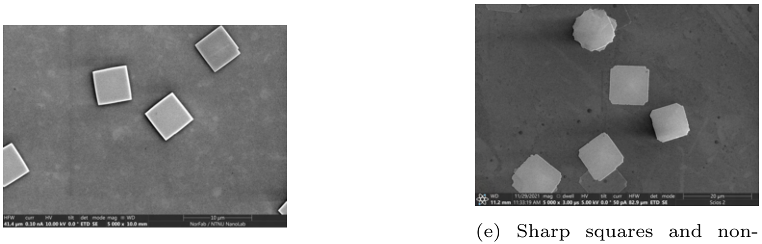

(d) Sharp square.

(e) Sharp squares and non-uniform stacking on silica N [1].

Figure 16: Squares imaged with OM and SEM.

The small squares were viewed as more well-defined compared to larger squares which exhibited nanoframe-like structure. These nanoframes exhibited a taller edge called a frame, and a thinner center. In Figure 17a these are seen as large squares with a white rim and grey center. The large grey squares with the white rim were first noticed when using an OM, but also recognized in the SEM because of the large size, distinctive shape, large quantity, and known location at the center of the silica N. In the SEM in Figures 17b, 17c and 17d it became obvious that these large squares had an elevated edge, which corresponds to a grey center and white frame seen in the OM. Furthermore, Figure 17e probably shows an initial formation of these nanoframes as the center has not completely been exposed.

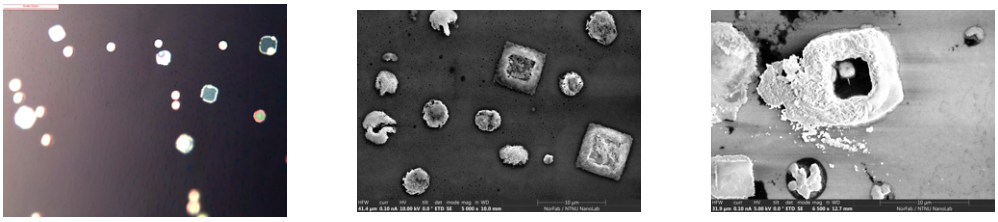

(a) Grey nanoframe in OM. (b) Nanoframe (c) Nanoframe

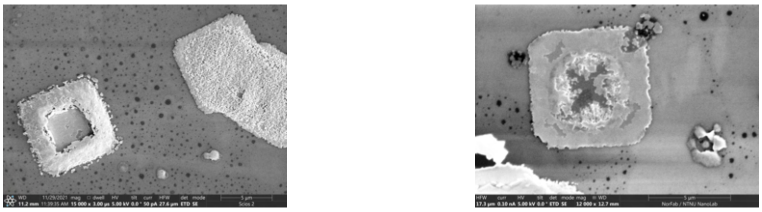

(d) Nanoframe [1] (e) Nanoframe

Figure 17: Various BiOCl nanoframes detected in OM and SEM.

The squares were also discovered to have a layered structure where the layers were non-uniform thus the individual BiOCl sheets became evident in Figure 18. Some of the blue circles in Figure 24 illustrates this viewed in OM.

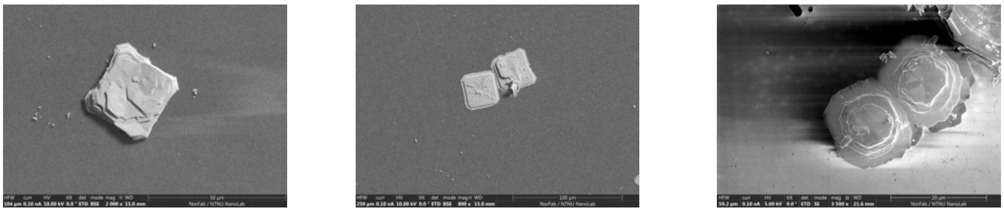

(a) Non-uniform layers stacked together. (b) Squares with distinguishable layers. (c) Non-uniform layered squares.

Figure 18: Layered BiOCl crystals.

With the SEM instrument, the large brown spots observed in the OM in Figure 19a were discovered to be flower-like structures compromised of BiOCl plates, as seen in Figure 19b. Additionally, the blue circles in Figure 24 could also identify these flower structures as it appears to be multiple crystals stacked together. The flowers were noticed to be frequently observed in the vicinity of visible white powder on the substrate surface, thus the location could often be predicted. This white powder was most likely unreacted precursor. In previous research, these were observed for the first synthesis, and discoveries of them in the OM were reduced when decreasing the amount of precursor BiCl3 [1]. Figure 19b exhibits a commonly observed flower-like structure with sharp petals made of BiOCl. The flower in Figure 19c shows a less observed flower on silica with blunter petals pointing upwards. The basis of the flower is visible in this Figure and it can be seen that the base is made up of BiOCl sheets clustered together. Another shape noticed in the SEM was squares with flower formation covering the surface, like seen in Figures 19d and 19e where the squares can be perceived as templates for further growth. Figure 19f shows a flower formation where the petals do not stick outwards, but are restricted to only pointing up. Another feature that became apparent was that some crystals had a small flower-like structure growing in the center of the crystal surface, as seen in Figure 19g. These structures consisted of an irregular shaped crystal with a small flower at the center. Figure 19h shows sheets curving upwards in an initial stage of flower formation.

A prominent observation done for growth on silica and mica substrates is that for mica the flower-like structure appeared frequently, few squares were noticed and no octagons were observed. On the silica substrates, the opposite was discovered to be true, where there was a predisposition to observing squares and octagons while flowers were detected in a smaller quantity.

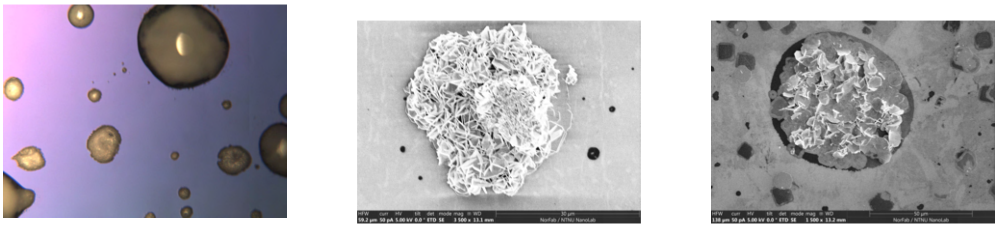

(a) Brown spot observed with OM [1].

(b) Flower [1]

(c) Flower [1]

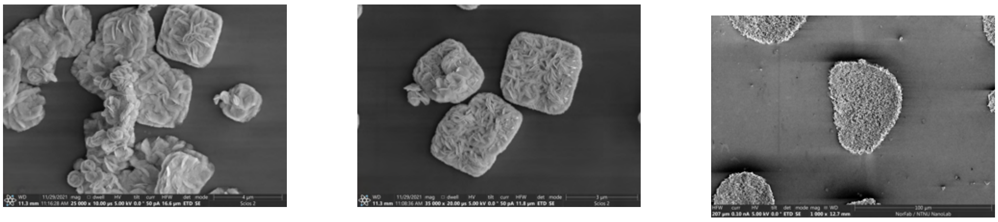

(d) Flowers growing on crystals on silica substrate [1].

(e) Flower formation on square crystals [1].

(f) Flower on silica [1].

(g) Flower deposition on BiOCl flake.

(h) Bent sheet in the initial stage of forming flower [1].

Figure 19: Flowers imaged in OM and SEM.

With the use of SEM cracked surfaces and broken crystals were observed regularly for different morphologies. For a square in Figure 20a, an octagon in Figure 20b and 20d, lastly irregular shaped crystals in Figure 20c.

In addition to cracked surfaces, there were observations of broken crystals, which were observed in SEM in Figure 20c. Additionally, these were noticed when using an OM in Figure 20e red circle No. 2 shows a broken crystal. Circles No. 1 and 3 illustrate a possible nanoframe and possible octagon, respectively. Further observations of these are illustrated in Figures 20f and 20g.

Additionally, formation of screw dislocations was frequently observed as seen in Figure 21a which clearly illustrates how these looks like a staircase. These were mostly detected in the vicinity of flower structures, as seen in Figure 21b. Figure 21c illustrates another dislocation with a different shape than the one in Figure 21a. Screw dislocations were easily identified in the SEM and hard to recognize in OM, but in Figure 24 the blue circles exhibit stacked crystals and some of the stacking could arise from screw dislocations.

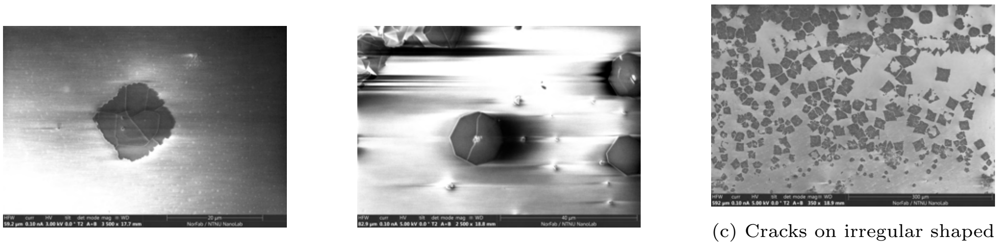

(a) Cracks on a square.

(b) Cracks on an octagon.

(c) Cracks on irregular shaped crystals and some broken ones can be detected.

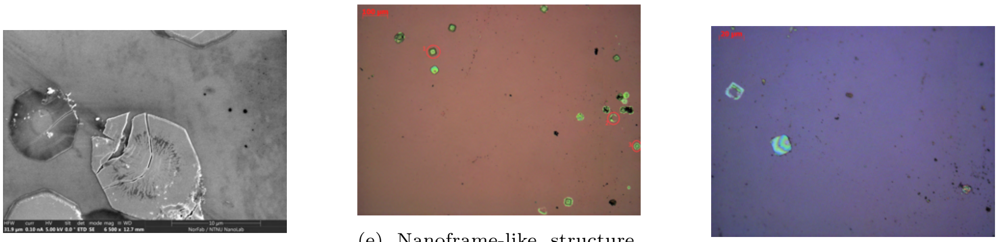

(d) Broken octagon.

(e) Nanoframe-like structure, broken crystal and an octagon on NO.

(f) Broken crystal on silica.

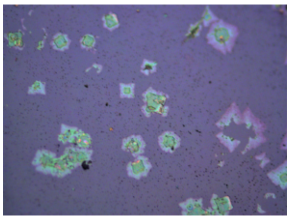

(g) Irregular shaped crystals and broken crystal.

Figure 20: Broken or cracked BiOCl crystals images with OM and SEM.

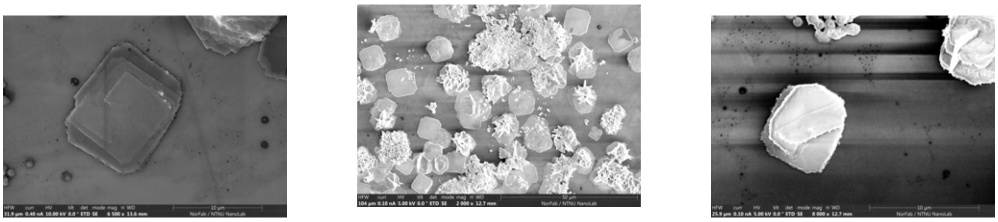

(a) Screw dislocation [1].

(b) Screw dislocations marked with red circles.

(c) Screw dislocation.

Figure 21: Screw dislocation noticed in SEM.

An asymmetrical stacked structure is imaged with an OM in Figure 18a resembling a cross-like structure, which could be caused by screw dislocation or discrepancy in the layers. This structure is also imaged in SEM in Figure 18b. This can also be seen in OM in Figure 22c where the red circles marks structures that look like crosses, or octagons with rounded sides. Figure 22d shows a star-like structure which could also originate from stacking, as can be seen in Figure 22e. This image clearly shows that the sheet is rotated before being stacked making the edges point out like a star. Non-uniform stacking of seemingly well-defined BiOCl sheets is displayed in Figure 22f. All the variety of shapes and different morphology that did not fit into the characteristics of squares, flowers, circles, or octagons were categorized as irregular shapes in the size distribution analysis.

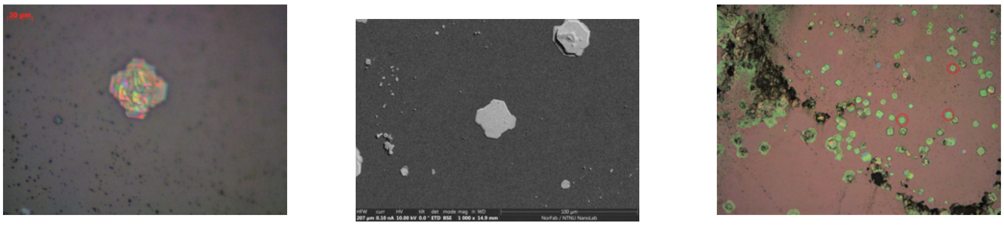

(a) Stacked cross-like structure imaged with OM.

(b) A cross-like structure.

(c) Layered structures and cross-like structure on silica.

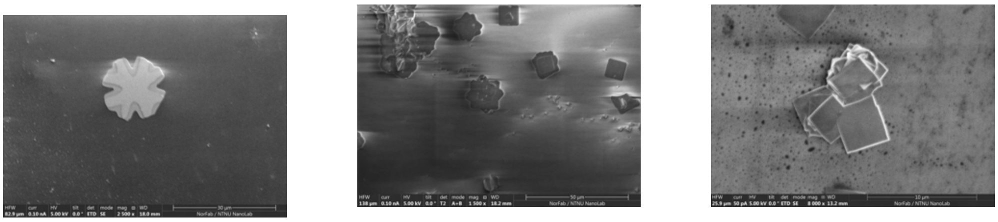

(d) A star-like structure.

(e) A layered, star shaped structure.

(f) Sheets stacked non-uniformly.

Figure 22: Various layered BiOCl shapes discovered in SEM and OM.

Figure 23 illustrates irregular shapes that were commonly observed in areas where there was an excess of white powder on the substrate deemed most likely to be unreacted precursor $BiCl_3$. Figure 23a shows the OM image of these structures imaged with SEM in Figures 23b and 23c. The irregular shapes in Figure 23d and 23e were mostly noticed at the center of the substrate, most likely due to the precursor placement being here for the synthesis scheme.

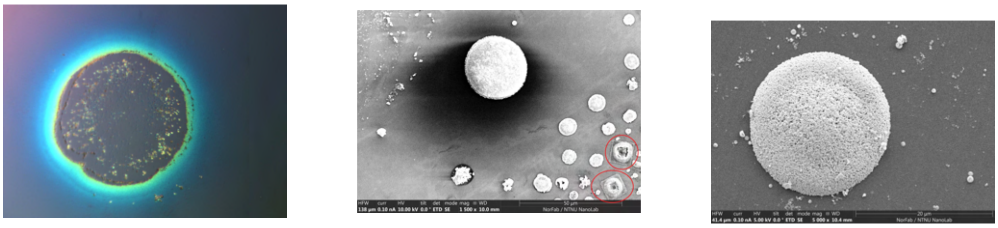

(a) Circular shape observed with OM [1].

(b) Circular structures and nanoframes circled in red.

(c) A circular shape.

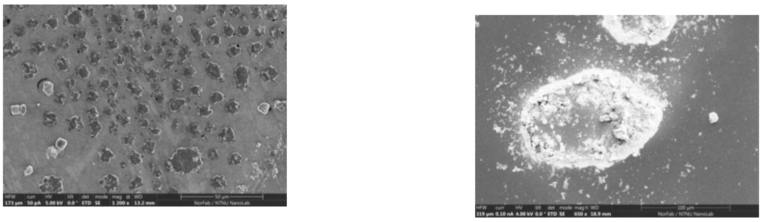

(d) Spots denoted as irregular shapes.

(e) Hollowed out area.

Figure 23: Irregular shapes of unreacted precursor discovered in SEM and OM.

In Figure 24 using Alicona Infinite Focus microscope detailed the layered structure. The red circles identify squares with another distinguishable square stacked on top. It is easy to see the separate squares as the top one is either twisted or smaller so the stacking of two individual squares is clear. The blue circles are areas or crystals with multiple layered structures on top of initial single crystals. The green circles marks squares with a seemingly circular crystal on top. This stacking leaves some of the bottom crystal exposed, and most of the square crystal is covered except for the outer edge.

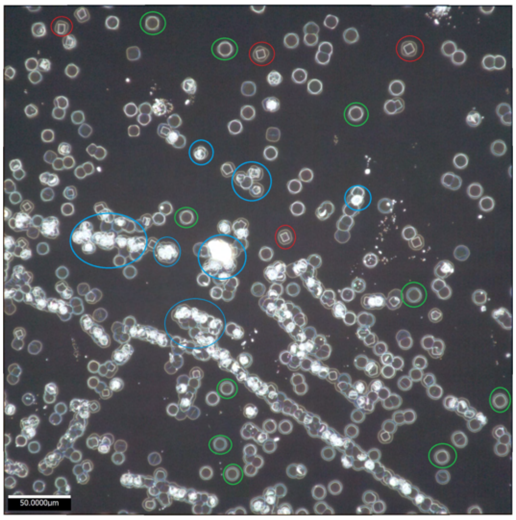

Figure 24: Layered crystals exhibiting various morphology.

4.1.3 Synthesis parameter

The surface of the source substrates were divided into three sections of interest, as illustrated in Figure 25. This was done to observe growth across the substrate and eventual differences in size and morphology. The side facing the magnetron was marked and the other sides were labeled side A, side B and side C as can be seen in the same figure. Two SEM pictures were taken for each point (1.1, 1.2 and so on), one displaying an overview image in order to see growth and density in the area, see example Figure 68d, 68e and 68f in Appendix B. The crystal density is illustrated in tables. The other was a magnified SEM image which was used in the size analysis, see Figures 68a, 68b and 68c in Appendix B. The average size of the crystals was calculated from these images as explained in Section 3.6 and the morphology was noted. From this, an average size for each section was computed with regard to morphology. This means an average was made for squares for section 1 (1.1, 1.2, and 1.3) and a separate average was made for octagons/circles and in some cases flower petal thickness. This was repeated for sections 2 and 3. Note that the table entries containing an "X" indicates that either the crystal morphology was not observed or that there were irregular shapes in the entire section thus a size analysis was not achievable. The same applies to the graphs where there is no measurement in a section.

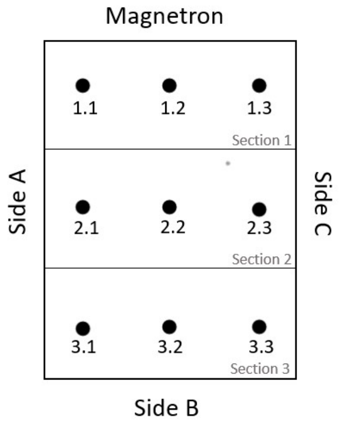

Figure 25: Illustration of how the substrate was divided for size distribution analysis.

4.1.4 Microwave time

Microwave time was changed, from 1 min, 3 min, and 5 min. The resulting size distribution is shown in Figure 27 with one standard deviation. From size distribution in Figure 27 there is one striking trend in crystal growth upon changing the microwave time, and that is the decrease in size for 3 min and 5 min for both squares and octagons compared to 1 min. Therefore, indicating that a microwave time of 1 min produces the largest crystals. This is also exhibited in Figure 26 which shows the difference in size between octagons for 1 min and 3 min, where the 3 min SEM image has the larger magnification and thus smaller crystals.

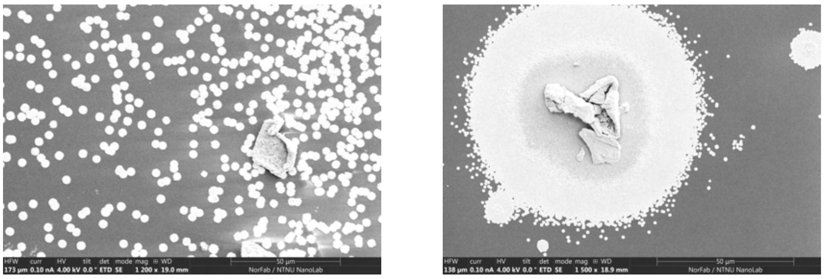

(a) 1 min (b) 3 min

Figure 26: Illustration of size difference of 1 min vs 3 min at 1.1 with a scale bar of 50 µm.

When it comes to morphology, there were some differences detected. Si-1min section 2 had flower growth on circle-shaped crystals as illustrated in Figure 19g, and the same occurrence was observed for section 3. For Si-5min with a microwave time of 5 min, at the whole section 2, there were irregular shaped, cracked crystals, like the crystal exhibited in Figure 20a and flower formation, and no octagons. Therefore, it was decided to not analyze this image as the shape could not be definite categorized.

Furthermore, octagons are increasing in size moving across the Si-1min substrate from sections 1 to 3, thus further away from the magnetron. As for the growth of squares, the size decreases at the center of the substrate in section 2, and it is larger for sections 1 and 3. For source substrate Si-3min, both morphologies are smaller than Si-1min, see Figure 27. There is a gradual size decrease moving from section 1 to 3 for squares, while no obvious size trend can be seen for octagons. The analyzed images as well as overview images for Si-3min section 3 can be seen in Appendix B Figure 69. For Si-5min, the smallest squares were displayed in section 2 on the substrate. The "X" in section 2 which can be seen in Table 2 makes it more strenuous to make conclusions.

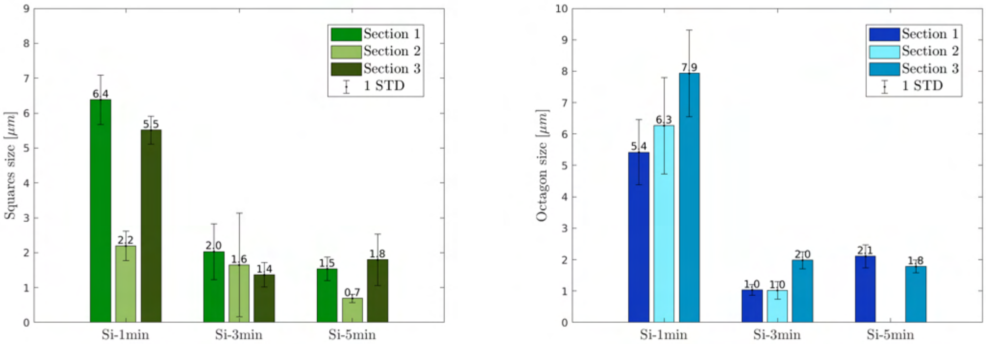

(a) Squares (b) Octagons

Figure 27: Size analysis of microwave time synthesis.

From Table 2 it is clear that on a general basis there were a lot of crystals on these substrates.

However, the crystals were mostly observed at the edges of substrate with a lot of vacant areas in between. Flowers were also observed at the center. Additionally, irregular shapes and visible stacking of crystals was noticed along the edges of the substrate. Si-1min had few squares compared to octagons for every section. Si-1min also had the least amount of squares compared to the other substrates but many octagons. The density on Si-3min can be seen in Appendix B in Figure 69. As the values in the table are similar, neither of the substrates stands out considering crystal density.

		Section 1 [#]	Section 2 [#]	Section 3 [#]
Si-1min	Squares	21	12	73
	Octagons/circles	457	105	112
Si-3min	Squares	33	102	244
	Octagons/circles	225	256	82
Si-5min	Squares	187	27	167
	Octagons/circles	306	X	112

Table 2: Density of squares and octagons/circles in each section for each parallel in the microwave time synthesis.

4.1.5 Distance from magnetron

The synthesis scheme investigated the impact the distance from the magnetron had on the crystal growth. The resulting size distribution is displayed in Figure 29. From the figure, it is evident that the squares on the substrate placed at the middle distance of 15.5 cm displayed the biggest size.

All the substrates exhibit irregular shaped crystals at either section 1 or section 2 of either squares or octagons. For section 1 on Si-15.5cm, all the octagons had a crack in the structure, thus these were not analyzed. It was noted that for sections 1, 2, and 3 of this substrate there were observations of cracked crystals and deformed crystals for all the analyzed images. In general, across the substrate, it was difficult to find crystals with no cracks or imperfect stacking. The size of broken or cracked crystals were not incorporated into a size analysis, as the aim of the thesis is to synthesize complete, undamaged crystals.

It was also observed an increased amount of cracked and irregular shaped crystals in section 3 compared to section 1 for Si-21.5cm. These irregular shaped crystals were formed by nanoplates stacking on other nanoplates imperfectly. Additionally, for the Si-9.5cm substrate, there were a lot of observed cracked crystals and irregular shaped ones. In section 2 there were a lot of stacking of crystals on top of each other of different size and shapes.

In general, Si-9.5cm had more irregular shapes and non-uniform stacking and Si-15.5cm reportedly had more well-defined crystals as can be seen in Figure 28. Si-21.5cm had less irregular shapes than Si-9.5cm, but also exhibited numerous crystals with a round shape.

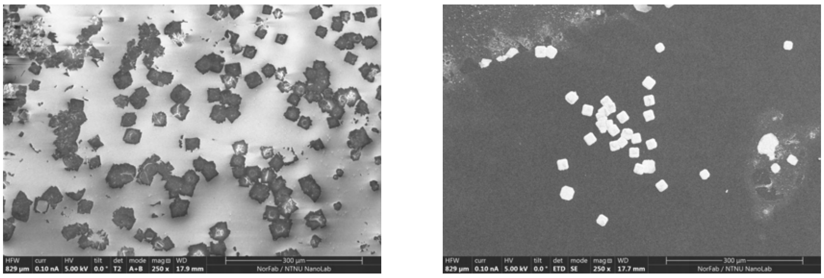

(a) Irregular shapes with stacking Si-9.5cm.

(b) Well-defined squares Si-15.5cm.

Figure 28: Shape comparison between Si-9.5cm and Si-15.5cm in section 1.

As for octagons across the parameter change, no trend can be deduced. For the first source substrate, Si-21.5cm, situated farthest away from the magnetron, the octagons/circles in section 3 are much larger than the squares, see Figure 29. For the center placed source substrate, Si-15.5cm, there is a possible trend of larger crystals of both morphologies moving from section 1 to section 3 which is illustrated in Figure 29. However, there were no octagons in section 2 without a cracked or destroyed surface so an analysis could not be obtained. For Si-9.5cm the squares were smaller for section 2, while no apparent trend can be deduced for octagons, see Figure 29.

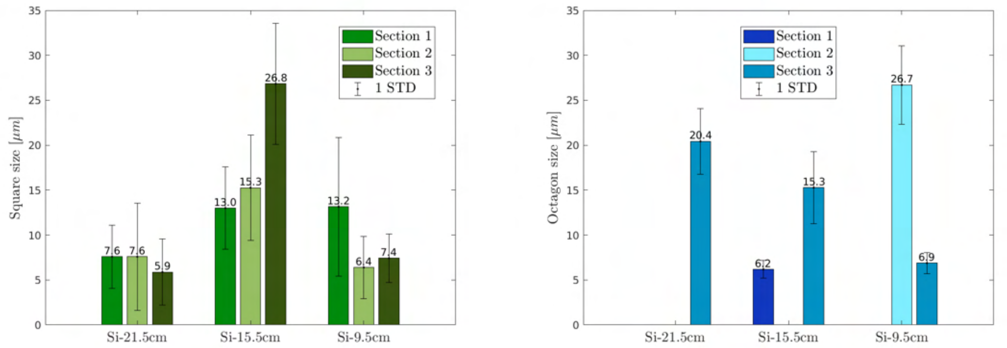

(a) Squares (b) Octagons

Figure 29: Size analysis of distance synthesis.

Generally there were few octagons observed for this parameter. Si-9.5cm had more crystals on a general basis than Si-15.5cm, see Table 3.

		Section 1[#]	Section 2 [#]	Section 3 [#]
Si-21.5cm	Squares	40	60	42
	Octagons/circles	X	X	13
Si-15.5cm	Squares	105	47	42
	Octagons/circles	56	X	13
Si-9.5cm	Squares	78	76	96
	Octagons/circles	X	11	15

Table 3: Density of squares and octagons/circles in each section for each parallel in the distance synthesis.

4.1.6 Microwave power

The microwave power was varied between 500 W, 750 W and 900 W. The results of a size distribution are displayed in Figure 31. It appears from this figure that Si-900W has the largest crystals for all the sections regarding squares as can be seen in Figure 30 where the Si-750W image is magnified more than Si-900W. The Si-900W also has the largest octagons in section 2. Based on the size, the 900 W is presumably the preferred microwave power setting if the aim is to synthesize the largest crystals.

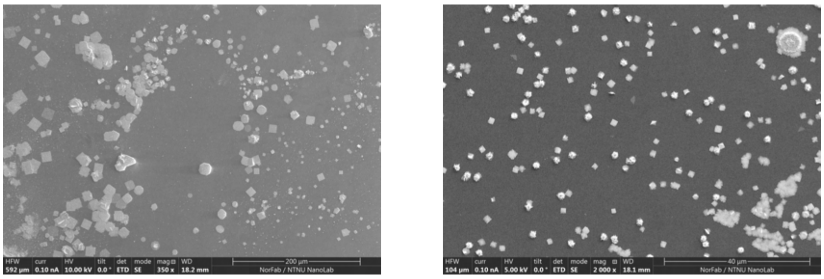

(a) Si-900W (b) Si-750W

Figure 30: Shape comparison between Si-900W and Si-750W at 1.2.

In section 1 on Si-500W, there were different structures observed. At position 1.1 on the substrate, flowers formed on round crystal sheets are exhibited in Figure 19g. While at 1.2 there were irregular shapes. Lastly, sharp and well-defined squares were observed for 1.3. Generally, throughout the Si-750W substrate, the crystals were observed as small and difficult to find with the SEM, and a lot of small, irregular dots as displayed in Figure 23d. There were also a lot of round-shaped crystals with flowers growing on them. For the Si-900W substrate, there was also a lot of white powder visible on the surface, making it difficult to detect any crystals. Especially in section 3, hence the "X" in this section for octagons/circles in Table 4.

The squares on Si-500W in sections 1 and 3 were smaller than the ones in section 2. The opposite occurs for octagons, where there is a decrease in size for section 2. Furthermore, there were few observations of crystals on the side A and on that side of the substrate, there was visible white powder on the surface which in the SEM appeared as illustrated in Appendix B in Figure 72.

From Figure 31 the Si-750W source substrate, had an approximately uniform size of squares across the substrate. Compared to the other substrate, these square sizes were small.

Si-900W had the largest octagons in section 2 compared to the other source substrates. While sections 1 and 3 had no octagons/circles. Squares grow progressively larger moving away from section 1 towards section 3, hence from magnetron side to side B of the substrate.

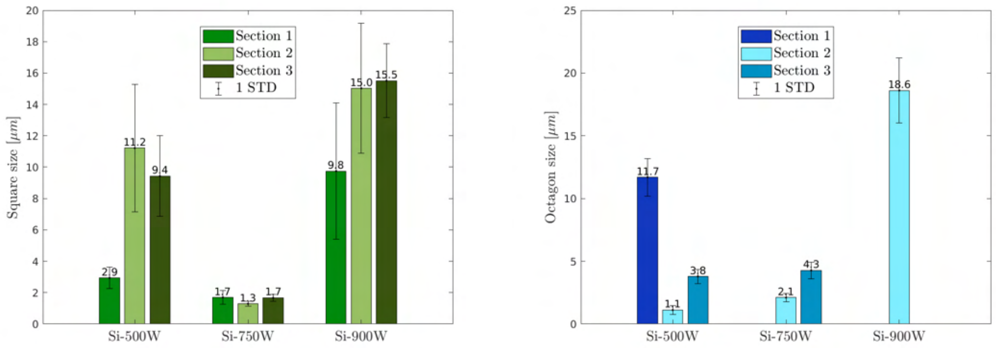

(a) Squares (b) Octagons

Figure 31: Size analysis of microwave power.

		Section 1 [#]	Section 2 [#]	Section 3 [#]
Si-500W	Squares	165	195	125
	Octagons/circles	30	67	20
Si-750W	Squares	15	30	76
	Octagons/circles	X	41	82
Si-900W	Squares	72	24	11
	Octagons/circles	X	32	X

Table 4: Density of squares and octagons/circles in each section for each parallel in the microwave power synthesis.

4.1.7 Mica with microwave power change

To give a basis for comparison between growth on a different substrate, a synthesis scheme was done on mica substrates while changing the microwave power. The size distribution is given in Figure 34. Note that no octagons/circles were observed on either substrate, but flower petals were analyzed instead as this structure was discovered on these mica substrates. Additionally, it was a prominent structure for Mica-750W and Mica-900W, but not noticed on Mica-500W as can be seen in Figure 32.

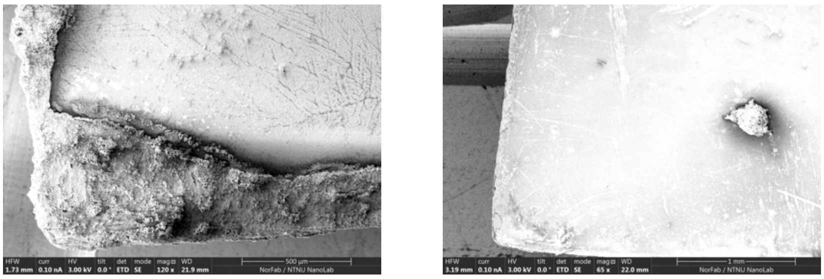
(a) Mica-750W (b) Mica-500W

Figure 32: 1.1 overview images showing shape comparison between Mica-750W and Mica-500W.

The squares observed on the three substrates do not differ too much, but Mica-900W has the largest ones. The thickness of the flower petals of Mica-750W and Mica-900W does not differ significantly.

For section 2 on Mica-500W, there were a lot of irregular shapes and powder covering the area, and generally few observations of any crystals. The most striking observation was that there were no flowers on Mica-500W, which dominated on the Mica-750W and Mica-900W substrates as can be seen in Figure 33. However, for Mica-900W the flowers were sharper like exhibited in Figure 33 compared to Mica-750W flower with clumpier petals.

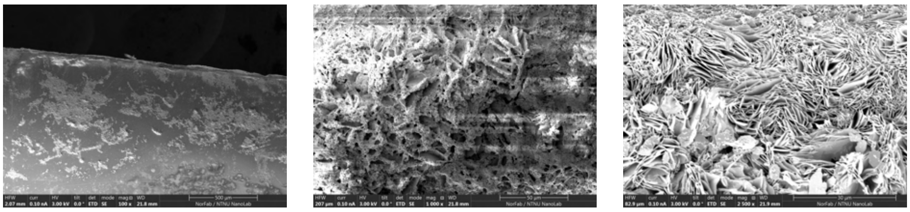
(a) Mica-500W (b) Mica-750W (c) Mica-900W

Figure 33: Shape comparison on Mica-500W, Mica-750W and Mica-900W at section 2.

Mica-500W resulted in a few sections adequate for size analysis. Mica-750W also had few observed crystals and the squares observed were the smallest for this synthesis scheme. No flowers were detected for section 2. The flowers for Mica-900W in section 2 were thinner than in the other sections, while the squares observed in section 2 were larger than for the other source substrates.

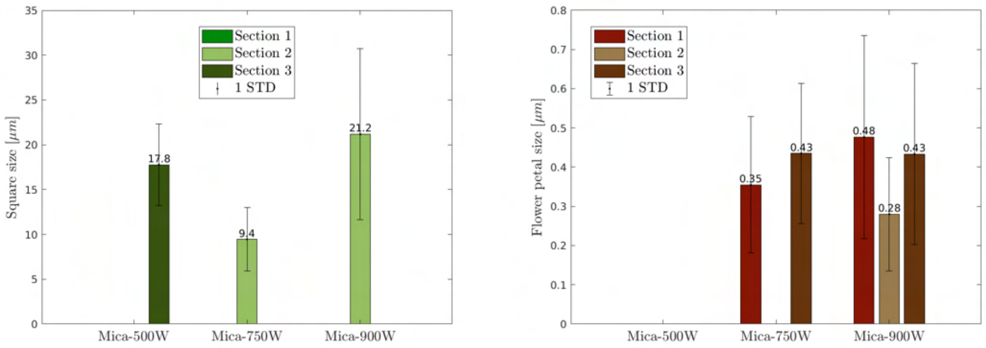

(a) Squares

(b) Flower petals

Figure 34: Size analysis of mica and microwave power.

From Table 5 it is clear that there were a lot of sections that could not be analyzed, and generally for Mica-500W and Mica-900W there were few squares.

		Section 1 [#]	Section 2 [#]	Section 3 [#]
Mica-500W	Squares	X	X	8
	Octagons/circles	X	X	X
Mica-750W	Squares	X	93	X
	Flower petals	18	X	24
Mica-900W	Squares	X	5	X
	Flower petals	44	52	45

Table 5: Density of squares and octagons/circles in each section for each parallel in the mica and microwave power synthesis.

4.1.8 Amount of source

A synthesis scheme revolved around changing the amount of source BiCl3 inside the confined space. No quantitative measurements can be given for the amount of source due to challenges with the precursor as explained in Section 3.4.1, but pictures were taken of the systems and are given in Appendix F, Figure 90. The resulting size distribution is given in Figure 36, and from this Si-large exhibits the largest squares in general.

For all the substrates, no octagons were detected in section 2 and generally few crystals were analyzed as can be seen in Table 6. Figure 35 illustrates how few crystals were present on the substrate surface for a small amount compared to an exaggerated amount. In section 2 of Si-small there were generally observed a lot of unwanted spots, like the ones presented in Figure 23d.

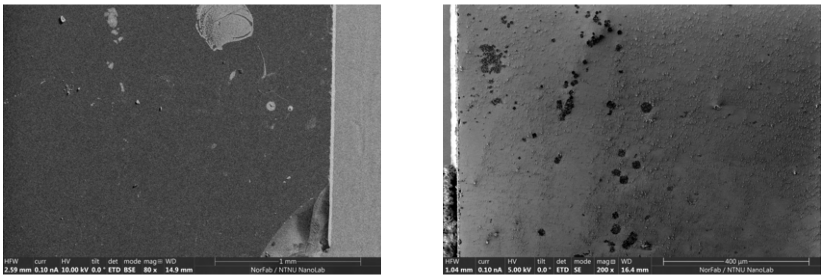

(a) Vacant space at Si-small.

(b) Crystals on Si-large.

Figure 35: Comparison between Si-small and Si-large in section 1.

A small amount was placed on the Si-small substrate see Figure 90a, which resulted in a larger average size of squares in section 2 and for octagons in section 1. It is difficult to catch any trend for octagons as in sections 2 and 3 this morphology was not detected.

For Si-medium the amount of precursor was increased, see Figure 90b. This medium amount was visually considered to be the baseline used in all the other syntheses done. This parallel resulted in a trend with an increase in size for the squares moving from sections 1 to 3.

Lastly in this scheme, the amount of source was exaggerated to cover the entire substrate surface of Si-large, see Figure 90c. A large amount of source resulted in an increasing size for the squares compared to the other substrates for sections 2 and 3, while section 1 had small crystals. For octagons, a conclusion can not be done as section 2 was not analyzed, although the size of octagons/circles was not that different from the other substrates. Based on the size of squares a large amount of source is seemingly favorable.

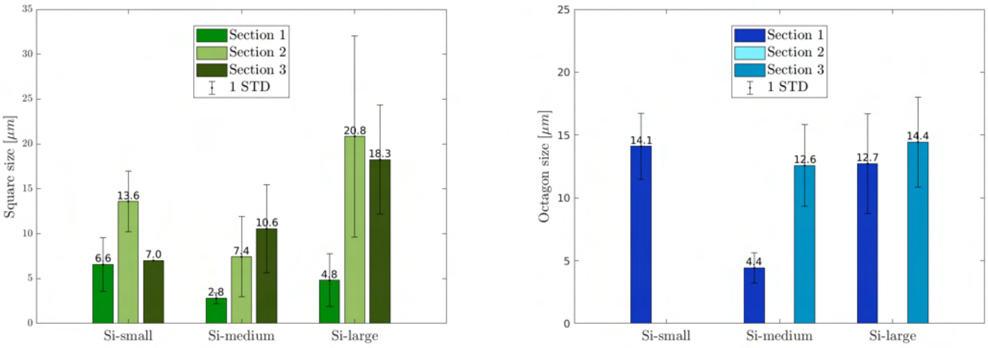

(a) Squares

(b) Octagons

Figure 36: Size analysis of amount of source synthesis.

		Section 1 [#]	Section 2 [#]	Section 3 [#]
Si-small (see Figure 90a)	Squares	52	19	29
	Octagons/circles	18	X	X
Si-medium (see Figure 90b)	Squares	11	42	49
	Octagons/circles	50	X	23
Si-large (see Figure 90c)	Squares	29	7	5
	Octagons/circles	6	X	8

Table 6: Density of squares and octagons/circles in each section for each parallel in the amount of source synthesis.

4.1.9 Substrate location

The silica N substrate had the dimensions of 15 x 20 mm. At the short side edge of the substrate, small circles of BiOCl nanocrystals were noticed with decent space between them and this was consistent around the entire substrate. These circles had a range of different colors and started appearing at some distance from the edge, as seen in Figure 38a consistent with the point No. 1 in Figure 37a. In the SEM these circles were identified as octagons.

Moving towards the center of the substrate to point No. 2 in Figure 37a these small octagons of average size 4.4 µm were observed at a higher count, compressed together exhibiting a large density of these crystals at any area in this section of the substrate, as displayed in Figure 38b. At point No. 3 in Figure 37a closer to the center these small octagons became larger with average size of 5.3 µm, while exhibited the same vibrant color range. In addition to appearing larger, the observed crystal density decreased as seen in Figure 38h.

(a) Illustration of movement on silica N starting from point 1 to 6.

(b) Schematic of morphologies detected at the different locations.

Figure 37: Schematic illustration of the growth trend across N silica.

Then upon moving further towards the center of the substrate to point No. 4 in Figure 37a, squares appeared with an equal color template as the octagons displayed. The two geometries appeared to be equally sized through most of the substrate as exhibited in the Figure 13a, where the octagon is 12.2 µm and the square is 11.5 µm. There was not an image only showing this occurrence, so Figure 13a is used to illustrate the similarity in size. The red circles illustrate the observed size similarity for octagons and squares. This can also be seen in Figure 38l in red circle No. 1. In this figure the red circle No. 1 indicates a large octagon with an average length of 10.9 µm and a small square with a length of 9.4 µm showing that the two geometries appeared equal in size. In Figure 37b this is also illustrated.

This gradual increase in size was true for octagons and squares when moving down the substrate from the short edge to the center. However, there were occurrences where the size increase was more sudden. As can be seen in Figure 38d the red circle No. 1 marks a small octagon of average size 6.1 µm, No. 2 emphasize a large octagon of average size 10.8 µm, No. 3 a small square with size 11.4 µm and No. 4 is a large square measured to be 16.6 µm. The size of the large circle and small square are equally the same. This image is taken at the orange point in Figure 37a. This sudden crystal size increase was observed frequently when moving from the long edge towards the center instead of from the short edge, see orange arrow in Figure 37a. This can be because there is less space between the long edge and center than the short edge and center.

Additionally, when moving further down the substrate from the long edge, brown spots emerged at point No. 5 in Figure 37a. The small squares had length of 9.2 µm and in between the brown spots few or no crystals were observed, see Figures 38e, 38f and 38g. This is also illustrated in Figure 37b. When almost reaching the center at point No. 6 in Figure 37a, visually larger squares started to appear in the vicinity of these brown spots. This can be seen in Figure 38l. Red circle No. 2 marks the observation of larger squares with a measured length of 12.4 µm and the No. 3 emphasize the brown spots.

The large squares can also be seen in Figure 38i, 38j and 38k. These large squares were accompanied by a distinguishable change in color scheme and shape. Oppositely to one color observed for each individual square and octagon, there were multiple colors on each large square. A strenuous effort had to be made in order to find crystals located at the center that was not composed of two or more colors as seen in Figure 38i. In this figure, the circled squares are composed of either a blue and pink or a yellow, red, and blue color scheme. Various arrangements of colors were observed and the average length of these squares is 12.1 µm. It was also observed on multiple large squares that the color consistently changed from the edges to the center of the crystal, see the circled squares in Figures 38k and 38i. The circled squares in Figure 38k seem to have a small blue dot at the center and have an average size of 8.1 µm.

Among all the vibrant colors there was one noticeable feature regarding the large squares, and that was an easily recognizable grey color as can be seen for the squares circled with red in Figure 38j. This grey color was either very dark or brighter, but only observed for the visually largest squares. In Figure 38j the red circles No. 2 and 4 exhibits a darker grey than No. 1, while No. 3 and 5 have the brightest grey color. The average size for these grey squares was 8.9 µm. The grey squares also exhibited a white rim, which varied in width from square to square. Furthermore, cracks on the surface of square No. 3 and 5 can be seen in the figure.

In addition to this multitude of observed colors, it was observed in the OM that large squares had a more deformed shape. Compared to the smaller squares which had sharp edges, these exhibited a rounder shape, and occurrences of irregular morphology were detected, this can especially be seen in Figures 38j and 38k compared to Figures 38l and 38i.

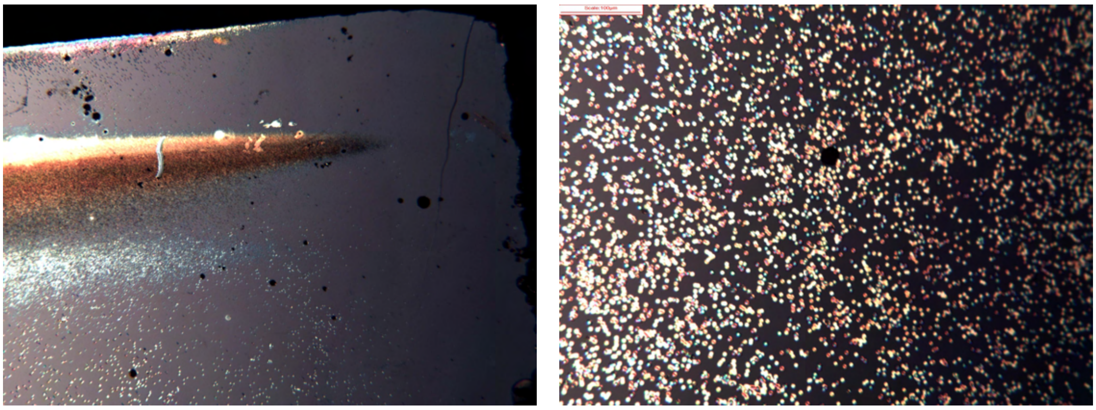

(a) Short side edge, magnetron side.

(b) Large density of small octagons.

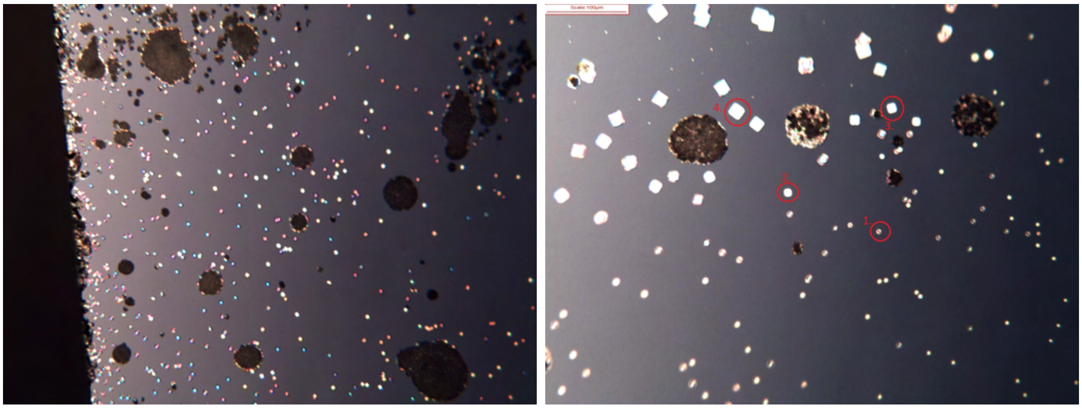

(c) Long side edge with small octagons.

(d) Large octagons to small squares.

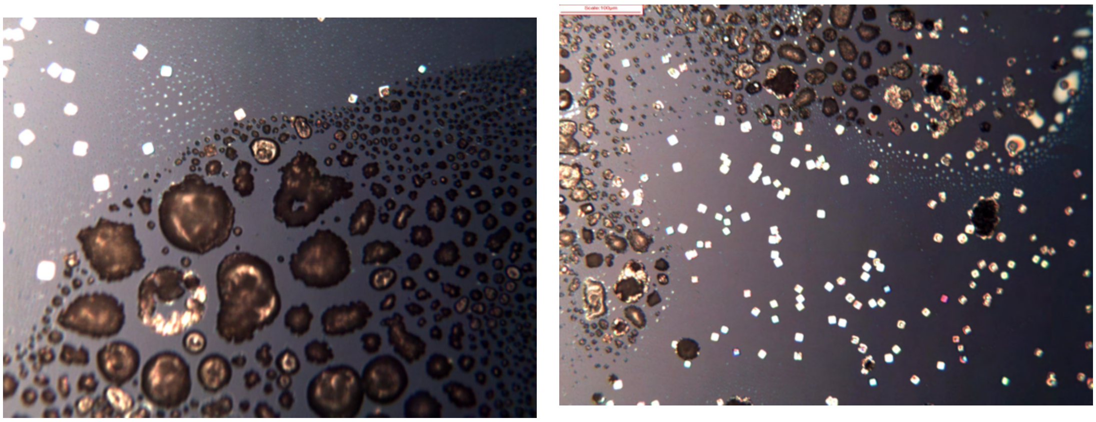

(e) Boundary between squares and brown spots.

(f) Boundary between squares and brown spots.

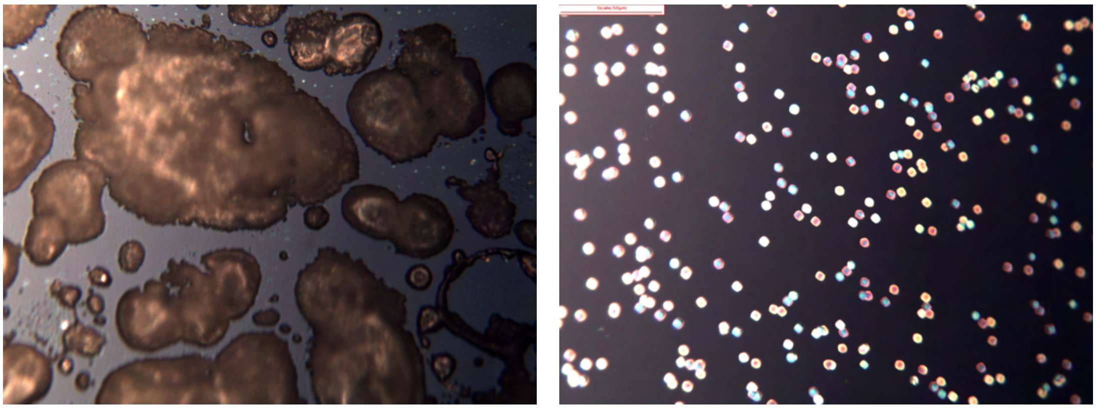

(g) Brown spots with few crystals in the area.

(h) Area with large octagons.

Figure 38: Observed trend on silica N taken at UC Berkeley.

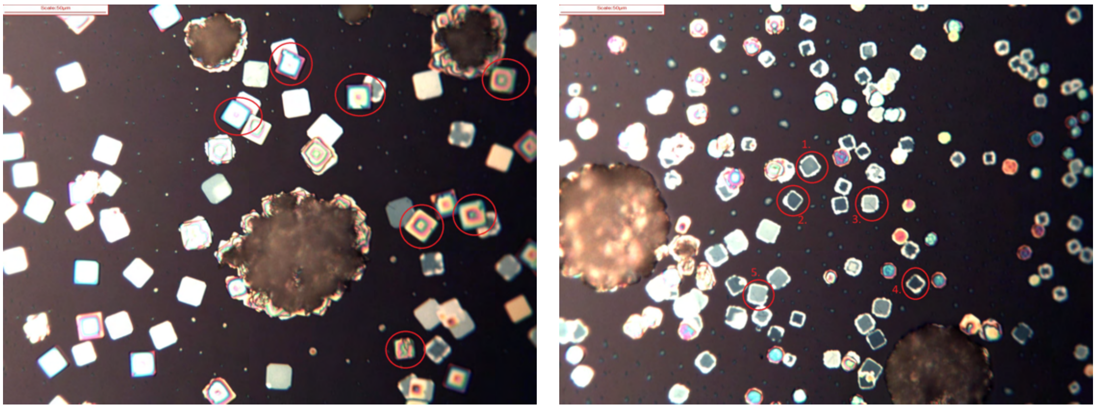

(i) Large squares around brown spots.

(j) Some nanoframe-like structures circled in red.

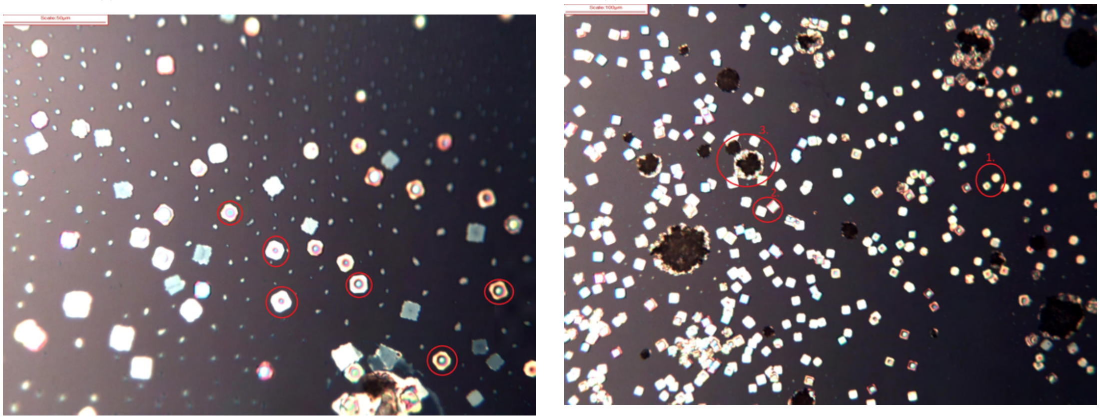

(k) Large squares with similar colors circled in red.

(l) Large octagons to small squares to large squares and brown spots

Figure 38: Observed trend on silica N taken at UC Berkeley.

The growth and morphology trend explained in this section for silica N is illustrated in Figure 39. It is important to notice that this trend occurred when moving from the magnetron side to the substrate center, as well as moving from the opposite side of the magnetron towards the center.

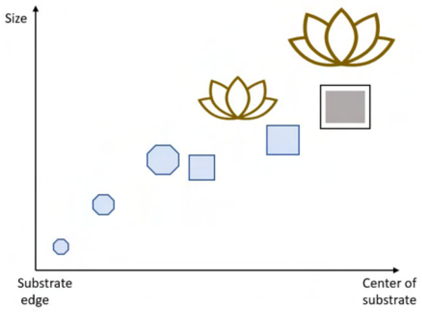

Figure 39: Illustration of how morphology and size changed towards the center of silica N substrate.

4.1.10 Size distribution of silica N

Silica N was performed at UC Berkeley for 1000 W and 1 min. Size analysis was done in order to compare with substrates of similar growth conditions and synthesis parameters. These are Si-1min, Si-15.5cm, Si-900W and Si-medium.

These source substrates and silica N substrate can be compared to give a basis for understanding the differences between UC Berkeley and NTNU. The silica N from UC Berkeley was from a synthesis done at 1000 W, 1 min at equal conditions as these substrates, but due to the limitation of the microwave oven the NTNU substrates had a power of 900W. This difference of 100W is considered negligible in this regard.

Comparing the values for silica N in Figure 40 with for instance Si-1 min in Figure 27 there seems to be no noticeable similarities. For silica N the squares in section 2 are the largest, while the opposite is true for Si-1min. For octagons on N silica, the same trend as for squares is detected, thus there is an increase in size for both morphology at the center of the substrate in section 2. This verifies the observations done in OM and SEM, where the crystals grew larger towards the center of the substrate, and the smaller ones were observed growing outwards on both sides of the center, i.e., towards the magnetron side and side B, see Figure 25.

Furthermore, the morphology shift observed on silica N where octagons grew close to the edges and squares in the middle were expected to hold for the mentioned source substrates as the growth conditions were nearly equal. However, this was not the case and in Figure 27 it is clear that octagons were significantly larger than squares at the center part of the substrate, section 2. Furthermore, on the silica N, there were more observations of flowers compared to these NTNU source substrates.

The Si-medium in Figure 36 does not display similar trend as silica N for squares or octagons. Neither does Si-15.5cm, see Figure 29, nor Si-900W, see Figure 31.

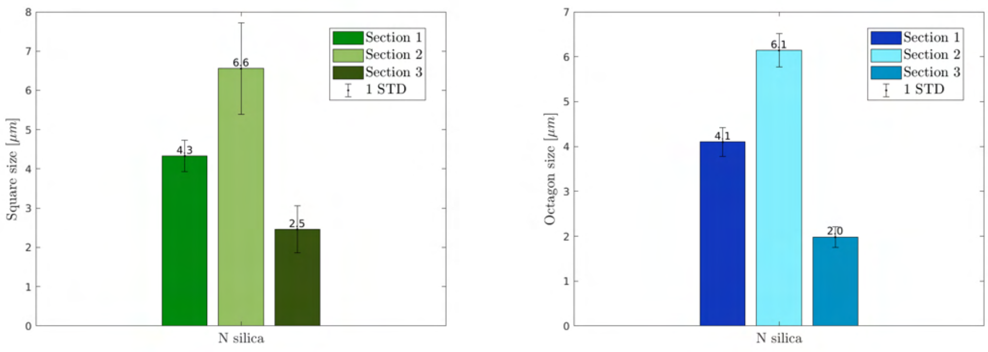

(a) Squares

(b) Octagons

Figure 40: Size analysis of silica N of source synthesis.

		Section 1 [#]	Section 2 [#]	Section 3 [#]
Silica N	Squares	28	144	82
	Octagons/circles	158	20	107

Table 7: Density of squares and octagons/circles in each section for each parallel in the silica N synthesis.

4.2 Energy dispersive X-ray spectroscopy (EDS) results

The source substrates were analyzed further by using an EDS detector in the SEM instrument with various technique modes, resulting in different reports of elemental mapping, spectra and other qualitative results.

The images shown below, Figure 41, display the result from an EDS analysis of the silica N substrate from a synthesis done at UC Berkeley [1]. Figure 41 illustrates the chemical analysis of the given area, and displays both mapping and semi-quantitative spectrum of the elemental components present in the area of interest.

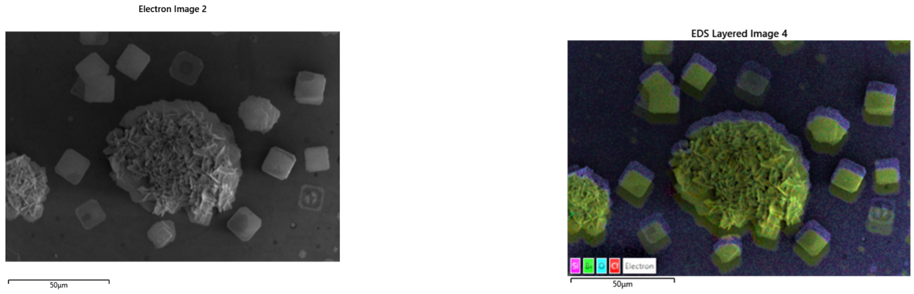

(a) Image of area that is being analyzed with EDS.

(b) Illustration of the EDS layered image.

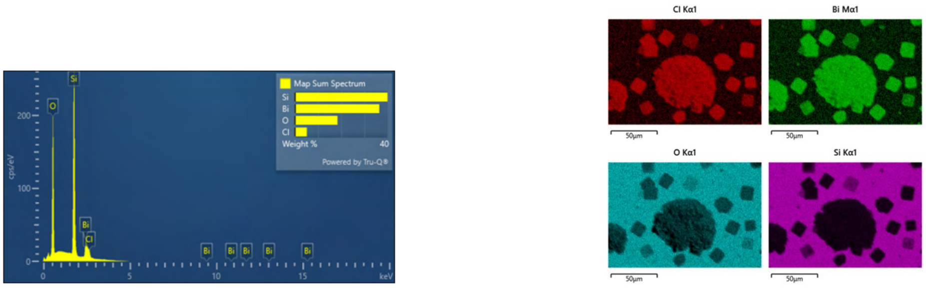

(c) The captured EDS spectrum.

(d) Image of the EDS elemental mapping.

Figure 41: EDS analysis of a flower-like structure and surrounding squares of BiOCl on silica N performed at UC Berkeley.

The EDS analysis reports of silica N given in Figure 41 are performed on a flower-like structure as well as the surrounding squares, as seen in Figure 41a. From Figure 41b it is clear that there is an abundance of bismuth, Bi, on both flower-like structures and squares demonstrated by green dots coloring the structures, but not the substrate. In a similar manner, it can be observed that the red dots corresponding to chlorine, Cl, is also covering the structures. A greater effort is needed for observing and determining the remaining elements oxygen, O, and silicon, Si, corresponding to the colors turquoise and pink, respectively. The substrate silica, SiO_2/Si, is made up of both elements thus observations of O and Si at the substrate in Figure 41b would be expected. Figure 41c illustrated the measured levels of each element in the image shown in Figure 41b. Here it is evident that silicon is highly present in the EDS analysis, and the signal is arising from the substrate. Additionally, bismuth is measured at high levels as seen in the Map Sum Spectrum in the upper right corner in Figure 41c which is in accordance with the green color observed at the flower-like structure and squares in Figure 41b. The oxygen peak in Figure 41c is also quite high, but detected at a lower level than silicon and bismuth. Lastly, chlorine is measured as the least detected element. This is contradicting the chemical composition, specifically the ratio of elements and stoichiometry of BiOCl. The elemental mapping shown in Figure 41d illustrated where the elements are detected. For silicon, displayed with a pink color, it is confirmed that the signal comes from the substrate as previously noted. The opposite applies to the green color for bismuth where the measurements clearly stem from the flower-like structure and squares. However, some green dots are also present on the substrate. The same phenomenon is seen for chlorine where there is a clear red signal from the flower-like structure and squares, but also some dots are observed on the substrate. For oxygen, the signal comes from both the structures and the substrate, and as expected there is a heavier signal from the substrate which aligns with the elemental ratios of two oxygen atoms for SiO_2/Si compared to the one in BiOCl.

Figure 42 illustrates EDS analysis of BiOCl on silica L done at UC Berkeley. It shows the area being analyzed, corresponding elemental mapping analysis and spectrum.

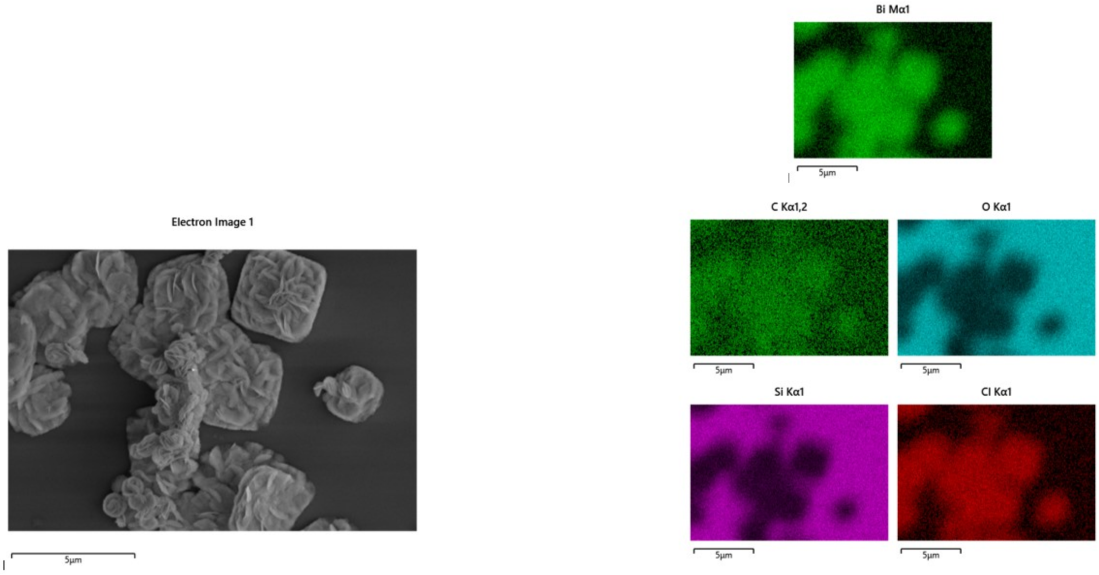

(a) Image of area analyzed with EDS.

(b) EDS elemental mapping.

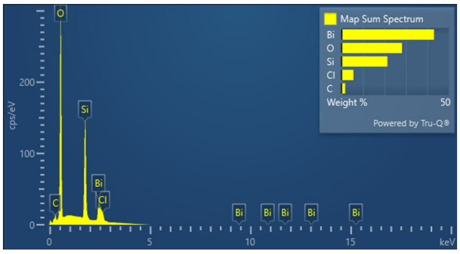

(c) EDS spectrum.

Figure 42: The EDS analysis of squares with flower-like BiOCl on silica L substrate done at UC Berkeley.

For silica L the area that was analyzed at UC Berkeley is displayed in Figure 42a which shows square crystals with flower formation. The corresponding elemental mapping is shown in 42b and EDS spectrum in Figure 42c. The elemental mapping gives a clear demonstration of where the pre-determined elements are detected and differentiating substrate from BiOCl structure. Figure 42b shows that there are strong signals of both bismuth and chlorine which outlines the structure. There are also some observations of green dots corresponding to bismuth from the substrate, as also noticed for silica N. As expected, oxygen is heavily detected from the substrate, and as mentioned previously in this section, this is from the composition of silica SiO_2/Si, and additionally, a signal is measured from the BiOCl structure. Furthermore, silicon is detected at the substrate and displayed in pink color. Unlike the silica N, this analysis incorporated carbon which is detected across the whole area, but appears stronger from the area where the structure is located rather than the substrate. This could arise from surface contamination of carbon in the EDS analysis, and as mentioned in Section 2.5.2 it does not necessarily entail that it comes from an organic molecule, but could be accumulated during the analysis in the electron microscope. From Figure 42c it can be seen that bismuth is detected at high levels, as well as oxygen. However, chlorine is detected at a lower level which is contradictory to the elemental ratio of the as-synthesized BiOCl crystals, similar to the EDS spectra of silica N in Figure 41c. Furthermore, the silicon level in the EDS spectra of silica L is placed lower relative to the other substrates than on silica N where it was the most detected element. This is most likely due to the different levels of the exposed substrate surface of the two analyzed areas.

The Figures 43 and 44 shows the EDS analysis performed at NTNU of mica L substrate from UC Berkeley. The substrate mica L was coated with Pd/Pt and one analysis was done where these elements were included, and another analysis was performed without considering these. The results are displayed below.

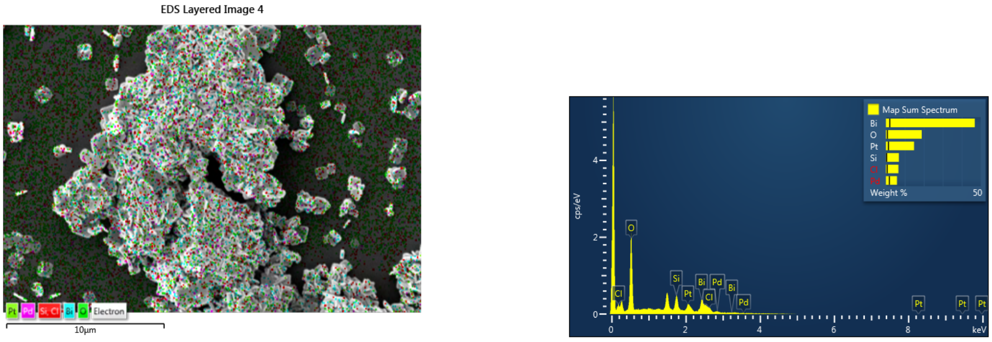

(a) EDS layered image of mica L with Pd and Pt.

(b) EDS spectra with Pd and Pt.

Figure 43: Illustration of EDS analysis of mica L at NTNU with Pd and Pt.

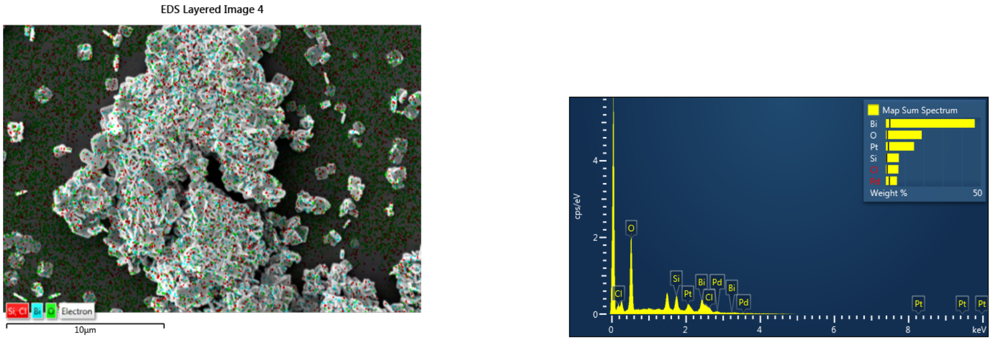

(a) EDS layered image of mica L without Pd and Pt.

(b) EDS spectra without Pd and Pt.

Figure 44: Illustration of EDS analysis of mica L at NTNU without Pd and Pt.

For the analysis of mica L, the layered image shown in Figure 43a and corresponding spectra in Figure 43b has Pd and Pt incorporated in the analysis. Although the two different green colors representing platinum and oxygen are difficult to distinguish, there is a green signal throughout the area. Palladium, Pd, in pink color is consistently observed across the area. Bismuth, Bi, in turquoise color is observed in the grey area of the flower-like structure, and this is also true for the red color corresponding to silicon and chlorine. Figure 43b shows that is signal for bismuth is the strongest, then oxygen, platinum, and silicon. Lastly, a small detection signal is chlorine and palladium. For the EDS layered image in Figure 44a there is no significant difference from the analysis with Pd and Pt, except that these elements are not incorporated in the analysis.

Figure 45 displays the elemental mapping of silicon, bismuth, chlorine and oxygen. It is a similar analysis to the one shown in Figure 44a, but without showing the structure in the picture.

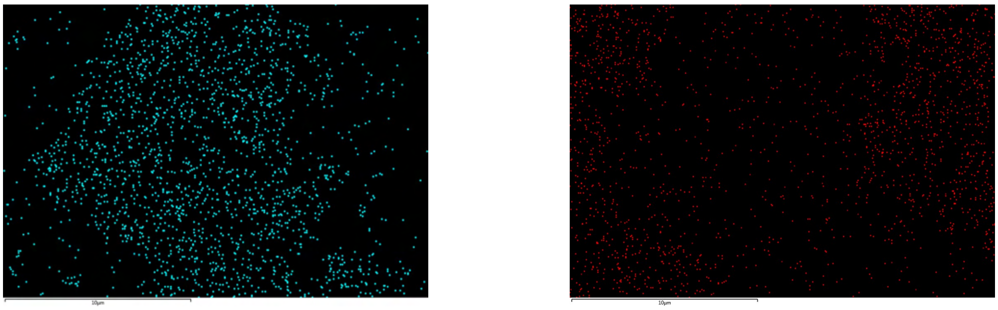

(a) Bismuth mapping.

(b) Silicon mapping.

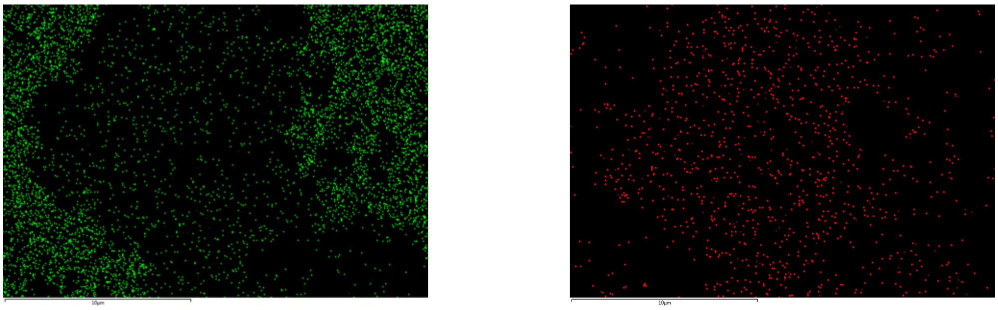

(c) Oxygen mapping.

(d) Chlorine mapping.

Figure 45: Illustration of signal from pre-determined elements of area in Figure 44a.

Figure 45 shows the same type of analysis done in Figure 44a, but without the structure present in the image which makes it easier to detect the different colors and to identify the elemental signals. For the bismuth in Figure 45a there is a heavier signal from the center of the structure, likewise for chlorine in Figure 45d. However, colored dots are appearing on the sides of the cluster of flowers for chlorine and bismuth. These signals could stem from the single crystals surrounding the main structure that can be seen in Figure 44a. For oxygen, the opposite is true where there is a more prominent signal from the substrate than at the center of the structure, as seen in Figure 45c. Lastly, silicon is scattered across the area but with a higher signal count from the exposed substrate surface than the flower-like structure at the center, see Figure 45b. The EDS software detects signals for both silicon and oxygen from the substrate and for the oxygen, the signal is stronger from the substrate than the cluster of flower-like structures. This is in accordance with the chemical components of mica which consists of numerous elements including oxygen and silicon as listed in Section 2.3.7, and as explained oxygen is especially significant in the substrate composition.

A weakness with this type of analysis seen in Figure 43a is that when silicon and chlorine is represented with the same color, a distinction could not be done. This means that an assumption has to be made that the red signal from the structure has to come from chlorine in the BiOCl, and that it is not from silicon. Additionally, the two green colors representing platinum and oxygen are hard to distinguish which is unfavorable when analyzing the images. Furthermore, the substrate is dark which makes it more difficult to observe colored dots compared to the brighter structure. An improvement of this could be an analysis like the one given in Figure 45 where the structure is not displayed, thus the color and contrast of the structure versus the substrate is not influential on the ability to detect the colored signals corresponding to the elements. On the basis of these shortcomings, this type of analysis can only be perceived as an indicator of chemical composition, and knowledge of the structure has to be acquired in advance of performing an EDS analysis.

4.3 Atomic force microscopy (AFM) results

Large and small squares and octagons on the silica N substrate were analyzed in AFM and images from the analysis are shown below.

Nanoframes are illustrated in Figure 46a, where the structure displays a thicker frame and a thinner center. The peak force error image of this square is shown in Appendix D, Figure 79a and the thickness profile of this large square is shown in Figure 46b clearly showing the thickness difference across the structure.

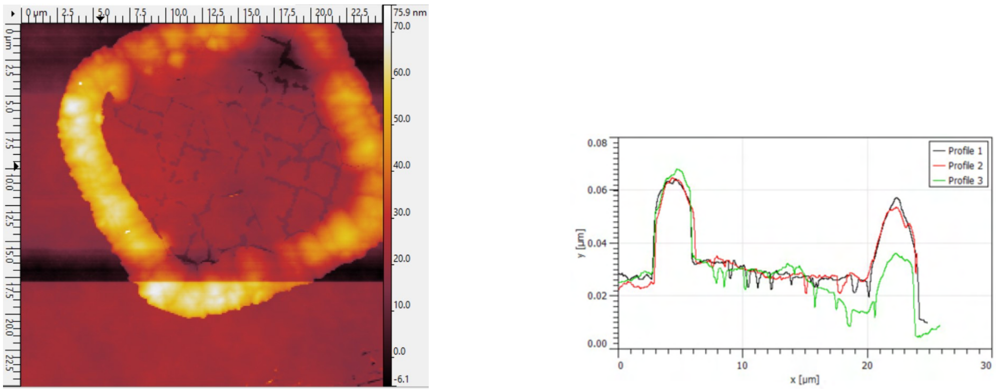

(a) Large, carved out square with ZSensor imaging.

(b) Corresponding thickness profile of the structure.

Figure 46: Illustration of AFM analysis of a nanoframe.

Octagons are shown in Figure 47a. The thickness profile of the octagon to the left in the image is illustrated in Figure 47b. A typical thickness profile of a small square is shown in Figure 48a.

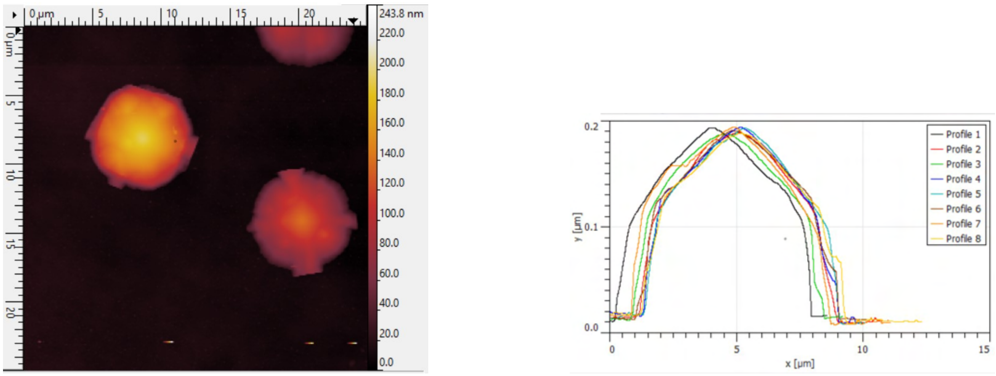

(a) Large octagons with ZSensor imaging.

(b) Thickness profile of the large octagon.

Figure 47: Illustration of a typical AFM analysis of an octagon.

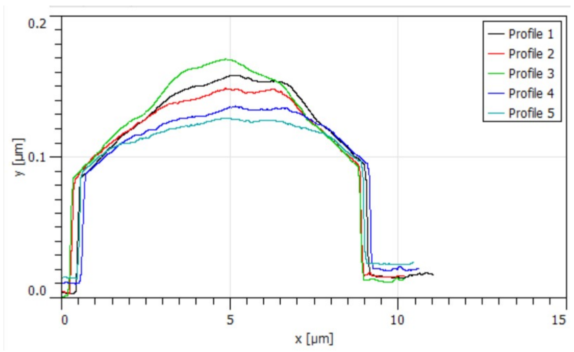

(a) Typical thickness profile of small square.

Figure 48: Illustration of AFM thickness profiles for square.

AFM analysis of an octagon is shown in Figure 49. The thickness distribution given in Figure 49b is based on the octagon at the centre-right in Figure 49a.

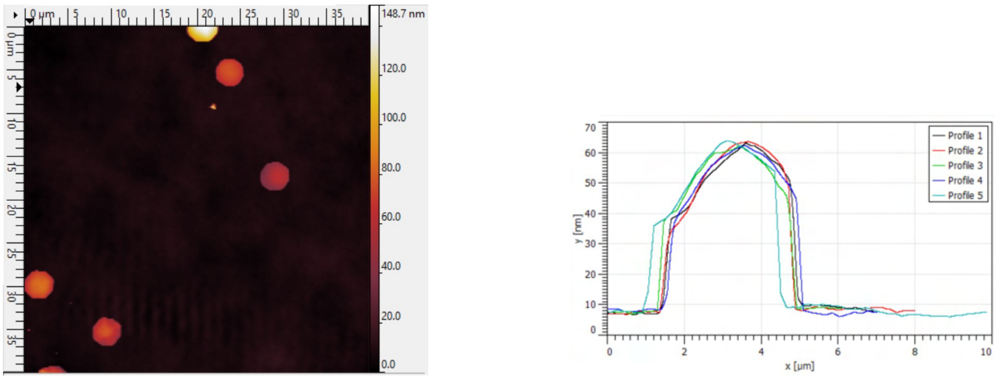

(a) Small octagons

(b)

Figure 49: Illustration of ZSensor image and thickness profile for an octagon.

Cracked structures became visible in the AFM measurement, as seen in Figure 50a. The corresponding thickness profile through the center of the structure to the left in Figure 50a is presented in Figure 50b.

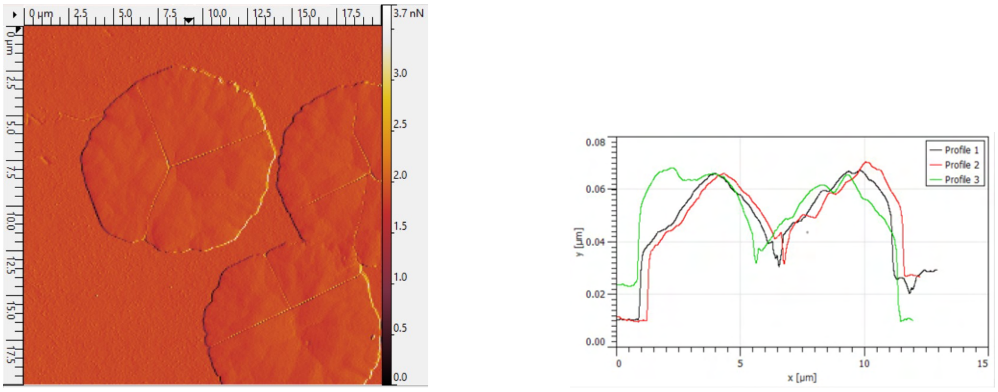

(a) Peak force error image of cracked crystals.

(b) Thickness profile of a cracked crystal through the center.

Figure 50: Illustration of AFM analysis of a cracked crystal.

Both height and length were measured, and based on the literature that states that one nanoplates is comprised of four unit cells of BiOCl, the number of nanoplates in the crystals was calculated from the height measurements, as stated in Section 3.8. The average thickness in each AFM image is given in Table 8. The table also displays the calculated number of nanoplates and measured lengths. Additionally, the AFM image was analyzed to produce the results given in the table.

Morphology	Average thickness [nm]	#Nanosheets	Length[µm]	From figure
Octagons	69.2	23	2.9	49
	157.4	53	7.0	47
	43.0	15	12.6	77
	40.4	14	11.5	76
	168.9	57	11.7	78
Nanoframes	39.4 (frame: 60, center: 18.7)	13	21,0	46
	44.5 (frame: 59.3, center: 29.3)	15	17.6	80
	36.7 (frame: 47.8, center: 25.6)	12	24.3	81
	36.8 (frame: 51.3, center: 22.2)	12	21.6	82
Square	152.6	52	11.4	48
Cracked crystal	283.3	81	10.0	50

Table 8: Results of AFM measurement analysis for octagons, nanoframes, squares and a cracked crystal.

All the large squares have an elevated edge. The structure is made up of a tall surrounding edge and a lower-middle part, thus the average thickness is given in Table 8 in addition to the thickness of the tall frame and the thinner center. The thickness profile through the center of the cracked structure is shown in Figure 50b, which evidently displays a decline in the middle where the fracture is located. These round structures were measured to be the thickest.

In addition to the thickness measurements linked to the morphology, a thickness analysis was done of various colors observed for the crystals, the results are presented in Table 9. Small squares were chosen to be analyzed because all the large squares discovered portrayed a nanoframe-like structure and multiple color schemes. Additionally, small squares were on a general basis larger than octagons hence it was easier to discover the square shape when using the AFM instrument.

Color	Thickness [nm]	#Nanosheets	Length [µm]	From Figure
Yellow	45.4	15	9.2	88
Yellow and red	80.0	27	12.3	85
Yellow	96.1	33	10.9	83
Blue	132.6	45	7.7	86
Blue, red and yellow	134.8	46	11.8	89
Blue	173.3	59	9.7	87
Blue and red	175.6	60	8.0	84

Table 9: AFM thickness measurements of crystals with varying colors.

4.4 Raman spectroscopy results

The Raman spectres done on substrates with BiOCl are given in Figures 51b, 53 and 56. A comparative spectra of clean silica substrate is given in Figure 54. It is clear that the Raman peaks appear at similar values of frequency and any small variation in Raman band position may be due to stress state [188].

Raman spectroscopy performed at UC Berkeley was done on silica substrates F and N, examining both flower-like structure and a square crystal. Firstly, the flower-like structure was detected on the silica F and analyzed with Raman, the area of irradiation for Raman analysis is shown in Figure 51a. The resulting spectra with peak values are displayed in Figure 51b.

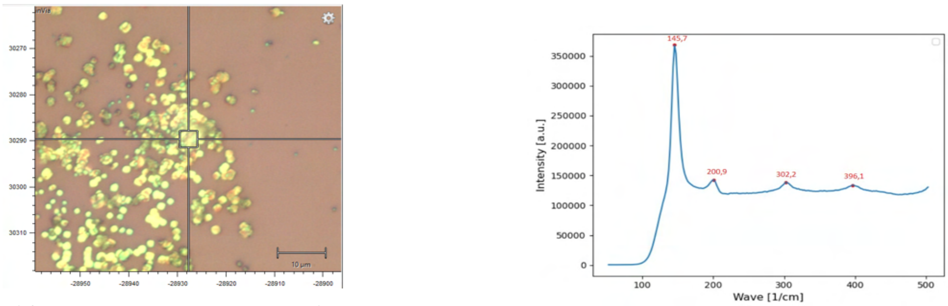

(a) Capture of flower-like structure on silica F for Raman analysis.

(b) Raman spectra of the flower-like structure.

Figure 51: Raman analysis of BiOCl flower-like structure on silica.

Then Raman analysis was done at UC Berkeley of a square crystal on the silica N substrate, shown in Figure 52, to give both a narrow and wide spectra displayed in Figure 53. First, a wide spectra analysis was carried out, as can be seen in Figure 53a. Then, a more narrow range spectrum was produced to discover any eventual small peaks in the specified area, that could have gone undetected in the large range spectrum. The narrow spectra is shown in Figure 53b.

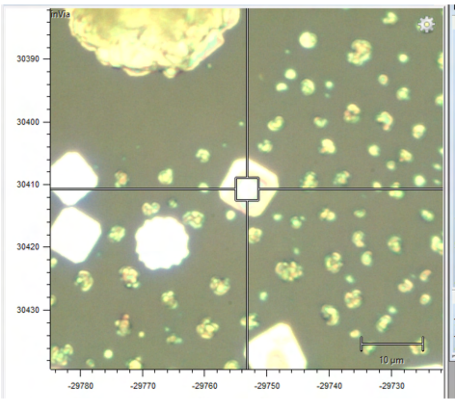

Figure 52: Illustration of square crystal on silica N for Raman analysis done at UC Berkeley.

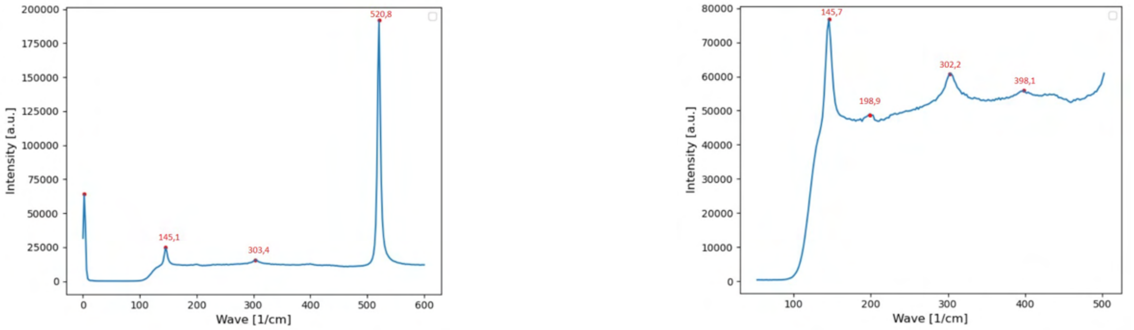

(a) Raman analysis with 10 accumulations, 5 sec exposure time and 40 % laser power with static scan type, giving a wide spectra.

(b) Raman analysis with 5 accumulations, extended scan type and 100% laser power resulting in a narrow, detailed spectra.

Figure 53: The figure illustrates the Raman spectra of BiOCl on silica substrate N performed at UC Berkeley.

Additionally, Raman was performed at UC Berkeley on a clean silica substrate giving both a wide and a narrow spectra illustrated in Figure 54.

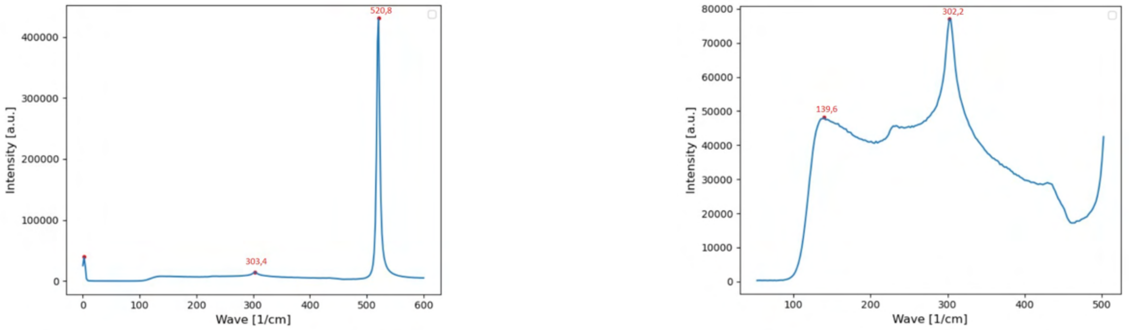

(a) Raman analysis of silica substrate, wide spectra.

(b) Raman analysis of silica substrate, narrow spectra.

Figure 54: The figure illustrates the Raman spectra of clean silica substrate performed at UC Berkeley.

At NTNU silica substrate D and mica substrate F were analyzed with Raman spectroscopy. For the silica D analysis a square crystal was irradiated, see Figure 55. The resulting Raman spectra as displayed in Figure 56.

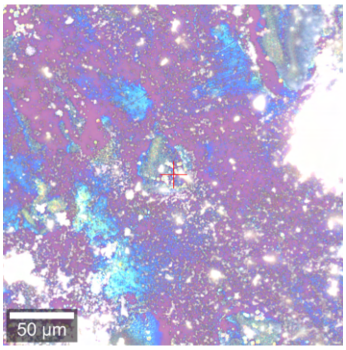

Figure 55: Illustration of square crystal on silica D for Raman analysis done at NTNU.

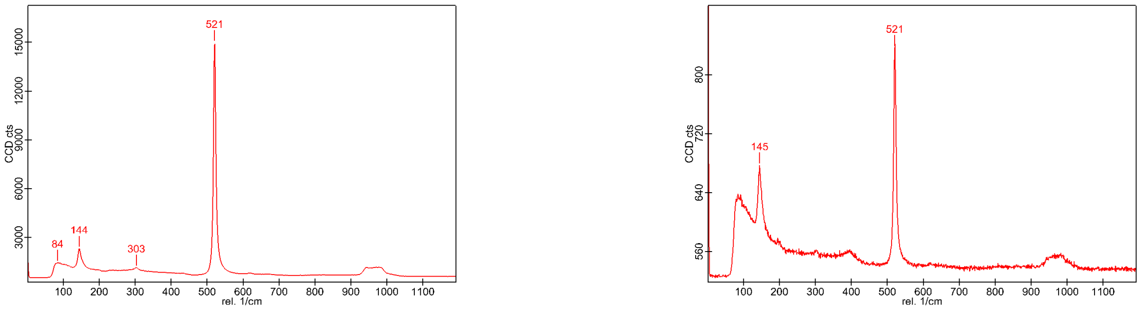

(a) Raman analysis of silica substrate D, wide spectra.

(b) Raman analysis of silica substrate D middle spectrum.

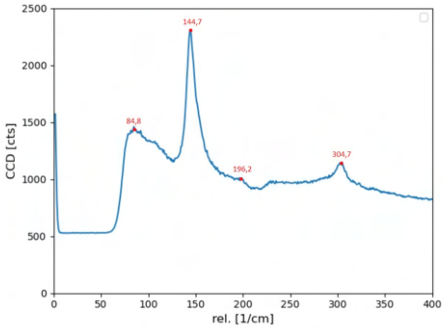

(c) Raman analysis of silica substrate D, narrow spectra.

Figure 56: The Raman spectra of BiOCl on silica D done at NTNU with 6 accumulations and 10 seconds integration time.

For the mica F Raman analysis a flower-like structure was irradiated, see Figure 57. The resulting spectres are shown in Figure 58.

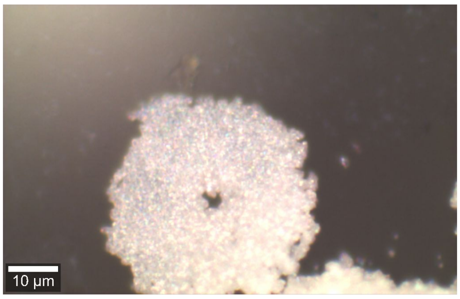

Figure 57: Flower on mica F where Raman analysis was performed.

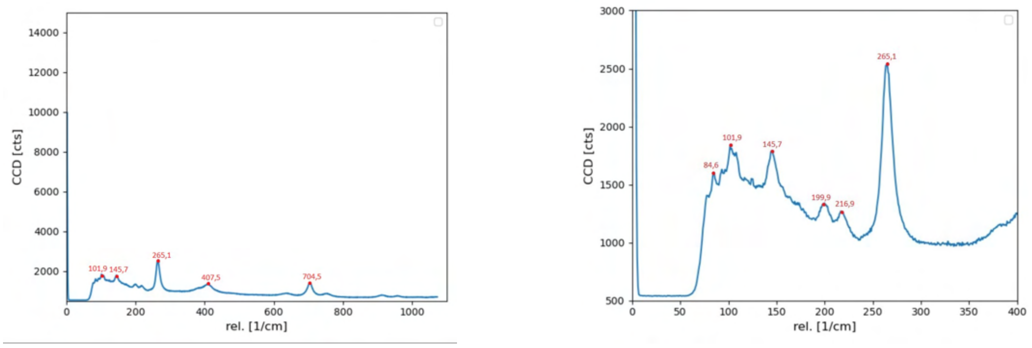

(a) Raman analysis of BiOCl flower on mica F substrate, wide spectra.

(b) Raman analysis of BiOCl flower on mica F substrate, narrow spectra.

Figure 58: The Raman spectra of BiOCl flower mica F substrate with 5 accumulations and 40 seconds integration time done at NTNU.

Table 10 gives an overview of the Raman analysis of BiOCl done on silica and mica, where ”X” signifies that the peak was detected on that substrate. In the table the corresponding modes and vibrational bonds are also stated.

Mode and vibrational bonds	**Raman shift** [cm^{-1}]	**Silica**	**Mica**
A_{1g} external stretching vibration of Bi-Cl	60		
Raman signal of BiOCl	84		X
B_g mode for muscovite mica	100		X
A_{1g} mode for internal Bi-Cl symmetric stretching	145	X	X
E_g internal Bi-Cl stretching mode	200	X	X
A_g mode for muscovite mica	216		X
A_g mode for muscovite mica	265		X
weak Raman signal from the silicon, Si, substrate	303	X	
B_{1g} and E_g modes, movement of the oxygen	400	X	X
First order Raman active (Stokes) phonon of silicon	521	X	
B_g mode for muscovite mica	704		X

Table 10: Raman modes for BiOCl grown on silica and mica substrates.

There are some peaks that are observed for all the Raman analysis of BiOCl on either substrates and these are 145, 200 and 400 cm^{-1}, see Table 10. The strong peak at around 144 - 145 cm^{-1} shown in all the Raman spectres of BiOCl on both silica and mica is ascribed to the A_{1g} mode for internal Bi-Cl symmetric stretching, see Figure 59 [6, 38, 194, 195, 26, 196, 197]. This peak appears intense and it is known that symmetric vibrations are stronger than asymmetric vibrations [38, 26]. Likewise, the Raman band at around 200 cm^{-1} appears in all the narrow Raman spectres of BiOCl on both mica and silica substrates in Figures 51b, 53b, 56c and 58b. Oppositely, it does not appear in the wide spectres of the Raman analysis in Figures 53a, 56a and 58a which can be due to the peak being weaker thus harder to detect for a wide range. However, there is a small indication of a peak at 200 cm^{-1} for the wide spectra of silica N in Figure 53a and the same applies for the middle spectra of silica D in Figure 56b. This peak at 200 cm^{-1} is assigned to the E_g internal Bi-Cl stretching mode [38, 195, 26, 6, 196, 198, 197].

Lastly, the consistent peak at 398 cm^{-1} is attributed to the B_{1g} and E_g modes produced by movement of the oxygen atoms in BiOCl [38, 196, 195, 198, 26, 197]. This peak is seen in Raman analysis of flower on silica F, square on silica N, and flower on mica F in Figures 51b, 53b, 58a, respectively. The only BiOCl analysis it did not appear in is the square on silica D, however an indication of a peak at around 400 cm^{-1} can be seen in Figure 56b. It is most likely a weak Raman signal hence more challenging to detect for a wide range. Which is supported by the fact that it is not visible in the wide spectres in Figure 53a and 56a.

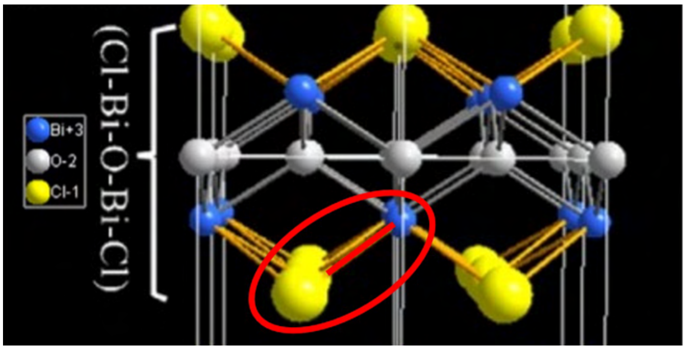

Figure 59: Illustration of the Raman active Bi-Cl bond in BiOCl marked in red [38].

Oppositely to the consistent peaks found on both substrates mentioned above, there was one peak at 84 cm^{-1} which was only discovered in the Raman analysis performed at NTNU of flowers on mica F and square on silica D, seen in in Figures 56 and 58b. After efforts of identifying this peak, one study states that this peak is ascribed to a Raman signal of BiOCl and that upon doping it will increase corresponding to a blueshift in frequency [26]. The reasoning behind why it was not detected in the UC Berkeley analysis could be due to instrumental differences or other causes which will be discussed in Section 6.1.

Furthermore, two peaks did not appear in either the analysis from NTNU or UC Berkeley of both flowers and squares. From literature it is stated that a peak around 60 cm^{-1} would be expected as this is ascribed to the A_{1g} external stretching vibration mode of the Bi-Cl bond [38, 26, 195, 198, 196, 197]. However, this expected peak does not appear in the Raman analysis of BiOCl on either substrate and this is a common occurrence for multiple Raman analyses of BiOCl. This absence is believed to be caused by the limitation of the spectrophotometer to detect low intensities [38]. As for the other undetected peak, and the last E_g external mode of Bi-Cl stretching, the signal is hypothesized to be masked by the strong signal at around 145 cm^{-1} [38]. The reason for this is explained by the fact that asymmetric vibrations are weaker in intensity than their symmetric counterparts, thus the asymmetric Bi-Cl E_g external stretching mode is concealed by the 145cm^{-1} symmetric A_{1g} internal Bi-Cl stretching mode [38, 26].

Out of all the ascribed peaks, there is only one peak that remains unaccounted for, and that is the 139.6 cm^{-1} Raman band detected in the Raman analysis of clean silica substrate in Figure 54b. In theory, this clean substrate analysis should only produce signals corresponding to the composition SiO_2/Si. No successful matches in the literature were found for common contaminants such as carbon compounds, thus it is deduced that this peak most likely stems from the substrate. It can also be seen vaguely by a change in slope before the 145 cm^{-1} peak in silica F in Figure 51b and silica N in Figure 53 and may be further masked by the strong peak at 145 cm^{-1}. In silica D analysis it could be masked by the 84 cm^{-1} peak. From a study, a broad and weak Raman peak at 140 cm^{-1} appears in an analysis of densified SiO_2 glass. It is linked to the bond length between Si-Si and the study further suggests that the Raman spectra can be explained from this and the structural change occurring within the densified glass compared to undensified glass [199].

All the above-mentioned peaks are assigned to the BiOCl, however some peaks that were detected originated from the substrate. The peak at 521 cm^{-1} comes from the silica substrate and is present in all the specters involving this type of substrate, from both universities. This peak corresponds to silicon's only first-order Raman active (Stokes) phonon located at the center of the Brillouin-zone, k=0 [200, 201]. Further, it is stated in a study that this peak arises from the creation of triple degenerate, long-wavelength transverse optical phonon. The long-wavelength used in this study was a 514 nm argon-ion laser, with 10 MW power [201]. Additionally, will the silica substrate correspond to the peak at 302.2 cm^{-1} which is ascribed to a weak Raman signal from silicon, Si [38]. This peak is consistent in all the analyses of BiOCl on silica substrates, and there are no large differences detected for NTNU and UC Berkeley analyses. It can also be seen in the Raman spectra for the clean silica substrate.

As for the Raman spectra of mica, there are numerous peaks that are not ascribed to any modes of BiOCl. These peaks are located at 101.9, 216.9, 265.1 and 704.5 cm^{-1}. It is thus deduced that these stems from the mica substrate and this is supported in literature. The Raman band at 101.9 cm^{-1} and 704. 5 cm^{-1} corresponds respectively to the 101 cm^{-1} and 704 cm^{-1} from B_g modes of muscovite mica. The peak at 216.9 cm^{-1} as well as the 265.1 cm^{-1} peak corresponds to the A_g modes at 217 cm^{-1} and at 265 cm^{-1}, respectively [112, 202, 203].

4.5 X-ray diffraction (XRD) results

XRD analysis with gracing incident, angle set to 1°was performed on silica I with product attached to the surface and the XRD pattern is shown in Figure 60. The figure also shows the XRD peaks for contamination of wavelengths for WL_{α_1}, WL_{α_2} and CuK_{β} corresponding to a pink, green and yellow color, respectively. The reasoning for this contamination incorporation in the spectra is explained in Section 2.5.4. The blue XRD pattern is for BiOCl, PDF 01-083-07690, from a database [191].

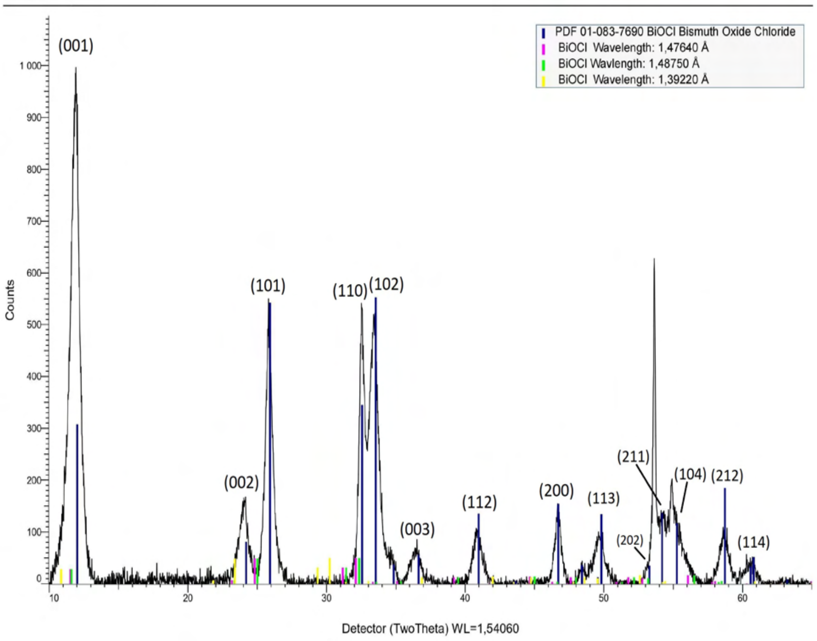

Figure 60: XRD spectra of BiOCl on silica I with wavelength contamination and corresponding facets.

In Figures 60 and 61 possible contamination from WL_{α_1}, WL_{α_2} and CuK_{β} are incorporated into the diffractograms. This was taken into account for both analysis of mica J and silica I, and none of the observed diffraction peaks coincided with contaminating wavelengths.

The XRD pattern of silica I is illustrated in Figure 60 with incorporated lines from the product BiOCl from a database, PDF 01-083-7690. There are certain aspects of the matching between the blue lines and the observed XRD pattern that are noteworthy.

One of the interesting aspects is the visible difference in intensity between several peaks in the XRD analysis of silica I and the database BiOCl in Figure 60. The intensity is illustrated on the y-axis and is measured for a specific diffraction angle 2θ given on the x-axis.

From the XRD pattern of silica I in Figure 60 it is clear that the most intense peak is the 2θ=11.92 linked to the (001) facet. The (001) peak appears more intense than the standard BiOCl, which may indicate that for the as-synthesized BiOCl on silica I there is a higher exposure of the (001) lattice plane. This demonstrates that the BiOCl crystals on silica I have a preferential orientation of these lattice planes and that the growth possibly occurs in the [001] direction. The other peaks with a higher measured intensity than the database is the (002) and (110) while some peaks show less measured intensity such as (102), (112), (113), and (212). The peaks displaying less intensity entail that these facets were less detected in the crystals compared to the database BiOCl. The higher intensity of (002) supports the preferential [001] growth direction, while the (110) facet corresponds to a different growth direction than [001]. This means that the product is not a single domain film with only [001] growth direction, but a crystal comprised of various growth directions. However, the biggest detected intensity stems from the (001) facets, and is supported by an intensity increase for (002), this suggests that the preferential growth of as-synthesized BiOCl crystals is [001], and that the crystals are mainly comprised of BiOCl sheets with exposed (001) planes.

Although it appears to be a good matching of peak position of blue lines for BiOCl and observed peaks for silica I in Figure 60, there is one large intensity peak that does not fit the PDF 01-083-7690 at 2θ=53.64°. The peak does not match with unreacted precursor $BiCl_3$, contamination from either C or H, or the silica substrate SiO_2/Si, and these mentioned elements were individually tested. The same thing occurs for the (104) facet at 55.26°for the database, which for silica I is detected at 54.89°. This mismatch can be seen in Figure 60 where the as-synthesized BiOCl has a peak position shift towards the left. This is not something that occurs in the mica XRD analysis as can be seen in Figure 63, which means that it most likely could be due to the silica substrate although no match was made.

Additionally, a XRD analysis was done for the mica J with an incident angle of 1°, and the analyzed diffractogram is shown in Figure 61.

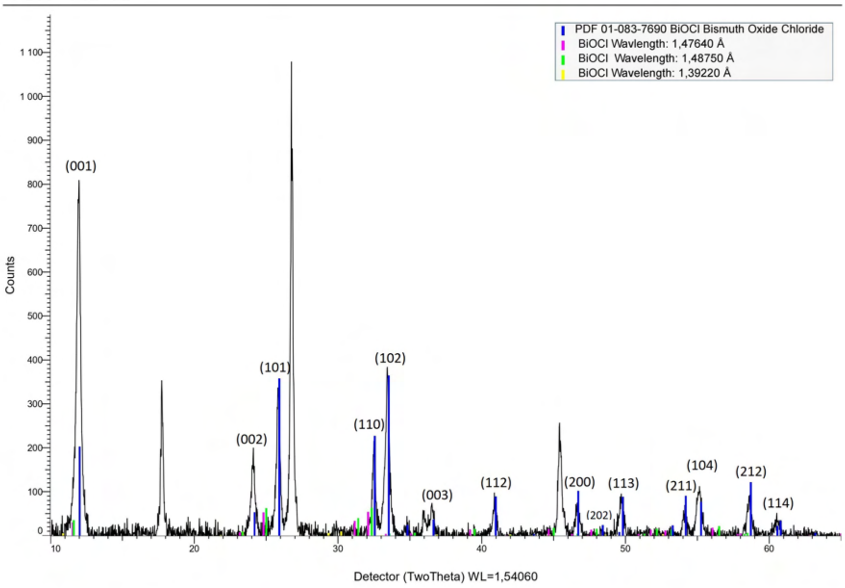

Figure 61: XRD spectra of mica J with wavelength contamination and corresponding facets.

From the XRD analysis of mica J displayed in Figure 61 there are certain aspects worth noticing linked to the fit of the blue lines regarding both peak positions and intensity. The blue lines illustrated the database BiOCl, PDF 01-083-7690.

Firstly, for the mica J XRD pattern in Figure 61 there is also an apparent intensity difference between the observed peaks and blue lines for BiOCl, similar to the silica I. The same intensity increase is observed for the (001) facet, indicating that the as-synthesized BiOCl on mica J also has a preferential orientation of these facets. This is supported by the intensity increase for the (002) facets like what was observed for the silica I.

Another feature worth noticing in the diffractogram of mica J in Figure 61 is the peak fit with the database BiOCl, blue lines. Disregarding the intensity variation, all the values of 2θ from the database BiOCl coincides with an observed peak for mica J. The peaks that are only observed for mica J and do not coincide with the database stem from the mica substrate. This was confirmed from a database and literature, stating that these peaks are from the muscovite mica sheets [204, 205, 206]. It is further stated that the 2θ equal to 18°corresponds to calcite, 27°peak indicates illite, 36°is for quartz, and lastly that 45°is linked to albite. In the study, it is said that illite has the highest percentage composition in the mica and that it results in the most intense peak [205]. This peak at 26.78°appears most intense in the mica J XRD pattern in Figure 61, indicating a high percentage of illite in the substrate.

The unmatched peaks for mica J in Table 12 is matched with the muscovite XRD pattern given in the RRUFF™ database with a RRUFF ID of R040104.1 which are diplayed in Table 11 [207, 208].

Observed unmatched peak [°]	17.75	26.78	35.98	45.45
Peak from RRUFF™ database [°]	17.79	26.82	36.03	45.46
Facet (hkl)	(0 0 4)	(0 0 6)	(0 0 8)	(0 0 10)

Table 11: Unmatched peaks from mica J with database diffraction angle and facets.

A comparison of mica J produced with a gracing incident angle of 1°and mica F with an angle of 2°is displayed in Figure 62. The mica J is displayed in red and the mica F is the black spectra.

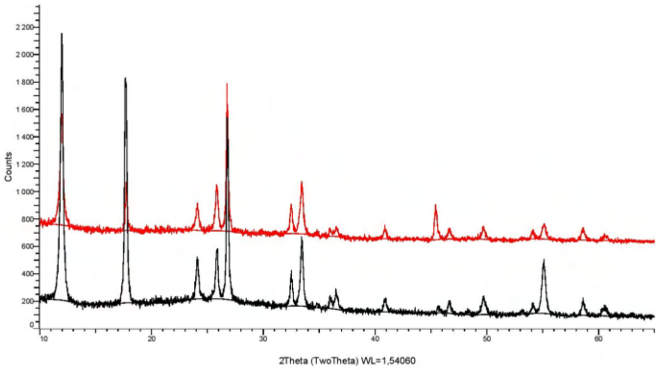

Figure 62: XRD spectra of mica F (black) and mica J (red).

The peaks linked to BiOCl, PDF 01-083-07690, are specified by a database and displayed with blue lines in Figure 60 and Figure 61.

The observed diffraction peaks for silica I and mica J, as well as corresponding peaks for database BiOCl and facets are displayed in Table 12.

2θ Silica I [°]	11.92		24.10	25.83		32.53	33.41		36.47	40.88		46.69	49.84	53.45	53.64[1]	54.18	54.89	58.66	60.63
2θ Mica J [°]	11.97	17.75	24.10	25.86	26.78	32.51	33.45	35.96	36.53	40.90	45.45	46.65	49.72	53.36		54.18	55.14	58.62	60.58
PDF 01-083-07690 2θ [°]	12.03		24.20	25.92		32.56	33.54		36.65	40.98		46.72	49.83	53.30		54.20	55.26	58.73	60.58
Facet (hkl)	(001)		(002)	(101)		(110)	(102)		(003)	(112)		(200)	(113)	(202)		(211)	(104)	(212)	(114)

Table 12: All the observed diffraction angles for silica and mica as well as corresponding facets and database diffraction angle,

From the values in Table 12 and Equation 3 the lattice spacing d was calculated for each diffraction angle and facet, see calculation in Appendix E. The values for lattice spacing, d, were then used in Equation 4 to calculate a corresponding lattice constant c. Then an average lattice constant c for both silica and mica XRD analysis was calculated. The average lattice constant c was equal to 0.73816 nm for silica and 0.73793 nm for mica. For database BiOCl c was equal to 0.73489 nm [191]. It is clear from the lattice constant calculations that there is not a huge difference between produced BiOCl on silica and mica compared to the database.

In this calculations the database lattice constant a = 0.388551 nm was used, however, this differs from the literature value given in Section 2.2.3 which was used in the AFM thickness analysis in Section 4.3. The values differ some, therefore this indicates there is some uncertainty regarding the values of the lattice constant. In the XRD calculations, the value from the database BiOCl was chosen for comparison reasons.

A comparative analysis was done for the mica J shown with the red XRD pattern and silica I illustrated with the black spectra in Figure 63.

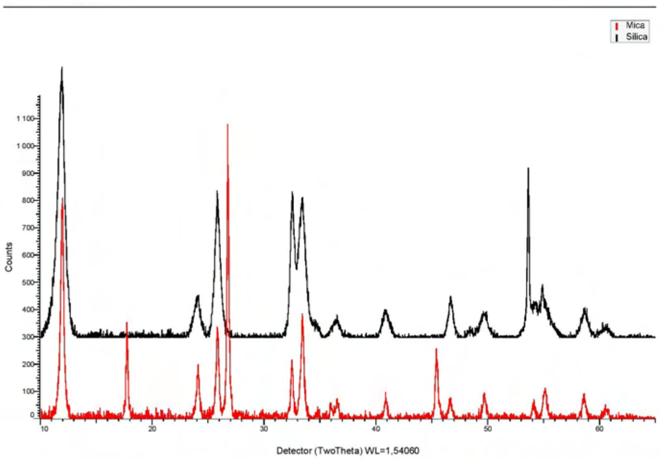

Figure 63: XRD spectra of silica I (black) vs mica J (red).

---

[1] Unidentified peak

5 Discussion

This section consists of a discussion around the observed growth trend. Influential aspects will be considered across the substrate in regards to morphology at the specific location. Then the observed morphologies will be detailed and why these might occur at the specific places on the substrate. Lastly, the synthesis part involve discussion around each changed parameter and its influence on the crystal growth and morphologies observed on the substrate.

5.1 Growth trend

The distinctive and prominent trend discovered on the silica N explained in Section 4.1.9 can give an insight into nucleation and subsequent growth of the commonly observed BiOCl structures; squares, octagons and flowers. The structures were discovered at specific places on the substrate surface. By associating the size, color, shape and density of crystals a discussing can be made of how these develop and what conditions facilitates the growth of the different structures. The main observations were that octagons grew at the substrate edges, while squares grew when moving towards the substrate center before flowers appeared, and lastly nanoframes became evident at the center.

Based on this, a hypothesis of growth may be deduced where first there is initial nucleation, then diffusion of atoms or nuclei grows into an octagon where growth along with directions [110] and [100] are equal. Then more atoms will diffuse to the octagon and growth in the [010] direction is reduced and the (101) facet disappears resulting in squares. Upon the continuous diffusion of adatoms to the squares, these will stack together and screw dislocations will emerge. Flowers will be generated from a multitude of squares in a small area due to curving within the nanoplate and colliding together. Additionally, will nanoframes and crystals with cracked surfaces develop at the center due to etching by produced HCl which will be detailed in Sections 5.2.2 and 5.2.3, respectively. This morphology development is summed up in an illustration in Figure 64.

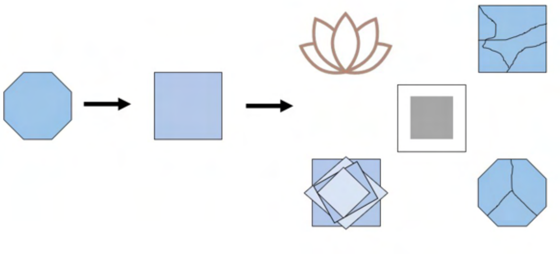

Figure 64: A proposed morphology development.

The octagons grew mostly at the substrate edges at a high density, before growing bigger towards the center accompanied by a decrease in crystal density. The reason for the growth location could be due to the precursor placement. $BiCl_3$ was placed at the substrate center thus there was a lower amount of atoms at the edges. This facilitated growth of octagons since this morphology is believed to develop under diffusion-limited conditions. Furthermore, the low concentration of precursor at the edge generated a high nucleation rate, but restricted growth. This is deducted from the observations of high crystal density towards the substrate edges but with a smaller size compared to crystals emerging further towards the substrate center. The squares developed closer to the center and in less quantity, probably due to a higher amount of precursor being available to diffuse to the crystal. This decreased the crystal density as the adatoms contributed to growth rather than developing new nucleation sites. Then flowers and nanoframes developed in the center with an abundance of precursor accessible. The crystals also exhibited non-uniform layering creating peaks at the center. These crystals displayed multiple colors on the crystal surface caused by this peak, as can be seen in figures in Appendix D.4. This can be caused by a higher concentration of precursor at the center, thus more BiOCl nanoplates are created here available for stacking on top of each other.

Most frequently the flowers were detected in the area of visible unreacted precursor. This can occur as a response to an excess amount of precursor, contributing to the growth of multiple BiOCl nanoplates which will migrate on the substrate. With an abundance of nanosheets on the substrate, there will be an inevitable increase in collisions and upon colliding with other nanosheets curvature is created which subsequently will generate flowers. This curvature process occurs after the nanosheets experiences microstrain within the sheets and in wet-chemistry methods, this occurs due to interaction with precursor ions, Cl^- and Bi^{3+}, which will curve the nanosheet. These curved nanosheets will collide with other curved nanosheets and thus grow vertical, and point upwards. An illustration of this mechanism is provided in Figure 66. This synthesis does not involve liquids thus the microstrain may occur, but at a smaller degree as the ions can not freely roam the substrate surface in an equal manner as in a liquid in wet-chemistry methods.

The distinctive growth and morphology trend on silica N was not discovered for the similar synthesis of 900W, 1 min, medium amount of precursor $BiCl_3$ and middle distance in the microwave oven performed at NTNU. Synthesis of Si-15.5cm, Si-1min, Si-900W, Mica-900W and Si-medium are all performed under equal conditions. There could be numerous reasons why that is; at NTNU a different precursor grade was used, a different microwave oven, a 10 nm thinner SiO_2 layer on the silica substrates and a different glass dish that may have had another height than the one used at UC Berkeley. Among these features, the precursor grade is deemed most likely to be the most influential due to the challenges described in Section 3.4.1.

Some similarities between synthesis at UC Berkeley and NTNU were detected. In all cases, more flowers emerged by increasing the microwave time. This supports the hypothesis that flowers are generated when squares are subjected to additional diffusion by increased microwave time. In addition to this, flowers emerged in areas where white unreacted precursor was visible on the substrate surface, which supports the fact that these structures are generated where there is an abundance of precursor. The enhanced nucleation and suppressed growth at the N silica edges caused by low concentration of precursor were also discovered for the NTNU substrates. Consequently, a high concentration would lead to enhanced growth which was observed for the NTNU synthesis where the largest amount of precursor generated the largest squares which can be seen in Section 4.1.8. Lastly, it was discovered at both universities that flowers typically grew on mica while squares and octagons mostly grew on silica. This could be due to differences between silica and mica. This will be discussed in Section 5.2.1.

The most noticeable variation between the synthesised crystals from the two universities was the differences in size. Silica N exhibits small crystals compared to the similar source substrates at NTNU. Additionally, it was detected less flowers on the NTNU substrates compared to silica N. This could be linked to the type of precursor used, see Section 3.2 and 3.3, where during operations in the glovebox it was noticed that the type used at NTNU was more coarse than the powder at UC Berkeley. This could indicate that the larger powder at NTNU took a longer time to decompose into the precursor ions thus it would take more time to initiate growth. Therefore, there were larger individual BiOCl nanoplates at NTNU that had not yet generated flowers. This could impact the size of the squares, explaining the larger analyzed crystals for the NTNU source substrates Si-15.5cm, Si-1min, Mica-900W, Si-900W and Si-medium.

Furthermore, for the NTNU source substrate it was discovered that crystals grew in much large quantity and clustered together on the edges of the mica and silica substrates, as can be seen in the analyzed SEM images in Appendix B. At NTNU the crystals grew on the substrate edges rather than close to the them, as it did for silica N. There are two reasons why that might occur, which are deduced in cooperation with experiments done by Jiayun Liang. Firstly, there is a higher quantity of dangling bonds at the substrate edges which enhances the chemical reactivity of the edges compared to any other area of the substrate surface. The dangling bonds will serves as active nucleation sites enhancing further nucleation. Secondly, the flow pattern varies across the surface, and turbulence may be more experienced at the edges than other areas. In literature the gas flow pattern of a CVD space-confined system is explained in detail, and some of the aspects could be considered for the space-confined system in this thesis. It is stated in Section 2.3.3 that a reduction of flow velocity induces a decrease in nucleation density and growth rate of deposited compound. At the substrate edges, the turbulent flow entails faster gas flow velocity which subsequently induces an increase in nucleation density and growth.

As initially hypothesized, there were less diffusion of atoms at the substrate edges. In a CVD system a mass-transport (diffusion) limited growth is preferred over surface-reaction limited for synthesizing high-quality, large-area 2D single crystals. The limited diffusion to the edges could also be the reason why there were observations of high crystal density at the edges for NTNU source substrates.

Lastly, the problems arising with the precursor placement and sticking was the biggest deviance in the synthesis at the various universities. This could have lead to precursor being more spread across the substrate at NTNU before microwave heating as explained in Section 3.4.1. The precursor slid off the substrate, but because of the quartz combustion boat edges it stuck at the substrate sides during heating. This would explain why there were more observations of crystals growing at the edges for the source substrates at NTNU compared to silica N. Thus, growth trends similar to the one discovered for silica N would be hard to detect and to either verify or refute with the difference in precursor grade.

5.2 Observed structures

Various structures and shapes were detected when using OM, SEM and AFM for characterisation of the source substrates. The creation and location of these will be discussed in this section, and an emphasis will be made in regards to the explained and discussed growth trend.

5.2.1 Squares, Octagons and Flowers

Among the different morphologies detected on the source substrates, squares, octagons and flowers were the most numerous ones. Squares and octagons were most frequently detected on silica substrates, while flowers were dominating on mica.

A feature with silica substrates that could influence the different crystal growth is the amount of dangling bonds. According to studies in Section 2.3.7 silica has dangling bonds at the surface as a result of surface silicon atoms remaining unbonded with unpaired electrons readily to form bonds. Because of these dangling bonds on silica, the substrate will then have a higher amount of reactive sites which will enable further nucleation and hinder free migration of adatoms thus obstruct growth. This corresponds well with the high density of octagons at the substrate edges and the smaller crystal size. This occurrence is unfavorable for growth of 2D materials, but favorable for 3D growth which is consistent with the 40-283 nm thick BiOCl crystals obtained on silica. These are not within the definition of 2D materials with a maximum thickness up to 10 atoms. Mica does not have any dangling bonds on the surface, which entails that there will be free migration of adatoms on the mica surface and there will be diffusion growth. This is advantageous as diffusion limited growth is favored for obtaining 2D materials. Hence, it is easy to grow 2D materials on mica, but the initiating nucleation stage is harder. This is because mica evidently lacks high-energy nucleation sites and has a lower absorption of reactants compared to silica, which is also supported in studies mentioned in Section 2.3.7. However, it is deemed plausible that mica also has some dangling bonds at the edges as it is observed a higher amount of BiOCl crystals here.

Additionally, because of the dangling bonds it is deduced that migration is more difficult on silica. This could be the reason why flowers are less detected on silica. A reduced migration could imply that it takes additional time for the atoms to merge with nuclei and form crystals. This initial growth stage is then slowed down and morphology development is delayed and the reaction could be stopped before flowers have the time to form. The obstructed migration could also entail that there will be less collisions of BiOCl nanoplates, thus less flowers are generated.

The reason for obtaining flowers on mica could stem from surface properties. Mica is cleaved into thin, elastic sheets ready to be used as substrates, but the cleaving process induced a negatively charged sheet surface. This negative charge could contribute to inducing microstrain within the

BiOCl nanoplates initiating the self-assembly process of flowers. Additionally will the negative charge on the mica substrate surface attract positively charged contaminating particles from the environment, where carbon compound is deemed the biggest contaminant such as CO_2, CO and CH_4. However, the exposure to ambient air for the mica in this thesis is relatively low, and just approximated to be max 10-15 min. The preparation of mica by cleaving in this thesis was normally done within 5-8 min in ambient air. Then the sheets were transported to the glove box where there was inert gas and then left in ambient air for maximum 1 min with precursor attached to it as detailed in Section 3. Thus, there was a restricted exposure time to ambient air which minimizes the contamination. The exposure time to ambient air for mica substrates could be an influential feature in this regard. For studies synthesizing crystals on mica surfaces the exposure time to ambient air may have been greater which evens out the surface negative net charge, and could then generate less flowers.

Generally, it is stated earlier in Section 2.3.3, that 2D material growth prefers atomically flat substrates with low roughness, as this will ensure free migration of atoms across the surface. This is because diffusion limited growth condition can be facilitated by reducing the substrate surface roughness. It is known that cleaving mica substrates in directions differing from the natural cleavage direction along the K ions in, shown in Figure 5, will form cracks. This can be seen in Appendix A, Figure 67, where it is obvious that the surface has deformities which could lead to higher surface roughness. These attributes of the mica substrate counteracts diffusion-limited growth which could lead to 2D material formation being less favored, and thus growth of clusters flower-like structures could be more favorable.

Additionally, from an energy perspective there could be reasoning for flowers growing predominantly on mica. Mica is an insulating material which entails that heat will be less easily transferred through the material. Therefore, as there could be a lack of energy conducted on the mica surface a more favorable structure could be one more clustered together, like the as-synthesized flowers.

To summarize, flowers could grow on mica due to growth of the nanoplates occurring faster, which leads to increase in collisions generating flowers. But it could also be due to more surface roughness caused by the cleaving method which will leads to less diffusion-growth thus 3D growth is more inclined to occur. Out of these, it is believed that the former reason is most likely. This is because squares were detected on mica, while octagons were not and according to the hypothesized growth mechanism squares were generated after octagons.

There are multiple studies presented in Section 2.3.7 using mica and obtaining nanosheets of 1 to 4 nm by CVD and 8.7 nm by a space-confined microwave-assisted method. These displays thinner crystals than those obtained in this thesis. This could be due to variations with the method in regards to set-up, precursors or other influential factors.

Composition Despite the dominating structures, both squares and flowers were discovered on both silica and mica. EDS was used on flowers and squares on silica substrates, in addition to an analysis of flowers on mica substrate. From the squares and flower-like structure on silica N it is clear from Figure 41b that there is no observable difference in elemental components. This is also supported in Figure 41d where the elemental mapping is consistently the same for both types of structures; squares and flowers.

The semi-quantitative elemental spectra for mica in Figure 44b compared to silica L in Figure 42c and silica N in Figure 41c displays some differences in each analysis. For mica L and silica L, the largest weight % stems from bismuth. Then oxygen, silicon, and lastly chlorine which gives the weakest weight %, when disregarding the impurities palladium and platinum for mica L and carbon for silica L. For silica N, there is a shift in this order where the most detected signal comes from silicon, then bismuth, oxygen, and lastly chlorine. The reason for silicon being detected at such high levels for the silica N in Figure 41a may have been because more of the substrate area was arguably incorporated in the EDS analysis, compared to the analyzed area of silica L, Figure 42a. A weaker silicon signal was expected for mica substrates compared to silica substrates, because of the chemical composition of mica where silicon is less significant as mentioned in Section 2.3.7. Despite the difference in highest weight %, the sequence of bismuth, oxygen, and chlorine remains the same for each analysis. Bismuth is detected more strongly than oxygen, which again has a higher weight % than chlorine. The lower detection of oxygen could be due to the problems with quantitative analysis in EDS for lighter elements as explained in Section 2.5.2. Oxygen has an atomic number of 8 and thus can be categorized as a lighter element. It is significantly lighter than bismuth ($Z = 83$) and chlorine ($Z = 17$). Furthermore, as EDS is a more insensitive analytic method it will detect heavier elements at a higher limit as specified in Section 2.5.2. These heavier elements as categorized as using L or M lines which is the case for bismuth. This could be the reason why bismuth is detected as such high levels, while oxygen at low levels. However, the reason for the low detection of chlorine still remains unknown.

Despite this deviance, the EDS analysis indicate that square crystals and flower-like structures have the same composition, see Section 4.2 which is also supported in literature in Section 2.4.5 where it is stated that flower-petals are BiOCl nanoplates conglutinated at the center.

To further investigate the composition, Raman analysis was carried out of flowers and squares on silica substrate in addition to an analysis of flower on mica substrate.

The Raman analysis done at UC Berkeley of flower-like structure on silica F and square on silica N was performed to give a basis of comparison and check for any variation in composition between the two morphologies. From Figure 51b and Figure 53 it is clear that the spectres share similar peaks, with only small differences in values. The similarity in Raman peaks supports that there are no differences in composition between the two morphologies, and the small observed variations could be caused by stress states within the material [188].

As there were no compositional differences between flowers and squares, a Raman analysis was performed at NTNU of flower on mica and square on silica. This was done in order to see if there were any differences between a structure grown on mica compared to one grown on silica. The Raman spectra of BiOCl flower on mica F seen in Figure 58 has peaks which corresponds well with the Raman bands discovered for the BiOCl square on silica D seen in Figure 56. Weak Raman peaks at around 200, 300 and 400 cm^{-1} could also be observed for silica D analysis in Figure 56b. Disregarding the Raman bands corresponding to the individual substrates, this indicates that there are no significant differences in composition between BiOCl grown on mica and silica. Furthermore, the NTNU Raman analysis supports the findings from the UC Berkeley analysis, that there is no difference in composition between flowers and squares.

Additionally, the NTNU Raman analysis of silica D was done in order to compare and explore for any deviance from the silica N analysis done at UC Berkeley, where both analyses are done on squares. The most distinguishable difference is the peak at 84 cm^{-1} which appears clearly in the silica D spectra from NTNU in Figure 56, while in the silica N spectra in Figure 53 from UC Berkeley there is no indication of a peak at this value. The peak is linked to the Raman signal of BiOCl, and it may not appear in the UC Berkeley analysis due to instrumental parameters. Instrumental parameters could give rise to small differences as various equipment and settings were used, as detailed in the Section 3.9. Except for this Raman band, the two analyses display similar peaks at approximately the same values suggesting that there is just one distinguishable difference between the analysis performed at the two universities.

Both morphologies on either substrates were consistent with modes from the Bi-Cl bond and oxygen motion in BiOCl. Thus implying that there was no compositional differences detected by using either substrates for synthesizing BiOCl flowers and squares. Furthermore, the lattice constant c calculated for silica equal to 0.7382 nm and mica equal to 0.7379 nm, is approximately consistent with the one for the BiOCl database equal to 0.7349 nm, indicating that BiOCl was successfully synthesized on the two substrates in this thesis.

Crystallinity As flowers were discovered to be dominating on mica while squares and octagons detected in abundance on silica, it could be likely that a silica XRD analysis may give insight into the square and octagon structure and an XRD analysis of mica may do the same for flowers.

XRD analysis of silica and mica showed an exceedingly large intensity for the (001) facet compared to the database BiOCl meaning that there is a preferential orientation of (001) planes. This is plausible considering that BiOCl squares and octagons are most likely constructed by (001) planes on top an bottom sheet as mentioned in Section 2.4.1. The large exposure of (001) facets is aligned with the fact that the [001] growth occurs more rapidly than [110], because (001) have a higher density of oxygen atoms as explained in Section 2.4.5. The BiOCl (001) facet also grows faster because it has the highest surface energy and thermodynamic stability which is linked to faster growth. In studies presented in Sections 2.3.1 and 2.4.5 involving organic compounds, specifically glycerol, dulcitol and mannitol, these were discovered to suppresses anisotropic growth in the [001] direction. This was done by steric hindering the growth due to the compounds binding to the oxygen rich (001) facets, thus in these studies the most prominent growth direction was [110]. Furthermore, as there are no organic compounds utilized in the synthesis the [001] growth direction was not suppressed.

Because of the advantageous photocatalytic activity of the (001) facets, multiple and strenuous effort have been made in order to synthesize BiOCl with high exposure (001) in a controlled way. It is mentioned in Section 2.4.1, obtaining an (001) oriented BiOCl can be achieved by low concentration of precursor ions Bi^{3+} and low pH value in a hydrothermal approach. Disregarding the difference in approaches, if the same conditions applied for the solid-state decomposition occurring in this thesis it could explain why there is high exposure of (001) plane in the as-synthesized BiOCl. In this thesis the concentration of Bi^{3+} were kept lower than Cl^- due to the ratio in the precursor $BiCl_3$. Additionally, with the difficulties with attaching the precursor to the substrate there is a likelihood that only a small precursor amount stuck. As for the lowering of pH, in the synthesis reaction HCl is a byproduct, see reaction in Equation 1 which will lower the pH value during heating.

On silica the (110) facet is measured at an intensity exceeding the database intensity, while on mica it matches the database. This means that there is more exposure of the (110) facets of as-synthesized BiOCl on silica compared to a standard random oriented sample of BiOCl. This can be because there are octagons present on the substrate. Octagons develops if the growth direction along [110] is approximately equal to [100] direction, and squares are formed if [010] growth direction is either stopped or reduced, and the (101) facet disappears as detailed in Section 2.4.1. The shape and facets of octagons are proposed in Section 2.4 in Figure 7 where the vertical edge plane gets a tilt before reaching the top compared to the facets in a square where the tilt is less obvious. In this thesis there was no measurement or imaging done to confirm the facet, but this shape and tilt can be seen in thickness profiles of octagons by using an AFM in Section 4.3. In the thickness profiles of squares, this tilt is less apparent. Based on these AFM results, the facets of octagons and squares will be assumed equal to the hypothesized structure in Figure 7 [123].

Furthermore, it is stated in Section 2.4.5 that that growth of BiOCl structure in the [110] direction would result in thinner and larger crystals. This is supported in this thesis where the squares and octagons with enhanced exposure of (110) facets had a thickness range of 40 - 169 nm from AFM analysis in Table 8. While the as-synthesized flower petals with no enhanced exposure of (110) facets had a thickness of 280 - 480 nm, which can be seen in the size distribution analysis of mica in Figure 34. Thus, the BiOCl flower petals grown on mica are thicker than the BiOCl squares and octagons grown on silica. This is also supported in the XRD analysis of the two substrates which shows peak broadening for the BiOCl on silica indicating smaller particle size at this substrate in Figure 63. This indicates that the squares and octagons are thinner and smaller. The narrow peaks of mica imply that the flowers are more well-crystallized.

The preferential growth of as-synthesized BiOCl flowers along [001] direction is contradicting of studies presented in Section 2.4.5 which claims that the intensity ratio of (110)/(001) facets are higher for BiOCl flowers than nanoplates, meaning that the flowers grow in the [110] direction. This is not the case for the flowers grown on mica in this thesis, which are found to grow mostly in [001] direction. The more exposed (001) facets in the as-synthesized BiOCl flowers compared to the BiOCl flowers mentioned in literature could be due to no use of organic compounds. It is also reported in literature that if growth along [110] direction is preferred over [001] direction, the resulting crystals are thinner and larger. Studies reports BiOCl flowers grown in [110] direction as having a nanopetal thickness of 10, and 17 - 23 nm, which is much thinner than the nanopetal thickness for as-synthesized BiOCl flowers in Figure 34 with a range of 280 nm to 480 nm for Mica-750W and Mica-900W with preferential orientation of (001) facets.

Furthermore, in literature it is stated that BiOCl with crystal oriented along the (110) plane will have a smaller band gap than those oriented along the (001) facet. In literature it is mentioned that BiOCl flowers have smaller band gaps compared to BiOCl nanoplates due to higher exposure of (110) planes, and in this thesis this might not be the case as squares and octagons exhibit more exposure of this facet compared to random-oriented BiOCl sample while flowers exhibited approximately the same exposure as the BiOCl sample. Thus, it could indicate that the synthesized BiOCl squares and octagons have a smaller band gap than database BiOCl and flowers all due to higher exposure of (110) facets. Therefore, it would be interesting to conduct band gap measurements.

For flowers with high exposure of (001) lattice plane the band gap is measured in various studies to be 2.7, 2.87 and 2.92 eV. Flowers synthesized in this thesis is believed to have a larger band gap due to more exposed (001) planes than (110) facets. Thus, it would be of interest to measure the band gap of as-synthesized BiOCl flowers and compare it to literature values. Nevertheless, the photocatalytic activity is expected to exceed BiOCl nanoplates. This is due to the large BET surface area, high phase purity and thin structure which have multiple reflection within center of structure of flower, charge carriers move faster from center to surface to participate in redox reactions at the surface.

Despite the differences, it is deemed likely that the as-synthesized BiOCl structures have a better photocatalytic activity than database BiOCl due to the increased exposure of (001) facets. However, simulated XRD pattern for database BiOCl and the observed intensity differences is not sufficient enough to directly relate to facet exposure. It can indicate higher facet exposure, but a Rietveld refinement should be carried out in order to deduce the reason for the measured intensity with a higher accuracy as the method takes other factor into account such as sample displacement.

With both the visual and structural confirmation from SEM, and compositional confirmation from both EDS and Raman analysis squares and flower-like BiOCl structures with high exposure of (001) facets have been synthesized in this thesis. These photocatalytic advantageous structures were synthesized without utilizing organic surfactants and templates, as most studies and methods relies on. Thus this method eliminates the use of toxic organic solvents making the synthesis of flowers with exposed (001) facets more environmental friendly.

Additionally, the method presented in this thesis could then have the potential as an alternative strategy to replace the hydrothermal process which is commenly used to obtain BiOCl nanoplates with exposed (001) lattice planes as mentioned in Section 2.3.1 [177].

Thickness, size and color It is hypothesized that the octagons develop when there is a scarcity of precursor, while squares grows when there is a sufficient amount. From the synthesis analysis in Section 4.1.8 it is clear from the size distribution in Figure 36 that squares grew to the largest size with the excess amount of precursor, but for octagons the result are more inconclusive.

Regardless of the crystal length, it is clear from the thickness of both octagons, nanoframes, and squares in Table 8, that they are all considered 3D structures as the thickness exceeds one unit cell as defined for 2D materials in Section 2.1. The thickness is consistent with other synthesis studies which also fabricated thicker crystals, where 2D BiOCl was layered together to form these plates, see Section 2.3.5. To be able to get single layers, further processing needs to take place, for instance with methods such as micromechanical exfoliation explained in Section 2.1.

However, there are some differences within the morphologies. It was noticed that small octagons, size of 3-7 µm had a thickness of 70-160 nm, while the large ones were 12-13 µm with thickness of 40-170 nm. Thus from this, it does not seem that crystal size and thickness are correlating, and small octagons can be as thick as larger ones. These results are also supportive of the OM observations that there were no change in color scheme for octagons despite different sizes. This could be because these structures were mostly located at the substrate edges where there may have been more uniform layering of the nanoplates due to generally less precursor. This can explain the lack of thickness variation, and this may suggest that there is more uniform growth towards the edges where nucleation is favored above growth. For the square morphology the small squares were 11 µm with thickness of 153 nm and the nanoframes were 17-24 µm with average thickness of

40 nm. Both the average thickness and frame thickness are significantly thinner than the smaller squares. This indicates that the further away from the substrate center the thicker the squares.

The crystals located at the substrate center consisted of multiple colors, where each crystal exhibited 2 or more colors on its surface. It was discovered in the AFM that squares of this type had either a peak at the center or displayed a nanoframe-like structure. The peak can be linked to non-uniform stacking of plates or BiOCl nucleating on already synthesized squares as a template. This could due to more precursor situated at the substrate center, which will facilitate more growth of BiOCl nanoplates. These nanosheets will stack together creating layered structures and if the growth of BiOCl nanosheets are inhomogeneous, the stacking could create structures with peaks. Thus, observation of these squares with associating peaks could indicate that growth of BiOCl squares had been exceeded and prolonged into the next growth phase.

A thickness analysis was performed on different colored squares, as it was hypothesized to be a link between observed color in the OM and thickness. Values from Table 9 can indicate that the thickest crystals are associated with a blue color. This is supported by the fact that the yellow and red crystal is thinner than the yellow, red, and blue crystal. Thus, by exhibiting a blue color the measured thickness increased. All the large squares in Table 8 are known to be grey which can be observed in the captured images in Section D and by observations of nanoframe-like structures in the OM. Therefore, the grey color can be associated with the average thickness of these large squares which is calculated to be 39 µm. This thickness bears more resemblance to one of the yellow squares, and is a great deal thinner than the other colors analyzed. This is reasonable as these structures were observed in the SEM to have an elevated edge, thus a thinner center is expected.

The yellow and red square had a peak at the center, which can be seen in Appendix D.4, Figure 85 and the center is linked to a red color. A peak in the center is also seen in the blue, red, and yellow square in Appendix D.4, Figure 89b where it can also be seen that the center is blue.

There is a deviating thickness value for both the two yellow squares analyzed and the two blue squares. In Appendix D.4, Figure 88 the yellow square had a thickness of 45.4 µm displaying a thickness profile similar to the nanoframe-like structures with an elevated edge. This is not occurring for the other yellow square displayed in Appendix D.4, Figure 83. However, for this yellow square there are red-colored spots throughout the surface. This color is also detected in the Zsensor image where there are certain points measured as thicker. These discrepancies may imply that the analysis needs more measurements in order to get a reliable average, where the colors can be at a higher accuracy associated with a certain thickness range. Though blue is seemingly linked to a heightened thickness, whether it is covering the whole surface or at the center forming a peak.

Generally, it seems that whenever the crystals are composed of more than one color it is accompanied by a peak at the center, or a nanoframe-like thickness profile. These crystals were mostly noticed at the center of the substrate for silica N explained in Section 4.1.9.

5.2.2 Nanoframe

The thickness analysis of the nanoframes in Appendix D.4 supports the connection between the OM observations of the darkest grey colored squares also had the most elevated frame, thus exhibiting a larger difference between frame and center. This is in accordance with various studies mentioned in Section 2.4.3 which synthesized nanoframes by a facet-targeted etching by using HCl [138, 139, 140, 134]. In the reaction used in this thesis of precursor $BiCl_3$ to the product BiOCl as seen in Equation 1, HCl gas is produced as a byproduct. Therefore, this HCl gas could be the facilitating condition that induces etching of the observed nanoframe-like structure and this is illustrated in Figure 65.

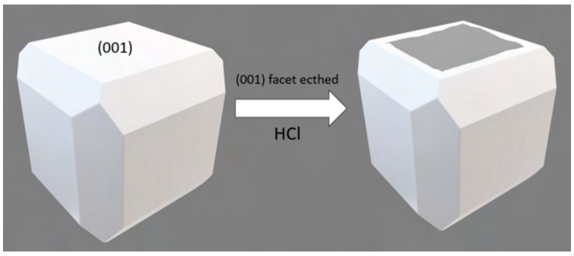

Figure 65: Proposed mechanism of nanoframe development.

The (001)-Cl plane exhibited the highest thermodynamic stability of the BiOCl facets, and this facets is exposed when cleaving along the nonbonding interaction site illustrated in Figure 4 given in Section 2.2.3. This (001) facets has the highest surface energy, as mentioned in Section 2.4.1, thus this is arguably the facet most prone to etching. This is because the most vulnerable sites to etching are the ones with the highest energy, see Section 2.4.3.

The location of these structures are also interesting, as in Section 4.1.9 the growth trend on silica N is explained and grey, large squares are only observed at the center of the substrate and in a large quantity. On other parts of the substrate the crystals exhibits a vaster range of color. The average thickness of these grey nanoframe-like structures are 39 µm which is distinctly thinner than all the colored squares presented in Table 9. Therefore, it can be deduced that if the carved out crystal is caused by produced HCl the concentration of this compound is higher at the substrate center where these structures were found. This can also be linked to the effort in placing the precursor $BiCl_3$ in the middle of the substrate, as mentioned in Section 3, thus the reaction will occur here and generate HCl. Thus there is a substantial etching at the substrate center compared to edges, and as the thickness is reduced the color palette changes.

5.2.3 Surface cracks

Cracked surfaces can be clearly detected and exhibited in Figures 46a and 50a.

The HCl byproduct of the decomposition reaction, Equation 1, that was hypothesized to cause etching of nanoframe-like structures in Section 5.2.2 could arguably be the cause of the cracked surfaces based on knowledge from Section 2.4.4. This occurs as etching induces physical stress within the crystals.

In Section 2.4.4 it is described that rounder shaped crystals (tuncated corners) experienced radial cracks while more random crack formation occurred on square shaped crystals (un-truncated corners). For the square shaped crystal a progressively longer reaction time would increase the crack size until the crystal was completely etched away and this type of cracks is displayed in SEM Figure 20a, OM Figure 38j square No. 3 and 5 and AFM Figure 46a. The possible etching by the produced HCl could also be an influencing factor for the formation of radial cracks that can be seen in SEM Figure 20b and the AFM Figure 50a. However, since the radial cracks appears differently it is also proposed in the Section 2.4.4 that air bubbles could be an additional influencing factor. This reasoning is not applicable for this thesis as no air stream was introduced to the synthesis, and as radial cracks are energetically unfavorable there must be an external factor that causes these to emerge. However, the HCl produced and hypothesized to be causing the etching exists in gas phase. Thus similar to air bubbles these HCl gas bubbles may induce the physical stress needed to get radial cracks.

5.2.4 Stacked structures

Various stacked structures were detected and some were observed as having a cross-like shape, star shape or screw dislocation.

In Figure 22, the star-shaped, cross-like and layered structures are displayed. These can all be a results of either uniform plates stacked randomly, or non-uniform plates stacked together creating a peak at the center. This is a consequence of lowering the total surface energy during growth, which is the driving force of stacking structures together. It is believed that these stacked structures occur at places where there is an excess of precursor as they were often observed at the substrate center. Larger amount of precursor thus more precursor ions contributing to growth rather than nucleation. Thus forming new nucleation sites is less emphasised therefore it is favorable to continue growth on already synthesized crystals.

Additionally, stacking of the structures increases with increasing time according to growth mechanism of wet-chemistry methods detailed in Section 2.4.1. This observation in wet-chemistry methods could be considered for the purpose of explaining the occurrences of stacked structures in the solid-state decomposition in this thesis. Thus if the irregular shapes are indeed a result of non-uniform stacking, an increase in microwave time could induce more irregular shapes as increased stacking will occur after growth of square BiOCl nanoplates have been completed. This can be seen for Si-5min which reportedly have irregular shapes, cracked crystals and flower formation.

In addition to these, there were observations of circular structures as seen in SEM and OM deemed to be unreacted precursor as seen in Figure 23. As well as irregular spots displayed in Figure 23d. These were mostly found at the center of the substrate, thus supporting the assumption that this is unreacted precursor. A study in Section 2.3.5 emphasises that substrates should be put under running water to ensure removal of unreacted $BiCl_3$. This was done in the thesis, but arguably not at a sufficient level.

Screw dislocations occurs under weak supersaturated conditions which can be seen in correlation with the abundance of precursor at the initial stage versus final stage of the microwave heating. Thus by increasing microwave time consequently there will be a decrease of precursor concentration towards the end of the heating, in likelihood more so on 5 min than 1 min. Therefore, if the heating is stopped before this weak supersaturated condition occurs there will be few or no screw dislocations observed. However, for the UC Berkeley substrate silica N heated for 1 min there were observations of multiple screw dislocations at the center of the surface in the vicinity of flowers and is displayed in Figure 21b. Therefore, stopping the microwave time at 1 min does not prevent formation of screw dislocations. This may be considered in view of the induction period and reaction kinetics explained in Section 2.3.6. Since the induction period of $BiCl_3$ decomposition to BiOCl via $BiCl_3 \cdot H_2O$ takes 622 min in room temperature, the increased temperature when irradiating the precursor with 900 W could be enough to reduce the reaction time vastly thus a microwave time of 1 min could be enough to get unwanted screw dislocations.

5.3 Synthesis conditions

Various synthesis parameters were changed throughout the synthesis scheme in this thesis. In addition to the alternated parameters, there were some growth conditions that were consistent during the scheme which also influenced the resulting crystals in different ways. In this section the impact all these parameters and growth conditions had on crystal growth will be discussed alongside theory-based arguments and discoveries from different studies presented in the theory section.

5.3.1 Microwave time

Microwave time was investigated with the substrates; Si-1min, Si-3min and Si-5min. This parameter was investigated in order to see how the change of microwave time influenced crystal growth. As explained in Section 4.1.3, the Si-1min resulted in the biggest crystals of either morphology, see Figure 27. This could mean that 1 min is sufficient time for nucleation and growth.

The biggest take away from the microwave time parameter was that by increasing time there was more formation of flowers and irregular shapes, smaller squares and octagons. No conclusion could be deduced from the density for the three substrates, which could indicate that the microwave time mostly influenced crystal growth.

For the Si-5min there was noticed flower formation which were not registered on Si-3min and Si-1min, except for flower growth on a circular shaped crystal on Si-1min. This supports the hypothesis that by increasing microwave time, this could lead to further formation of flowers and a subsequent decrease in BiOCl nanoplates as these are the components of nanopetals in flowers. In literature, this was discovered to be true in a hydrolytic synthesis where by increasing reaction time the amount of flowers increased, parallel to a decrease in nanosheets [143]. This is based on the fact that flowers are a result of a self-assembly mechanism by the BiOCl nanoplates. Therefore the reaction process should be stopped before this mechanism occurs. This is illustrated in Figure 66 where the BiOCl nanoplates are curved over time, collides with other nanoplates and grows vertically clustered together.

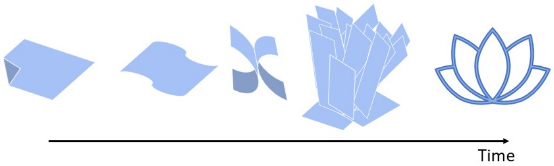

Figure 66: A proposed flower formation mechanism.

Additional to flower formation, there seems to be a threshold where the growth of the crystals will be impacted in a negative way and start forming irregular shapes, denoted with an ”X” in substrate section 2 on Si-5min in Table 2. The irregular shapes noticed for Si-5min could be non-uniform stacked structures or screw dislocations. These structures are believed to occur more often upon increasing the microwave time beyond the time it takes to synthesis BiOCl crystals. This is also supported by findings done by Kang et al. in Section 2.3.5 specifying a maximum microwave time of 5 min if the aim is to get uniform square crystals. Thus, to avoid irregular shapes and to obtain uniform larger-sized crystals a microwave time of 5 min should not be utilized.

The Si-5min and Si-3min parallels also generated relatively small crystals compared to Si-1min. This can be due to the larger crystals are clustered together and forming flowers. It could be that by increasing the microwave time, this will give the synthesized BiOCl time to migrate more on the substrate surface which will eventually lead to collision with stacked structures or other BiOCl sheets which can cause curvature within the sheets ultimately creating flowers. Therefore, to obtain large-area crystals it is crucial to stop the microwave time after growth has come to a satisfying limit, and the results indicate that this limit is at 1 min.

5.3.2 Distance

The distance in the microwave oven was investigated with the aim of studying how this would affect the crystal growth. This was done as literature states that conventional microwave oven has a nonhomogeneous heating problem where location, size and geometry of the load could impact the operating frequency, detailed in Section 2.3.4. As the other influencing factors i.e size and geometry of the system were kept constant throughout the synthesis scheme, only location of the system and its influence on crystals growth was investigated.

The most important results from changing the distance from the magnetron was that Si-15.5cm generated biggest squares and more well-defined shapes compared to Si-21.5cm which resulted in most irregular shaped crystals. Regarding the density, this was somewhat equal throughout the three parallels, however Si-9.5cm had slightly more crystals than Si-21.5cm and Si-15.5cm.

From literature it is stated that the highest temperature rising rate is at the center of a microwave oven, then the position furthest away from the magnetron exhibited 28% of center rate. Lastly, the position closest to the magnetron had the worst temperature rising rates with only 6% of the center rate as described in Section 2.3.4. This is believed to influence the growth as higher temperature rising rates will give a rapid heating and thus decreasing the reaction time making it transpire faster.

From the Table 3 the Si-9.5cm in total has the most crystals then Si-15.5cm and lastly Si-21.5cm, although there is not a huge difference. The observed higher count of crystals on Si-9.5cm indicates that this substrate had a higher nucleation rate and thus generating more crystals than Si-15.5cm and Si-21.5cm. In light of temperature rising rate this location has the worst merit.

Both Si-15.5cm and Si-21.5cm possesses higher temperature rising rate than Si-9.5cm, while also having less crystals thus lower nucleation rate. This could entail that a low nucleation rate accompanied by higher temperature rising rate could result in enhanced growth rather than multiple nucleation sites. Meaning that the rising temperature contributes to growth rather than further nucleation. By this reasoning, Si-15.5cm which exhibits the highest temperature rising rate should have the least amount of crystals, but have the largest crystals. From Figure 29 it is evident that Si-15.5cm had the largest crystals, supporting this reasoning, but Si-15.5cm did not have the least amount of crystals. However, both Si-15.5cm and Si-21.5cm had less crystals than Si-9.5cm while exhibiting a higher temperature rising rate, which supports said reasoning. Additionally by the reasoning, Si-9.5cm should have the smallest crystals as this position has the highest nucleation rate and lowest temperature rising rate, and this is not consistently true as can be seen in the size distribution in Figure 29.

Reportedly, the crystals at Si-21.5cm had more irregular shaped, cracked and non-uniform stacked crystals, whilst on the middle position Si-15.5cm displayed sharper, more well-defined squares. This can also correlate to the temperature rising rates which gives fast nucleation then subsequently growth. A low rate gives insufficient growth because the nucleation stage dominates the time frame. While a high rate in the center position gives fast nucleation and thus sufficient time for growth of well-defined squares as there is enough time for diffusion of atoms to the crystal. Thus, from these results the preferred location for large-area, well-defined squares is 15.5 cm from magnetron, or center position.

5.3.3 Microwave power

By changing the microwave power, there was some aspects of the results that were interesting. The Si-900W exhibited the largest crystals. However rather unexpectedly the Si-750W had the smallest crystals but the most uniform size across the substrate. Regarding density, the Si-500W had the most crystals detected in the analyzed images.

Microwave power is believed to be linked to decomposition rate of the precursor. The precursor $BiCl_3$ will immediately start to form the intermediate hydrate $BiCl_3 \cdot H_2O$ when exposed to air, and the subsequently decomposition to BiOCl will take 622 min at room temperature, as explained in Section 2.3.6. Thus by increasing the microwave power this reaction will most likely occur more rapidly.

By comparing the sizes the distribution in Figure 31 for the three parallels it is evident that the Si-900W one exhibits the largest crystals of both morphologies. This can indicate that an increasing microwave power is linked to rapid precursor decomposition, which will induce nucleation faster which subsequently will promote growth of the nuclei.

By this reasoning a low microwave power is linked to a slower reaction rate, thus the nuclei will have less growth, hence the 500 W parallel should have the smallest crystals. However, the smallest crystals is measured for the 750 W parallel, which can be caused by systematic errors or errors with the precursor. In addition to generating largest squares, the 900 W microwave power setting resulted in sections without octagons/circles. This could be because the rapidness in precursor decomposition will lead to fast nucleation and growth, therefore diffusion of other atoms to the octagons may happen such that these grow in to squares. This implies that if the aim is to synthesize large-area squares the 900 W is favorable.

The study by Kang et al. in which the synthesis scheme in this thesis is based on, produced square BiOCl of edge size up to 10 µm by microwave settings of 1-3 min, 700 W and center placement [6]. Thus, this can be compared with the Si-750W produced with a microwave time of 1 min. From the size distribution of squares on Si-750W in Figure 31, the produced square BiOCl had edge size of 1.3 to 1.7 µm, and by this exhibiting much smaller squares. The crystals produced by Kang and colleagues were produced under similar set-up and conditions, although the precursor type is not specified and neither is the microwave time that ultimately lead to the 10 µm sized squares. Kang et al. reported microwave time to be crucial for the resulting crystals, and in this thesis it seems to also be an indication that the precursor type is significant. Thus, these factors could be the reason why there was such a deviance between size of crystals produced by Kang et al. and produced on Si-750W substrate.

5.3.4 Mica with power change

The mica synthesis gave the most distinctive crystal growth by having a predominance of flower-like structure and rarely observations of square crystals. Furthermore, the most striking outcome of this parameter is that Mica-500W had no flowers while this structure was prominent on Mica-750W and Mica-900W. Furthermore, Mica-750W had more clumpier petals than Mica-900W, and generally on Mica-500W there were few crystals detected.

It is not reasonable to compared the crystal sizes of the silica microwave power synthesis to the mica one, because of the difference in synthesized morphologies.

Throughout there is a high inconsistency for the morphologies on Mica-500W and few squares were detected and no flowers. It is stated that there were white powder visible on the substrate surface which could be the reason why there was so few crystals. For a microwave power setting of 500 W this could have been insufficient for decomposition of the precursor. This can be argued from an energy perspective. Mica is an insulating substrate which will entail that this material has a higher specific heat capacity making it more time consuming to raise the temperature of the material as heat transfers slowly in material. In a microwave oven the heat is generated from movement by aligning and realigning the dipoles to an external electric field in a material. This will increase the heating of the mica, but the heat transfer and temperature increase in the overall substrate could take a longer time than for conductive materials. This can imply that for mica there is a need for a high energy input in order to facilitate growth of 2D crystals, thus the 500 W could be inadequate and that is the reason for the irregularities observed on this substrate. It is also known that mica it is more difficult to initiate nucleation on mica because it evidently lacks high-energy nucleation sites and lower absorption of reactants compared to silica. Furthermore, the unreacted precursor visible on the surface could be a verification of this. It could also be the reason why there was less growth on the edges of Mica-500W compared to Mica-750W as displayed in Section 4.1.7 in Figure 32.

As flower-like structures are composed of BiOCl nanoplates, the Mica-750W and Mica-900W has arguably more of the nanoplates than Mica-500W. Which is also attributed to the insufficient nucleation on Mica-500W due to inadequate power.

Furthermore, there is a considerable difference between the flower petal thickness for Mica-750W and Mica-900W. Mica-750W has 0.35 to 0.43 µm while Mica-900W has 0.28 to 0.48 µm thick petals. The measured thickness of as-synthesized flower petals for both Mica-750W and Mica-900W are significantly larger than from literature which reported 10 nm on Si substrates and 17 to 23 nm on L-Lysine templates in Section 2.4.5. Upon reducing thickness of any nanostructure there will be an increase in surface energy for the nanosheets which makes them thermodynamically unstable. This is the reason for the sheets stacking together in a layered structure, which decreases the total surface energy. By using mica in this thesis there will be less energy transferred on this insulating material, thus there will be a greater effort of the BiOCl sheets to stack together in a thicker layered structures. These thick, layered nanoplates will become the nanopetals in the as-synthesized flowers. This could be the reason why the nanopetals are much thicker than for conducting Si substrate or by wet-chemistry method using L-Lysine as template.

Furthermore, this energy reasoning could explain the distinct difference between the design of the flower petals, where Mica-750W has clumpier petals while Mica-900W has sharper, more well-defined petals. Although the Mica-750W petals reportedly has a smaller thickness range, the sharpness of Mica-900W petals would most likely be preferred as it is more well-defined with a smoother surface.

5.3.5 Amount of source

The change in amount of source was done because of majority of flower observations where in areas with visible unreacted precursor on the substrate surface. Additionally, with less flowers there were more squares observed in the Specialization Project [1]. Because of this is was believed that an excess amount of precursor lead to more flowers and consequently less squares. For the result in this thesis from this parameter change it was concluded with Si-large being favorable for growth of large squares and octagons. Generally, there were a lot of vacant spaces for both Si-small and Si-large despite the amount of precursor.

It was believed that an excess amount of precursor $BiCl_3$ would generate more areas where it was not possible to detect crystals because of unreacted precursor as seen in Appendix, Figure 72. However, a connection between large amount of precursor and unreacted precursor was not made. This is because unreacted precursor was observed randomly for NTNU substrates, while consistently using a medium amount of precursor. Furthermore, the elemental mapping of silica N by EDS shown in Figure 41d, shows that both bismuth and chlorine are detected at the silica N substrate surface. This could be due to residues of the precursor $BiCl_3$ or more likely the intermediate hydrate $BiCl_3 \cdot H_2O$, as the precursor is easily hydrolyzed, that has not grown into a crystal. A medium amount of precursor was also used for the silica N synthesis.

From theory in Section 2.4.5, increasing the amount of precursor NaCl induced an increase from 30 nm well-defined BiOCl nanosheets to 60 nm large BiOCl nanoplates with a thickness of 10 nm. Furthermore, in Section 2.2 it was discovered that an excessive concentration of Cl source increased the width and thickness of BiOCl crystals to a large degree, while for the opposite case of insufficient Cl source there would be irregular shapes. From this it was deduced in literature that the perfect precursor ratio of Bi and Cl was 1:1, and this obtained 3-7 nm thick BiOCl 2D nanosheets preferential for photocatalytic performance. Upon comparison with thicker BiOCl nanosheets these 3-7 nm thick BiOCl nanosheets displayed an increased degradation of Rhodamine B (RhB) under visible light.

As the precursor used in this synthesis has a Bi:Cl ratio of 1:3, there is sufficient Cl for growth, and this could result in larger and thicker crystals. This can explain why the Si-large exhibits the largest squares of around 20µm in the size distribution in Figure 36. Additionally, it could explain the AFM measurements for the 11-24µm large squares with thickness of 40-153 nm and 3-12µm large octagons exhibiting a thickness of 70-158 nm. The synthesized crystals in this thesis are thicker than the 3-7 nm thick BiOCl nanosheets generated by 1:1 precursor ratio. In addition to this, there could arguably be insufficient Cl source compared to Bi source which could cause the irregular shapes detected at various source substrate that visually had the same amount of precursor.

Literature study stated that an increase of precursor BiI_3 lead to a rise in collision frequency of the molecules within the confined space, and this subsequently increased the amount of absorbed precursor. However, the favorable conditions for 2D nucleation and growth was low concentration [89]. This is based on the fact that diffusion-limited kinetics can be facilitated in a confined space by uniformly distributing the reactive species by reducing the concentration [94].

On the opposite spectrum, in literature by a hydrothermal approach it was noticed that a low concentration of Bi^{3+} formed nuclei with suppressed growth, thus generating small nanocrystals that would assemble into granular structure with higher percentage of (001) facets favorable for photocatalytic activity. The Si-small did not create the smallest squares or octagons out of the three parallels, but has smaller squares than Si-large. Furthermore, in literature in Section 2.4.5 with a low amount of NaCl source, well-defined BiOCl nanosheets were synthesized by a wet-chemistry approach. However, for this thesis this was not the case as a low amount of $BiCl_3$ generated squares with a rounder shape. This could be because the literature studies were wet-chemistry methods which can differ in growth mechanism from a solid-state decomposition like the one in this thesis. It can also be because the precursor used in the studies was NaCl and bismuth source was bismuth nitrate pentahydrate, $Bi(NO_3)_3 \cdot 5\,H_2O$. $Bi(NO_3)_3 \cdot 5\,H_2O$, giving a ratio of Bi:Cl equal to 1:1 which was deemed the favorable ratio for 2D growth.

By looking at the Table 6 it is obvious that there are few crystals detected for parallel with a large amount of source. For the parallels with a small amount and medium amount of source there were more crystals. However, since it was extra difficult to attach the precursor in these parallels it is hard to deduce any reasoning behind the density occurrence.

Thus, theory states that a low concentration is favorable for growth of 2D crystals and with an increase in amount of precursor the resulting crystals would become larger. As it is true in this thesis that the largest amount of precursor generated the largest crystals, if the aim is to synthesis large-area BiOCl the deduced conclusion is that an abundant of precursor is seemingly favorable.

5.3.6 Precursor treatment

The issues with attaching the precursor as detailed in Section 3.4.1 could possibly stem from the precursor only being exposed to air for a maximum of 1 min. From an ongoing experiment done by Jiayun Liang the preliminary results shows that 6 min exposure time to ambient air results in the precursor $BiCl_3$ sticking better to the substrate while keeping below the acceleration limit of the reaction where precursor form the intermediate hydrate $BiCl_3 \cdot H_2O$. This limit is 8 min, as stated in Section 2.3.6. In this thesis the exposure time of precursor to ambient air before microwave irradiation was 1 min, which could then be an influential feature that lead to the precursor sliding off the substrates when creating the confined space by stacking them together.

When the precursor did not stick to substrate at the center, where it was originally placed, this could have lead to a distribution of source as it was spread out on the overall substrate surface. Thus, any trends caused by growth and migration across the surface of different morphologies may be hard to detect. In some cases it was noticed that the precursor also had fallen off the substrate entirely and into the quartz combustion boat as seen in Appendix F, Figure 91. Thus, for each synthesis the amount of precursor was not controlled and this is a parameter that is important to control in future experiments.

5.3.7 Confined space

Based on studies presented in Section 2.3.3 it is known that the confined space traps gas molecules such as O_2 and HCl gas produced during heating see reaction Equation 1. This entrapment leads to a reduced energy barrier of precursor decomposition which leads to an increased growth rate. Although, no effort was made to test the effect the confined space had on crystal growth in this thesis, as it was deemed outside the scope. Confined-space effect was reportedly investigated by Kang et al, which reported both microwave time and confined space as the two most critical factors in order to achieve uniform crystals [6]. This was also reported in another study obtaining square BiOI crystals, where a uniform space-confined gap was stated as favorable for synthesising atomically thin crystals [89]. In this thesis effort went into placing the precursor $BiCl_3$ at the center of the substrate. This could have resulted in a less uniform gap as it created a peak of precursor powder, thus less uniformly thin crystals.

5.3.8 Microwave oven

A microwave oven provides a rapid heat generation within the material, and the heating process can be started or stopped anytime ensuring more structure-controlled growth than conventional methods. The rapid heating reduces the reaction time and it is believed to increase nucleation rate. The increase in nucleation rate was discovered for a study which compared an electric furnace to a microwave oven, and found a decrease in crystal size for the microwave oven synthesized crystals [129]. Additionally, it is environmental friendly as no combustion gases will be produced during operation.

Heating by microwaves will provide an uniform nucleation environment due to uniform heating, thus resulting BiOCl crystals would be expected to have a narrow size distribution. In this thesis the size distribution of each parameter in Section 4.1.3 can be seen in Figures 27, 29, 31, 34 and

36. It is evident from these figures that on a general basis the size distribution is rather broad and divergent, but in some cases it is more narrow such as for Si-750W in Figure 31, Si-21.5cm in Figure 29 and Si-3min in Figure 27. This entails that the size distribution for a parallel within each investigated parameter was not narrow, but arguably rather broad. This can stem from the fact that the heat generated is depending on the materials ability to realign its dipoles in the applied electric field, however since there are reports of certain uniformity heating issues deviation could arise. It is stated in Section 2.3.4 that experienced electric field and consequently temperature rising rates are dependent on placement within the microwave oven, especially when using a stationary set-up like in this thesis. This location impact will be detailed in Section 5.3.2, but this could be the reason for not obtaining a narrow size distribution.

Additionally, there are reports of an increase in surface oxygen vacancies (OVs) for a microwave-assisted solvothermal approach compared to conventional method. These OVs are more stable at the surface of a material rather than in the bulk for high temperatures, and for BiOCl this surface is predominantly the (001) surface. This is because this plane was a high density of oxygen atoms, in consequence OVs are easily generated as explained in Section 2.2.5. The amount of Ovs was not investigated for the as-synthesized BiOCl crystals, but OVs could potentially be present in the (001) facet. This is because defects such as vacancies have excess energy, which makes them vulnerable to etching and as discussed in Section 5.2.2, the (001) facets is most likely the plane that is etched away to create the nanoframe-like structure. In summary, microwaves induces OVs which are easily generated on the (001) facet of BiOCl, both (001) facet and OVs are vulnerable to etching due to excess energy and it is deduced that this plane is etched away in the nanoframes. This may imply that OVs have in fact been generated on the as-synthesized BiOCl crystals. These OVs would improve the photocatalytic property of the material as well as narrowed the band gap.

5.4 Sources of error

The major source of error in this thesis revolves around the precursor. The fact that different grades were used for the two universities where the research was conducted, the precursor did not stick sufficiently for the synthesis at NTNU and that there were difficulties with the weigh in the glove box. Furthermore, as the precursor would not stick to the substrate instead of putting the substrate vertical in order to remove excess powder as done at UC Berkeley, a precursor peak at the center was instead created on the substrate surface. This lead to the precursor and top substrate sliding off easily and the center placement of the precursor could not be ensured. Accordingly any attempted measurements of the amount of precursor used was considered both inaccurate and impracticable to carry out.

6 Conclusion

In this thesis a confined-space microwave oven synthesis was performed which synthesized crystalline, stoichiometric BiOCl squares, octagons and flowers with exposure of (001) facets in an alternative approach to the traditional methods of hydrothermal and solvothermal. A range of synthesis parameters were altered and subsequently measurement of the effect these had on crystal growth was performed. The parameters investigated were microwave time, distance from magnetron, microwave power, growth on mica substrate with changing microwave power and amount of precursor. A growth trend was clearly visible for a substrate, where the different structures could be located at specific areas on the substrate. Initial nucleation and diffusion of atoms lead to formation of octagons at the substrate edges. With an increase in diffusion and more precursor accessible towards the substrate center, square emerged. Upon continuous diffusion further toward the substrate center, the squares stacked together and screw dislocations were formed. At the substrate center where there was an abundance of precursor, flowers were generated from multiple squares curving and colliding with each other. Nanoframes and cracked crystals did also form at the center due to etching by HCl. This was caused by diffusion of the precursor on the substrate surface. Furthermore, it was discovered that octagons and squares were the dominating structures on silica while flowers were dominating on mica, due to the different properties of the two materials. These properties are the amount of dangling bonds, eventual surface charge, insulating or conductive properties and surface roughness. The largest squares and crystals were measured to be 26.8 µm and were obtained for growth conditions of 1 min microwave time, 900 W power, with a large amount of source $BiCl_3$ on silica substrates placed at the center of the microwave oven.

However, there were one uncertainty for the synthesis scheme which was systematic challenges with the precursor, both placement and amount. A way to mitigate this is by using a finer grained precursor and implement a way of ensuring that the powder on the substrate stuck and would not slide off.

In addition to the synthesis parameters, the confined space was deemed crucial as it facilitated entrapment of produced gases which increased the growth rate. The microwave oven provided a more rapid heat generation than conventional methods, believed to increase nucleation rate.

The overall goal of the thesis was to synthesis stoichiometric, crystalline square BiOCl, with a uniform thickness of 3-4 nm and large-area of 10-20 µm, for use in various photocatlytic applications by using a space-confined, microwave assisted synthesis.A structure became evident and denoted as flowers or flower-like structure comprised of BiOCl nanoplates as petals. These structures were proven in other studies to have significantly higher photocatalytic activity than BiOCl nanoplates. Depending on parameters changed in the synthesis different structures, morphologies and size became evident. Although the synthesis method did not provide control of neither growth nor morphology, the observed structures and trends were of great structural and compositional interest. Additionally, would a measurement of band gap of the as-synthesised flowers, squares and octagons be interesting because of the difference in thickness, color, exposed facets and overall shape.

6.1 Further work

Some suggestions for further work are listed below.

- Due to the inconsistencies in Raman spectroscopy more investigation of stoichiometry is needed.
- The EDS analysis of both silica N, silica L and mica L shows that the composition is not completely consistent with BiOCl, as the EDS spectres shows higher levels of Bi than O and Cl. This could indicate that there is some discrepancies in the stoichiometry and further investigation of stoichiometry would be advantageous.
- To get more precise understanding of the facets and textures in the crystals, a more extensive XRD or TEM analysis could be done.
- Based on the XRD analysis showing a preferred orientation of (001) facets for both silica and mica analysis, it would be of interest in conducting band gap measurement. It would be advantageous to do so with an emphasis of the different structures, as the silica analysis also showed a higher exposure of (110) facets which is linked to a more narrow band gap. This narrowed band gap structure could potentially be used for photocatalytic applications within the visible light range.
- A more extensive analysis of color and thickness can be performed to a achieve a higher statistical significance of the results.

Bibliography

[1] Vibeke Rogde. 'Low-temperature microwave synthesis of ternary-layered 2D BiOCl crystals in a confined-space'. TMT4500: Materials Technology, Specialization Project. MA thesis. Dec. 2021.

[2] Liqun Ye et al. 'Recent advances in BIOX (X = cl, br and I) photocatalysts: Synthesis, modification, facet effects and mechanisms'. In: *Environmental Science: Nano* 1.2 (2014), p. 90. DOI: 10.1039/c3en00098b.

[3] Yang Yang et al. 'BiOX (X=Cl, Br, I) photocatalytic nanomaterials: Applications for fuels and environmental management'. In: *Advances in Colloid and Interface Science* 254 (2018), pp. 76–93. ISSN: 0001-8686. DOI: https://doi.org/10.1016/j.cis.2018.03.004. URL: https://www.sciencedirect.com/science/article/pii/S0001868617304128.

[4] Wenbin Li et al. 'Phase transitions in 2D materials'. In: *Nature Reviews Materials* 6.9 (2021), pp. 829–846. DOI: https://doi.org/10.1038/s41578-021-00304-0. URL: https://www.nature.com/articles/s41578-021-00304-0#citeas.

[5] Dattatray J. Late et al. 'Chapter 2 - Fundamentals and Properties of 2D Materials in General and Sensing Applications'. In: *Fundamentals and Sensing Applications of 2D Materials*. Woodhead Publishing Series in Electronic and Optical Materials. Woodhead Publishing, 2019, pp. 5–24. URL: https://www.sciencedirect.com/science/article/pii/B9780081025772000026.

[6] Lixing Kang et al. 'Space-confined microwave synthesis of ternary-layered BiOCl crystals with high-performance ultraviolet photodetection'. In: *InfoMat* 2 (2020), pp. 593–600. URL: https://onlinelibrary.wiley.com/doi/abs/10.1002/inf2.12033.

[7] Hao-Wei Guo et al. 'Stacking of 2D Materials'. In: *Advanced Functional Materials* 31.4 (2021), p. 2007810. DOI: https://doi.org/10.1002/adfm.202007810. URL: https://onlinelibrary.wiley.com/doi/abs/10.1002/adfm.202007810.

[8] Xiaolong Liu et al. '2D materials for quantum information science'. In: *Nature Reviews Materials* 4.10 (2019), pp. 669–684. DOI: https://doi.org/10.1038/s41578-019-0136-x. URL: https://www.nature.com/articles/s41578-019-0136-x.

[9] Rubén Mas-Ballesté et al. '2D materials: to graphene and beyond'. In: *Nanoscale* 3 (1 2011), pp. 20–30. DOI: 10.1039/C0NR00323A. URL: http://dx.doi.org/10.1039/C0NR00323A.

[10] Tripti Rimza et al. 'Chapter 19 - Two-dimensional nanomaterials for cancer application'. In: *Biosensor Based Advanced Cancer Diagnostics*. Ed. by Raju Khan et al. Academic Press, 2022, pp. 321–331. ISBN: 978-0-12-823424-2. DOI: https://doi.org/10.1016/B978-0-12-823424-2.00025-9. URL: https://www.sciencedirect.com/science/article/pii/B9780128234242000259.

[11] John Matson. *Graphene researchers Geim and Novoselov win Nobel prize in physics [updated]*. Oct. 2010. URL: https://www.scientificamerican.com/article/geim-novoselov-physics-novel/.

[12] Andrea Splendiani et al. 'Emerging Photoluminescence in Monolayer MoS2'. In: *Nano Letters* 10.4 (2010). PMID: 20229981, pp. 1271–1275. DOI: 10.1021/nl903868w. URL: https://doi.org/10.1021/nl903868w.

[13] Muvva D. Prasad et al. '2D Layered Structure of Bismuth Oxyhalides for Advanced Applications'. In: (), pp. 295–315. URL: https://pubs.acs.org/doi/abs/10.1021/bk-2020-1353.ch012.

[14] Bin Luo et al. 'Recent advances in 2D materials for photocatalysis'. In: *Nanoscale* 8 (13 2016), pp. 6904–6920. DOI: 10.1039/C6NR00546B. URL: http://dx.doi.org/10.1039/C6NR00546B.

[15] P. Rabu et al. 'Layered Organic–Inorganic Materials: A Way towards Controllable Magnetism'. In: *Advanced Engineering Materials* 5.4 (2003), pp. 189–210. DOI: https://doi.org/10.1002/adem.200310082. URL: https://onlinelibrary.wiley.com/doi/abs/10.1002/adem.200310082.

[16] Gao Yang et al. 'Structure of graphene and its disorders: a review'. In: *Science and Technology of Advanced Materials* 19.1 (2018). PMID: 30181789, pp. 613–648. DOI: 10.1080/14686996.2018.1494493. URL: https://doi.org/10.1080/14686996.2018.1494493.

[17] Armin VahidMohammadi et al. 'The world of two-dimensional carbides and nitrides (MXenes)'. In: *Science* 372.6547 (2021), eabf1581. DOI: 10.1126/science.abf1581. URL: https://www.science.org/doi/abs/10.1126/science.abf1581.

[18] Sajedeh Manzeli et al. '2D transition metal dichalcogenides'. In: *Nature Reviews Materials* 2.8 (2017). DOI: 10.1038/natrevmats.2017.33.

[19] Tengfei Xu et al. 'Ternary 2D Layered Material FePSe3 and Near-Infrared Photodetector'. In: *Advanced Electronic Materials* 7.8 (2021), p. 2100207. DOI: https://doi.org/10.1002/aelm.202100207. URL: https://onlinelibrary.wiley.com/doi/abs/10.1002/aelm.202100207.

[20] Wei Gao et al. 'Novel two-dimensional monoelemental and ternary materials: growth, physics and application'. In: *Nanophotonics* 9.8 (2020), pp. 2147–2168. DOI: doi:10.1515/nanoph-2019-0557. URL: https://doi.org/10.1515/nanoph-2019-0557.

[21] Vrinda Narayanan et al. 'How to 'train' your CVD to grow large-area 2D materials'. In: *Materials Research Express* 6.12 (2019), p. 125002. DOI: 10.1088/2053-1591/ab5383.

[22] J.D. Yao et al. 'Production of large-area 2D materials for high-performance photodetectors by pulsed-laser deposition'. In: *Progress in Materials Science* 106 (2019), p. 100573. ISSN: 0079-6425. DOI: https://doi.org/10.1016/j.pmatsci.2019.100573. URL: https://www.sciencedirect.com/science/article/pii/S0079642519300556.

[23] 'nanotechnologies — vocabulary — part 13: graphene and related two-dimensional (2d) materials'. Version Version 4.19.0. In: (). ISO/TS 80004-13:2017(en). URL: https://www.iso.org/obp/ui/#iso:std:iso:ts:80004:-13:ed-1:v1:en.

[24] Tuang Poh et al. 'Inhaled nanomaterials and the respiratory microbiome: clinical, immunological and toxicological perspectives'. In: *Particle and Fibre Toxicology* 15 (Nov. 2018). DOI: 10.1186/s12989-018-0282-0.

[25] Rafaela B. Marcelino et al. 'Towards visible-light photocatalysis for environmental applications: Band-gap engineering versus photons absorption—a review'. In: *Environmental Science and Pollution Research* 26.5 (2018), pp. 4155–4170. DOI: 10.1007/s11356-018-3117-5.

[26] Jun Yang et al. 'Dy(III) Doped BiOCl Powder with Superior Highly Visible-Light-Driven Photocatalytic Activity for Rhodamine B Photodegradation'. In: *Nanomaterials* 8.9 (2018). ISSN: 2079-4991. DOI: 10.3390/nano8090697. URL: https://www.mdpi.com/2079-4991/8/9/697.

[27] Hao Li et al. 'Oxygen Vacancy-Mediated Photocatalysis of BiOCl: Reactivity, Selectivity, and Perspectives'. In: *Angewandte Chemie International Edition* 57 (2018), pp. 122–138. URL: https://onlinelibrary.wiley.com/doi/abs/10.1002/anie.201705628.

[28] Nina Hwang et al. 'BET surface area analysis of nanoparticles'. In: *The Connexions project* (2011), pp. 1–11.

[29] Jing Zhang et al. 'The effect of pH on Synthesis of BiOCl and its photocatalytic oxidization performance'. In: *Materials Letters* 186 (2017), pp. 353–356. ISSN: 0167-577X. DOI: https://doi.org/10.1016/j.matlet.2016.09.117. URL: https://www.sciencedirect.com/science/article/pii/S0167577X16315798.

[30] Le Zhang et al. 'Tuning band gaps and optical absorption of BiOCl through doping and strain: insight form DFT calculations'. In: *Phys. Chem. Chem. Phys.* 19 (31 2017), pp. 20968–20973. DOI: 10.1039/C7CP03276E. URL: http://dx.doi.org/10.1039/C7CP03276E.

[31] Jie Li et al. 'Facet-Level Mechanistic Insights into General Homogeneous Carbon Doping for Enhanced Solar-to-Hydrogen Conversion'. In: *Advanced Functional Materials* 25.14 (2015), pp. 2189–2201. DOI: https://doi.org/10.1002/adfm.201404178. eprint: https://onlinelibrary.wiley.com/doi/pdf/10.1002/adfm.201404178. URL: https://onlinelibrary.wiley.com/doi/abs/10.1002/adfm.201404178.

[32] Xue Zhang et al. 'The stabilities and electronic structures of single-layer bismuth oxyhalides for photocatalytic water splitting'. In: *Phys. Chem. Chem. Phys.* 16 (47 2014), pp. 25854–25861. DOI: 10.1039/C4CP03166K. URL: http://dx.doi.org/10.1039/C4CP03166K.

[33] Kang Xu et al. 'First-principles study on the electronic structures and diffusion behaviors of intrinsic defects in BiOCl'. In: *Computational Materials Science* 203 (2022), p. 111088. ISSN: 0927-0256. DOI: https://doi.org/10.1016/j.commatsci.2021.111088. URL: https://www.sciencedirect.com/science/article/pii/S0927025621007588.

[34] Hongyu Chen et al. 'New concept ultraviolet photodetectors'. In: *Materials Today* 18.9 (2015), pp. 493–502. ISSN: 1369-7021. DOI: https://doi.org/10.1016/j.mattod.2015.06.001. URL: https://www.sciencedirect.com/science/article/pii/S1369702115001972.

[35] Hefeng Cheng et al. 'Engineering BIOX (X = cl, br, I) nanostructures for highly efficient photocatalytic applications'. In: *Nanoscale* 6.4 (2014), p. 2009. DOI: 10.1039/c3nr05529a.

[36] Kun Zhao et al. 'Surface Structure-Dependent Molecular Oxygen Activation of BiOCl Single-Crystalline Nanosheets'. In: *Journal of the American Chemical Society* 135.42 (2013). PMID: 24116848, pp. 15750–15753. DOI: 10.1021/ja4092903. eprint: https://doi.org/10.1021/ja4092903. URL: https://doi.org/10.1021/ja4092903.

[37] Cui-Huan Ge et al. 'Band gap engineering of atomically thin two-dimensional semiconductors'. In: *Chinese Physics B* 26.3 (Mar. 2017), p. 034208. DOI: 10.1088/1674-1056/26/3/034208. URL: https://doi.org/10.1088/1674-1056/26/3/034208.

[38] Sihai Cao et al. 'A novel BiOCl film with flowerlike hierarchical structures and its optical properties'. In: *Nanotechnology* 20 (June 2009), p. 275702. URL: https://doi.org/10.1088/0957-4484/20/27/275702.

[39] Meili Guan et al. 'Vacancy Associates Promoting Solar-Driven Photocatalytic Activity of Ultrathin Bismuth Oxychloride Nanosheets'. In: *Journal of the American Chemical Society* 135.28 (2013), pp. 10411–10417. DOI: 10.1021/ja402956f. URL: https://doi.org/10.1021/ja402956f.

[40] Ke-Lei Zhang et al. 'Study of the electronic structure and photocatalytic activity of the BiOCl photocatalyst'. In: *Applied Catalysis B: Environmental* 68.3 (2006), pp. 125–129. ISSN: 0926-3373. DOI: https://doi.org/10.1016/j.apcatb.2006.08.002. URL: https://www.sciencedirect.com/science/article/pii/S0926337306003547.

[41] Yaohui Lv et al. 'Room-temperature synthesis and high visible-light-induced photocatalytic activity of AgI/BiOI composites'. In: *Journal of Environmental Chemical Engineering* 1.3 (2013), pp. 526–533. ISSN: 2213-3437. DOI: https://doi.org/10.1016/j.jece.2013.06.019. URL: https://www.sciencedirect.com/science/article/pii/S221334371300081X.

[42] 'The crystal structure of BiOCl'. In: *Zeitschrift für Kristallographie - Crystalline Materials* 205.1 (1993), pp. 35–40. DOI: doi:10.1524/zkri.1993.205.Part-1.35. URL: https://doi.org/10.1524/zkri.1993.205.Part-1.35.

[43] Changhua Wang et al. 'Photocatalytic properties BiOCl and Bi2O3 nanofibers prepared by electrospinning'. In: *Scripta Materialia* 59.3 (2008), pp. 332–335. ISSN: 1359-6462. DOI: https://doi.org/10.1016/j.scriptamat.2008.03.038. URL: https://www.sciencedirect.com/science/article/pii/S1359646208002662.

[44] Dandan Cui et al. 'Band-gap engineering of BiOCl with oxygen vacancies for efficient photooxidation properties under visible-light irradiation'. In: *J. Mater. Chem. A* 6 (5 2018), pp. 2193–2199. DOI: 10.1039/C7TA09897A. URL: http://dx.doi.org/10.1039/C7TA09897A.

[45] Jiating Lu et al. 'Electronic Structures and Lattice Dynamics of Layered BiOCl Single Crystals'. In: *The Journal of Physical Chemistry Letters* 11.3 (2020). PMID: 31945297, pp. 1038–1044. DOI: 10.1021/acs.jpclett.9b03575. URL: https://doi.org/10.1021/acs.jpclett.9b0357.

[46] Xiaochao Zhang et al. 'Facile composition-controlled preparation and photocatalytic application of BiOCl/Bi2O2CO3 nanosheets'. In: *Applied Catalysis B: Environmental* 150-151 (2014), pp. 486–495. ISSN: 0926-3373. DOI: https://doi.org/10.1016/j.apcatb.2013.12.054. URL: https://www.sciencedirect.com/science/article/pii/S0926337314000058.

[47] Yangyang Guo et al. 'Controlled synthesis and enhanced luminescence of BiOCl:Eu 3+ ultrathin nanosheets'. In: *RSC Adv.* 7 (Jan. 2017), pp. 2629–2636. DOI: 10.1039/C6RA26310K.

[48] Xiaoli Yang et al. 'Synthesis, Functional Modifications, and Diversified Applications of Hybrid BiOCl-Based Heterogeneous Photocatalysts: A Review'. In: *Crystal Growth & Design* 21.11 (2021), pp. 6576–6618. DOI: 10.1021/acs.cgd.1c00866. eprint: https://doi.org/10.1021/acs.cgd.1c00866. URL: https://doi.org/10.1021/acs.cgd.1c00866.

[49] Kelvin H L Zhang et al. 'P-type transparent conducting oxides'. In: *Journal of Physics: Condensed Matter* 28.38 (July 2016), p. 383002. DOI: 10.1088/0953-8984/28/38/383002. URL: https://doi.org/10.1088/0953-8984/28/38/383002.

[50] Tao Jing et al. ‘The photocatalytic properties of ultrathin bismuth oxychloride nanosheets: a first principles study’. In: *Phys. Chem. Chem. Phys.* 18 (10 2016), pp. 7261–7268. DOI: 10.1039/C5CP07437A. URL: http://dx.doi.org/10.1039/C5CP07437A.

[51] An Zhang et al. ‘Nickel Doping in Atomically Thin Tin Disulfide Nanosheets Enables Highly Efficient CO2 Reduction’. In: *Angewandte Chemie International Edition* 57.34 (2018), pp. 10954–10958. DOI: https://doi.org/10.1002/anie.201806043. eprint: https://onlinelibrary.wiley.com/doi/pdf/10.1002/anie.201806043. URL: https://onlinelibrary.wiley.com/doi/abs/10.1002/anie.201806043.

[52] Jie Li et al. ‘Giant Enhancement of Internal Electric Field Boosting Bulk Charge Separation for Photocatalysis’. In: *Advanced Materials* 28.21 (2016), pp. 4059–4064. DOI: https://doi.org/10.1002/adma.201600301. eprint: https://onlinelibrary.wiley.com/doi/pdf/10.1002/adma.201600301. URL: https://onlinelibrary.wiley.com/doi/abs/10.1002/adma.201600301.

[53] Xiaoyu Li et al. ‘Solvent co-mediated synthesis of ultrathin BiOCl nanosheets with highly efficient visible-light photocatalytic activity’. In: *RSC Adv.* 7 (17 2017), pp. 10235–10241. DOI: 10.1039/C6RA27606G. URL: http://dx.doi.org/10.1039/C6RA27606G.

[54] Rongan He et al. ‘Review on nanoscale bi-based photocatalysts’. In: *Nanoscale Horizons* 3.5 (May 2018), pp. 464–504. DOI: 10.1039/c8nh00062j.

[55] Hilmi Ünlü. ‘A thermodynamic model for determining pressure and temperature effects on the bandgap energies and other properties of some semiconductors’. In: *Solid-State Electronics* 35.9 (1992), pp. 1343–1352. ISSN: 0038-1101. DOI: https://doi.org/10.1016/0038-1101(92)90170-H. URL: https://www.sciencedirect.com/science/article/pii/003811019290170H.

[56] Jinyan Xiong et al. ‘Well-crystallized square-like 2D BiOCl nanoplates: mannitol-assisted hydrothermal synthesis and improved visible-light-driven photocatalytic performance’. In: *RSC Adv.* 1 (8 2011), pp. 1542–1553. DOI: 10.1039/C1RA00335F. URL: http://dx.doi.org/10.1039/C1RA00335F.

[57] Shujuan Zhang et al. ‘A novel F-doped BiOCl photocatalyst with enhanced photocatalytic performance’. In: *Materials Chemistry and Physics* 173 (2016), pp. 298–308. ISSN: 0254-0584. DOI: https://doi.org/10.1016/j.matchemphys.2016.02.016. URL: https://www.sciencedirect.com/science/article/pii/S0254058416300864.

[58] Changlin Yu et al. ‘Novel B-doped BiOCl nanosheets with exposed (001) facets and photocatalytic mechanism of enhanced degradation efficiency for organic pollutants’. In: *Science of The Total Environment* 694 (2019), p. 133727. ISSN: 0048-9697. DOI: https://doi.org/10.1016/j.scitotenv.2019.133727. URL: https://www.sciencedirect.com/science/article/pii/S0048969719336654.

[59] Zhao Li et al. ‘One-pot synthesis of BiOCl nanosheets with dual functional carbon for ultra-highly efficient photocatalytic degradation of RhB’. In: *Environmental Research* 182 (2020), p. 109077. ISSN: 0013-9351. DOI: https://doi.org/10.1016/j.envres.2019.109077. URL: https://www.sciencedirect.com/science/article/pii/S0013935119308734.

[60] Fei Chang et al. ‘Poly(vinyl pyrrolidone)-assisted hydrothermal synthesis and enhanced visible-light photocatalytic performance of oxygen-rich bismuth oxychlorides’. In: *Journal of Colloid and Interface Science* 459 (2015), pp. 136–145. ISSN: 0021-9797. DOI: https://doi.org/10.1016/j.jcis.2015.08.023. URL: https://www.sciencedirect.com/science/article/pii/S0021979715301181.

[61] Xiaoli Jin et al. ‘Bismuth-rich strategy induced photocatalytic molecular oxygen activation properties of bismuth oxyhalogen: The case of Bi24O31Cl10’. In: *Applied Catalysis B: Environmental* 165 (2015), pp. 668–675. DOI: https://doi.org/10.1016/j.apcatb.2014.10.075. URL: https://www.sciencedirect.com/science/article/pii/S092633731400695X.

[62] Chu-Ya Wang et al. ‘Novel Bi12O15Cl6 Photocatalyst for the Degradation of Bisphenol A under Visible-Light Irradiation’. In: *ACS Applied Materials & Interfaces* 8.8 (2016), pp. 5320–5326. DOI: 10.1021/acsami.5b12092. URL: https://doi.org/10.1021/acsami.5b12092.

[63] Xin Xiao et al. ‘Oxygen-rich bismuth oxyhalides: generalized one-pot synthesis, band structures and visible-light photocatalytic properties’. In: *J. Mater. Chem.* 22 (43 2012), pp. 22840–22843. DOI: 10.1039/C2JM33556E. URL: http://dx.doi.org/10.1039/C2JM33556E.

[64] Yu Huang et al. 'Chapter 10 - Synthesis and Applications of Nanomaterials With High Photocatalytic Activity on Air Purification'. In: *Novel Nanomaterials for Biomedical, Environmental and Energy Applications.* Ed. by Xiaoru Wang et al. Micro and Nano Technologies. Elsevier, 2019, pp. 299–325. ISBN: 978-0-12-814497-8. DOI: https://doi.org/10.1016/B978-0-12-814497-8.00010-2. URL: https://www.sciencedirect.com/science/article/pii/B9780128144978000102.

[65] Hongyan Liu et al. 'Correlation of oxygen vacancy variations to band gap changes in epitaxial ZnO thin films'. In: *Applied Physics Letters* 102.18 (2013), p. 181908. DOI: 10.1063/1.4804613. eprint: https://doi.org/10.1063/1.4804613. URL: https://doi.org/10.1063/1.4804613.

[66] Chen Dai et al. 'Defect engineering of 2D BiOCl nanosheets for photonic tumor ablation'. In: *Nanoscale Horiz.* 5 (5 2020), pp. 857–868. DOI: 10.1039/C9NH00707. URL: http://dx.doi.org/10.1039/C9NH00707E.

[67] J. Varalda et al. 'Oxygen diffusion and vacancy migration thermally-activated govern high-temperature magnetism in Ceria'. In: *Scientific Reports* 9.1 (2019). DOI: 10.1038/s41598-019-41157-6.

[68] Han Zhao et al. 'A special synthesis of BiOCl photocatalyst for efficient pollutants removal: New insight into the band structure regulation and molecular oxygen activation'. In: *Applied Catalysis B: Environmental* 256 (2019), p. 117872. ISSN: 0926-3373. DOI: https://doi.org/10.1016/j.apcatb.2019.117872. URL: https://www.sciencedirect.com/science/article/pii/S0926337319306186.

[69] 'Photocatalytic study of BiOCl for degradation of organic pollutants under UV irradiation'. In: *Journal of Photochemistry and Photobiology A: Chemistry* 215.1 (2010), pp. 76–80. ISSN: 1010-6030. DOI: https://doi.org/10.1016/j.jphotochem.2010.07.026. URL: https://www.sciencedirect.com/science/article/pii/S1010603010002972.

[70] Jing Tian et al. 'Enhanced photocatalytic activity of BiOCl with regulated morphology and band structure through controlling the adding amount of HCl'. In: *Materials Letters* 272 (2020), p. 127860. ISSN: 0167-577X. DOI: https://doi.org/10.1016/j.matlet.2020.127860. URL: https://www.sciencedirect.com/science/article/pii/S0167577X20305656.

[71] Makio Uwaha. '8 - Growth Kinetics: Basics of Crystal Growth Mechanisms'. In: *Handbook of Crystal Growth (Second Edition).* Ed. by Tatau Nishinaga. Second Edition. Boston: Elsevier, 2015, pp. 359–399. ISBN: 978-0-444-56369-9. DOI: https://doi.org/10.1016/B978-0-444-56369-9.00008-3. URL: https://www.sciencedirect.com/science/article/pii/B9780444563699000083.

[72] Govindhan Dhanaraj et al. 'Crystal Growth Techniques and Characterization: An Overview'. In: *Springer Handbook of Crystal Growth.* Ed. by Govindhan Dhanaraj et al. Berlin, Heidelberg: Springer Berlin Heidelberg, 2010, pp. 3–16. ISBN: 978-3-540-74761-1. DOI: 10.1007/978-3-540-74761-1_1. URL: https://doi.org/10.1007/978-3-540-74761-1_1.

[73] Qiaofeng Han. 'Advances in preparation methods of bismuth-based photocatalysts'. In: *Chemical Engineering Journal* 414 (2021), p. 127877. ISSN: 1385-8947. DOI: https://doi.org/10.1016/j.cej.2020.127877. URL: https://www.sciencedirect.com/science/article/pii/S1385894720339966.

[74] Min Xu et al. 'Performance enhancement strategies of bi-based photocatalysts: A review on recent progress'. In: *Chemical Engineering Journal* 389 (2020), p. 124402. ISSN: 1385-8947. DOI: https://doi.org/10.1016/j.cej.2020.124402. URL: https://www.sciencedirect.com/science/article/pii/S1385894720303934.

[75] Shujuan Zhang et al. 'Microwave-Assisted Synthesis of BiOCl/BiOBr Composites with Improved Visible-Light Photocatalytic Activity'. In: *Industrial & Engineering Chemistry Research* 54.41 (2015), pp. 9913–9919. DOI: 10.1021/acs.iecr.5b02332. eprint: https://doi.org/10.1021/acs.iecr.5b02332. URL: https://doi.org/10.1021/acs.iecr.5b02332.

[76] Yaru Shang et al. 'Effect of acetic acid on morphology of Bi2WO6 with enhanced photocatalytic activity'. In: *Materials Science in Semiconductor Processing* 89 (2019), pp. 240–249. ISSN: 1369-8001. DOI: https://doi.org/10.1016/j.mssp.2018.09.026. URL: https://www.sciencedirect.com/science/article/pii/S1369800118307054.

[77] Yang Li et al. 'Recent advances in bismuth oxyhalide photocatalysts for degradation of organic pollutants in wastewater'. In: *RSC Adv.* 11 (43 2021), pp. 26855–26875. DOI: 10.1039/D1RA05796K. URL: http://dx.doi.org/10.1039/D1RA05796K.

[78] Zhongwei Zou et al. 'Facile preparation and photocatalytic activity of oxygen vacancy rich BiOCl with 001 exposed reactive facets'. In: *Applied Surface Science* 463 (2019), pp. 1011–1018. ISSN: 0169-4332. DOI: https://doi.org/10.1016/j.apsusc.2018.09.025. URL: https://www.sciencedirect.com/science/article/pii/S0169433218324437.

[79] Barbora Stieberova et al. 'Sustainability assessment of continuous-flow hydrothermal synthesis of nanomaterials in the context of other production technologies'. In: *Journal of Cleaner Production* 241 (2019), p. 118325. ISSN: 0959-6526. DOI: https://doi.org/10.1016/j.jclepro.2019.118325. URL: https://www.sciencedirect.com/science/article/pii/S0959652619331956.

[80] Timothy Dontsos Yaser Dahman Kevin Deonanan et al. 'Chapter 6 - Nanopolymers'. In: *Nanotechnology and Functional Materials for Engineers.* Ed. by Yaser Dahman. Micro and Nano Technologies. Elsevier, 2017, pp. 121–144. DOI: https://doi.org/10.1016/B978-0-323-51256-5.00006-X. URL: https://www.sciencedirect.com/science/article/pii/B978032351256500006X.

[81] Vahid Mahmoodi et al. 'Facile Synthesis of BiOI Nanoparticles at Room Temperature and Evaluation of their Photoactivity Under Sunlight Irradiation'. In: *Photochemistry and Photobiology* 94.1 (2018), pp. 4–16. DOI: https://doi.org/10.1111/php.12832. eprint: https://onlinelibrary.wiley.com/doi/pdf/10.1111/php.12832. URL: https://onlinelibrary.wiley.com/doi/abs/10.1111/php.12832.

[82] Jianhua Hou et al. 'Narrowing the Band Gap of BiOCl for the Hydroxyl Radical Generation of Photocatalysis under Visible Light'. In: *ACS Sustainable Chemistry & Engineering* 7.19 (2019), pp. 16569–16576. DOI: 10.1021/acssuschemeng.9b03885. eprint: https://doi.org/10.1021/acssuschemeng.9b03885. URL: https://doi.org/10.1021/acssuschemeng.9b03885.

[83] Yuanyuan Sun et al. 'Photocatalytic defluorination of perfluorooctanoic acid by surface defective BiOCl: Fast microwave solvothermal synthesis and photocatalytic mechanisms'. In: *Journal of Environmental Sciences* 84 (2019), pp. 69–79. ISSN: 1001-0742. DOI: https://doi.org/10.1016/j.jes.2019.04.012. URL: https://www.sciencedirect.com/science/article/pii/S1001074219305108.

[84] Yang Long et al. 'A novel solvent-free strategy for the synthesis of bismuth oxyhalides'. In: *J. Mater. Chem. A* 6 (27 2018), pp. 13005–13011. DOI: 10.1039/C8TA04529A. URL: http://dx.doi.org/10.1039/C8TA04529A.

[85] Qi Jiang et al. 'Ionic liquid induced mechanochemical synthesis of BiOBr ultrathin nanosheets at ambient temperature with superior visible-light-driven photocatalysis'. In: *Journal of Colloid and Interface Science* 574 (2020), pp. 131–139. ISSN: 0021-9797. DOI: https://doi.org/10.1016/j.jcis.2020.04.018. URL: https://www.sciencedirect.com/science/article/pii/S0021979720304562.

[86] Lei Wu et al. 'Mechanochemical syntheses of bismuth oxybromides BixOyBrz as visible-light responsive photocatalyts for the degradation of bisphenol A'. In: *Journal of Solid State Chemistry* 270 (2019), pp. 458–462. ISSN: 0022-4596. DOI: https://doi.org/10.1016/j.jssc.2018.12.010. URL: https://www.sciencedirect.com/science/article/pii/S0022459618305516.

[87] Keyvan Bijanzad et al. 'Solid state preparation and photocatalytic activity of bismuth oxybromide nanoplates'. In: *Research on Chemical Intermediates* 42.3 (2015), pp. 2429–2447. DOI: 10.1007/s11164-015-2159-2.

[88] Fadri Gottschalk et al. 'The release of engineered nanomaterials to the environment'. In: *J. Environ. Monit.* 13 (5 2011), pp. 1145–1155. DOI: 10.1039/C0EM00547A. URL: http://dx.doi.org/10.1039/C0EM00547A.

[89] Wei Zeng et al. 'Synthesis of Large-Area Atomically Thin BiOI Crystals with Highly Sensitive and Controllable Photodetection'. In: *Advanced Functional Materials* 29.16 (2019), p. 1900129. DOI: https://doi.org/10.1002/adfm.201900129. eprint: https://onlinelibrary.wiley.com/doi/pdf/10.1002/adfm.201900129. URL: https://onlinelibrary.wiley.com/doi/abs/10.1002/adfm.201900129.

[90] Xiaozhi Xu et al. 'Ultrafast growth of single-crystal graphene assisted by a continuous oxygen supply'. In: *Nature Nanotechnology* 11.11 (2016), pp. 930–935. DOI: 10.1038/nnano.2016.132.

[91] Akitoshi Ishizaka et al. 'Low Temperature Surface Cleaning of Silicon and Its Application to Silicon MBE'. In: *Journal of The Electrochemical Society* 133.4 (Apr. 1986), pp. 666–671. DOI: 10.1149/1.2108651. URL: https://doi.org/10.1149/1.2108651.

[92] Xiaoyue Wang et al. 'Confined-space synthesis of single crystal TiO2 nanowires in atmospheric vessel at low temperature: a generalized approach'. In: *Scientific Reports (Nature Publisher Group)* 5 (Jan. 2015). Copyright - Copyright Nature Publishing Group Jan 2015; Last updated - 2017-08-18, p. 8129. URL: https://www.proquest.com/scholarly-journals/confined-space-synthesis-single-crystal-tio2/docview/1898206300/se-2.

[93] Shasha Zhou et al. 'Space-confined vapor deposition synthesis of two dimensional materials'. In: *Nano Research* 11.6 (2018), pp. 2909–2931. DOI: 10.1007/s12274-017-1942-3.

[94] Chiao-Chen Chen et al. 'Growth of Large-Area Graphene Single Crystals in Confined Reaction Space with Diffusion-Driven Chemical Vapor Deposition'. In: *Chemistry of Materials* 27.18 (2015), pp. 6249–6258. DOI: 10.1021/acs.chemmater.5b01430. eprint: https://doi.org/10.1021/acs.chemmater.5b01430. URL: https://doi.org/10.1021/acs.chemmater.5b01430.

[95] A.C. Metaxas. 'Microwave heating'. In: *Power Engineering Journal* 5.5 (1991), pp. 237–247. DOI: 10.1049/pe:19910047.

[96] C. Oliver Kappe. 'Controlled Microwave Heating in Modern Organic Synthesis'. In: *Angewandte Chemie International Edition* 43.46 (2004), pp. 6250–6284. DOI: https://doi.org/10.1002/anie.200400655. URL: https://onlinelibrary.wiley.com/doi/abs/10.1002/anie.200400655.

[97] Camelia Gabriel et al. 'Dielectric parameters relevant to microwave dielectric heating'. In: *Chem. Soc. Rev.* 27 (3 1998), pp. 213–224. DOI: 10.1039/A827213Z. URL: http://dx.doi.org/10.1039/A827213Z.

[98] D. Michael P. Mingos et al. 'Tilden Lecture. Applications of microwave dielectric heating effects to synthetic problems in chemistry'. In: *Chem. Soc. Rev.* 20 (1 1991), pp. 1–47. DOI: 10.1039/CS9912000001. URL: http://dx.doi.org/10.1039/CS9912000001.

[99] Mario L. Moreira et al. 'Structural and optical properties of CaTiO3 perovskite-based materials obtained by microwave-assisted hydrothermal synthesis: An experimental and theoretical insight'. In: *Acta Materialia* 57.17 (2009), pp. 5174–5185. ISSN: 1359-6454. DOI: https://doi.org/10.1016/j.actamat.2009.07.019. URL: https://www.sciencedirect.com/science/article/pii/S135964540900442X.

[100] Donglei Luan et al. 'Frequency distribution in domestic microwave ovens and its influence on heating pattern'. In: *Journal of Food Science* 82.2 (2016), pp. 429–436. DOI: 10.1111/1750-3841.13587.

[101] R.S. Vilayannur et al. 'SIZE AND SHAPE EFFECT ON NONUNIFORMITY OF TEMPERATURE AND MOISTURE DISTRIBUTIONS IN MICROWAVE HEATED FOOD MATERIALS: PART I SIMULATION'. In: *Journal of Food Process Engineering* 21.3 (1998), pp. 209–233. DOI: https://doi.org/10.1111/j.1745-4530.1998.tb00448.x. eprint: https://onlinelibrary.wiley.com/doi/pdf/10.1111/j.1745-4530.1998.tb00448.x. URL: https://onlinelibrary.wiley.com/doi/abs/10.1111/j.1745-4530.1998.tb00448.x.

[102] Yuichi Funawatashi et al. 'Numerical analysis of microwave heating of a dielectric'. In: *Heat Transfer—Asian Research* 32.3 (2003), pp. 227–236. DOI: https://doi.org/10.1002/htj.10087. eprint: https://onlinelibrary.wiley.com/doi/pdf/10.1002/htj.10087. URL: https://onlinelibrary.wiley.com/doi/abs/10.1002/htj.10087.

[103] Aron Wosylus et al. 'In-situ Study of the Solid-Gas Reaction of BiCl3 to BiOCl via the Intermediate Hydrate BiCl3·H2O'. In: *European Journal of Inorganic Chemistry* 2010.10 (2010), pp. 1469–1471. URL: https://chemistry-europe.onlinelibrary.wiley.com/doi/abs/10.1002/ejic.201000032.

[104] Paul Flowers et al. 'Chapter 7 Chemical Bonding and Molecular Geometry'. In: *Chemistry 2E*. OpenStax, XanEdu, Feb. 2019. URL: https://openstax.org/books/chemistry-2e/pages/7-2-covalent-bonding.

[105] Allan G. Blackman et al. *Aylward and Findlay's Si Chemical Data*. 7th. John Wiley amp; Sons Austraria, 2014. ISBN: 9780730302469.

[106] M. A. Pillers et al. 'Preparation of Mica and Silicon Substrates for DNA Origami Analysis and Experimentation'. In: *Journal of visualized experiments: JoVE* 101 (2015).

[107] *Properties and chemical composition of MICA grade V1GRADE classification of Muscovite Mica*. URL: https://www.tedpella.com/vacuum_html/Mica_Grade_V1_Properties.htm.

[108] Liu Yang et al. 'Anomalous Surface Fatigue in a Nano-Layered Material'. In: *Advanced materials (Deerfield Beach, Fla.)* 26 (Oct. 2014).

[109] Stephen Guggenheim et al. 'Muscovite Dehydroxylation—High-Temperature Studies'. In: *American Mineralogist; (USA)* 72:5-6 (Jan. 1987), pp. 537–550.

[110] Wester de Poel et al. 'Muscovite mica: Flatter than a pancake'. In: *Surface Science* 619 (2014), pp. 19–24. ISSN: 0039-6028. DOI: https://doi.org/10.1016/j.susc.2013.10.008. URL: https://www.sciencedirect.com/science/article/pii/S0039602813003038.

[111] Jacob N. Israelachvili et al. 'Preparing Contamination-free Mica Substrates for Surface Characterization, Force Measurements, and Imaging'. In: *ASC Publications* 20 (2004).

[112] David A. Mckeown et al. 'Vibrational analysis of the dioctahedral mica: 2M1 muscovite'. In: *American Mineralogist* 84.7-8 (1999), pp. 1041–1048. DOI: doi:10.2138/am-1999-7-806. URL: https://doi.org/10.2138/am-1999-7-806.

[113] Helmut Poppa et al. 'The surface composition of Mica substrates'. In: *Surface Science* 24 (1971), pp. 149–163. URL: https://www.sciencedirect.com/science/article/pii/0039602871902251.

[114] Jacob N. Israelachvili et al. 'Preparation of Mica and Silicon Substrates for DNA Origami Analysis and Experimentation'. In: *Journal of visualized experiments* 101 (2015).

[115] Rodica Ghita et al. 'Study of sio2/SI interface by surface techniques'. In: *Crystalline Silicon - Properties and Uses* (2011). DOI: 10.5772/23174.

[116] Lado Filipovic. *Molecular Structure of the Silicon-Silicon Dioxide Interface*. Dec. 2012. URL: https://www.iue.tuwien.ac.at/phd/filipovic/node27.html.

[117] Xiaobo Li et al. 'Controlled growth of large-area anisotropic ReS2 atomic layer and its photodetector application'. In: *Nanoscale* 8 (45 2016), pp. 18956–18962. DOI: 10.1039/C6NR07233J. URL: http://dx.doi.org/10.1039/C6NR07233J.

[118] Xinran Wang et al. 'Atomic Layer Deposition of Metal Oxides on Pristine and Functionalized Graphene'. In: *Journal of the American Chemical Society* 130.26 (2008), pp. 8152–8153. DOI: 10.1021/ja8023059. URL: https://doi.org/10.1021/ja8023059.

[119] Han Liu et al. 'The integration of high-k dielectric on two-dimensional crystals by atomic layer deposition'. In: *Applied Physics Letters* 100.15 (2012), p. 152115. DOI: 10.1063/1.3703595. URL: https://doi.org/10.1063/1.3703595.

[120] Qundong Fu et al. 'Ultrasensitive 2D Bi2O2Se Phototransistors on Silicon Substrates'. In: *Advanced Materials* 31 (2019), p. 1804945. URL: https://onlinelibrary.wiley.com/doi/abs/10.1002/adma.201804945.

[121] Wen-Wen Liu et al. 'Recent advances of bismuth oxychloride photocatalytic material: Property, preparation and performance enhancement'. In: *Journal of Electronic Science and Technology* 18.2 (2020), p. 100020. ISSN: 1674-862X. DOI: https://doi.org/10.1016/j.jnlest.2020.100020. URL: https://www.sciencedirect.com/science/article/pii/S1674862X20300173.

[122] Xing Zhang et al. 'Synthesis of a Highly Efficient BiOCl Single-Crystal Nanodisk Photocatalyst with Exposing 001 Facets'. In: *ACS Applied Materials & Interfaces* 6.10 (2014). PMID: 24797177, pp. 7766–7772. DOI: 10.1021/am5010392. URL: https://doi.org/10.1021/am5010392.

[123] Sujuan Wu et al. 'Controllable growth of BiOCl film with high percentage of exposed 001 facets'. In: *Applied Surface Science* 289 (2014), pp. 266–273. ISSN: 0169-4332. DOI: https://doi.org/10.1016/j.apsusc.2013.10.148. URL: https://www.sciencedirect.com/science/article/pii/S0169433213020175.

[124] Haijun Zhang et al. 'First-principles studies on facet-dependent photocatalytic properties of bismuth oxyhalides (BiOXs)'. In: *RSC Adv.* 2 (24 2012), pp. 9224–9229. DOI: 10.1039/C2RA20881D. URL: http://dx.doi.org/10.1039/C2RA20881D.

[125] C. Gatel et al. 'Comparative study of Pt, Au and Ag growth on Fe3O4(001) surface'. In: *Surface Science* 600.13 (2006), pp. 2650–2662. ISSN: 0039-6028. DOI: https://doi.org/10.1016/j.susc.2006.03.036. URL: https://www.sciencedirect.com/science/article/pii/S0039602806003864.

[126] Wenwen Liu et al. 'Enhanced performance of doped BiOCl nanoplates for photocatalysis: understanding from doping insight into improved spatial carrier separation'. In: *J. Mater. Chem. A* 5 (24 2017), pp. 12542–12549. DOI: 10.1039/C7TA02724A. URL: http://dx.doi.org/10.1039/C7TA02724A.

[127] Herman F. Cordes. 'Preexponential factors for solid-state thermal decomposition'. In: *The Journal of Physical Chemistry* 72.6 (1968), pp. 2185–2189. DOI: 10.1021/j100852a052. URL: https://doi.org/10.1021/j100852a052.

[128] Saeid Farhadi et al. 'Microwave-induced solid-state decomposition of the Bi[Fe(CN)6]·5H2O precursor: A novel route for the rapid and facile synthesis of pure and single-phase BiFeO3 nanopowder'. In: *Journal of Alloys and Compounds* 503.2 (2010), pp. 439–444. ISSN: 0925-8388. DOI: https://doi.org/10.1016/j.jallcom.2010.05.029. URL: https://www.sciencedirect.com/science/article/pii/S0925838810011485.

[129] Saeid Farhadi et al. 'Microwave-assisted solid-state decomposition of La[Co(CN)6]·5H2O precursor: A simple and fast route for the synthesis of single-phase perovskite-type LaCoO3 nanoparticles'. In: *Journal of Alloys and Compounds* 489.2 (2010), pp. 586–591. ISSN: 0925-8388. DOI: https://doi.org/10.1016/j.jallcom.2009.09.117. URL: https://www.sciencedirect.com/science/article/pii/S0925838809018623.

[130] David R. Baghurst et al. 'Application of microwave heating techniques for the synthesis of solid state inorganic compounds'. In: *J. Chem. Soc., Chem. Commun.* (12 1988), pp. 829–830. DOI: 10.1039/C39880000829. URL: http://dx.doi.org/10.1039/C39880000829.

[131] Tung-Han Yang et al. 'Noble-Metal Nanoframes and Their Catalytic Applications'. In: *Chemical Reviews* 121.2 (2021). PMID: 33275408, pp. 796–833. DOI: 10.1021/acs.chemrev.0c00940. URL: https://doi.org/10.1021/acs.chemrev.0c00940.

[132] Shuifen Xie et al. 'Synthesis of Pd-Rh Core–Frame Concave Nanocubes and Their Conversion to Rh Cubic Nanoframes by Selective Etching of the Pd Cores'. In: *Angewandte Chemie International Edition* 51.41 (2012), pp. 10266–10270. DOI: https://doi.org/10.1002/anie.201206044. URL: https://onlinelibrary.wiley.com/doi/abs/10.1002/anie.201206044.

[133] Taehyun Kwon et al. 'Catalytic Nanoframes and Beyond'. In: *Advanced Materials* 32.33 (July 2020), p. 2001345. DOI: https://doi.org/10.1002/adma.202001345. URL: https://onlinelibrary.wiley.com/doi/abs/10.1002/adma.202001345.

[134] Dokyoon Kim et al. 'Synthesis of Hollow Iron Nanoframes'. In: *Journal of the American Chemical Society* 129.18 (2007). PMID: 17439128, pp. 5812–5813. DOI: 10.1021/ja070667m. URL: https://doi.org/10.1021/ja070667m.

[135] Chi Xiao et al. 'High-Index-Facet- and High-Surface-Energy Nanocrystals of Metals and Metal Oxides as Highly Efficient Catalysts'. In: *Joule* 4.12 (2020), pp. 2562–2598. ISSN: 2542-4351. DOI: https://doi.org/10.1016/j.joule.2020.10.002. URL: https://www.sciencedirect.com/science/article/pii/S2542435120304591.

[136] Eugene D. Shchukin et al. 'IX - Principles of Physical-Chemical Mechanics'. In: *Colloid and Surface Chemistry*. Ed. by Eugene D. Shchukin et al. Vol. 12. Studies in Interface Science. Elsevier, 2001, pp. 649–732. DOI: https://doi.org/10.1016/S1383-7303(01)80011-9. URL: https://www.sciencedirect.com/science/article/pii/S1383730301800119.

[137] Zhi-Ping Zhang et al. 'Selective synthesis of rhodium-based nanoframe catalysts by chemical etching of 3d metals'. In: *Chem. Commun.* 51 (19 2015), pp. 3997–4000. DOI: 10.1039/C4CC10050F. URL: http://dx.doi.org/10.1039/C4CC10050F.

[138] Masaharu Tsuji et al. 'Formation of Rh frame nanorods using Au nanorods as sacrificial templates'. In: *CrystEngComm* 17 (36 2015), pp. 6955–6961. DOI: 10.1039/C5CE00357A. URL: http://dx.doi.org/10.1039/C5CE00357A.

[139] Chun-Hong Kuo et al. 'Fabrication of Truncated Rhombic Dodecahedral Cu2O Nanocages and Nanoframes by Particle Aggregation and Acidic Etching'. In: *Journal of the American Chemical Society* 130.38 (2008). PMID: 18761449, pp. 12815–12820. DOI: 10.1021/ja804625s. URL: https://doi.org/10.1021/ja804625s.

[140] Ya-Huei Tsai et al. 'Fabrication of Diverse Cu2O Nanoframes through Face-Selective Etching'. In: *The Journal of Physical Chemistry C* 117.46 (2013), pp. 24611–24617. DOI: 10.1021/jp4088018. URL: https://doi.org/10.1021/jp4088018.

[141] Ming Zhao et al. 'Ruthenium Nanoframes in the Face-Centered Cubic Phase: Facile Synthesis and Their Enhanced Catalytic Performance'. In: *ACS Nano* 13.6 (2019). PMID: 31145858, pp. 7241–7251. DOI: 10.1021/acsnano.9b02890. URL: https://doi.org/10.1021/acsnano.9b02890.

[142] Ronghua Yi et al. 'Crack Formation on Crystalline Bismuth Oxychloride Thin Square Sheets by Using a Wet-Chemical Method'. In: *ChemNanoMat* 6.5 (2020), pp. 759–764. DOI: https://doi.org/10.1002/cnma.202000145. URL: https://onlinelibrary.wiley.com/doi/abs/10.1002/cnma.202000145.

[143] Ping Ye et al. 'Hydrolytic synthesis of flowerlike BiOCl and its photocatalytic performance under visible light'. In: *Materials Letters* 108 (2013), pp. 168–171. URL: https://www.sciencedirect.com/science/article/pii/S0167577X13008707.

[144] Ji-Ming Song et al. 'Hierarchical Structured Bismuth Oxychlorides: Self-assembly from Nanoplates to Nanoflowers via a Solvothermal Route and Their Photocatalytic Properties'. In: *Crystengcomm* 12 (Nov. 2010).

[145] Yupeng Gao et al. 'Microwave-assisted synthesis of flower-like Ag–BiOCl nanocomposite with enhanced visible-light photocatalytic activity'. In: *Materials Letters* 136 (2014), pp. 295–297. URL: https://www.sciencedirect.com/science/article/pii/S0167577X14014827.

[146] Lang Chen et al. 'Facile synthesis of BiOCl nano-flowers of narrow band gap and their visible-light-induced photocatalytic property'. In: *Catalysis Communications* 23 (2012), pp. 54–57. URL: https://www.sciencedirect.com/science/article/pii/S1566736712000982.

[147] Guangfang Li et al. 'BiOX (X=Cl, Br, I) nanostructures: Mannitol-mediated microwave synthesis, visible light photocatalytic performance, and Cr(VI) removal capacity'. In: *Journal of Colloid and Interface Science* 409 (2013), pp. 43–51. URL: https://www.sciencedirect.com/science/article/pii/S0021979713007315.

[148] Yu S.-H. et al. 'General synthesis of single-crystal tungstate nanorods/nanowires: A facile, low-temperature solution approach'. In: *Advanced Functional Materials* 13.8 (2003), pp. 639–647. DOI: 10.1002/adfm.200304373. URL: https://www.scopus.com/inward/record.uri?eid=2-s2.0-0042967690&doi=10.1002%5C%2fadfm.200304373&partnerID=40&md5=e9fbd463966d1fcdd1b560ffe1365076.

[149] Zhengtao Deng et al. 'From Bulk Metal Bi to Two-Dimensional Well-Crystallized BiOX (X = Cl, Br) Micro- and Nanostructures: Synthesis and Characterization'. In: *Crystal Growth & Design* 8.8 (2008), pp. 2995–3003. DOI: 10.1021/cg800116m. eprint: https://doi.org/10.1021/cg800116m. URL: https://doi.org/10.1021/cg800116m.

[150] Chuan Zhang et al. 'Synthesis of Square Bi2WO6 Nanoplates as High-Activity Visible-Light-Driven Photocatalysts'. In: *Chemistry of Materials* 17.13 (2005), pp. 3537–3545. DOI: 10.1021/cm0501517. eprint: https://doi.org/10.1021/cm0501517. URL: https://doi.org/10.1021/cm0501517.

[151] Tharwat Tadros. 'Ostwald Ripening'. In: *Encyclopedia of Colloid and Interface Science*. Ed. by Tharwat Tadros. Berlin, Heidelberg: Springer Berlin Heidelberg, 2013, pp. 820–820. ISBN: 978-3-642-20665-8. DOI: 10.1007/978-3-642-20665-8_124. URL: https://doi.org/10.1007/978-3-642-20665-8_124.

[152] Liu B. et al. 'Mesoscale organization of CuO nanoribbons: Formation of "dandelions"'. In: *Journal of the American Chemical Society* 126.26 (2004). Cited by: 841, pp. 8124–8125. DOI: 10.1021/ja048195o. URL: https://www.scopus.com/inward/record.uri?eid=2-s2.0-3042734818&doi=10.1021%5C%2fja048195o&partnerID=40&md5=648398982f259e5a0fd546eab737898e.

[153] Dong-Hong Wang et al. 'Nanosheet-constructed porous biocl with dominant 001 facets for superior photosensitized degradation'. In: *Nanoscale* 4.24 (2012), p. 7780. DOI: 10.1039/c2nr32533k. URL: https://pubs.rsc.org/en/content/articlelanding/2012/nr/c2nr32533k.

[154] Cuihua Tian et al. 'Cellulose nanofibrils enable flower-like BiOCl for high-performance photocatalysis under visible-light irradiation'. In: *Applied Surface Science* 464 (2019), pp. 606–615. ISSN: 0169-4332. DOI: https://doi.org/10.1016/j.apsusc.2018.09.126. URL: https://www.sciencedirect.com/science/article/pii/S016943321832542X.

[155] Shang M. et al. In: *Cryst. Growth Des.* 8 (2008), pp. 991–996. URL: https://www.scopus.com/inward/record.uri?eid=2-s2.0-84870956358&partnerID=40&md5=62ec70684ac4573c14b7d30ddbb220cd.

[156] KD Vernon-Parry. 'Scanning electron microscopy: an introduction'. In: *III-Vs Review* 13.4 (2000), pp. 40–44.

[157] Joseph I Goldstein et al. 'Backscattered electrons'. In: *Scanning electron microscopy and X-ray microanalysis*. Springer, 2018, pp. 15–28.

[158] William J. Wolfgong. 'Chapter 14 - Chemical analysis techniques for failure analysis: Part 1, common instrumental methods'. In: *Handbook of Materials Failure Analysis with Case Studies from the Aerospace and Automotive Industries*. Ed. by Abdel Salam Hamdy Makhlouf et al. Boston: Butterworth-Heinemann, 2016, pp. 279–307. ISBN: 978-0-12-800950-5. DOI: https://doi.org/10.1016/B978-0-12-800950-5.00014-4. URL: https://www.sciencedirect.com/science/article/pii/B9780128009505000144.

[159] John Konopka. *Options for Quantitative Analysis of Light Elements by SEM/EDS*. 2013. URL: https://tools.thermofisher.com/content/sfs/brochures/TN52523_E_0713M_LightElement_H.pdf.

[160] Mats Halvarsson et al. *SEM/EDX analysis of boron*. Jan. 2011. URL: http://fy.chalmers.se/~f10mh/Halvarsson/EM_intro_course_files/SEM_EDX%5C%20Boron.pdf.

[161] Mats Halvarsson. *Introduction to Energy Dispersive X-ray Spectrometry (EDS)*. May 2022. URL: http://fy.chalmers.se/~f10mh/Halvarsson/EM_intro_course_files/EDX%5C%20intro%5C%202.pdf.

[162] Peter Atkins et al. 'Atkins' Physical Chemistry'. In: Oxford University Press, 2014, pp. 476–518.

[163] Derek Albert Long. 'Raman spectroscopy'. In: *New York* 1 (1977).

[164] Dana Cialla-May et al. 'Theoretical principles of Raman spectroscopy'. In: *Physical Sciences Reviews* 4.6 (2019), p. 20170040. DOI: doi:10.1515/psr-2017-0040. URL: https://doi.org/10.1515/psr-2017-0040.

[165] Ewen Smith et al. *Modern Raman spectroscopy: a practical approach*. John Wiley & Sons, 2019.

[166] John R Ferraro. *Introductory raman spectroscopy*. Elsevier, 2003.

[167] Richard Osibanjo et al. *Infrared Spectroscopy*. Aug. 2020. URL: https://chem.libretexts.org/Bookshelves/Physical_and_Theoretical_Chemistry_Textbook_Maps/Supplemental_Modules_(Physical_and_Theoretical_Chemistry)/Spectroscopy/Vibrational_Spectroscopy/Infrared_Spectroscopy/Infrared_Spectroscopy.

[168] H.D. Lutz et al. 'Infrared and Raman spectroscopy in inorganic solids research'. In: *Journal of Molecular Structure* 511-512 (1999), pp. 69–75. ISSN: 0022-2860. DOI: https://doi.org/10.1016/S0022-2860(98)00630-9. URL: https://www.sciencedirect.com/science/article/pii/S0022286098006309.

[169] Andrei A. Bunaciu et al. 'X-Ray Diffraction: Instrumentation and Applications'. In: *Critical Reviews in Analytical Chemistry* 45.4 (2015). PMID: 25831472, pp. 289–299. DOI: 10.1080/10408347.2014.949616. URL: https://doi.org/10.1080/10408347.2014.949616.

[170] Thayumanasamy Somasundaram. *Radiation Contaminations in Powder X-Ray Diffraction (PXRD) Patterns*. PXRD Radiation Contaminations. Nov. 2015.

[171] Hayat Khan et al. 'Experimental methods in chemical engineering: X-ray diffraction spectroscopy—XRD'. In: *The Canadian Journal of Chemical Engineering* 98.6 (2020), pp. 1255–1266. DOI: https://doi.org/10.1002/cjce.23747. URL: https://onlinelibrary.wiley.com/doi/abs/10.1002/cjce.23747.

[172] Sverre M. Selbach et al. *LX3: Powder X-ray diffraction (XRD) Basic principles and instrumentation.* June 2022.

[173] Ashish Chauhan et al. 'Powder XRD technique and its applications in science and technology'. In: *J Anal Bioanal Tech* 5.5 (2014), pp. 1–5.

[174] T Ungár. 'Microstructural parameters from X-ray diffraction peak broadening'. In: *Scripta Materialia* 51.8 (2004), pp. 777–781. ISSN: 1359-6462. DOI: https://doi.org/10.1016/j.scriptamat.2004.05.007. URL: https://www.sciencedirect.com/science/article/pii/S1359646204002738.

[175] T. Ungár. 'The Meaning of Size Obtained from Broadened X-ray Diffraction Peaks'. In: *Advanced Engineering Materials* 5.5 (2003), pp. 323–329. DOI: https://doi.org/10.1002/adem.200310086. URL: https://onlinelibrary.wiley.com/doi/abs/10.1002/adem.200310086.

[176] Jasmina Hafizovic et al. 'The Inconsistency in Adsorption Properties and Powder XRD Data of MOF-5 Is Rationalized by Framework Interpenetration and the Presence of Organic and Inorganic Species in the Nanocavities'. In: *Journal of the American Chemical Society* 129.12 (2007). PMID: 17341071, pp. 3612–3620. DOI: 10.1021/ja0675447. URL: https://doi.org/10.1021/ja0675447.

[177] Liping Zhang et al. 'Identification of preferentially exposed crystal facets by X-ray diffraction'. In: *RSC Advances* 10 (Feb. 2020), pp. 5585–5589. DOI: 10.1039/D0RA00769B. URL: https://pubs.rsc.org/en/content/articlelanding/2020/ra/d0ra00769b.

[178] J. S. J. Hargreaves. 'Some considerations related to the use of the Scherrer equation in powder X-ray diffraction as applied to heterogeneous catalysts'. In: *Catalysis, Structure & Reactivity* 2.1-4 (2016), pp. 33–37. DOI: 10.1080/2055074X.2016.1252548. URL: https://doi.org/10.1080/2055074X.2016.1252548.

[179] Thomas R. Gordon et al. 'Nonaqueous Synthesis of TiO2 Nanocrystals Using TiF4 to Engineer Morphology, Oxygen Vacancy Concentration, and Photocatalytic Activity'. In: *Journal of the American Chemical Society* 134.15 (2012). PMID: 22444667, pp. 6751–6761. DOI: 10.1021/ja300823a. URL: https://doi.org/10.1021/ja300823a.

[180] Peter Eaton et al. *Atomic force microscopy.* Oxford university press, 2010.

[181] *ISCapture.* URL: https://iscapture.software.informer.com/4.1/.

[182] *ImageJ Image Processing and Analysis in Java.* URL: https://imagej.nih.gov/ij/.

[183] OriginLab Corporation. *OriginPro 2022 The Ultimate Software for Graphing Analysis.* Version 2021b. URL: https://www.originlab.com/.

[184] Oxford Instruments. *AZtec.* Version Live. 29th Nov. 2021. URL: https://nano.oxinst.com/products/aztec/.

[185] Petr Klapetek David Nečas (Yeti). Version 2.60. URL: http://gwyddion.net/.

[186] Microsoft Corporation. *Microsoft Excel.* Version 2019 (16.0). 24th Sept. 2018. URL: https://office.microsoft.com/excel.

[187] Renishaw plc. *WiRE.* 8th Dec. 2021. URL: https://www.renishaw.com/en/raman-software--9450.

[188] Cornell University. *Introduction to Raman spectroscopy.* As a manual at cornell.edu. URL: https://www.ccmr.cornell.edu/wp-content/uploads/sites/2/2016/08/Wire4_Training_Modules_Compilation-Part-2.pdf.

[189] Oxford Instruments. *alpha300 R – Raman Imaging Microscope.* URL: https://raman.oxinst.com/products/Raman-microscopes/raman-imaging-alpha300R.

[190] Guido Van Rossum et al. *Python 3 Reference Manual.* Scotts Valley, CA: CreateSpace, 2009. ISBN: 1441412697.

[191] S. D Gates-Rector et al. *Life expectancy.* data retrieved from International Center for Diffraction Data. 2019. DOI: https://doi.org/10.1017/S0885715619000812. URL: https://www.icdd.com/.

[192] Bruker Corporation. *DIFFRAC.EVA.* URL: https://www.bruker.com/en/products-and-solutions/diffractometers-and-scattering-systems/x-ray-diffractometers/diffrac-suite-software/diffrac-eva.html.

[193] Bruker Corporation. *DIFFRAC.TOPAS*. Version 5. URL: https://www.bruker.com/en/products-and-solutions/diffractometers-and-scattering-systems/x-ray-diffractometers/diffrac-suite-software/diffrac-topas.html.

[194] A. Rulmont. 'Raman spectra of a single crystal of BiOCl'. In: *Spectrochimica Acta Part A: Molecular Spectroscopy* 30.1 (1974), pp. 311–313. ISSN: 0584-8539. DOI: https://doi.org/10.1016/0584-8539(74)80235-7. URL: https://www.sciencedirect.com/science/article/pii/0584853974802357.

[195] Feifan Xu et al. 'Insights into Promoted Adsorption Capability of Layered BiOCl Nanostructures Decorated with TiO2 Nanoparticles'. In: *ACS Sustainable Chemistry & Engineering* 4.12 (2016), pp. 7013–7022. DOI: 10.1021/acssuschemeng.6b01920. eprint: https://doi.org/10.1021/acssuschemeng.6b01920. URL: https://doi.org/10.1021/acssuschemeng.6b01920.

[196] Yuxiang Yan et al. 'NaBH4-Reduction Induced Evolution of Bi Nanoparticles from BiOCl Nanoplates and Construction of Promising Bi@BiOCl Hybrid Photocatalysts'. In: *Catalysts* 9.10 (2019). ISSN: 2073-4344. DOI: 10.3390/catal9100795. URL: https://www.mdpi.com/2073-4344/9/10/795.

[197] Sunxian Weng et al. 'Facile in situ synthesis of a Bi/BiOCl nanocomposite with high photocatalytic activity'. In: *J. Mater. Chem. A* 1 (9 2013), pp. 3068–3075. DOI: 10.1039/C2TA01004F. URL: http://dx.doi.org/10.1039/C2TA01004F.

[198] Yawen Li et al. 'Bi superlattice nanopolygons at BiOCl (001) nanosheet assembled architectures for visible-light photocatalysis'. In: *Materials Research Bulletin* 101 (2018), pp. 39–47. ISSN: 0025-5408. DOI: https://doi.org/10.1016/j.materresbull.2017.12.041. URL: https://www.sciencedirect.com/science/article/pii/S0025540817332580.

[199] Paul McMillan et al. 'A Raman study of pressure-densified vitreous silica'. In: *The Journal of Chemical Physics* 81.10 (1984), pp. 4234–4236. DOI: 10.1063/1.447455. URL: https://doi.org/10.1063/1.447455.

[200] J. H. Parker et al. 'Raman Scattering by Silicon and Germanium'. In: *Phys. Rev.* 155 (3 Mar. 1967), pp. 712–714. DOI: 10.1103/PhysRev.155.712. URL: https://link.aps.org/doi/10.1103/PhysRev.155.712.

[201] Paul Spizzirri et al. 'Nano-Raman spectroscopy of silicon surfaces'. In: *Materials Forum* 34 (Feb. 2010).

[202] E Loh. 'Optical vibrations in sheet silicates'. In: *Journal of Physics C: Solid State Physics* 6.6 (Mar. 1973), pp. 1091–1104. DOI: 10.1088/0022-3719/6/6/022. URL: https://doi.org/10.1088/0022-3719/6/6/022.

[203] L. V. Haley et al. 'An investigation of the lattice and interlayer water vibrational spectral regions of muscovite and vermiculite using Raman microscopy. A Raman microscopic study of layer silicates'. In: *Journal of Raman Spectroscopy* 13.2 (1982), pp. 203–205. DOI: https://doi.org/10.1002/jrs.1250130217. eprint: https://analyticalsciencejournals.onlinelibrary.wiley.com/doi/pdf/10.1002/jrs.1250130217. URL: https://analyticalsciencejournals.onlinelibrary.wiley.com/doi/abs/10.1002/jrs.1250130217.

[204] Siddesh Matti. 'Dry sliding wear behavior of Mica, Fly Ash and Red Mud particles reinforced Al7075 alloy hybrid metal matrix composites'. In: *Indian Journal of Science and Technology* 14 (Jan. 2021), pp. 310–318. DOI: 10.17485/IJST/v14i4.2081.

[205] Hussein I. Ally et al. 'Defluoridation of drinking water using coalesced and un-coalesced mica'. In: *Applied Water Science* 10.2 (Feb. 2020). Copyright - Applied Water Science is a copyright of Springer, (2020). All Rights Reserved. This work is published under http://creativecommons.org/licenses/by/4.0/ (the "License"). ISSN: 21905487. URL: https://www.proquest.com/scholarly-journals/defluoridation-drinking-water-using-coalesced-un/docview/2347101212/se-2.

[206] M. Gharrabi. 'The transformation of illite to muscovite in Pelitic Rocks: Constraints from X-ray diffraction'. In: *Clays and Clay Minerals* 46.1 (1998), pp. 79–88. DOI: 10.1346/ccmn.1998.0460109.

[207] Barbara Lafuente et al. '1. The power of databases: The RRUFF project'. In: *Highlights in Mineralogical Crystallography*. Ed. by Thomas Armbruster et al. De Gruyter (O), 2015, pp. 1–30. DOI: doi:10.1515/9783110417104-003. URL: https://doi.org/10.1515/9783110417104-003.

[208] Robert T. Downs et al. 'The American Mineralogist crystal structure database'. In: (July 2002). URL: https://rruff.info/Muscovite/R040104.

Appendix

A Additional OM images

Optical microscope images of cleaved mica substrate sheets from previous synthesis done at UC Berkeley [1].

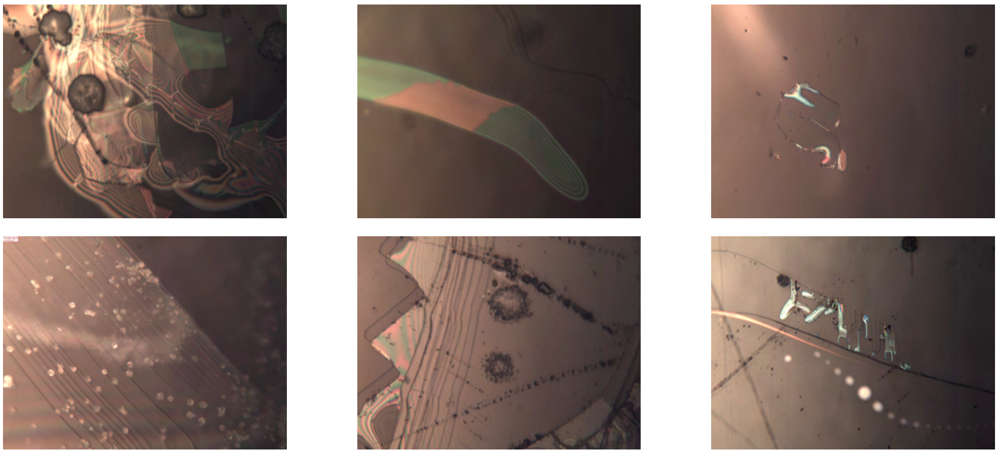

Figure 67: Irregularities and cracks observed on the mica substrate by using OM at UC Berkeley

B SEM size analysis

SEM images were taken for the nine points the substrate was divided into. At every point both an overview image and a zoomed in image used for size analysis was captured. Illustrated below are silica substrates and a mica substrate, this is done in order to show the difference in crystals structure on the two substrates.

For the silica substrate, one section shows few crystals, one shows an intermediate amount while the last one shows an abundance of crystals. This is done to give insight into how the crystal density could vary. Lastly, an image is given displaying how the substrate would look when it was covered in white powder making an analysis impossible.

Si-15.5cm substrate was analyzed, displaying an example of few crystals in section 1.

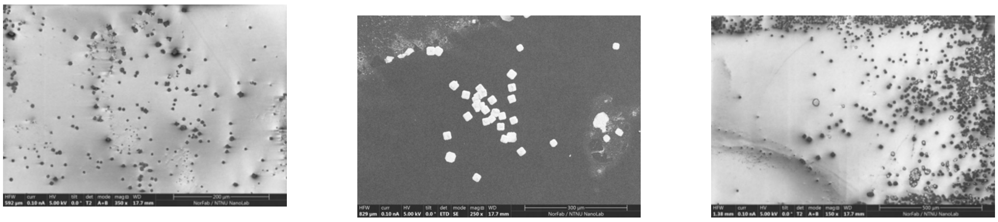

(a) Si-15.5cm 1.1 squares and circles.

(b) Si-15.5cm 1.2 squares.

(c) Si-15.5cm 1.3 squares.

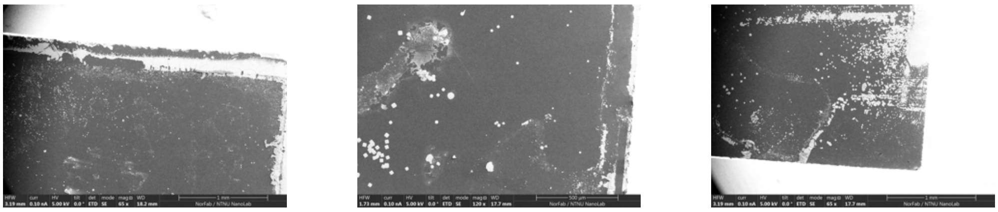

(d) Si-15.5cm 1.1 overview.

(e) Si-15.5cm 1.2 overview.

(f) Si-15.5cm 1.3 overview.

Figure 68: Si-15.5cm displaying low crystal density substrate section 1.

Section 3 of the Si-3min substrate displays a middle amount of crystals.

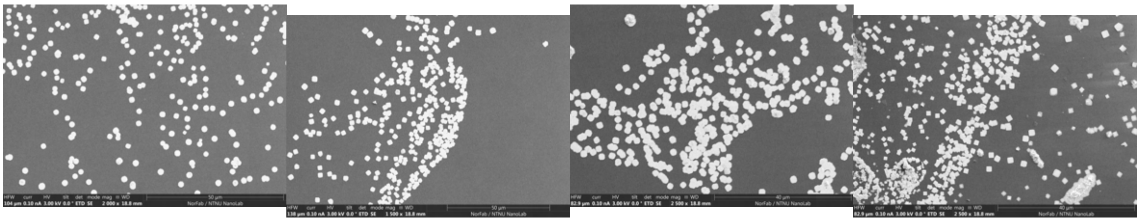

(a) Si-3min 3.1 squares and octagons/circles.

(b) Si-3min 3.1 squares.

(c) Si-3min 3.2 octagons/circles.

(d) Si-3min 3.2 squares.

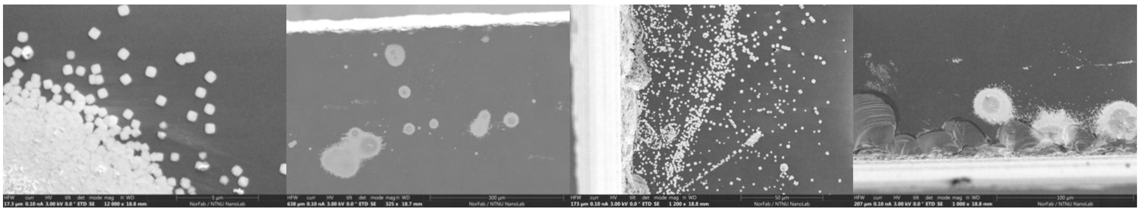

(e) Si-3min 3.3 squares.

(f) Si-3min 3.1 overview.

(g) Si-3min 3.2 overview.

(h) Si-3min 3.3 overview.

Figure 69: Si-3min section 3 displaying medium crystal density.

Section 1 of the Si-1min substrate shows growth of a large amount of crystals.

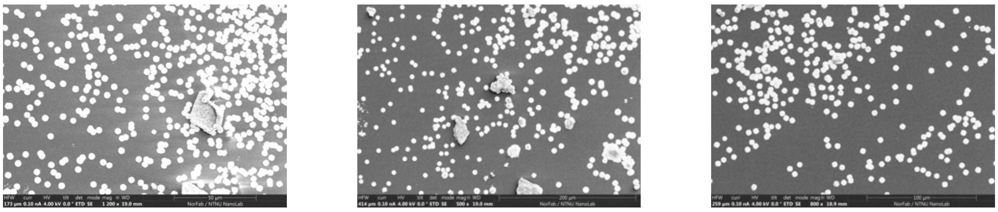

(a) Si-1min 1.1 octagons/circles.

(b) Si-1min 1.2 octagons/circles and few squares.

(c) Si-1min 1.3 octagons/circles.

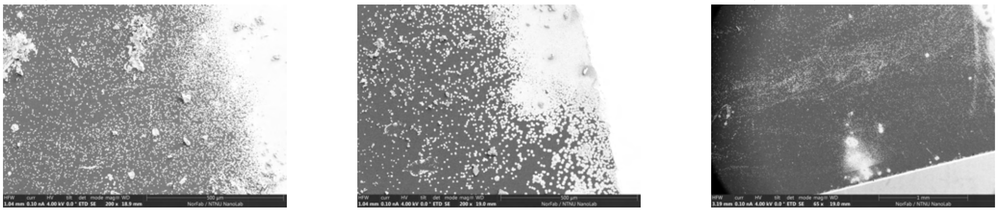

(d) Si-1min 1.1 overview.

(e) Si-1min 1.2 overview.

(f) Si-1min 1.3 overview.

Figure 70: Si-1min section 1 showing large crystal density.

A display of section 1 on Mica-900W substrate.

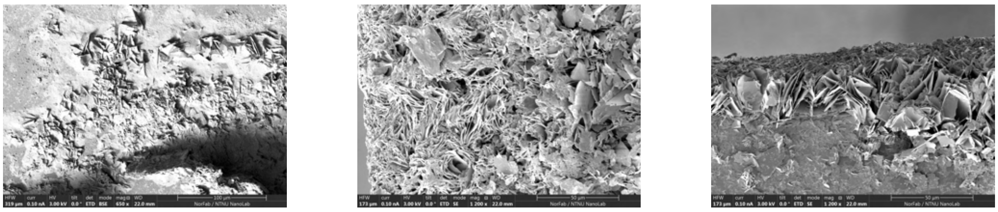

(a) Mica-900W 1.1 flower petals.

(b) Mica-900W 1.2 flower petals.

(c) Mica-900W 1.3 flower petals.

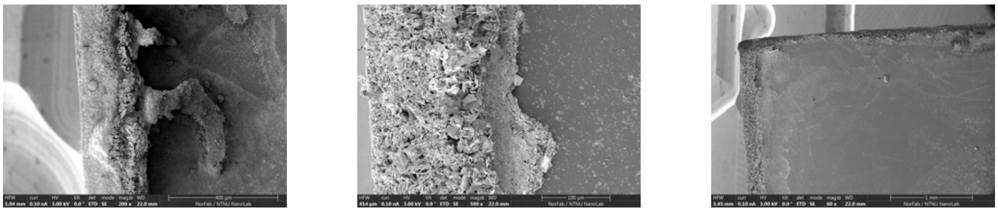

(d) Mica-900W 1.1 overview.

(e) Mica-900W 1.2 overview.

(f) Mica-900W 1.3 overview.

Figure 71: Mica-900W section 1 showing crystal growth on mica.

A display of a SEM picture obtained at a point where there was visible white precursor powder on the substrate surface.

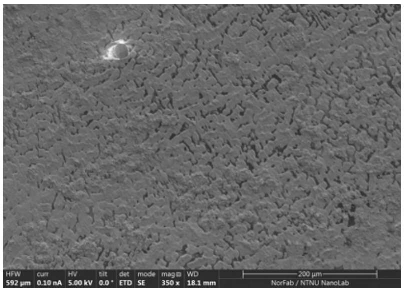

Figure 72: Image showing an area of the silica substrate that was covered in white powder.

C Additional EDS results

Following figures shows additional EDS results done at UC Berkeley. It illustrates areas of interest on the silica substrate L where there is noticeable flower-structure formation on square crystals. The aim was to analyze the flower-structure observed on the substrate.

Figure 73a shows a small area being analyzed for elemental composition thus leaving out the substrate, where each element is coordinated with one color. The narrow area being analyzed shows a flower-like structure growing on top of squares. It is clear that there is no silicon, and there is no chlorine detected. Carbon and bismuth corresponding to the green color is present, as well as oxygen identified by the turquoise color.

Similarly, the Figure 73b shows this type of analysis but for a wider area. In this figure carbon and bismuth are prominent.

The Figure 73c is an illustration of a elemental mapping, where detected elements are associated with a specific color which is displayed in the image. From this picture it is not straightforward to differentiate between the composition of the substrate and the structure. This is because it appears as all the elements are detected across the whole area without much contrast other than a small variation in intensity where some parts seems brighter than other.

A semi-quantitative plot of discovered elements are given in Figure 73d from the EDS layered image in Figure 73b. This EDS spectrum shows high levels of bismuth, oxygen, silicon and then chlorine which is supportive of results presented in EDS result Section 4.2.

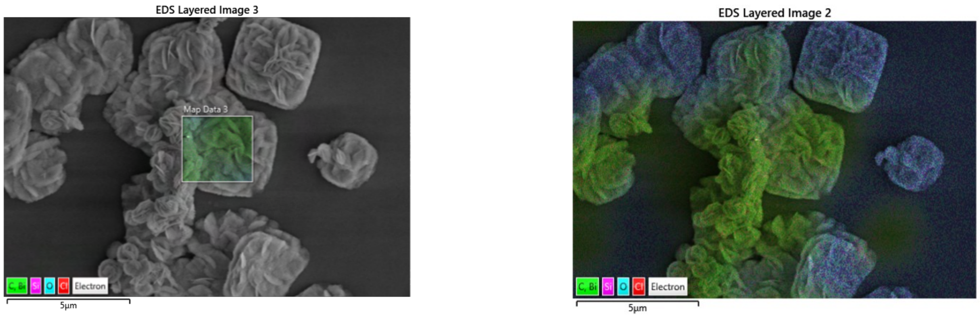

(a) Narrow area being analyzed.

(b) A layered image with detected elements.

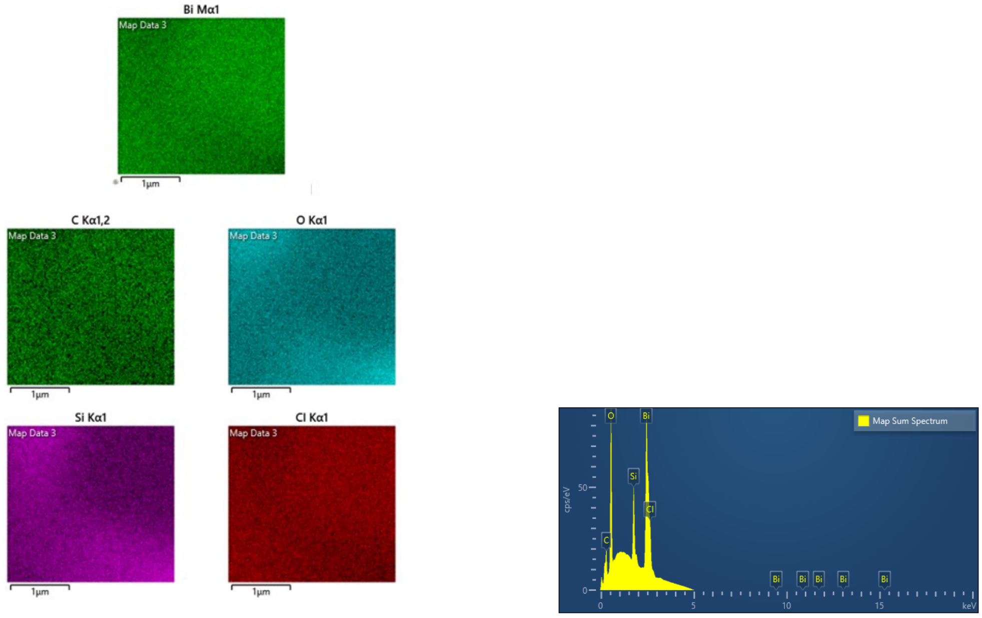

(c) Elemental distribution mapping of analyzed area.

(d) EDS spectrum of analyzed area.

Figure 73: Illustration of EDS results on silica L, where the aim was to identify elements in the flower-structure.

D Additional AFM images

In addition to the AFM images presented earlier in AFM result Section 4.3, this section contains images that were taken with the AFM. This section contains both observed structures as well as images that were analyzed for the measurements given in Table 8. In addition to these, there is a color and thickness analysis section.

D.1 Observations done

Figure 74 shows an irregular shaped crystal with a hole in the middle. This phenomenon observed in AFM was not analyzed for thickness measurements.

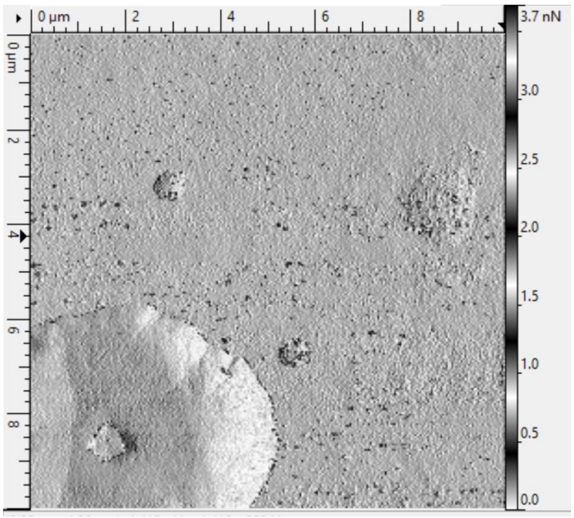

Figure 74: Irregular shapes with a hole in the center.

Figure 75 was as an illustration of a smooth surface crystal with no granular deposition and no crack as observed in Figure 50a. This figure is a peak force error image of the corresponding Zsensor image that was thickness analyzed shown in Figure 77.

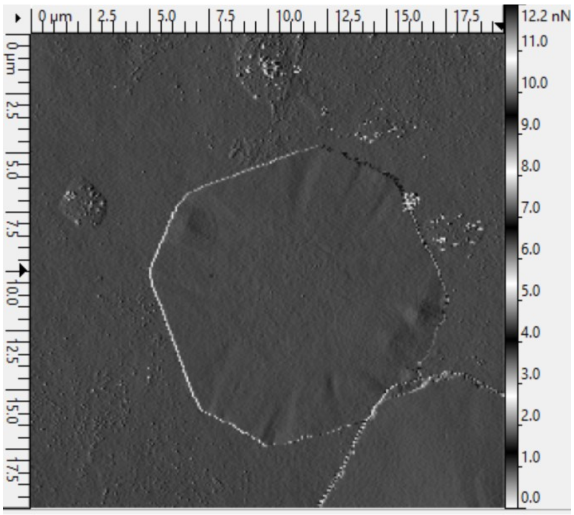

Figure 75: Figure of a smooth surface crystal.

D.2 Large octagons

The Figures 76, 77 and 78 where used in the measurements and analysis of large octagons. For Figure 76 the uppermost octagon was analyzed.

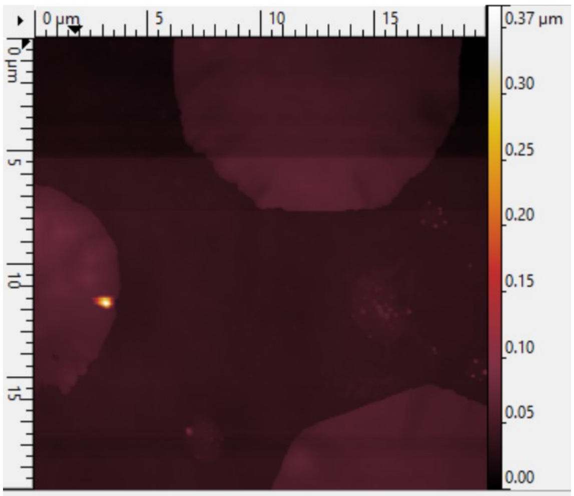

Figure 76: Picture of large octagon used in analysis.

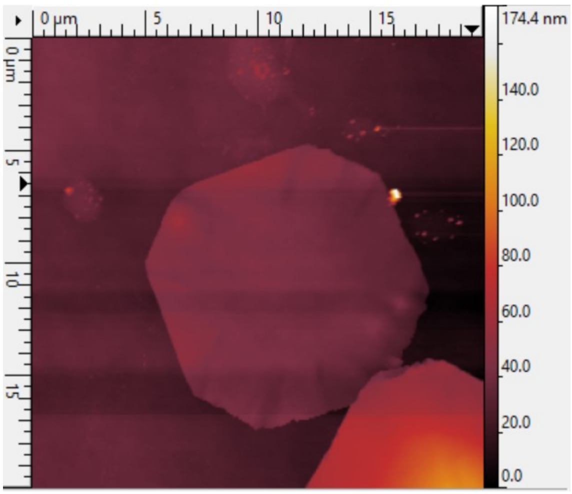

Figure 77: Picture of large octagon used in analysis.

For Figure 78 the octagon to the left was analyzed.

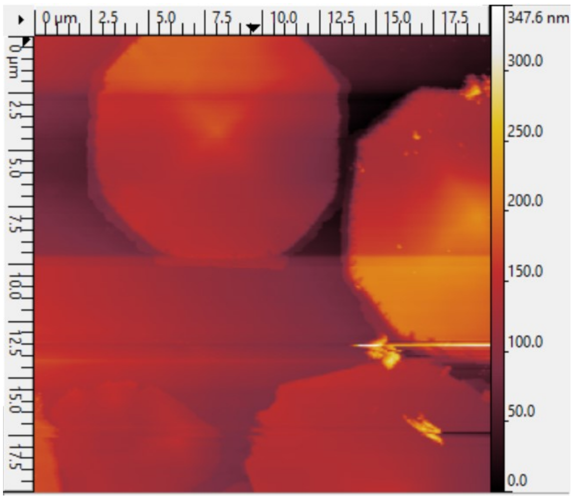

Figure 78: Picture of large octagon used in analysis.

D.3 Nanoframes

Figure 79 shows the peak force error image of the square crystal analyzed and illustrated in Figure 46a. This image is displayed to give a greater detail into the structure, where the cracks on the surface is more prominent.

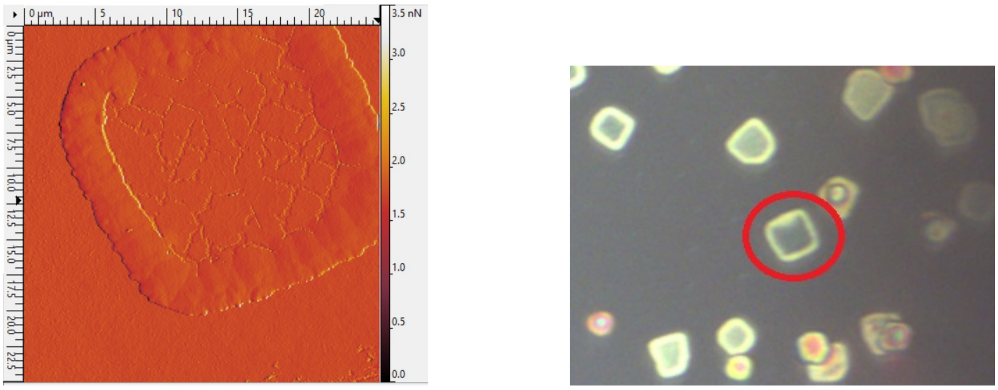

(a) Nanoframe with peak force imaging.

(b) Captured image.

Figure 79: Illustration of AFM images of a large nanoframe used in analysis.

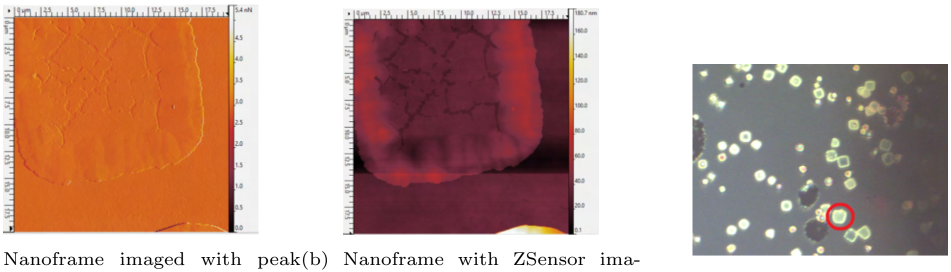

(a) Nanoframe imaged with peak force error.

(b) Nanoframe with ZSensor imaging.

(c) Captured image.

Figure 80: Illustration of AFM images of nanoframe used in analysis.

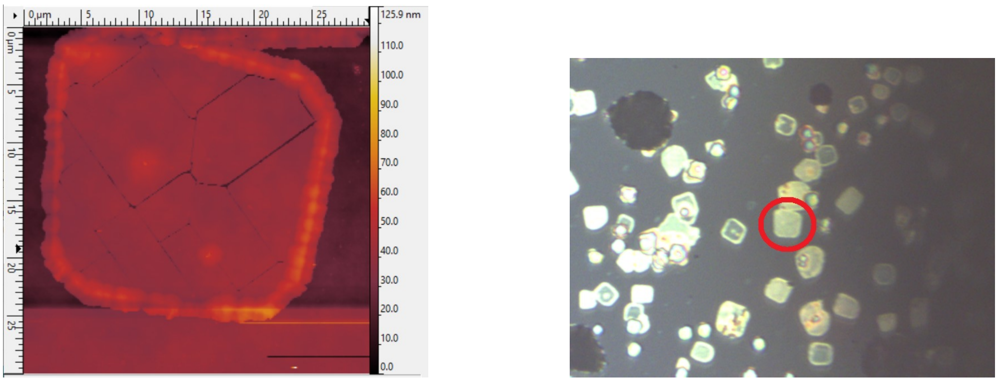

(a) Nanoframe with ZSensor imaging.

(b) Captured image.

Figure 81: Illustration of AFM images of a large nanoframe used in analysis.

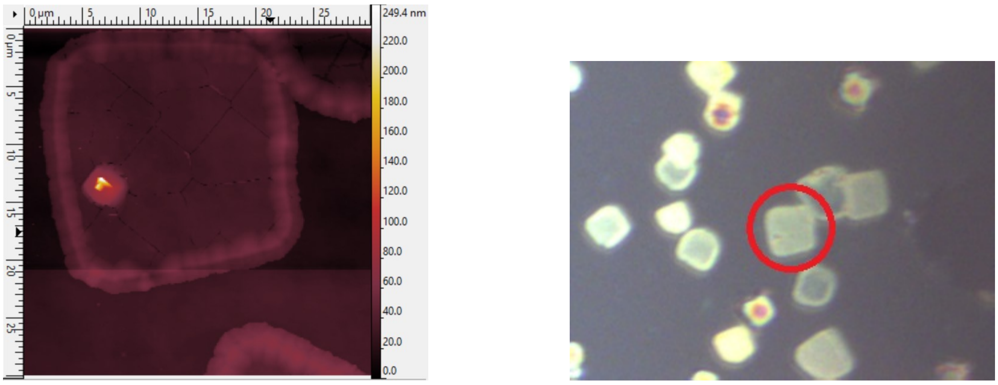

(a) Nanoframe with ZSensor imaging.

(b) Captured image.

Figure 82: Illustration of AFM images of a large nanoframe used in analysis.

D.4 Color and thickness analysis

The thickness of different colors was also done, solely focusing on square crystals and disregarding other morphologies.

The following figures were used in the thickness analysis presented in Table 9. The captured image is also displayed to give a visual of the color being analyzed.

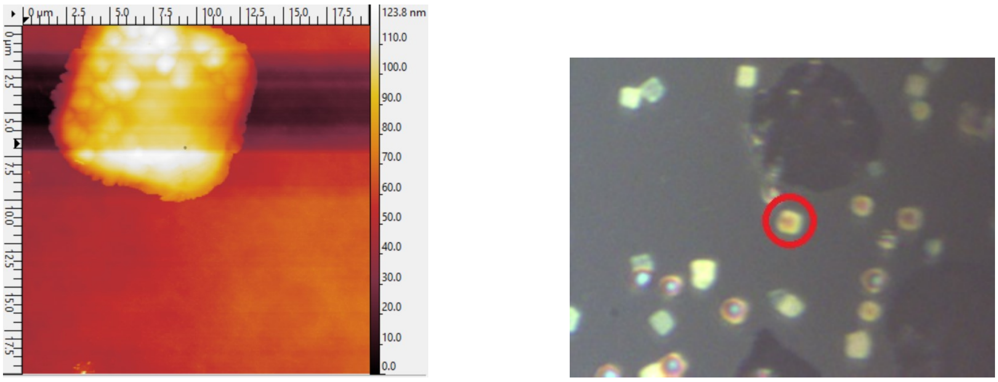

(a) Zsensor imaging of yellow square.

(b) Captured image of the yellow square being analyzed.

Figure 83: Illustration of AFM image of yellow square.

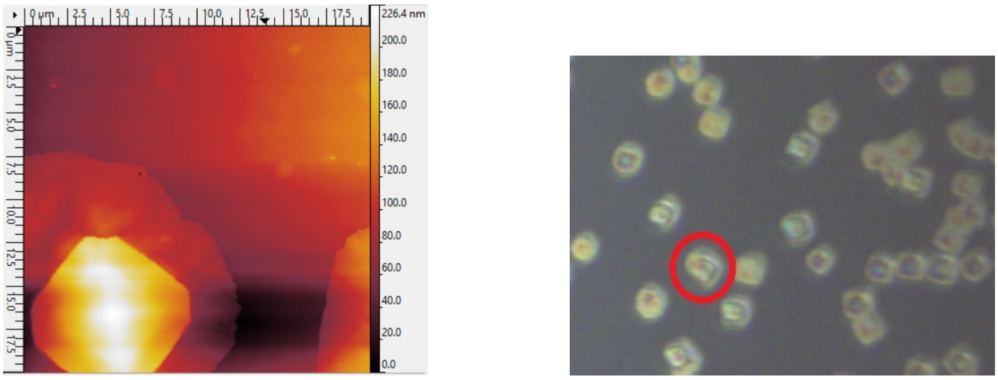

(a) Zsensor imaging of blue and red square.

(b) Captured image of the blue and red square being analyzed.

Figure 84: Illustration of AFM image of blue and red square.

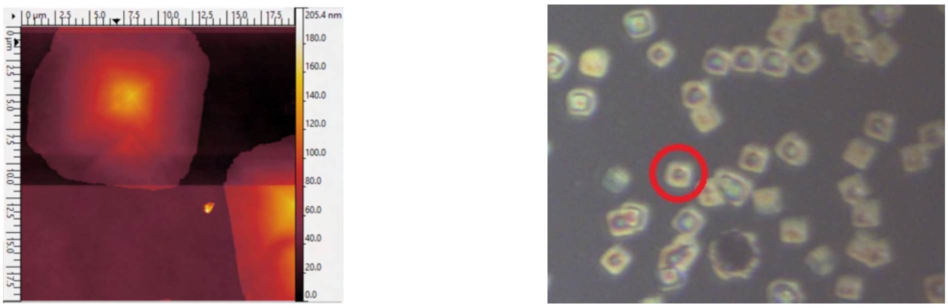

(a) Zsensor image of yellow and red square.

(b) Captured image of the yellow and red square.

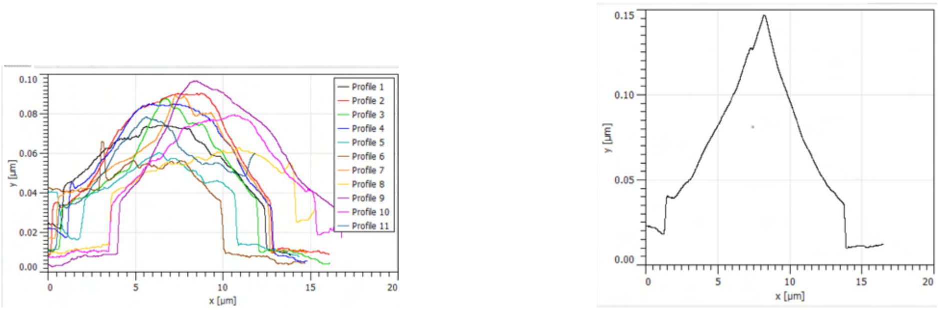

(c) Thickness profile.

(d) Peak appearing at the center of the crystal.

Figure 85: Illustrations of AFM analysis of a yellow and red square.

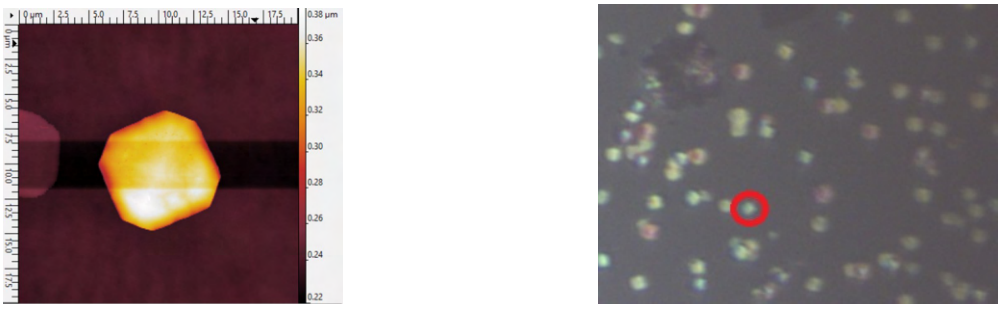

(a) Zsensor imaging of blue square.

(b) Captured image of the blue square being analyzed.

Figure 86: Illustration of AFM image of blue square.

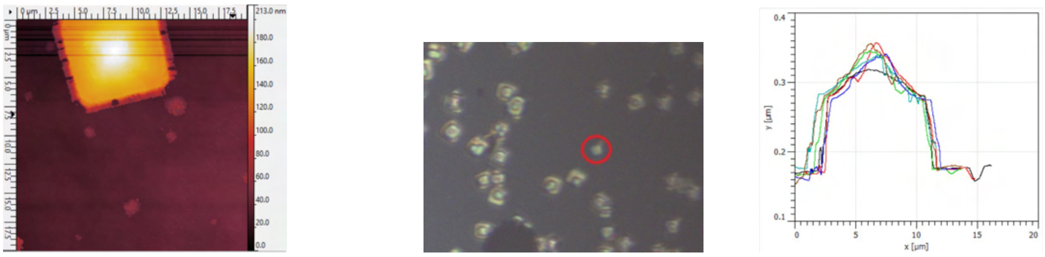

(a) Zsensor imaging. (b) Captured image. (c) Thickness profile.

Figure 87: Illustration of AFM analysis of blue square.

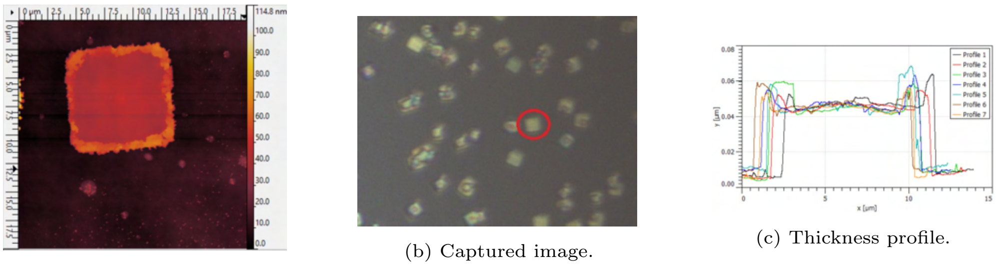

(a) Zsensor image. (b) Captured image. (c) Thickness profile.

Figure 88: AFM analysis of a yellow square.

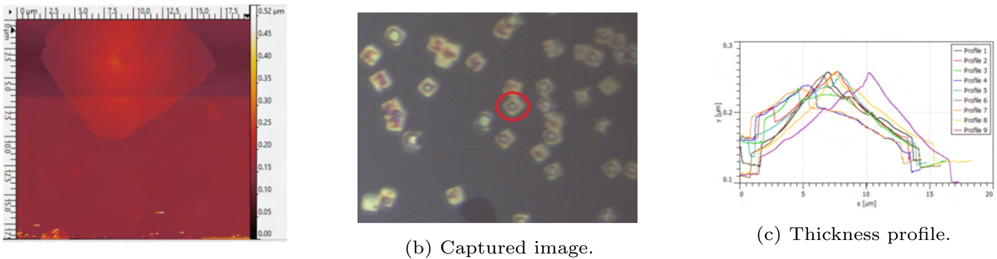

(a) Zsensor image. (b) Captured image. (c) Thickness profile.

Figure 89: AFM analysis of a blue, red and yellow square.

E XRD calculations

Calculations of lattice spacing, $\mathrm{d_{hkl}}$ was performed using Excel [186]. By using Bragg's law 3 given in Section 2.5.4 the lattice spacing d can be calculated for each diffraction angle.

Filling in n=1, $\lambda = 0.15406$ nm for copper (Cu) X-Rays, the θ is half of the diffraction angle and by reconstructing the Bragg's law, Equation 3, the lattice spacing, d can be calculated. Equation 6 shows the rearrangement of the Bragg's law, Equation 3, and calculation of d for the first diffraction angle of silica I, 2θ=11.92°.

$$d[nm] = \frac{n \cdot \lambda}{2 \cdot \sin\theta} = \frac{1 \cdot 0.15406}{2 \cdot \sin(5.96)} = 0.742 \tag{6}$$

2θ Silica I [°]	11.92	24.10	25.83	32.53	33.41	36.47	40.89	46.69	49.84	53.45	54.18	54.89	58.66	60.63
Facet (hkl)	(001)	(002)	(101)	(110)	(102)	(003)	(112)	(200)	(113)	(202)	(211)	(104)	(212)	(114)
$\mathrm{d_{hkl}}$ [nm]	0.742	0.369	0.345	0.275	0.268	0.246	0.221	0.194	0.183	0.171	0.690	0.167	0.157	0.153

Table 13: Silica 2θ values, facets and calculated lattice spacing

2θ Mica J [°]	11.97	24.10	25.86	32.51	33.45	36.53	40.90	46.65	49.72	53.36	54.18	55.14	58.62	60.58
Facet (hkl)	(001)	(002)	(101)	(110)	(102)	(003)	(112)	(200)	(113)	(202)	(211)	(104)	(212)	(114)
$\mathrm{d_{hkl}}$ [nm]	0.739	0.369	0.344	0.275	0.268	0.246	0.220	0.195	0.183	0.172	0.169	0.166	0.157	0.153

Table 14: Mica 2θ values, facets and calculated lattice spacing

After calculating the lattice spacing d, the lattice constant c was calculated for BiOCl on both silica and mica XRD analysis in order to compare with the database BiOCl. By using the Equation 4 and filling in known constants. The lattice constant a = 0.388551 nm [191]. This value is from the database BiOCl in order to see the eventual shift between calculated lattice constant c and the database established c.

The c was calculated for each facet (hkl) by rearranging Equation 4, using $a = 0.388551$ nm and using the calculated d from Table 13 and Table 14 for silica and mica, respectively. The rearranged equation is exhibited in Equation 7 showing calculation for silica's first diffraction angle at $2\theta = 11.92$°corresponding to the (001) facet. This procedure was repeated for every diffraction angle and corresponding facet. Then an average c was calculated for silica and mica. Silica $c = 0.73815858$ nm, mica $c = 0.737935716$ nm. Database BiOCl $c = 0.73489$ nm [191].

$$\begin{aligned} c[nm] &= \sqrt{\frac{l^2}{\frac{1}{d^2} - \frac{h^2+k^2}{a^2}}} \\ &= \sqrt{\frac{1^2}{\frac{1}{0.742^2} - \frac{0^2+0^2}{0.388551^2}}} = 0.742 \end{aligned} \tag{7}$$

F Synthesis with varying amount of source

From the last synthesis the parameter examined was amount of precursor. As the scale did not function adequate in the operational weight range, the difficulties with placing the precursor and preventing it from falling off the substrate, a quantitative value of amount of precursor could not be given. Instead pictures of the source substrates were taken to give an indication of the difference in precursor amount used in the parallels.

Figure 90 shows the variation in amount of precursor, $BiCl_3$ used in the three parallels for the last synthesis before heating. Where the first parallel used a small amount, the second used and the third used an exaggerated amount covering the whole substrate surface. It is worthy to note that the first parallel had an equal amount of precursor as the first two synthesis before changing the procedure of precursor handling. The amount used in the second parallel is approximately equivalent with the amount of $BiCl_3$ used in the synthesis schemes following the procedure change.

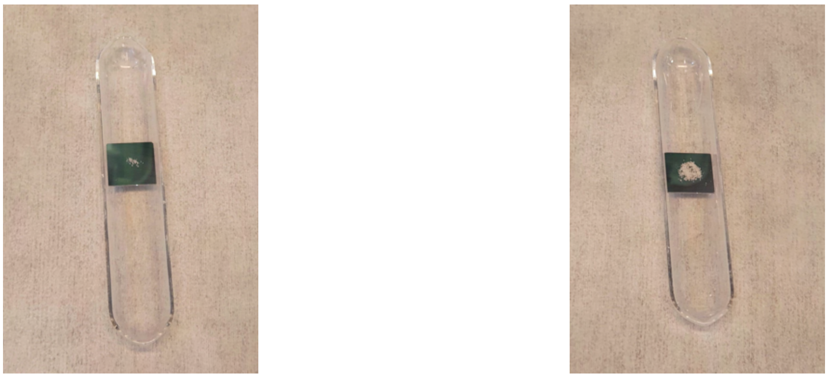

(a) Amount of $BiCl_3$ used in parallel 1, Si-small.

(b) Amount of $BiCl_3$ used in parallel 2, Si-medium.

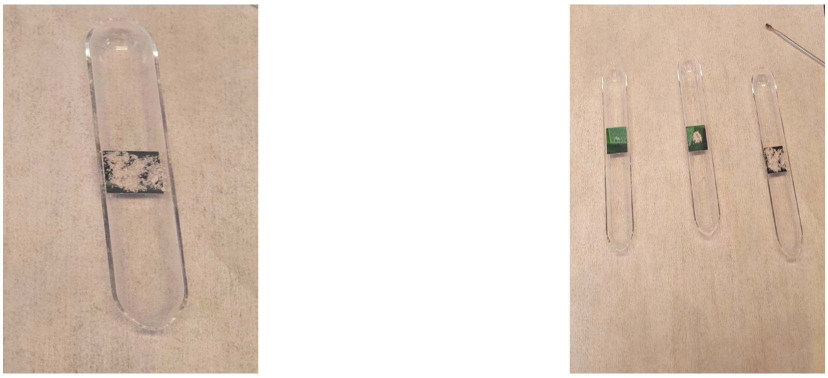

(c) Amount of $BiCl_3$ used in parallel 3, Si-large.

(d) Comparison of the three parallels before heating.

Figure 90: Illustration of the amount of precursor used in each individual parallel for the synthesis changing amount of precursor.

The quartz combustion boats for parallel 1 and parallel 3 after heating are illustrated in Figure 91b. This is an indication of how much source there was and that some, despite efforts, fell off the surface of the substrate and into the boat.

(a) Quartz combustion boat from parallel 1, Si-small.
(b) Quartz combustion boat from parallel 3, Si-large.

Figure 91: Illustration of the quartz combustion boats used in parallel 1 and 3.

G Code

The code for plotting Raman graphs from a text file with the intensity and wavelength is given below. The peak height threshold and peak distance threshold were changed depending on the dataset for each Raman plot.

```python
import matplotlib.pyplot as plt
import pandas as pd
from scipy.signal import find_peaks

# Variables
file_path       ='C:/Users/rogde/Desktop/Master/VibekeR_Raman/Spectrum--002--Spec.Data.txt'
peak_height_threshold = 1500
peak_dist_threshold   = 10

# Load data
data      = pd.read_csv(file_path, sep='\t',header=0, usecols=[0,1], names=['Wave','Intensity'])
intensity = data['Intensity'].to_numpy()
wave      = data['Wave'].to_numpy()

# Find peaks
peak_idx,peak_properties = find_peaks(intensity, height=peak_height_threshold,...
                                      distance=peak_dist_threshold)

# Plot
fig = plt.figure()
ax=fig.subplots()
ax.plot(wave,intensity,label='Spectrum')
ax.scatter(wave[peak_idx], intensity[peak_idx], color="r", s=35, marker=".",label='Peaks')
ax.legend()
plt.xlabel("Wave [1/cm]", fontsize=12)
plt.ylabel("Intensity [a.u.]", fontsize=12)
plt.show()
```

Vibeke Rogde

Low-temperature microwave synthesis of ternary-layered

NTNU
Norwegian University of
Science and Technology